Influence of Casting Process Parameters on Macrosegregation in Large Size Steel Ingots Using Experimentation and Simulation

by

Chunping ZHANG

MANUSCRIPT-BASED THESIS PRESENTED TO ÉCOLE DE TECHNOLOGIE SUPÉRIEURE IN PARTIAL FULFILLMENT OF THE REQUIREMENTS FOR THE DEGREE OF DOCTOR OF PHILOSOPHY PH.D.

MONTREAL, FEBRUARY 21ST 2020

ÉCOLE DE TECHNOLOGIE SUPÉRIEURE
UNIVERSITÉ DU QUÉBEC

ACKNOWLEDGMENT

and help in my work and life. We worked together on the experimentations and simulations and I appreciate his enthusiasm, attentiveness, carefulness, diligence and amazing ability. Great thanks go to Dr. Mahammad Saadati for training me on SEM and EBSD machine. Many thanks go to Dr. Davood Shahriari for his help in the first stage of the establishment of the FEM models, in the measurement of temperature profiles during casting and in the performance of tension and solidification tests using thermomechanical simulators. It was my pleasure to work with all these experts during my PhD pursuit.

My utmost gratitude goes to my parents Mr. Dongmin Zhang, Ms. Shuhua Yuan and my brothers, Mr. Zhigang Zhang and Mr. Zhiqiang Zhang, for their consistent support and love throughout my study.

Ultimately, I'm deeply indebted to my husband, Mr. Weimin Liu, and my son, Mr. Qikai Liu. Their unconditional love, unparalleled motivation, consistent encouragement and complete understanding enabled me to concentrate and focus on my work and make the PhD pursuit a possible journey.

Influence des paramètres du processus de coulée sur macroségrégation dans les grands lingots d'acier au moyen d'expérimentation et modélisation

Chunping ZHANG

RÉSUMÉ

Ce projet vise à développer un modèle numérique fiable qui peut prédire la sévérité et l'étendue de la macroségrégation dans un lingot de 40 tonnes métriques d'acier au carbone faiblement allié à haute résistance mécanique, ainsi que leurs changements en fonction des paramètres du processus de coulée, en vue de minimiser ce défaut important.

Pour atteindre cet objective, le code commercial d'éléments finis, Thercast®, était d'abord choisi pour le déroulement des simulations. Cette décision a été prise sur la base d'un examen critique de la littérature concernant les techniques de modélisation qui sont apparues ces soixante dernières années, sur la puissante capacité de ce logiciel, et aussi sur son fonctionnement de modélisations tridimensionnelles du remplissage et de la solidification à l'aide d'un modèle biphasé solide-liquide.

Dans un premier temps, les éléments susceptibles d'introduire l'incertitude ont été éliminés du modèle. Par exemple, un modèle 3-D axisymétrique un 24ème de la totalité du système du moulage a été considéré suffisamment représentatif pour l'exécution des simulations dans ce projet. Une taille moyenne de cellules de 35 mm a été définie pour la discrétisation du modèle, sur la base de la détermination des conditions d'équilibre entre précision et temps de calcul et aux études de sensibilité préliminaire. Les conditions limites du modèle ont été mises en place par les pratiques industrielles, qui ont pris en compte non seulement les conditions locales et les échanges thermiques entre l'acier et les composants du moule, mais aussi les échanges mutuels entre eux.

Les paramètres dépendants de la température des matériaux concernés, reflétant les comportements thermodynamiques, thermomécaniques et thermodiffusion, ont été déterminés par voie du logiciel Thermo-Calc®, de la littérature, des équations empiriques, de la base de données du logiciel Thercast®, de l'industrie, des calculs théoriques, ainsi que des essais de traction réalisés en laboratoire à différente température. L'applicabilité des logiciels et des équations a été vérifiée auparavant. La planification expérimentale a été basée sur des essais de simulation.

La loi de mélange s'est avérée une bonne approximation pour représenter la microségrégation et décrire le comportement physique du lingot de l'acier, après les examens comparatifs sur différents schémas de microségrégation. Le modèle thermomécanique a été pris comme formulation de base pour les études paramétriques subséquents en termes de l'influence du retrait thermomécanique et des aspects expérimentaux.

Par la suite, le comportement de solidification à a variation des paramètres du processus de moulage, tel que la vitesse de remplissage, la température surchauffe de fusion et la température de départ du moule, à l'aide du modèle fiable qui a été établi. Les trois

paramètres faisaient l'objet d'étude du fait de la manque de données pertinentes dans la littérature. Les variables étudiées concernaient les vitesses de remplissage de 0.084, 0.107, 0.145 m/min (avec une durée de remplissage de 38, 30, 22 min), les températures surchauffes de fusion de 75, 65, 55 °C et les températures de départ du moule de 50, 120, 250 °C. Ces paramètres de coulée formaient les conditions les plus fréquentes dans l'industrie pendant la coulée des lingots de grande taille.

Les résultats de cette étude ont permis de démontrer qu'une réduction du temps de remplissage, une surchauffe plus basse et un moule initialement plus froid peuvent contribuer à la diminution de l'intensité de macroségrégation, dans la portion supérieure du lingot, le long de l'axe de la pièce et dans la région centre/périphérie enrichie du soluté. Ces effets ont été associés aux courants du liquide, induits par l'opération de coulage, par la convection, par la déformation thermomécanique des phases, et par la variation du gradient de température et des vitesses de solidification. Les prévisions de tous les cas étudiés ont été validées par des données de laboratoire, telles que les structures macro et microscopiques, la distribution des concentrations de solutés, les modifications dimensionnelles du casting et les variations de la température sur la face extérieure du moule.

Les résultats recueillis favoriseront une meilleure compréhension des mécanismes sous-jacents à l'origine de la formation de macroségrégation dans le processus de la coulée. Ils pourraient être utiles pour la conception du processus de coulée d'un lingot donné. Ils peuvent servir à l'industrie pour améliorer la qualité du lingot de grande taille et la productivité des aciers à grande valeur ajoutée, qui sont susceptibles de macroségrégation.

Mots-Clés: macroségrégation, grands lingots d'acier, expérimentation, modélisation

Influence of casting process parameters on macrosegregation in large size steel ingots using experimentation and simulation

Chunping ZHANG

ABSTRACT

The present project aims to develop a reliable numerical model to predict the extent and severity of macrosegregation in a 40MT (metric ton) medium-carbon high strength steel ingot as a function of casting parameters with the view to minimize the occurrence of the macro-scale defect. For this purpose, the commercial finite element modeling (FEM) code Thercast® was at first determined to be used for the simulation work. This basis of such a decision rested on the critical literature review on the evolution of solidification modeling technique in the past 60 years, the powerful computing capability of the software and its performance of the three-dimensional simulations of mold filling and solidification based on a volume-averaged solid-liquid two-phase model.

The factors influencing model accuracies were eliminated one by one. For instance, an axisymmetric model in the dimension of 1/24 of the actual casting system was determined to be representative enough for the necessary simulation work. An average general cell size of 35 mm was identified to be the discretization parameter for its realization of the compromise between computational accuracy and efficiency based on series of sensitivity studies of solidification to mesh size. Modeling boundary conditions were set based on industrial practice, which took into account the local friction and the thermal exchange between the steel and the mold components, as well as the mutual exchange between mold components themselves in the casting system. Input temperature-dependent parameters of all concerned materials, reflecting their thermodynamic, thermomechanic and thermodiffusion behaviors, were identified by means of combined approaches of computational thermodynamics program Thermo-Calc® software, literature reports, published empirical equations, Thercast® software material database, industry sources, theoretic calculations, as well as room and high temperature tension tests in laboratory. The applicability of the used softwares and models was verified before applying them to the investigated steel. The experimental planning was strictly formulated based on simulation tests. Lever rule microsegregation model was ascertained to be the most reasonable depiction of the physical behavior of the steel in study in large-size cast ingot. This selection was made after comparative examinations of various microsegregation schemes against experimental measurements, together with subsequent adoption to the regions formed in different stages of the solidification process. A thermomechanical model was finally deemed as the baseline formulation for all the parametric studies in terms of the impact study of thermomechanical shrinkage on macrosegregation and its reproductions of experimental findings.

The dependence of the solidification behavior on the variations of filling rate, melt superheat and initial mold temperature was then investigated, respectively, using the established reliable model. The three casting control parameters were selected due to the shortness or confliction of relevant data in the literature, as well as the complication, high-cost or

impossibility of the employment of other macrosegregation control techniques. The studied casting variables included the filling rates of 0.084, 0.107 and 0.145 m/min (with filling times of 38, 30 and 22 min), the initial melt superheats of 75, 65 and 55 °C, the initial mold temperatures of 50, 120 and 250 °C. These casting parameters represented the conditions the most commonly encountered in industry during casting of large size ingot. The results indicated that a quicker filling operation, a lower melt superheat and a colder mold condition tended to decrease the macrosegregation intensity in the upper section of the casting, along the centerline, and in the mid-radius solute-enriched bands. The alleviation effect was associated with the changes in flows induced by pouring jet, thermosolutal convection, thermomechanical deformation of the phases, along with the variations of the temperature gradient in the casting and the solidification speed. The predictions of the studied cases were verified with experimental characterizations on the macro-/micro-structures, solutal distributions, dimensional change of the casting and the temperature variations on mold outside surface.

The findings in the dissertation allow for a better understanding of the underlying mechanisms responsible for the occurrence of macrosegregation in ingot casting process. They should also be helpful for the casting process design of a given ingot and could be used in industry to improve the quality of large size ingot production and the productivity of high value-added steels or other alloys which are prone to macrosegregation.

Keywords: macrosegregation, large size steel ingot, experimentation, simulation

LIST OF TABLES

XVI

LIST OF FIGURES

LIST OF ABREVIATIONS

ALE	Arbitrary Lagrangian-Eulerian
CET	Columnar-to-Equiaxed Transition
DC	Direct-Chill Casting
EVP	Elasto-Visco-Plastic
FE	Finite Element
FEM	Finite Element Modeling
LSRE	Local Solute Redistribution Equation
MT	Metric Tons
SDAS	Secondary Dendrite Arm Spacing
SN	Sensors
TC	Thermocouple
TH	Thermohydraulic model
TM	Thermomechanic model
VP	Visco-Plastic

LIST OF SYMBOLS

Symbol	Unit	Description
α	1/K	Coefficient of linear thermal expansion
α	-	Back-diffusion Fourier number
β	-	Solidification shrinkage
β_i	wt.%/K	Solutal expansion coefficient of solute i
β_T	1/K	Thermal expansion coefficient (/K)
ε_T	-	Steel emissivity
$\dot{\bar{\varepsilon}}$	-	Equivalent plastic strain rate
$\bar{\varepsilon}$	-	Equivalent plastic strain
$\dot{\varepsilon}$	s^{-1}	Strain rate tensor
η_l	-	Dynamic viscosity of the liquid,
λ	W/m/K	Thermal conductivity
μ	Pa·s	Dynamic viscosity of fluid
v	m/s	Linear local solid/liquid interface advance velocity
ν	-	Poisson's coefficient.
ρ	kg/m^3	Density
ρ_0	kg/m^3	Reference density (density at liquidus)
ρ_l	kg/m^3	Density of liquid
ρ_s	kg/m^3	Density of solid
$\bar{\sigma}$	MPa	Von Mises equivalent flow stress
σ_s	MPa	Yield stress
σ_T	W/m^2/K	Stephan-Boltzmann constant
ω_0	wt.%	Nominal composition
ω_0^C	wt.%	Nominal carbon content
ω_0^i	wt.%	Nominal concentration of solute i
ω^C	wt.%	Carbon content
ω^i	wt.%	Local concentration of solute i
ω_l^C	wt.%	Concentration of carbon in the liquid
ω_l^i	wt.%	Concentration of solute i in the liquid
ω_s	wt.%	Solute concentration at the solid/liquid interface
$\Delta\varepsilon_{tr}$	-	Solidification shrinkage
ΔH	kJ/kg	Enthalpy of reaction
∇T	°C or K	Temperature gradient
∇p	Pa	Pressure gradient
A	m^2	Cross-sectional area to flow
C_p	J/kg/°C	Specific heat capacity
C_R	°C/s	Cooling rate
d	m	Characteristic length
D	mm^2/s	Diffusion coefficient
D_0	cm^2/s	Diffusion frequency factor
d_1	μm	Primary dendrite arm spacing

d_2	μm	Secondary dendrite arm spacing
D_l^i	mm²/s	Diffusion coefficient of solute i in the liquid
D_s	μm²/s	Diffusivity of solute element in the solid phase
E	GPa	Young's modulus
f	-	Phase fraction
f_l	-	Volume fraction of liquid
f_s	-	Volume fraction of solid
f_α	-	Volume fractions of α-ferrite
f_γ	-	Volume fraction of γ-austenite
f_δ	-	Volume fraction of δ-ferrite
g	m/s²	Gravitational acceleration
h	W/m/°C	Heat transfer coefficient
h_{gap}	W/m/°C	Gap heat transfer coefficient
j	mol/s	Solute flux
k	-	Equilibrium partition coefficient
K	m²	Permeability of the mushy zone
k^i	-	Partition coefficient of solute i
K_{perm}	m²	Isotropic permeability
K_s	-	Viscoplastic consistency in the solid
K^{vp}	-	Viscoplastic consistency of the material
l	μm	Length scale of the microsegregation domain
L	m	Length over which pressure drop is taking place
L_f	kJ/kg	Latent heat of fusion
m	-	Strain-rate sensitivity coefficient
m_l	-	Slopes of liquidus line
m_l^i	-	Liquidus slope of solute i
m_s^i	-	Solidus slope of solute i
N	-	Number of solute elements in the steel
n	-	Strain hardening exponent
$\boldsymbol{n}$	-	Outward normal unit vector
p	MPa	Pressure
q	W	Heat flux
Q	cal/mol	Diffusion activation energy
Q_t	m³/s	Total discharge
R	cal/mol·K	Gas constant
Re	-	Reynolds number
R^i	-	Segregation ratio of solute i
R_v	1/s	Isotherm velocity
s	-	Cauchy stress tensor
t	s	Time
t_f	s	Diffusion time (local solidification time)
t_F	min	Filling time
T	°C or K	Temperature
T_0	°C	Steel pouring temperature
T_c	°C	Casting surface temperature

T_{conf}	°C	Coherency temperature
T_{ext}	°C	Exterior environmental temperature
T_m	°C	Melting temperature for pure iron
T_l	°C	Liquidus temperature
T_{mold}	°C	Initial temperature of molds
T_{ref}	°C	Reference temperature
T_s	°C	Solidus temperature
v	m/s	Average velocity
$\mathbf{v}$	m/s	Liquid velocity

INTRODUCTION

Ingot casting is still one of the important processes for the production of large-size semi-products of high-quality special steels. Macrosegregation, as one of the most significant defects, is difficult to be reduced by the subsequent thermo-mechanical treatments. The presence of the detrimental defect leads to heterogeneous properties in the final cast ingot, severely deteriorate the quality of final products, significantly affect their performance and suitability for different applications, and hence haunt the manufacturers over decades. It has therefore long been predominant concern in pursuit of the prediction on the occurrence, intensity and location of macrosegregation and the measures on the elimination or even clarification of macrosegregates.

Some countermeasures have been reported effective in the control of the degree of convection and diffusion in the liquid and solid, and thus of the solidification process at the outset. However, the dependence of the macrosegregation extent on the critical processing parameters, particularly with respect to multi-component low-alloyed steel ingots in the industrial-scale size, is still unclear and needs to be investigated.

Great endeavors have long been made in the development of finite element modeling (FEM) tools for the prediction of macro-scale solute distribution, due to their faster and less expensive design cycle, compared with the timely and costly trial-and-error approach. Despite dramatic progress have been made in the last 60 years, predictive capabilities of current available models are still limited. The effectiveness of models is prominently restrained by the computing powers due to the complexity of the involved phenomena, the inappropriateness of the model's geometry, meshes, boundary conditions, as well as the uncertainties associated with input parameters and auxiliary models. A lack of suitable experimental studies, with which model results can be compared, enhances the difficulty for the examination of models' viability. The development of a reliable macrosegregation predictive model will thus be of experimental and industrial significance for the macrosegregation research, the production process design and the optimization of the ingot manufacturing efficiency.

The current project, therefore, was initiated to explore the development of a reliable simulation model in order to predict the extent and severity of macrosegregation in a 40MT (metric ton) medium-carbon high strength steel ingot as a function of casting parameters with the view to minimize the occurrence of the macro-scale defect. For this purpose, systematic studies were performed. All the elements which could introduce uncertainties into the model were eliminated. And then a FEM model was constructed. The applicability of the established model to the studied steel and cast ingots was verified using experimental measurements on the chemical, thermal and dimensional profiles. The developed model was employed to investigate the impact of three casting parameters, i.e. filling rate, melt superheat and mold initial thermal conditions, on the thermomechanical evolution, macroscopic fluid flow and the macro-scale solute distribution in the course of filling and casting process. The beneficial effect of the corresponding adjustment of casting variables on the alleviation of macrosegregation was also quantitatively validated against experimental characterizations. All these works are given in detail in 8 chapters.

In Chapter 1, a critical literature review has been done about the macrosegregation formation and development mechanisms, the control methods usually taken to improve ingot quality and limit the intensity of macrosegregation, and the development of macromodeling technique in the past 60 years. The key difficulties of the performance of the countermeasures and the establishment of a reliable macromodel are also given. The viability of their use in an industrial environment is then assessed and the key factors limiting their effectiveness are highlighted.

The adopted methodology, which combined experimentation and simulation, is extensively presented in chapter 2. The material and ingot cast system in study are introduced. The ascertainment of each aspect regarding the model construction is comprehensively described, including the model algorithm, the optimization of model geometry and configuration, the determination of the grid size and the identification of the parameters of concerned materials. The involved softwares, the experimental apparatus, sampling and conditions are stated in the meanwhile.

Chapter 3 is devoted to the identification of the microsegregation model that best predicts macrosegregation in the studied steel ingot. The examined microsegregation models include the classical equilibrium lever-rule, the extreme non-equilibrium Scheil-Gulliver, as well as other treatments in the intermediate regime proposed by Brody and Flemings, Clyne and Kurz, Kobayashi and Ohnaka. Comparative analyses are performed on three regions, representing the initial, intermediate and final stages of the solidification process. The thermophysical properties calculated using each of the above microsegregation models are used for three-dimensional simulations of the solidification process of the studied 40MT steel ingot. The simulation predictions were compared with the experimental measurement for the validation of the reliability of the model.

The importance of solidification shrinkage and solid deformation in the large-size steel ingot solidification process is discussed in Chapter 4. A thermohydraulic model is developed to study heat and solute transport coupled with flow driven by thermosolutal convection (buoyancy-driven flow). A thermomechanic model (TM) is also set up where thermosolutal transport induced by the combined effects of buoyancy- and shrinkage-induced flow was considered. Both models are applied for the numerical study of the filling and cooling stages of the investigated ingot. Based on the comparison between simulation prediction and experimental results, the established model is further improved and decided to be the baseline for the exploration of casting variables.

The comprehensive performances of parametric studies are given in Chapters 5-8, using the determined reliable model. Three casting parameters are investigated: filling rate, initial melt superheat and mold initial temperature. Qualitative and quantitative examination of the occurrence and severity of macrosegregation as a function of the above parameters are conducted. Their associations with the evolution of solid shrinkage, air gap formation, temperature field, solid fraction change and melt velocity domain throughout the filling and cooling stages are explored. The results are analyzed in the framework of theories concerning heat and mass transfer and diffusion/convection-controlled solidification.

Three Annexes are added at the end, talking about the impacts of different segregation levels of alloying elements, thermophysical properties of materials and non-uniform temperature

distribution of the mold on the solidification and cooling behaviors. They act as supplements of the above chapters and preliminary studies of new model development and future work.

The findings in the dissertation allow for a better understanding of the underlying mechanisms responsible for the occurrence of macrosegregation in ingot casting process. They should also be helpful for the casting process design of a given ingot and could be used in industry to improve the quality of large size ingot production and the productivity of high value-added steels or other alloys which are prone to macrosegregation.

PROJECT CONTEXT AND DEFINITION

Ingot casting is required for production of high-cost heavy mono-block industrial components, such as the shaft rotor for steam turbine and the pressure vessels for nuclear power generation. During the solidification of alloys, solute is partitioned between the solid and liquid to either enrich or deplete interdendritic regions. This naturally leads to variations in composition on the scale of micrometers, i.e., to microsegregation, and on the length scales approaching the dimensions of the casting, i.e., to macrosegregation. For large size ingots, macrosegregation may be of the order of centimeters or meters (Pickering, 2013).

Microsegregation can be removed by homogenization heat treatment, because the distance is sufficiently small over which diffusion can take place to redistribute the alloying elements. Macrosegregation, however, is practically impossible to remove (as seen in Figure 1.1), due to the big distances over which species are required to move within available time scales (Campbell, 2011).
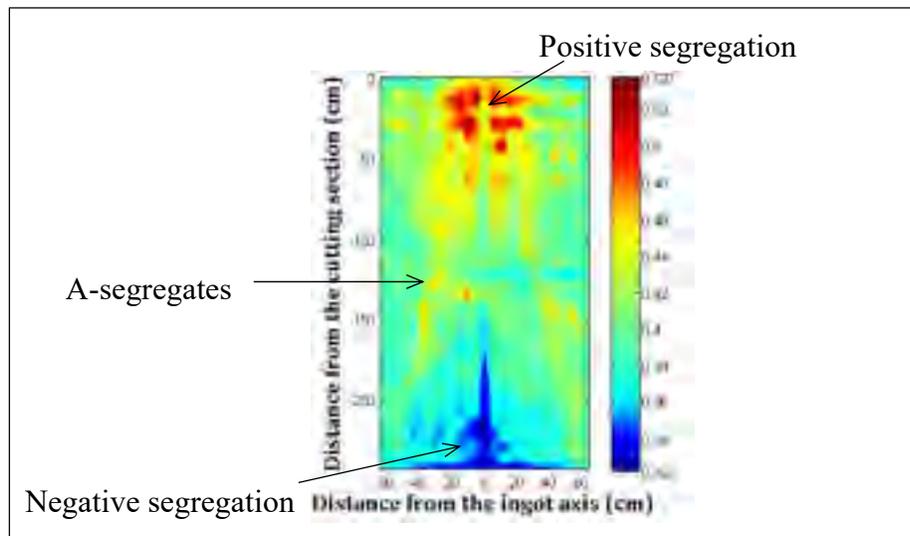
Figure 1.1 Carbon profile on longitudinal section of a 40 metric ton steel ingot from Finkle Steel with nominal composition of 0.36 wt% C after reheating and forging

Almost all macrosegregation is undesirable for casting manufacturers. As the chemical variations can lead to severe microstructural changes, it could deteriorate the quality of the cast products and significantly affect their performance and suitability for different applications. The effects of macrosegregation are critically significant. Thus, predicting the severity and location of macrosegregated zones and eliminating their detrimental effects have been and still remain a challenge to the industry. This chapter first reviews the macrosegregation types, formation mechanisms, common countermeasures and the development of predictive methods. The viability of their use in an industrial environment is then assessed and the key factor limiting their effectiveness is highlighted. The definition of the current project is given at the end of this chapter.

1.1 Macrosegregation

The first examination of macrosegregation in steel ingots can be traced back to 1920s (Hultgren, 1929). Since then, although our understanding of segregation development process has considerably improved, the same macrosegregation patterns can still be observed in ingots produced today (Campbell, 2011). These, as shown in Figures 1.1 and 1.2 (Pickering, 2013), include positive top segregation (with the carbon content more intense than the nominal one at the top of the ingot), negative base segregation (with the solute concentration smaller than the nominal one at the bottom of the ingot) and solute-enriched channel segregations (A- and V-segregate bands). A-segregations, pointing towards the top of the casting, are located near the boundary between center and the periphery, while V segregations are visible in the central part of the casting.

All types of macrosegregation are derived from the same basic mechanism: movement or flow of segregated liquid with respect to the solid framework of the mushy zone during the solidification process. The movement of enriched liquid and depleted solid can occur through a number of processes, as shown in Figure 1.3 (Pickering, 2013):

i) Convective flows due to density gradients caused by temperature and composition variations in the liquid (Figure 1.3a). The thermal and solutal convection contributions can either aid or oppose each other, depending on whether local temperature and concentration

fields cause liquid density to increase or decrease. The convection due to the coupled action of temperature and solute is known as thermosolutal convection.
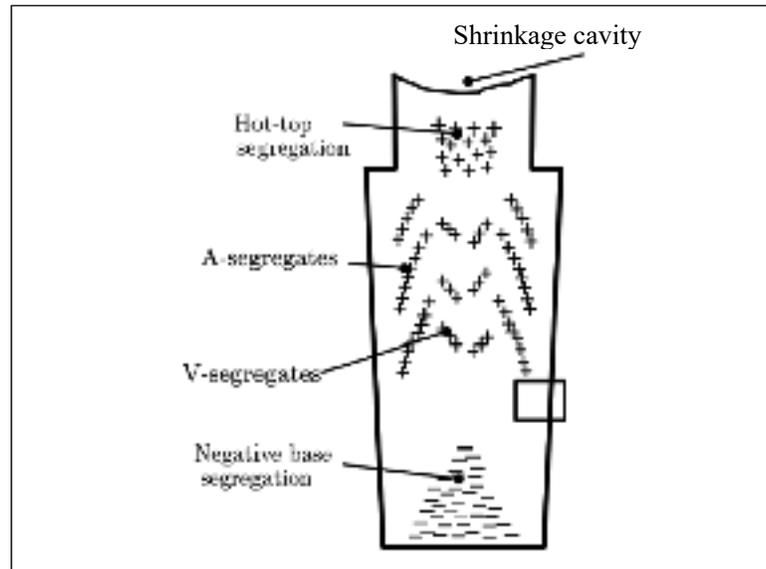
Figure 1.2 Schematic of macrosegregations in large ingots. Positive segregation is denoted by + symbols (regions enriched in solute) and negative by – (regions depleted in solute) (Pickering, 2013).

ii) Movement of small (equiaxed) grains or solid fragments, which have nucleated heterogeneously in the melt, become detached from the dendrites due to remelting/stress or have separated from the mold wall after pouring (Figure 1.3b). Equiaxed grains in steels are denser than the surrounding liquid and will hence tend to sink. This mechanism, along with convective fluid flow, is a dominant macrosegregation process in large size ingots.

iii) Flow that feeds solidification shrinkage and thermal contraction of the liquid and solid during cooling (Figure 1.3c).

iv) Deformation of the solid network in the mushy zone due to thermal stresses, shrinkage stresses and metallostatic head (i.e., the pressure provided by the liquid metal above) (Figure 1.3d), or external forces on the solid shell (such as those from the rolls in continuous casting of steel).

v) Imposed flows due to pouring, motion of gas bubbles, vibration, applied electromagnetic fields, stirring, rotation etc.

In ingot casting of steels, the positive segregations dominantly result from the thermosolutal convective flow. The negatively segregated cone is caused by the sedimentation of the equiaxed crystals, formed early in the solidification process, owing to their own weight and a downward motion of liquid along the wall induced by thermal convection. The A-segregates are the results of solutal convection through the columnar dendritic zone in the same direction as, but at a faster speed than, the isotherm velocity. The V-segregates arise from equiaxed crystals settling in the core (Pickering, 2013).
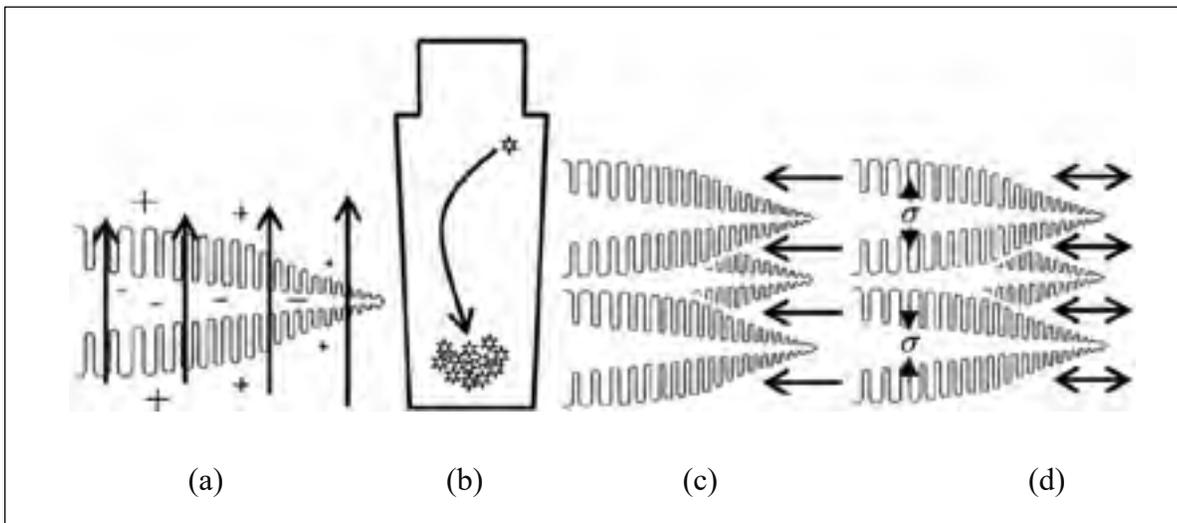
Figure 1.3 Schematic of the processes leading to mass transport during ingot solidification. (a) Convective flows in the interdendritic liquid (+ symbols denote enrichment in solute, whilst - denote depletion (b) Grain sedimentation (more generally solid movement) (c) Liquid flow to feed solidification shrinkage (d) Mushy-zone deformation (Pickering, 2013).

1.2 Measures to control macrosegregation

It has been found that the extent of segregation depends greatly on the degree of convection or diffusion in the liquid and solid, thus depending upon the cooling conditions in the solidification. Careful control of casting process parameters at the outset could therefore be

the effective method to control the extent and intensity of macrosegregation. So far, intensive researches have been underway, and some critical process parameters have been identified and used as 'countermeasures' to produce sound ingots with improved quality and limited macrosegregations:

1)   Control of alloy composition

Alloys, by definition, are always multicomponent. Different alloying elements can have opposite contributions to the density of the mixed melt, to the buoyancy force (i.e. the upward force exerted by a fluid that opposes the weight) and to the overall flow. As a result, they can affect the overall contribution of solutal convection (i.e. motion of fluid induced by composition variation) to the macrosegregation (Du, Eskin et Katgerman, 2007). Furthermore, different concentrations of alloying elements exert different effects on the partition coefficient k, (defined as the ratio of the solid composition to the liquid composition). That is, they affect its deviation from unity (no partitioning of solute elements between liquid and solid phases during solidification, and therefore no segregation) and whether it is less than or greater than 1 (determining the extent and pattern of macrosegregation). It has been reported that the A-segregation could be reduced by increasing molybdenum and decreasing silicon and manganese within the specified range (Suzuki et Taniguchi, 1981). The reduction was related to the stable density stratification (i.e. variations in density) in the solute-rich liquid, and the decreased and more neutral buoyancy at the temperature within the freezing zone.

2)   Employment of multipouring technique

Multipouring technique refers to sequential pouring of molten steel from multiple ladles with different concentrations of alloying elements. Each ladle content, temperature, weight and flow rate are carefully controlled at optimum condition. The purpose is to build an initial delaminated concentration distribution (i.e. an initial disparate chemical distribution) for the solidification of steel ingots (Duan, Shen et Liu, 2015). It has been argued that the multipouring process is effective to suppress macrosegregation in large size steel ingots by

reversing the initial concentration distribution in the top and the bottom section of the steel ingot before solidification starts (Tu, Shen et Liu, 2015).

3)   Adjustment of ingot dimension and configuration

The average ratio of height to diameter of the steel ingot was found to be a factor relevant to the macrosegregation of steel ingot (Lesoult, 2005). Improving insulating effects and increasing the height and reducing the taper of the hot-top result in the formation of channel segregates in the hot-top (Flemings, 1975). With increasing insulating ability of sleeve, the light melt at the top overcomes more segregated carbon floating from the lower part of the ingot, and the positive segregation could be decreased (Comon, Delorme et Bastien, 1973).

4)   Introduction of forced melt flow

The forced melt flow, or convection, could be imposed by stirring, rotating or oscillating the crucible, introducing a rotating magnetic or electromagnetic field. The aim is to reduce the contact pressure between the melt and mold, broaden the mushy zone, promote heterogeneous nucleation, reduce temperature gradient and weaken the effect of gravity (Zhang, Cui et Lu, 2003; Zhang et Cui, 2003). As a result, significant refinement of the cast microstructure can occur, solute distribution in the ingot can be improved, and macrosegregation of alloy elements can be reduced (Zhang, Cui et Lu, 2003; Zhang et Cui, 2003; Zhao, Cui et Nagumi, 2005).

5)   Control of casting parameters

Stringent control of casting parameters, as the most practical 'countermeasure', has attracted the attention of many researchers (Pickering, 2013). Numerous studies have been performed on the effect of different parameters on the solidification behavior of castings.

i)   Filling rate

It has been reported that the variation of the filling rate can give rise to the change in the flow characteristics (Im, Kim et Lee, 2001; Lee, Mok et Hong, 1999), the solidification speed (Im, Kim et Lee, 2001;), the temperature and thermal stress fields (Lee, Mok et Hong, 1999;), the

metal front migration, the heat transfer at the early stages of the casting process (Lee, Mok et Hong, 1999;) and the cold shuts formation (Ravindran et Lewis, 1998). It has also been revealed that residual flow due to filling effects can significantly affect the shape of the mushy zone and delay the development of solutal convection (Yadav et al., 2009). All these actions result in less intense macrosegregation near the cold wall and a farther distance of A-segregates from the cold wall (Yadav et al., 2009). However, the effect of filling velocity on macrosegregation in large size steel ingots has not yet been reported, either numerically or experimentally.

ii)   Initial melt superheat

Superheat is excess of the casting temperature above the liquidus (Campbell, 2011). In the past decade, many studies have been carried out on the impact of melt superheat on macrosegregation. The findings, however, present two different views:

On one hand, it was pointed out that a higher superheat enhanced the convection velocities (Liu et al., 2011; EI-Bealy et Hammouda, 2007), coarsened the equiaxed dendritic grains and increased secondary dendritic arm spacing (Zhong et al., 2012). Meanwhile, a higher superheat can reduce the height of bottom negative segregation cone (Liu et al., 2011) and decrease the intensity of carbon segregation (EI-Bealy et Hammouda, 2007; Zhong et al., 2012; Pikkarainen, et al., 2016;).

On the other hand, it was reported that a lower melt superheat results in weakened flotation of grains (Sun et al., 2016), favored equiaxed structures (Mäkinen et Uoti, 2006) and increased nucleation density of crystals (Sun et al., 2016). A decreased severity of macrosegregation is also ascribed to a lower melt superheat (Sun et al., 2016), including a less intense centerline macrosegregation (Mäkinen et Uoti, 2006) and V-shaped segregation (Guan et al., 2018). It was observed that a lower melt superheat favored the stability of equiaxed crystals, resulting in more uniform rejection of solutes in the mushy zone, and subsequently a reduction in segregation severity (Choudhary et Ganguly, 2007).

In view of the above conflicting findings on the effect of melt superheat on macrosegregation, it is of great necessity to turn to further investigations for an answer.

iii)   Initial mold temperature

The initial mold temperature, as a casting parameter, is not specified in production and often fixed at or close to room temperature. It was found, however, that a rise in initial mold temperature was accompanied by coarsened grains (Zhang et al., 2016; Li et al., 2017), increased secondary dendrite arm spacing (SDAS), aggravated shrinkage porosities (Li et al., 2017; Haj, Bouayad et Alami, 2015) and a prolonged solidification time (Haj, Bouayad et Alami, 2015; Li et al., 2017). However, the impact of initial mold temperature on macrosegregation in large size steel ingots is still not clear and needs to be quantified.

In order to minimize the occurrence of macrosegregation in a heavy steel ingot, stringent control of the aforementioned parameters is of critical importance. Quantification of their impact on macrosegregation, however, is a great challenge, particularly using the costly and timely 'trial and error' approach. Finite element method (FEM), thus, becomes where to turn for help.

1.3   Macrosegregation modeling

Simulation by FEM method is a good choice for quantitative predictions of the occurrence and severity of solidification defects, for performance of parametric studies to control and improve casting quality and for understanding the basic physical mechanisms. Particularly, when large ingot manufacture is involved and it is too complicated or impossible to optimize the process and compositions just simply by trial and error approach, FEM method performs a faster and less expensive design cycle.

However, predictive capabilities of current models are still limited despite dramatic progress have been made in the last 60 years. Computing power is arguably the most prominent restraint on the effectiveness of current models, and there is also a lack of suitable experimental studies with which model results can be compared.

Solidification models are very complex and require large computing resources in their solutions, because they often must simultaneously consider many aspects of a solidification process. As illustrated in Figure 1.4 (Pickering, 2013), phenomena to be considered include heat transfer, solute transport, fluid flow, solid movement, thermal gradients, cooling rates, melt convection, alloy composition, melt superheat, mold temperature, and deformation at the (macroscopic) scale of the casting, as well as phase equilibrium, nucleation, structure formation, segregation, and flow at various microscopic scales. Many of the above parameters interact in casting processes (Beckermann, 2000) and some of them vary with time and position during solidification, as observed by Willers et al. (Willers et al., 2005). Any factor that affects the flow and the microstructure also influences macrosegregation, and vice versa. Today, it is certainly not desirable to generate a solidification model that includes all listed effects, since a model of such complexity would hardly be useful in practice. The attention is therefore attracted to the researches where *some* of these interactions are taken into account in order to address industrially relevant solidification problems.
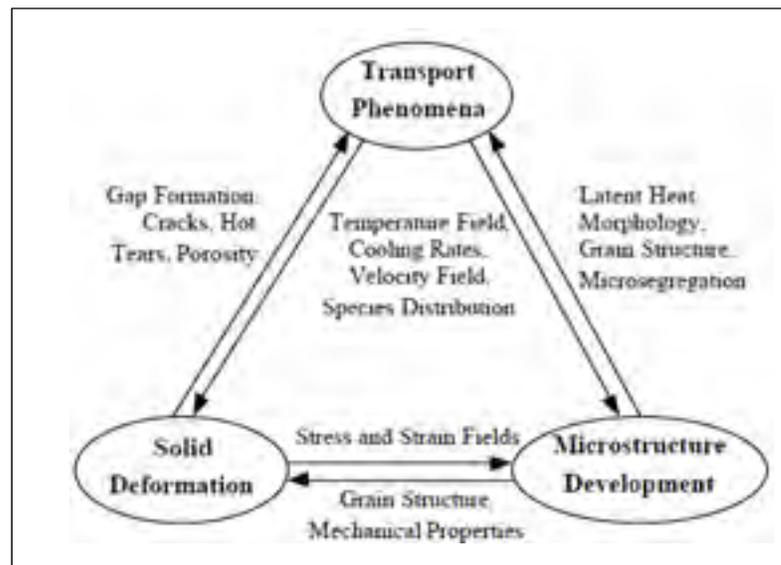
Figure 1.4 Potentially important interactions in modeling
solidification in castings (Pickering, 2013).

1.3.1   Development of solidification modeling

1)   Models of Flemings and coworkers

The pioneering work on the effect of macroscopic fluid flow on solute distribution was made by Flemings *et al*. in the late 1960s (Schneider et Beckermann, 1995; Scheneider et al., 1997). They developed the local solute redistribution equation (LSRE) by conserving mass and solute within a volume-element of mush (Figure 1.5 (Fleming, 2000)). They assumed that mass transfer was the result of density-driven fluid flow due to solidification shrinkage only (i.e. the density difference between solid and liquid), and that the solid was stationary with constant density and no formation of pores:

$$\frac{\partial f_l}{\partial C_l} = \left(\frac{1-\beta}{1-k}\right)\left[1 + \frac{v \cdot \nabla T}{\partial T/\partial t}\right]\frac{f_l}{C_l} \tag{1.1}$$

where f_l is the volume fraction of liquid, C_l is the concentration of the liquid in wt.%, $\beta = (\rho_s - \rho_l)/\rho_s$ the solidification shrinkage, in which ρ_s and ρ_l are the densities of the solid and liquid, respectively, k the equilibrium partition ratio, v liquid velocity vector, ∇T the temperature gradient, t time, and $\partial T/\partial t$ is the rate of the temperature change. With zero interdendritic flow, velocity v vanishes, and no shrinkage ($\beta = 0$) or no flow to exactly feed solidification shrinkage, Equation (1.1) reduces to the well-known Scheil equation (Boettinger et al., 1995).

Positive segregation results when the flow velocity is slower than the shrinkage velocity or flow is in an opposite direction (in the direction of increasing temperature, towards regions of lower solid fraction). In contrast, if it is of greater magnitude in the same diretion as the shrinkage flow (i.e. in the direction of decreasing temperature), negative segregation results. Analytical solutions of the LSRE were supported by experimental work (Boettinger et al., 1995) and thus were used to predict the formation of solute-rich and solute-poor bands as a result of thermal fluctuations, They were also used to show the formation of inverse and hot-top segregation by assuming a linear temperature gradient within the mushy zone (values of

liquid fraction and the rate of solidification were fixed) for unidirectional solidification with planar isotherms.
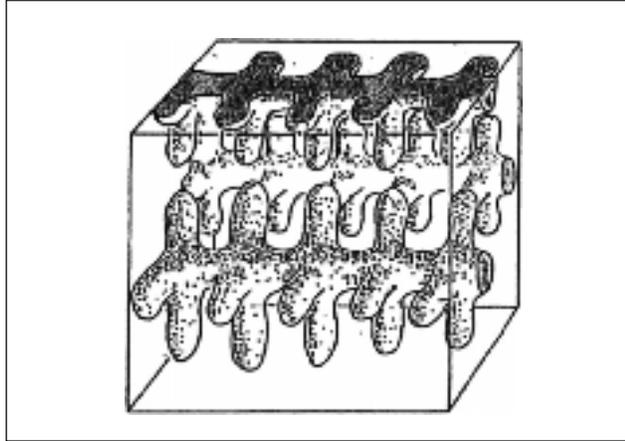
Figure 1.5 Schematic of volume element in mushy zone considered when developing conservation equations (Fleming, 2000).

The LSRE model was later expanded by the same group by including buoyancy-driven flows to account for the fluid flow in the mushy zone (Mehrabian et Flemings, 1970). Differences in liquid density were resulted from both thermal and solutal effects (thermosolutal convection). However, because a temperature gradient within the mushy zone was still assumed (and concentration related to temperature via the phase-diagram liquidus), the density of the liquid was a function only of local temperature. Because the resistance to liquid movement, provided by the dendritic network, was taken into consideration, Darcy's law* for flow within a porous medium (proved reasonable when applied to slow, laminar flow with uniform and constant liquid fraction (Piwonka et Flemings, 1966; Ganesan et Poirier, 1990)) was then combined with conservation equations. Liquid flow velocities *v* was then calculated according to gravity and pressure drops across a volume element of dendritic mush:

$$v = -\frac{K}{\mu f_l}(\nabla p + \rho_l g)$$

(1.2)

where μ is the dynamic viscosity of interdendritic fluid, K is the permeability of the mushy zone (m^2), ∇p the pressure gradient (Pa), and $\boldsymbol{g}$ the gravity vector (m/s^2).

If the simple LSRE is considered momentarily, by recognizing that $(\partial T/\partial t)/\nabla T$ is equivalent to the isotherm velocity R_v, Equation (1.1) can be re-written as

$$\frac{\partial f_l}{\partial C_l} = \left(\frac{1-\beta}{1-k}\right)\left[1 + \frac{v}{R_v}\right]\frac{f_l}{C_l} \tag{1.3}$$

It can be seen that local remelting (i.e., an increase in liquid fraction) occurs if fluid velocities in the direction of isotherm movement are greater than the isotherm velocities (flow instability): $\frac{|v|}{R_v} > 1$ as $\partial f_l/\partial C_l$ becomes positive. In other words, the movement of cooled enriched liquid towards the liquidus results in local remelting and the formation of persistent channels, such as A-segregation.

However, the requirement of a temperature gradient in the mushy zone, the neglect of fluid flow in the bulk liquid and coupled flows between the bulk and mushy regions, the shortage of energy conservation to find the transient value, the dependent relation between solute concentration and temperature and their fixed profiles (the composition of liquid was determined by the phase diagram at a given temperature) result in limiting simplifications for the two aforementioned models. It is not until the development of multi-domain models, and later continuum models, in 1980s, that the simplifications were gradually removed.

---

*Darcy's law describes the proportional relationship between the instantaneous flow of a fluid through a homogeneously permeable porous medium over a given distance: $Q_t = -\frac{KA\,(p_b-p_a)}{\mu L}$ (Liu et al., 2016). The total discharge, Q_t (units of volume per time, e.g., m^3/s) is equal to the product of the intrinsic permeability of the medium, K (m^2), the cross-sectional area to flow, A (m^2), and the total pressure drop p_b - p_a (pascals), all divided by the dynamic viscosity, μ (Pa·s) and the length over which the pressure drop is taking place L (m).

2)   Multi-domain models

In multi-domain models, conservation equation for mass, solute, momentum and energy are developed for each region (liquid, mushy, and solid) and coupled across the moving boundaries between them. For instance, fluid momentum in the bulk liquid is typical described by Navier-Stokes equations for laminar convection flow, whilst in the mushy zone Darcy's law is used. Perhaps the first truly predictive multi-domain model was developed by Szekely and Jassal in 1978 (Szekely et Jassal, 1978) to examine bulk-liquid flow by using expressions for energy and momentum in the solid, mushy and bulk-liquid zones, coupled the equations using temperatures and velocities at the domain boundaries. In 1979, Fujii *et al*. examined the macrosegregation in a low-alloy steel so as to predict transient mushy zone temperature fields by coupling energy and momentum equations through the use of a modified LSRE for multicomponent alloys (Fujii, Poirier et Flemings, 1979). In their model, complete solid diffusion of interstitials atoms (lever rule behavior) and Scheil behavior for substitutional atoms were accounted for. The density of the liquid was a function of both local concentration and temperature and the two fields were no longer fixed. In 1981, Ridder *et al*. examined the effect of natural convective flows in the bulk liquid on interdendritic flows in the mushy zone by coupling equations for flow velocity and pressure in each domain across the liquidus interface (Ridder, Kou et Mehrabian, 1981). For the bulk liquid, energy and momentum equations were used but solute effects were not considered. However, the multi-domain approach requires the tracking of the boundaries between solid, mushy zone and bulk liquid. This is often a difficult task, particularly as the boundaries can take on complex morphologies. In using continuum models, this difficulty is removed as they comprise a single set of equations which are equally valid over the solid, mushy zone and bulk liquid.

3)   Continuum models/single-domain models

Inspired by the work of Flemings et al., as well as by other theoretical work in the early 1980s, Bennon and Incropera produced a continuum model in 1987 for a binary system by combining constitutive equations (Bennon et Incropera, 1987) (with momentum equations based on Navier-Strokes equations and Darcy's law) through simple mixture when they

recognized the suitability of continuum formations for the liquid-solid transformation. Assumptions included laminar Newtonian flow in the liquid with constant viscosity and the Boussinesq approximation (differences in liquid density are neglected, but weight differences are included). The coupling of the enthalpy and solutal fields was accomplished by assuming lever-rule equilibrium solidification (Bennon et Incropera, 1987). The boundary conditions were applied only to external domain surfaces. As a result, the first direct numerical predictions of A-segregation were presented. In 1988, Beckermann and Viskanta developed a set of similar continuum equations (Beckermann et Viskanta, 1988) with a different momentum equation through a volume-averaging approach (generally thought to be more rigorous (Beckermann et Viskanta, 1993) to obtain a single set of macroscopic equations valid in all the regimes of the solidification systems (solid, mushy, and liquid regions) by averaging the microscopic equations over a suitable volume element (Voller et Brent, 1989; Ganesan et Poirier, 1990). Following the pioneering works highlighted above, many studies used similar or modified versions of the continuum or volume-averaged equations to examine a number of different solidification phenomena, including channel formation in directional-solidified alloys (Nandapurkar et Poirier, 1991; Felicelli, Heinrich et Poirier, 1993; Poirier et Heinrich, 1994), the effect of solidification shrinkage and pore formation (Xu et Li, 1991; Chiang et Tsai, 1992; Naterer, 1997; Heinrich et Poirier, 2004) and the effect of transformation-induced strains (Ei-Bealy, 2000, Part I et Part II).

Considering that the early continuum approaches didn't account for the interaction between liquid and solid phase and that important solidification features, such as local solid concentrations, were simply averaged over both phases leading to strange model results (Beckermann et Viskanta, 1988), Ni and Beckermann developed a 'two-phase' model, in 1991, in which separate volume-averaged conservation equations were used for the solid and liquid phases (Ni et Beckermann, 1991; Prakash, 1990, Part I et II). The relative movement of solid and liquid (and the momentum transfer between them) was accounted for by using an effective solid viscosity, the value of which changed according to the local solid fraction (infinity for a solid with a continuous structure, value between zero and infinity for a no continuous solid). In 1996, Wang and Beckermann introduced a grain envelope (Figure 1.6 (Taguchi, Miyamura et Soga, 1984), a fictitious boundary between the interdendritic and

extradendritic liquid (across which microscopic equations describing grain growth and liquid composition could be linked to macroscopic terms), to the two-phase model to examine features of equiaxed dendritic solidification. The settling of equiaxed grains and the columnar-to-equiaxed transition (CET) were included (Wang et Beckermann, 1996, Part I, Part II et Part III).
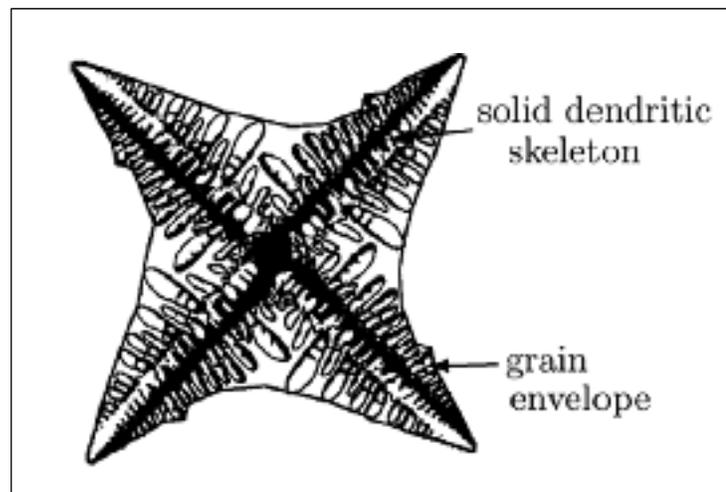
Figure 1.6 Representation of a grain by an envelope
containing a solid skeleton and interdendritic liquid
(Taguchi, Miyamura et Soga, 1984).

From the mid-1990s, macrosegregation modelers began to adapt their continuum formulations to deal with multicomponent systems of varying complexity. Schneider and Beckermann presented the most comprehensive early multicomponent two-phase model and applied it to a low-alloy steel ingot (Schneider et Beckermann, 1995). They solved species conservation equation in the liquid and solid for each system component, coupled the energy and species conservation equations through thermodynamic equilibrium requirements at the solid/liquid interface, and accounted for varying levels of solid-state diffusion. It was later applied to freckle formation in Ni-based superalloys, producing one of the earliest studies in 3D (Schneider et Gu, 1997; Boetting et al., 1995; Felicelli et al., 1997; Felicelli, Poirier et Heinrich, 1998). Other multicomponent approaches presented by Vannier (Vannier, Combeau et Lesoul, 1993), Krane and Incropera (Krane et Incropera, 1997, II et II) are not widely used.

4)   Latest modeling development

In the past decade, many studies have focused on the generation, growth and movement of equiaxed grains in convective melts, and in particular the CET by extension of two-phase models or generation of new formulations (Ciobanas et Fautrelle, 2007, I et II).

Beckermann highlighted the need for such research in 2000 (Beckermann, 2000) and it is certainly key for the prediction of negative base segregation in ingots, and possibly an essential starting point for the prediction of V-segregation and the location of A-segregates (A-segregation is not found in equiaxed zones). Martorano et al. examined the viability of a CET criterion based on the arrest of columnar solidification by the solute field of growing equiaxed grains ahead (so-called 'soft-blocking' (Martorano, Beckermann et Gandin, 2003). Biscuola and Martorano (Biscuola et Martorano, 2008) studied the mechanical blocking of the columnar front during the CET by quantitatively comparing the CET positions obtained with one stochastic model (a tool for estimating probability distributions of potential outcomes by allowing for random variation in one or more inputs over time) and two deterministic models (the output of the model is fully determined by the parameter values and the initial conditions) for the unidirectional solidification of an Al-Si alloy. Wang and Beckermann (Wang et Beckermann, 1994) developed a numerical model to calculate the CET position based on a multiphase approach, which accounts for heat and solute diffusion, as well as for grain nucleation, growth, and morphology. Gandin (Gandin, 2000), combining simulations obtained from a numerical model and experimental results, proposed a CET criterion based on the position of the maximum velocity of the columnar/dendritic interface, suggesting a continuous increase in velocity up to a maximum value of about two-thirds the length of the ingot, where the transition is supposed to occur. Badillo and Beckermann (Badillo et Beckermann, 2006) developed numerical simulations of the CET in directional solidification. A parametric study was performed to investigate the effects of the applied thermal gradient and pulling speed, the seed spacing and nucleation undercooling for the equiaxed grains, and the crystalline anisotropy strength on the CET. In the study, presented by Dong et al. (Dong et al., 2004), a coupled cellular automata – finite difference model was applied to predict the CET in directionally solidified nickel-based superalloys. The influence

of thermal gradient and solid-liquid interface growth rate on CET were investigated and the results were combined on a CET map, showing that a decrease in thermal gradient and an increase in tip growth velocity favour the CET. Banaszek et al. (Banaszek et al., 2007) extended a meso-scale front-tracking model of nonequilibrium binary alloy dendritic solidification to incorporate Kurz, Giovanola, and Trivedi dendrite kinetics and a Scheil solidification path to predict the CET in castings in the presence of natural thermal convection. In their work, direct simulation of equiaxed solidification was carried out, and when done simultaneously with columnar growth simulation, the CET was computed. Noeppel et al. (Noeppel et al., 2009) presented a model for simulating the CET during solidification under microgravity conditions. In the model, melt convection was not taken into account and the heterogeneous nucleation of equiaxed grains was supposed to occur on nucleates characterized by a density. In contrast, the model developed by Martorano et al. (Martorano, Beckermann et Gandin, 2003), to predict the CET during solidification of binary alloys, is based on solutal interactions between the equiaxed grains and the advancing columnar front. The model was validated by predicting the CET in unidirectional solidification involving Al-Si alloys of three different compositions. The review of CET presented by Spittle (Spittle, 2006) considered the proposed mechanisms of equiaxed grain formation, the influence of alloy and processing conditions on the CET, criteria for the termination of columnar growth and deterministic/stochastic models for predicting the structural transition. Wu and Ludwig (Wu et Ludwig, 2007) proposed a three-phase mixed columnar-equiaxed solidification model which considers the influence of the melt convection and grain sedimentation in the CET, and accounts for the different behaviors of globular and dendritic equiaxed grains (the phases were stationary columnar solid, equiaxed solid and parent melt) (Ludwig et Wu, 2005; Wu et Ludwig, 2006; Tanzer et al., 2009). For the group, the interdendritic melt and the solid dendritic, confined in a grain envelope, were regarded as one hydrodynamic phase sharing the same velocity, with the other being the extradendritic liquid. The solid dendritic, the interdendritic melt and the extradendritic melt were treated as three distinct thermodynamic phase regions. They used the two-phase method and computed the velocities of hydrodynamic phases, whilst solving for mass transport and solute over three phase regions (Rappaz et Thevoz, 1987; Wang et Beckermann, 1993; Wu et Ludwig,

2000, Part I et part II). This model was subsequently extended to mixed columnar-equiaxed solidification which required three hydrodynamic phases (the same as in their original three-phase treatment) and five thermodynamic phase regions: solid dendrites in equiaxed grains, the interdendritic melt between equiaxed dendrites, solid dendrites in the columnar zone, the interdendritic melt between columnar dendrites, and the extradendritic melt (Wu et Fjeld, 2010; Wu et Ludwig, 2010). It was found that the results of the two and three phase simulations were significantly different, and the simplified columnar-only two-phase scheme more accurately reproduced experimental findings. It was suggested that the three-phase approach could have introduced too many equiaxed grains, or that the experimental ingot had undergone mostly columnar solidification (Li et al., 2012).

Other studies have examined the particular formulations and assumptions of the original models (Poirier et Nandapurkar, 1988; Rappaz et Voller, 1990; Poirier, Nandapurkar et Ganesan, 1991; Schneider et Beckermann, 1991), worked for the optimization of numerical solution methods and solution schemes (Sung, Poirier et Felicelli, 2001; Voller, Mouchmov et Cross, 2004; Gouttebroze, Bellet et Combeau, 2007; Pardeshi et al., 2008; Ferreira et al., 2009; Liu et al., 2010) (following on from Ahmad et al. in 1998 (Ahmad et al., 1998) as well as the incorporation of mechanical stresses into simulations (Liu, 2005; Bellet et al., 2012). A significant body of work, however, has been completed using highly-simplified binary single-phase simulations (Sung, Poitier et Felicelli, 2002; Ma et al., 2004; Singh, Basu et Ghosh, 2006; Liu, Kang et Sang, 2011) significantly because of the complexities and excessive computing times associated with large multiphase simulations.

Today, macromodels which include the generation, growth, and settling of equiaxed grains are restricted to binary systems and small geometries to struggle to resolve A-segregates, and are too computationally expensive for use in industry (Ludwig et Mu, 2005; Li et al., 2012). Indeed, many recent studies resorted to the original treatments by Bennon, Incropera and Beckermann et al. to deliver their predictions (Szekely et Jassal, 1978; Fujii, Poirier et Flemings, 1979; Ridder, Kou et mehrabian, 1981; Ganesan et Poirier, 1990).

Based on the above reviews, the liquid-solid 'two-phase' model, with separate volume-averaged calculations and the coupled conservation of mass, momentum, energy and solute,

species, could be a good choice for large-scaled problem predictions and the balance between the industry practice and computational cost.

1.3.2   Model uncertainties

It seems to be unwise to rely on even the best macrosegregation models of ingot casting for quantitative results because basic trends are often not predicted reliably (Bennon et Incropera, 1987, Part I et Part II). The reasons for this appear to stem from two sources: the computational requirements of complex models (which in turn impose constraints and compromises on models) and uncertainties associated with model geometry, mesh size, input material properties and auxiliary models, etc..

1)   Model, geometry and meshes

Gu and Beckermann recognized in 1999 (Bennon et Incropera, 1987, part II) that in order to predict macrosegregation patterns in a large commercial ingot (65 t, 1.016 × 2.083 × 2.819 m^3) by using the multicomponent two phase model of Schneider and Beckermann (Schneider et Beckermann, 1995) and reduced geometry, computing times would be years for required mesh size.

Reducing the size of the model system, increasing mesh size or introducing significant simplifications can drastically reduce times, and using symmetry is certainly essential, but results can only be scaled up to larger problems with caution (macrosegregation will not normally arise in small ingots). Increasing mesh sizes often means that certain features, such as A-segregates, are not resolved and changes can significantly affect computed segregation patterns. Introducing too many simplifications can also gravely impact a model's predictive power.

2)   Input material properties

Macrosegregation models depend significantly on the input parameters fed into them. Typical input properties in solidification modeling include the temperature-dependent parameters reflecting material thermophysical (density, thermal conductivity, dendrite arm

spacings, specific heat capacities, latent heats, emissivity), thermomechanical (Young's modulus, strain-rate sensitivity, strain sensitivity, dynamic viscosity, Poisson's ratio, yield stress, solute shrinkage factor, thermal expansion coefficient) and thermodiffusion behaviors (partition coefficients, liquidus slopes, thermal expansion coefficient, solutal expansion coefficient of each solute). Slight variations in such values have been found to influence (often significantly) model results (Schneider et Beckermann, 1995; Wu et Ludwig, 2006; Wu, Ludwig et Fjeld, 2010, Part II). Although there are software packages which are able to deliver some of these parameters in steels, outputs from them can be limited in their current form (for instance, only values for equilibrium solidification are calculated) and certain parameters, such as those relating to equiaxed grain nucleation and dendrite arm spacings, can only be determined experimentally (Rappaz, 1989).

3)   Auxiliary models

Similar uncertainty surrounds the auxiliary models of microsegregation and permeability which must be supplied to macrosegregation simulations. Microsegregation models are of utmost importance to macrosegregation investigators. It is the microsegregation of elements on the dendritic scale which ultimately leads to the enrichment and paucity of the liquid and macroscale segregation of chemical species, through thermosolutal convection currents in the course of ingot solidification. As early as 1969, Fridberg et al. pointed out the significant impact of the microsegregation model selection on the predicted solidification (Fridberg, Torndahl et Hillert, 1969). As shown in Figure 1.7 (Fridberg, Torndahl et Hillert, 1969), the liquid fraction profiles for a 0.5C-3Mn-3Ni (wt.%) alloy calculated by the standard equilibrium lever-rule microsegregation model (complete diffusion in the solid) and Scheil cases (null diffusion in the solid) are compared with the results obtained using the approximate microsegregation equations (characterized by incomplete solution diffusion in the solid) proposed by Brody-Flemings (Brody et Flemings, 1966), Clyne-Kurz (Clyne et Kurz, 1981), Ohnaka-Kobayashi (Ohnaka, 1984; Kobayashi, 1988) and Ganesan-Voller-Beckermann (Ganesan et Poirier, 1989; Voller et Beckermann, 1999).

Significant separation on the temperature-dependent liquid fraction is reflected on the movement of the predicted curves, obtained using different microsegregation models, to the

different lower solidus temperatures and their varied inclinations. Such important deviation in the freezing zones can affect the permeability of the mushy zone (Kurz et Fischer, 1989), the thermophysical features, and the resulting chemical distribution behavior. The selection with of the appropriate microsegregation model is thus of utmost significance for the accuracy of any macrosegregation predictions (Guan et al., 2018).
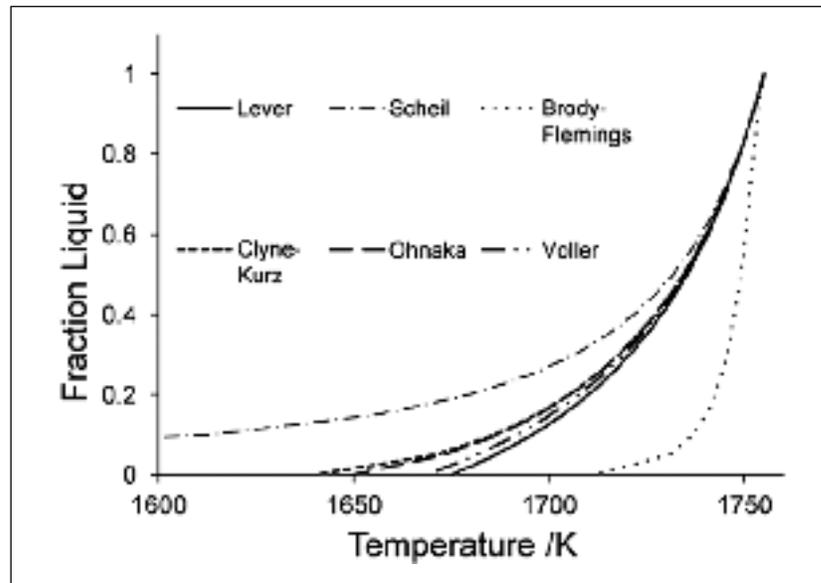
Figure 1.7 Liquid fraction vs temperature plots for a 0.5C-3Mn-3Mo (wt.%) alloy using various microsegregation models (Fridberg, Torndahl et Hillert, 1969).

4)   Solid thermomechanical deformation

In the available FEM simulation analyses, the solid is treated in two ways. On one hand, the solid was assumed to be a rigid, fixed and stationary phase (i.e. thermomechanical shrinkage is ignored) (Beckermann, 2002). On the other hand, important variables in solidification shrinkage and the deformation of the solid skeleton, such as solidification contraction ratio (Ehlen et al., 2003), casting speed (Chiang et Tsai, 1992; Gao et al., 2017), feeding length (Lan et Zhang, 2014), or the flow velocity (Heinrich et Poirier, 2004), were considered constant due to the unavailability of material temperature-dependent thermomechanical

parameters (Ehlen et al., 2003), or appropriate modeling tools (Reikher et al, 2010). Both assumptions are far from the realistic observations on huge ingots of the formation of top shrinkage and radial contraction (Figure 1.8) and could result in inaccuracies because changes in the composition and mechanical properties of the solidified phase are not taken into consideration (Beckermann, 2002). For this reason, there is always a need to clarify if the solid thermomechanical deformation should be taken into consideration, at the expense of computational cost, for the numerical study of the solidification behavior of large size ingots.

(a)   (b)
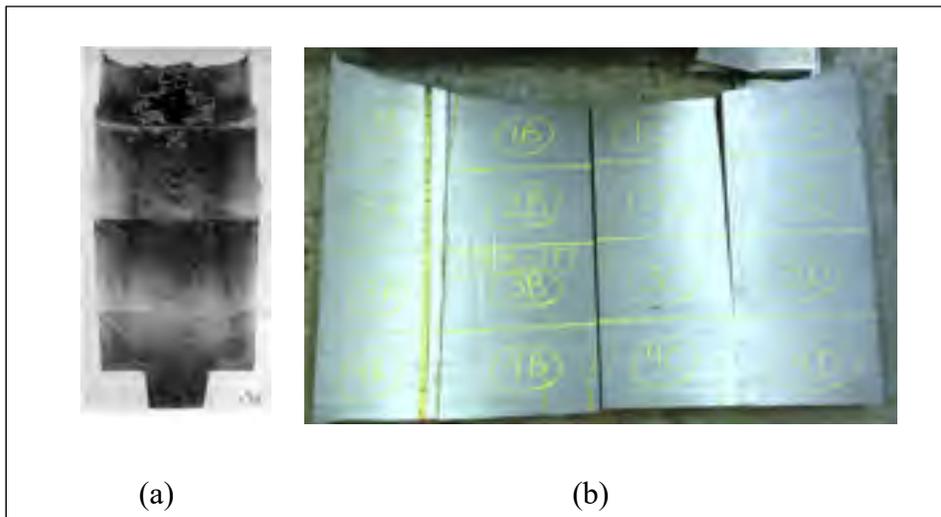
Figure 1.8 Observed top shrinkage in large size steel ingots. (a)
Longitudian section of a 65 MT steel ignot (Lesoult, 2005) (b)
Lognitudian section of the hot-top and upper section of a 40 MT
steel ingot from Finkle Steel

1.4 Project definition and methodology

The material in study is a high-strength medium-carbon low-alloy steel. Its nominal chemical composition is listed in Table 1-2. The steel is provided by the Finkle Steel, the largest ingot casting factory in Canada, which is known for its alloy steels used in the making of mold for plastic injection industry.

Table 1-1 Chemical composition of the investigated steel (wt.%).

C	Si	Mn	S	Cr	Mo	P	Ni	Fe
0.36	0.4	0.85	0.0023	1.82	0.45	0.01	0.16	Balance
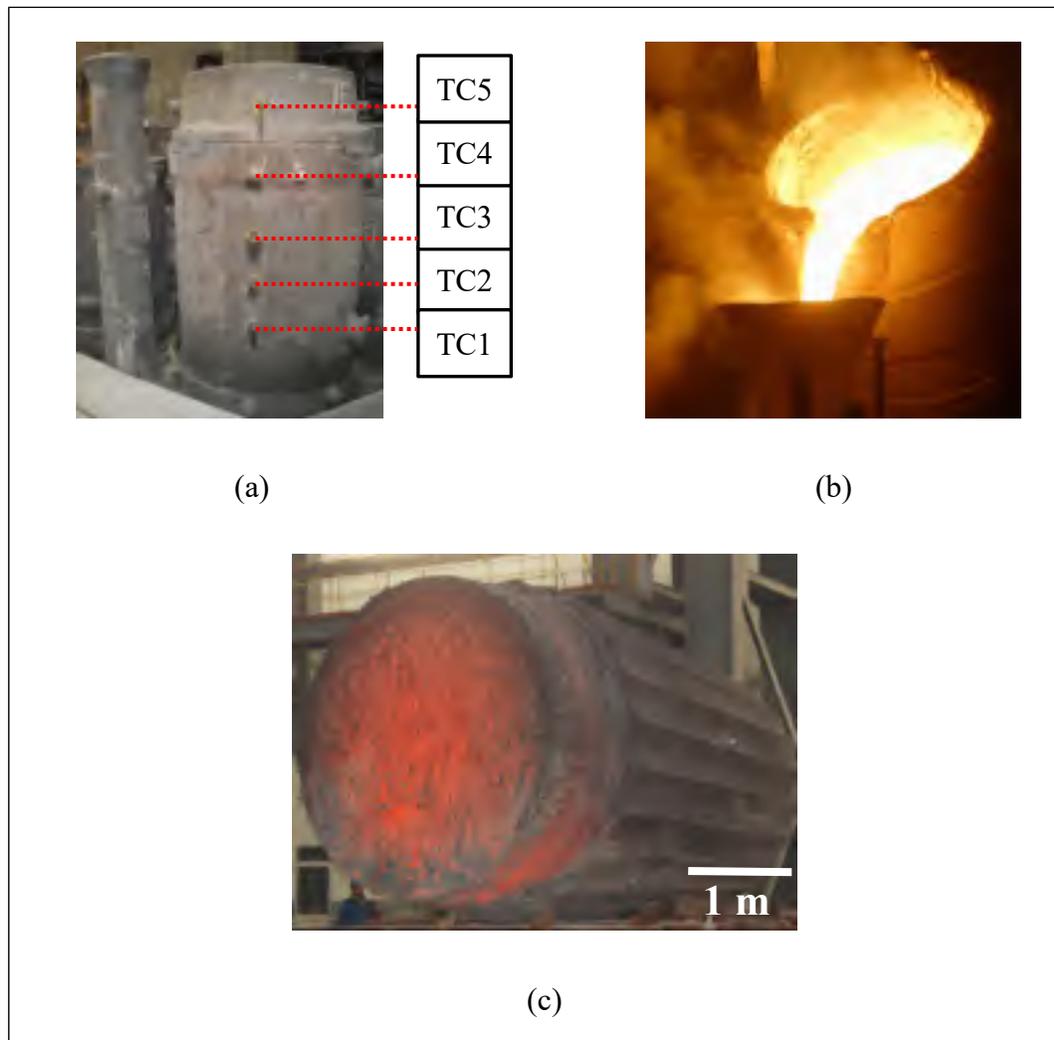
Figure 1.9 Bottom-pouring casting system, process and the 40MT steel ingot.
(a) 40MT ingot casting system (b) Bottom-pouring process (c) 40MT steel ingot.

The investigated ingots are nearly cylindrical shaped, with 250 cm in height and 150 cm in mean diameter, and weight 40 metric tons (MT). They were cast in big-end-up cast iron mold, as shown in Figure 1.9a. The hot-top, 70 cm in height as an extension of the ingot, was made

in the mold lined inside with insulting tiles. During the production process, molten steel with the nominal composition was first produced in a 45-ton electric arc furnace by melting scrap material, with alloying elements introduced. The liquid alloy was then teemed into a ladle before refining and vacuum degassing in an argon atmosphere. Then it was smoothly bottom poured into the mold at a designed temperature with a designed filling times, as shown in Figure 1.9b, until the mold was filled to the top of the insulating tiles. After solidification, the ingots were demolded, Figure 1.9c, and cooled in air.

The present project aims to identify effective measures to minimize macrosegregation intensity in the studied 40 MT steel ingots by means of simulation and experimentation for verification. To realize this objective, series of experimental and numerical works have to be conducted. As shown in Figure 1.10, they were split into three parts: experimental work, establishment of a reliable model and application of the established model. The experimental work is the source of the material properties necessary for the simulation, and the basis for the verification of predicted thermal, structural and chemical patterns of the numerical model.
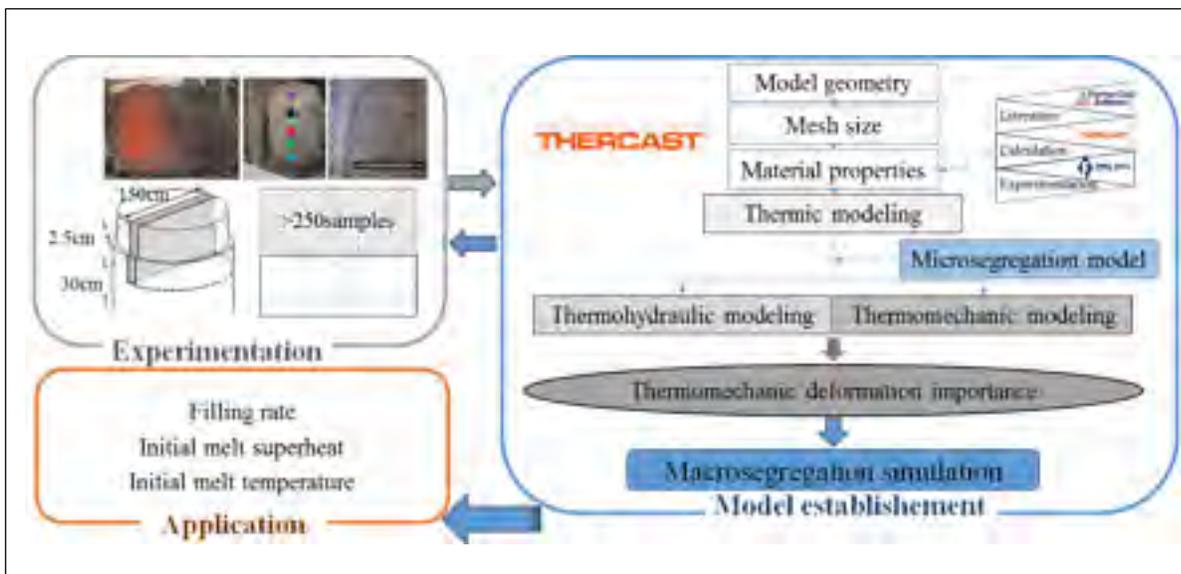
Figure 1.10 Schematic of the works involved in the experimental and modeling processes

1.4.1   Experimental work

In order to study the impact of casting process variables on extent and severity of macrosegregation, 4 ingots were fabricated with different filling rate, initial melt superheat and initial mold temperature, as listed in Table 1-3. Their chemical distribution profiles, mold outside surface temperature variation, and/or macro-/microstructures were characterized, and these experimental measurements were used to verify the simulation results.

Table 1-2 Ingots fabricated with varied casting parameters for the current project.

Ingot	Pouring temperature (°C)	Initial superheat (°C)	Filling time (min)	Initial mold temperature (°C)	Mold temperature measurement	Chemical characterization
1	1570	75	30	50	yes	yes
2	1570	75	22	50	no	yes
3	1557	62	30	50	no	yes
4	1576	81	34	80&120	yes	no

During the casting process of ingots n° 1 and 4, as indicated in Table 1-3, the temperature of the mold outside surface was monitored continuously throughout the casting procedure using Chromel-Alumel thermocouples (TC, type K) located in specified positions, as presented in Figure 1.9a. Each thermocouple was cemented into holes drilled 2.5cm into the mold from the exterior surface. Temperature measurements from each thermocouple were made every 90 seconds from the start of the steel pouring until the ingot was removed from the mold.

For ingots n° 1, 2 and 3, after solidification and stripping out, a block comprised of the hot-top and 30 cm thick section of the ingot's main body was transversely cut off for investigation, as seen in Figure 1.11a. Then, two plates ($130 \times 70 \times 1.5$ cm^3) were sliced on each side of the axial plane, as illustrated in Figure 1.11b. One slice was sectioned at regularly spaced intervals into over 250 samples ($6.5 \times 4.5 \times 1.5$ cm^3, Figure 1.11c). All the faces in the centerline plane along the longitudinal axis were ground, and then chemically

mapped using the Thermo Scientific ARL^{TM} 4460 Optical Emission Spectrometer (Thermo Fisher Scientific Inc., USA). The axial face of the other slice (Figure 1.11d) was prepared by grinding and macroetched in a 50 % HCl solution at 50 °C to reveal macrosegregation patterns.
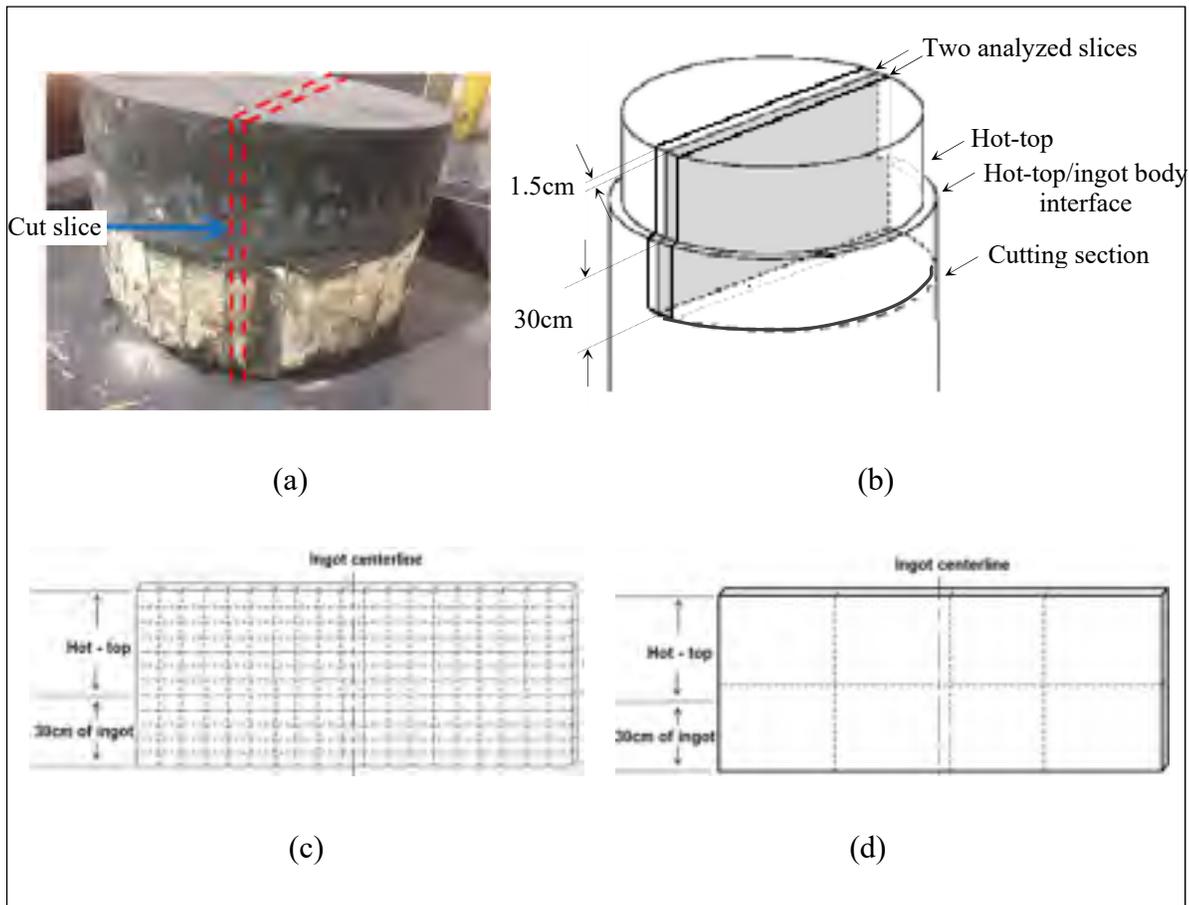
Figure 1.11 Cutting diagram for chemical and macrostructure analysis. (a) Photo of the cut block with the hot-top (with white insulating tiles) and 30 cm top section of the ingot (b) Cutting diagram of the analysed block (c) Slice cut into small samples for chemical characterization (d) Slice cut into large samples for macro etching.

The chemical composition of each specimen was obtained by averaging out 3 random spectrometer measurements and calculated using the relation (Duan et al., 2016):

$$R^i = (\omega^i - \omega_0^i)/\omega_0^i \tag{1.4}$$

Here, R^i is the segregation ratio for solute element i, ω^i is the solute's local concentration and ω_0^i is its nominal concentration value. A positive R^i value corresponds to positive segregation, and conversely, a negative R^i to negative segregation. Segregation ratio patterns of different elements on the longitudinal section of the entire block were then reconstructed using MATLAB® (MATLAB, 2012) by filling the areas between the isolines using constant colors corresponding to the local segregation intensities. Segregation intensity inside the solute-enriched A-type bands were examined with a sampling density of $0.9 \times 0.9 \times 1.5$ cm³ using the Thermo Scientific ARL™ 4460 Optical Emission Spectrometer (Thermo Fisher Scientific Inc., USA).

Microstructure analysis was performed on selected regions, which were metallographically prepared and etched in Oberhoffer's etchant (100cm³H₂O + 100cm³alcohol + 3cm³HCl + 0.2gCuCl₂*2H₂O + 3gFeCl₃*6H₂ + 0.1gSnCl₂*2H₂O) at room temperature, and then optically observed using a binocular microscope. Secondary dendrite arm spacing (SDAS) was determined by analyzing the micrographs based on the gray shades captured using the software Image J® (Abramoff, Magalhaes et Ram, 2004; Schneider, Rasband et Eliceiri, 2012) and the intercept method.

1.4.2   FEM model establishment

To establish a reliable model, a commercial FEM code Thercast® was first selected (TherCast 8.2®, 2012) due to its powerful computing capability and its performance for three-dimensional simulations of mold filling and solidification based on a volume-averaged solid-liquid two-phase model. Due to the combination of multi-scale phenomena, the segregation model consists of two parts: a macroscopic part with momentum, mass, heat, solute conservation equations, and a microscopic part that describes local solute transport. The analysis of fluid flow, temperature and solute distribution in the solidifying material is formulated by computing the thermal convection in the liquid pool and the mushy zone, the change of the metal volume and mass in the mold during the filling phase, and the deformation in the solid regions.

Then, for the model accuracy, the factors which could introduce uncertainties, as mentioned in section 1.3.2, were eliminated one by one using a combined experimentation and simulation approach:

1) The geometry and dimension of the model incorporates all the accurate geometric, structural and configuration features of the constitutional components of actual industrial casting system. Small modifications and a significant reduction in the model system size were performed based on the rotational symmetry condition to minimize the computation cost. The validity of the relevant changes was verified using series of comparative analyses.

2) The local friction and the thermal exchange between the steel and the mold components and the mutual exchange between mold components themselves in the casting system were close to the industrial practice.

3) The grid size for the discretization of the casting model was determined based on the sensitivity studies of the solidification predictions to the mesh size.

4) The input parameters used in the modeling of macrosegregation are temperature dependent, reflecting thermodynamic, thermomechanic and thermodiffusion behaviors of the investigated steel. The determination of the parameters were carried out by means of the combined approaches of computational thermodynamic software, simulation models, experimental room and high-temperature tension tests, calculations based on linearized binary phase diagram with respect to iron, as well as data from the industry, the literature and the Thercast$^{®}$ material database. The applicability of the used software and the modeling equations were verified before applying them to the investigated steel.

5) The microsegregation model that best predicts macrosegregation in the studied ingot was identified based on comparisons between predictions and experimental measurements. This performance evaluation was conducted after applying different microsegregation models to determine the thermophysical properties and solidification behavior of the studied steel. The sensitivity of the microsegregation behavior to the typical dendritic

structures (i.e. secondary dendritic arm spacing (SDAS)), which formed in the different stages of the solidification process, was also taken into consideration when the selection of the microsegregation model was conducted.

6) The importance of solid thermomechanical deformation in the solidification process of the large size ingot in study was examined by means of the comparative study between the thermohydraulic and thermomechanic behaviors in the studied industrial-scale casting system.

After the elimination of all the above uncertainties, the reliability of the developed model was validated using the experimentally measured top cavity dimension, the casting duration, the thermal profiles on the outside of the mold surface obtained using thermocouples, and the carbon distribution profile via mass spectrometer analysis.

1.4.3   Application of established model

Using the developed model, qualification and quantification of the impacts of three casting parameters (filling velocity, initial melt superheat and initial mold temperature condition) on the severity and extent of macrosegregation in the studied as-cast ingot were investigated. These casting parameters were determined, out of the five common countermeasures on the macrosegregation control, as presented in Section 1.2, to be the subject of the current project in consideration of several facts:

1) It is too laborious, time-consuming or even impossible to collect all necessary parameters for modeling and to carry out suitable experimental studies with which model results can be compared, when different materials are involved, particularly for large-size ingots. The techniques associated with varied materials include the optimization of alloy composition and the employment of multipouring operation.

2) It is too complicated and costly for an industry to adjust the existent casting tools. Drastically high cost and suspension of production could occur when such techniques are

implicated as the change of ingot dimensions and configurations, the introduction of multipouring technique and the application of forced melt flow.

3) Stringent control of casting parameters is the most imminent, practical, convenient and economic choice in industry, for a given material and existing casting system for large ingot manufacture. In addition, the data related to the impact of the three casting process variables are missing or conflicting in literature.

The obtained numerical and experimental results were interpreted in the framework of the theories of heat and mass transfer, and the diffusion and solidification of alloyed systems. The adjustments of the three casting variables were proposed for the control of the evolution of macrosegregation in the studied ingot. The beneficial effects of the adjustments on the alleviation of macrosegregation were quantitatively validated against experimental characterizations for the first time.

The model establishment was given systematically in Chapters II-VI, and the contents related to the appropriate microsegregation model determination and the importance of solid deformation in solidification process were explored into two articles. The work associated with the application of the established model for the examination of the impact of filling rate, initial melt superheat and initial mold temperature was formulated into four other articles and presented in detail in Chapters V-VIII. Other preliminary studies for the heterogeneity of material thermophysical properties resulting from the formation of macrosegregation, the microsegegation model investigations and the impact of non-uniform mold temperature were also performed and presented in three international conferences, which are given in Appendixes I-III.

The findings of the project are expected to contribute to a better understanding of the macrosegregation formation mechanisms. They could also be used in industry to improve the quality of large-sized ingot production and the productivity of high value-added steels or other alloys, which are prone to macrosegregation.

PRILIMINARY MODLE ESTABLISHEMENT

2.1 Model constitutive algorithm

The three-dimensional simulations of mold filling and solidification were performed in the finite element (FE) code Thercast®, based on a volume-averaged solid-liquid two-phase model (TherCast 8.2®, 2012). An Arbitrary Lagrangian-Eulerian (ALE) formulation was used for computing the thermal convection in the liquid pool and the mushy zone. The ALE approach was also used for managing the change of metal volume and mass in the mold during the filling phase. A Lagrangian method was employed for calculating the deformation in solid regions. Due to the combination of multi-scale phenomena, the segregation model consists of two parts: a macroscopic part with momentum, mass, heat, solute conservation equations, and a microscopic part that describes local solute transport. Sedimentation of equiaxed grains and the deformation of molds are not taken into account within the modeling, because they are not considered in the FE code or to reduce the computation times. Effects of small disturbances in the fields (e.g. dispersion fluxes, supercooling of the liquid, etc.) are neglected.

Two types of models were examined and compared in the present study: thermohydraulic model and thermomechanic one. For the thermohydraulic model, the heat and solute transport coupled with flow are driven by thermosolutal convection (buoyancy-driven flow). The thermomechanic model is developed where the thermosolutal transport induced by the combined effects of buoyancy- and shrinkage-induced flow was considered. For the former model, the density of the alloy was assumed not to change during solidification (i.e. $\rho_s = \rho_l$) so that the solid was assumed to be rigid and stationary. Except for that, all the following is the same for the two established models unless otherwise stated.

Before simulation, some assumptions were made to simplify the numerical models:

1) The liquid was assumed incompressible Newtonian and the fluid flow is laminar.

2) The mushy region was considered as an isotropic porous solid medium saturated with liquid (i.e. $f_s + f_l = 1$, where f_s and f_l denote the volumetric solid and liquid fraction, respectively). The permeability components depend on the model linking the macroscopic equations to microscopic effects. Its isotropic permeability K_{perm} is defined by the Carman-Kozeny formula (Farup et Mo, 2000):

$$K_{perm} = \frac{d_2^2 f_l^3}{180(1-f_l)^2} \tag{2.1}$$

in which d_2 is the average secondary dendrite arm spacing.

3) In the liquid phase, the gravity-driven natural convection loops were created by local density variation. These convective flows are mainly of two types: i) thermal convection flows induced by thermal expansion and temperature gradients, and ii) solutal convection flows induced by solutal expansion and concentration gradients. This is also the buoyancy term of the momentum equation:

$$\rho_l = \rho_0\left(1 - \beta_T\left(T - T_{ref}\right) - \sum_{i=1}^{n} \beta_i\left(\omega_l^i - \omega_0^i\right)\right) \tag{2.2}$$

Here, ρ_l is the density of the liquid, ρ_0 is the reference density taken at the reference temperature T_{ref} (imposed equal to the liquidus temperature), β_T and β_i are the thermal and solutal expansion coefficients, respectively, T is the temperature, ω_l^i is the solute concentration in liquid, and ω_0^i is the initial solute concentration for solute element i.

4) Microscopic diffusion in the liquid was assumed to be perfect. The diffusion of carbon in the solid is assumed to be complete (Level Rule behavior), while the diffusion of other solutes in the solid is supposed to be null (Scheil equation). The carbon concentration in the liquid with level rule behavior is expressed by:

$$\omega_l^C = \omega_0^C / \left(f_l + k^C(1 - f_l)\right) \tag{2.3}$$

The concentration of other solutes in the liquid with Scheil behavior is expressed by:

$$\omega_l^i = \omega_0^i / f_i^{k^i-1} \tag{2.4}$$

In the two equations, ω_0^i is the initial solute concentration, k_i is the partition coefficient by which the slope of solidus m_s^i and liquidus m_l^i (extracted from a linearized binary phase diagram with respect to iron) are connected together, $k^i = m_s^i / m_l^i$, to translate the non-homogeneous repartition of the chemical element i between the solid and the liquid. Other microscopic diffusion models for carbon were also considered and compared with the above two classical laws, which will be discussed in detail in Chapter 3.

5) Local temperature was considered as a function of the liquid concentration composition ω_l^i and the liquidus slope m_l^i:

$$T = T_m + \sum_{i=1}^{N} m_l^i \, \omega_l^i \tag{2.5}$$

where T_m is the melting temperature of the pure iron and N is the number of solute elements in the steel. This allows to express the total (combined thermal and solutal) buoyancy forces as $B \propto \sum_i (m_l^i \beta_T + \beta_\omega^i) \Delta \omega_l^i$.

6) The heat flux is determined by the law of Fourier and given by the sum of natural convection and radiation contribution:

$$q = -\lambda \nabla T \cdot n = h(T - T_{ext}) + \varepsilon_T \sigma_T (T^4 - T_{ext}^4) \tag{2.6}$$

where n denotes the outward normal unit vector, h (W/m/°C) is the heat transfer coefficient and T_{ext} is the external temperature (temperature of the mold), ε_T is the steel emissivity (assumed to be 0.8), σ_T is the Stephan-Boltzmann constant (= 5.776 × 10⁻⁸ W/m²/K). The value of heat transfer coefficient h depends on time or on the interface temperature between the part and the mold, simulating the casting/mold contact or loss of contact (formation of air gap) during the cooling of the metal.

7) The solute flux is determined by Fick's law:

$$j = -D_l^i \nabla \omega_l^i \tag{2.7}$$

where D_l^i is the diffusion coefficient of the chemical element i in the liquid.

Based on these hypotheses, the analysis of fluid flow, temperature, and solute distribution in a solidifying material amounts to the coupled solution of the equations stating the conservation of mass, momentum, energy and solute. A coupled computation of the stress fields is also performed.

The thermal problem treatment is based on the resolution of the heat transfer equation (energy conservation):

$$\rho \frac{\partial H}{\partial T} \frac{dT}{dt} - \nabla \cdot (\lambda(T)\nabla T) = 0 \tag{2.8}$$

where ρ (kg/m³) denotes the density, T (°C) is the temperature, λ (W/m/°C) is the thermal conductivity and H (J) is the enthalpy, which can be defined as:

$$\frac{\partial H}{\partial T} = C_p(T) + L_f \frac{\partial f_l(T)}{\partial T} \tag{2.9}$$

where C_P (J/kg/°C) is the specific heat, f_l is the volume fraction of liquid, L_f (J/kg) is the specific latent heat of fusion.

Redistribution of each solute i is governed by solute conservation equation:

$$\frac{\partial \omega^i}{\partial t} + v \cdot \nabla \omega_l^i - \nabla \cdot \left(f_l D_l^i \nabla \omega_l^i\right) = 0 \tag{2.10}$$

The mechanical equilibrium is governed by the momentum conservation equation (conservation of quantity of movement, fundamental equation of dynamics):

$$\nabla \cdot s - \nabla p + \rho g = \rho \frac{dv}{dt} \tag{2.11}$$

where s is the Cauchy stress tensor, p is pressure, g is the gravitational acceleration, v is the average velocity.

To simulate the cooling of the material from the liquid state, the mushy state to the solid state, a hybrid constitutive model is used, and the averaged mass balance is metal state

dependent. In the liquid, metal is treated as a thermo-Newtonian fluid using ALE. The behavior is dealt with by the Navier-Stokes equation with temperature-dependent terms:

$$\bar{\sigma} = \eta_l(T)\sqrt{3}^2 \dot{\bar{\varepsilon}} \qquad (2.12)$$

where $\bar{\sigma}$ is the Von Mises equivalent flow stress, η_l is dynamic viscosity of the liquid, T is the temperature, $\dot{\bar{\varepsilon}}$ is the equivalent plastic strain rate. In the solid state (below the solidus temperature T_s), the metal is assumed to be thermo-elasto-viscoplastic and treated in a Lagrangian formulation. The law II of Kozlowski et al. can be reformulated:

$$\bar{\sigma} = K_s(T)\bar{\varepsilon}^{n(T)}\dot{\bar{\varepsilon}}^{m(T)} \qquad (2.13)$$

where K_s is the viscoplastic consistency in the solid, $\bar{\varepsilon}$ is the equivalent plastic strain, n the strain hardening coefficient and m the sensitivity coefficient of the flow stress to the strain rate.

The mushy state is approximated as a single continuum that behaves as a generalized non-Newtonian (viscoplastic) fluid. Two different behaviors of the metal in mushy state are distinguished by a so-called coherency temperature T_{conf}, which is the temperature at which liquid volumetric fraction $f_l = 0.3$.

Above the temperature T_{conf}, the semi-liquid material at high liquid fraction is treated as the liquid circulating in a solid skeleton. A thermo-viscoplastic (VP) behavior with a behavior of the Norton-Hoff type is considered:

$$\bar{\sigma} = K^{vp}(T)\sqrt{3}^{m(T)+1}\dot{\bar{\varepsilon}}^{m(T)} \qquad (2.14)$$

where K^{vp} is the viscoplastic consistency of the material. The strain rate tensor $\dot{\varepsilon}$ is split into a viscoplastic (nonreversible) component and a thermal component. The solidification shrinkage is calculated from the equation: $\Delta\varepsilon_{tr} = (\rho_s - \rho_l)/\rho_l$, where ρ_s, ρ_l denotes densities at the solidus and liquidus temperature, respectively. And the continuity equation (equation of conservation of mass):

$$\nabla \cdot v = 3\alpha(T)T + \dot{f_s}(T)\Delta\varepsilon_{tr} \tag{2.15}$$

Where α is the coefficient of linear thermal expansion.

Below the temperature T_{conf}, the semi-solid metal at low liquid fraction is supposed to obey a thermo-elasto-viscoplastic (EVP) constitutive behavior modeled by the Perzyna law with threshold type:

$$\bar{\sigma} = \sigma_s + K^{evp}(T)\sqrt{3}^{\,m+1}\bar{\varepsilon}^n \dot{\bar{\varepsilon}}^m \tag{2.16}$$

The strain rate tensor $\dot{\varepsilon}$ is split into an elastic part, a visco-plastic part, and a thermal part. And the continuity equation (equation of conservation of mass):

$$\nabla \cdot v = -\left(\frac{\dot{p}}{x} - \frac{\dot{x}}{x^2}p\right) + 3\alpha(T)\dot{T} + \dot{f_s}(T)\Delta\varepsilon_{tr} \tag{2.17}$$

Here, $x = \frac{E}{3(1-2v)}$, E is the Young's modulus (MPa), v is the Poisson's coefficient.

Thermodynamic equilibrium is assumed at the solid-liquid interface. This requires continuity of the flow stress at the coherency temperature (T_{cohe}) ensured by requiring equality of the data (consistency, strain rate sensitivity coefficient) and nullity of the threshold of elasticity:

$$\begin{aligned} K^{evp}(T_{cohe}) &= K^{vp}(T_{cohe}) \\ m^{evp}(T_{cohe}) &= m^{vp}(T_{cohe}) \\ \sigma_s(T_{cohe}) &= 0 \end{aligned} \tag{2.18}$$

In the resolution stage, a coupled computation of the stress and temperature fields was performed so that equations were solved iteratively using a prescribed time step. The solution procedure is composed of the following steps:

1) Solution of the energy conservation equation (possibly time step optimization), output H;

2) Solution of the solute conservation equation, output ω;

3) Local resolution, at each node, and calculation of f_l, T and ω_l with the microsegregation model, using the latest calculated values of ω and H provided by the above two steps;

4) Solution of the mass and momentum conservation equations, output p and v.

The detailed derivation of the associated auxiliary equation can be found in reference (TherCast 8.2®, 2012) and they will not be repeated here.

2.2 Determination of model geometry

Initially, each component of the casting mold was constructed in the CATIA ™ software (CATIA V5 R20). The geometries and dimensions of each piece were set up in reference to the actual casting system (Figure 1.9a). Once all the parts were ready, they were transferred to and assembled in the software Thercast® where the modeling was done. As presented in Figure 2.1, the established 360° model incorporates all geometric and structural features, such as all constitutional components, lugs on the exterior mold surface, square flange on the lower section of hot-top mold, 24 corrugations on the interior surface of the big-end-up gradual tapering mold, 24 flutings on the exterior surface of the cylindrical steel ingot and 1.05° slope angle of the ingot. Such configuration has bilateral symmetry and thus requires one-half of the system to be modeled.

In order to reduce the computation times, simplifications were made in two ways: 1) lugs on the lower mold outside surface were removed (total mass of the lugs = 389 kg), Figure 2.2a, to realize 4 rotational symmetries and 4 reflection symmetries, so that 1/8 (45°) of the system is representative enough for the casting assembly, as shown in Figure 2.3a; (2) all lugs on the mold outside surface were removed (total mass of the lugs = 486 kg) and the square flange on the lower part of the hot-top mold was modified to be circular with the height and volume unchanged, as shown in Figure 2.2b. The aim of the second modification is to realize rotational symmetry of order 24 (due to 24 flutings) and 24 lines of reflective symmetry (half of one fluting) so that 1/24 (15° model, Figure 2.3b) of the casting system can be modeled. For both changes, all interior features of the mold and the ingot, together with the system components are untouched, as compared between Figures 2.1b and 2.3c.
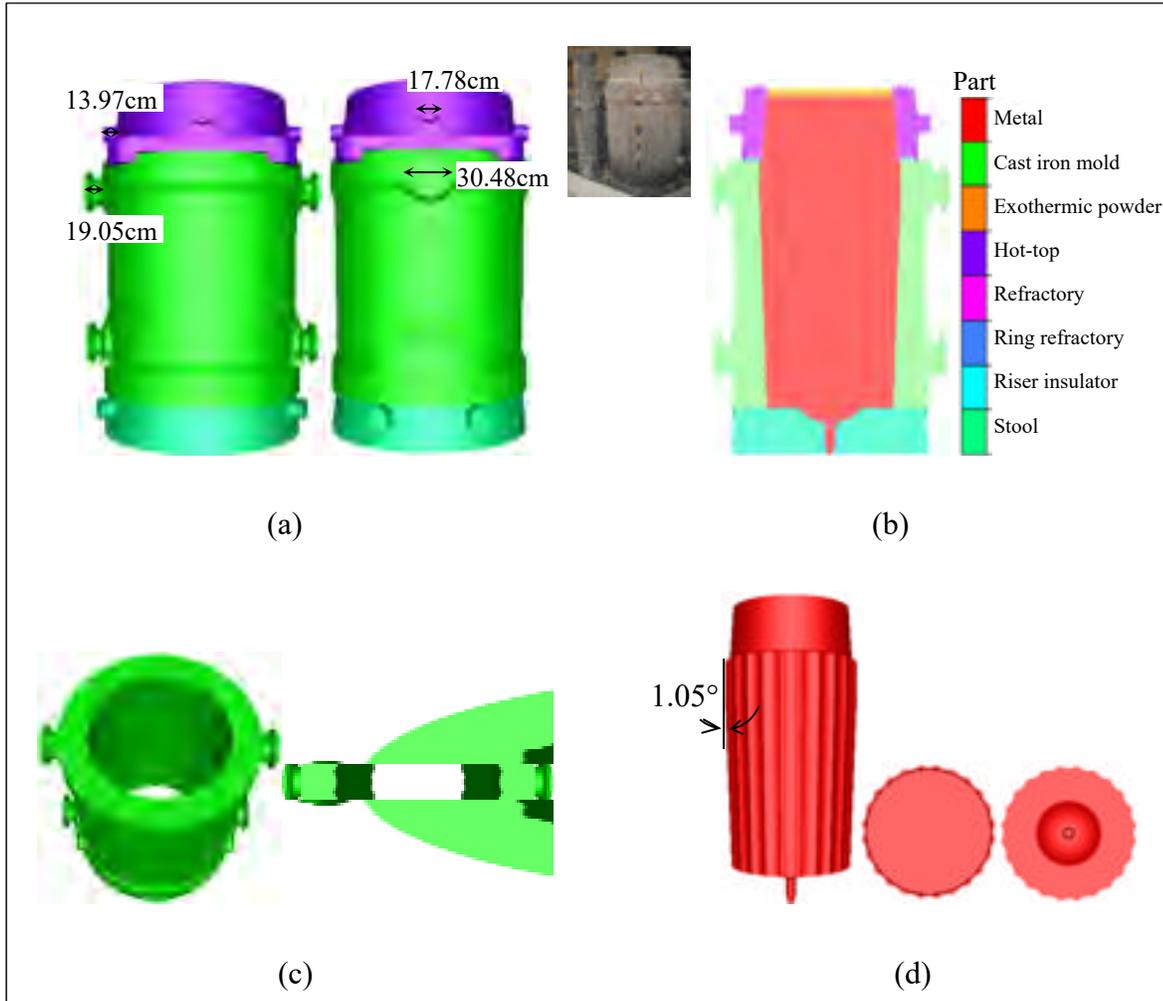
Figure 2.1 360° 3D model established based on actual casting system. (a) Front and side views of the entire system (b) Components of the system (c) Big-end-up cast iron mold with 24 corrugations (or flutings) on interior surfaces (d) Cylindrical ingot with 24 flutings on the outside surface as well as top and bottom views.

When only thermic behavior (pure conduction) was taken into consideration, the similarity on predictive capability between models 45M and 15M1 was reflected on the solidification time predictions (10min difference), as compared between Figures 2.4b and 2.5b. Similar tendency was also observed when thermomechanic behavior was calculated (Figures 2.4c and 2.5c, 32min difference in solidification time as a result of finer meshes in 15M1). Temperature profiles captured by the sensors (SN) located at the same position of the experimental thermocouples (TC) were almost identical between the two examined models,

as compared between Figure 1.9a and the image on the upper right corner of Figure 2.6. All the above calculations were performed using the available properties of the 25CrMo4 steel (with compositions similar to the steel in study, as listed in Table 2-1) under the boundary conditions of ingot n° 1 (given in Table 1-2). These results demonstrate that the decrease of the model size from 1/8 to 1/24 casting system does not indeed result in divergence, and the simplification of the model based on symmetry conditions is reasonable.

(a)   (b)
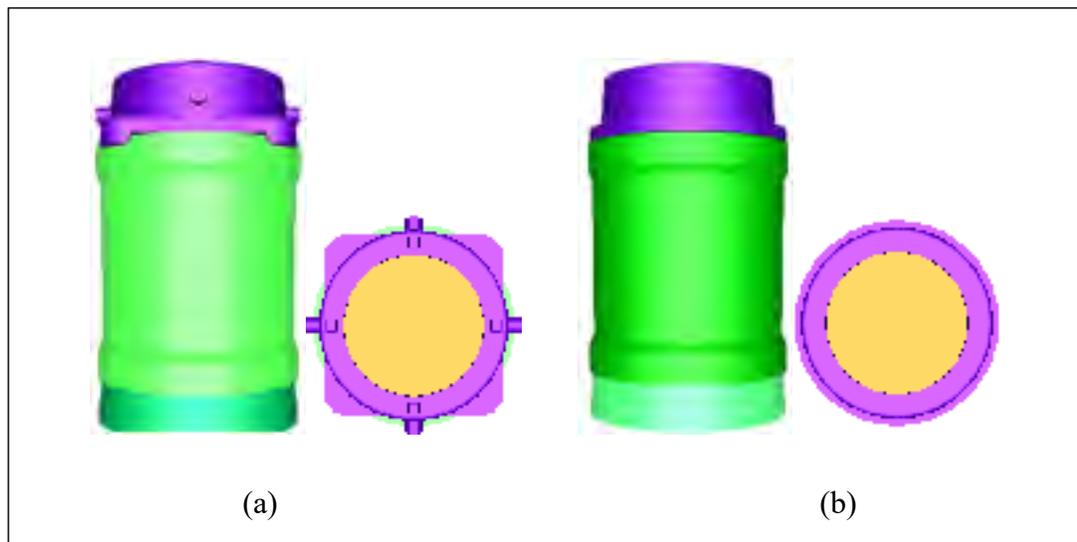
Figure 2.2 Side and top views of 360° 3D simplied models. (a) Simplified model with rotational symmetry of order 8 (b) Simplified model with rotational symmetry of order 48.

Table 2-1 Chemical composition of the steel 25CrMo4 (wt.%).

C	Si	Mn	S	Cr	Mo	P	Fe
0.25	0.4	0.9	0.035	1.2	0.3	0.035	Balance

It cannot be ignored that the decrease in the mold size from 45M to 15M1 with similar grid size led to a significant reduction in the computation times from weeks to 12 hours. Furthermore, a finer mesh in 15°C model produced less noise on the solid front (Figures 2.4d

and 2.5d). All the above efficient and accurate elements make the 15° model decided to be the baseline geometry for all the rest simulation work.

2.3   Determination of mesh

A good mesh is the basis of an accurate simulation. A low-quality mesh will not only result in inaccurate simulation results but might even cause the solver to produce an error due to instability. However, a higher quality mesh equates to significantly high computational cost. Hence, the balance between the level of mesh fineness and the computational cost was explored.
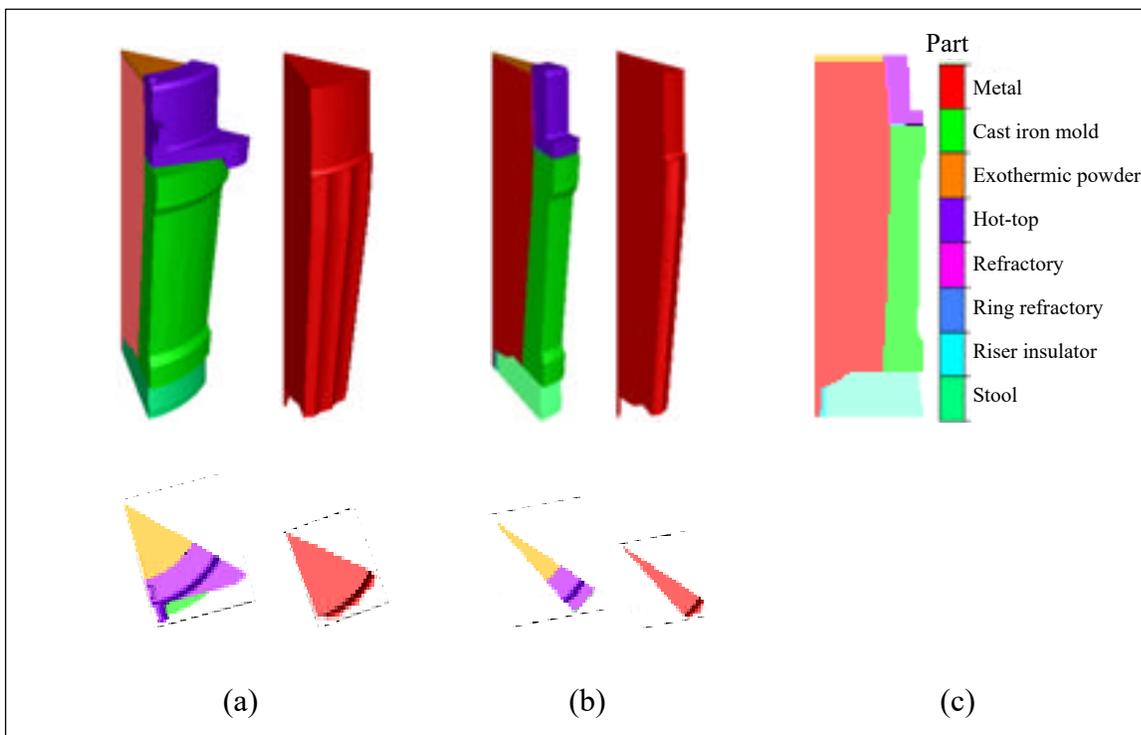
Figure 2.3 Simplied models to different extents with side and top views of the casting system and ingot. (a) 1/8 (45°) model (b) 1/24 (15°) model (c) Casting system components.

Based on the experimentally measured 30mm and less in width for the A-segregated bands on the centerline cross section of ingots n°1 and 2, the meshes used to determine the model size (in Figure 2.5a with an average grid size of 55 mm) need to be refined so as to realize

the prediction on channel segregates. Two finer overall grid sizes (linear tetrahedral elements) were designated to the determined 15° model: one is with the average general cell size of 35 mm (Figure 2.7a), and the other is with the cell size of 25 mm (Figure 2.8a). For both of them, the interface regions between the ingot and the mold wall were further refined to improve computation accuracy, as shown in the images, placed next to Figures 2.7a and 2.8a of the enlarged corresponding regions framed in blue. More detailed meshing data for the casting system have been given in the last two columns of Table 2-2 (models 15M2 and 15M3).

Solidification time simulations in thermic (Figures 2.7b and 2.8b) and thermomechanic calculation modes (Figures 2.7c and 2.8c) were performed in the 15° model for the steel 25CrMo4 (with compositions similar to the steel in study, as listed in Table 2-2) with the two different grid sizes under the casting condition of ingot n°4 (Table 1-2). Comparative examination of solidification time revealed a difference of about 15min between them, corresponding to 2 % deviation.

(a) (b) (c) (d)
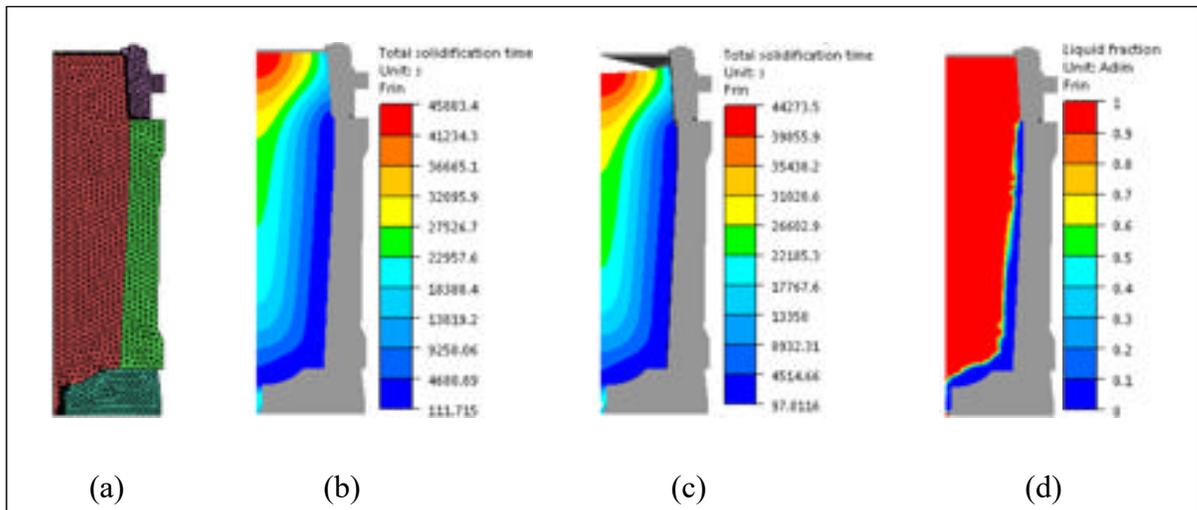
Figure 2.4 45° model (45M). (a) Mesh image with 31877 elements (15-60 mm grid size) (b) Predicted total solidification time from thermic calculation (12 h 43 min) (c) Predicted total solidification time from thermomechanic calculation (12 h 18 min) (d) Liquid fraction pattern at the end of filling stage.
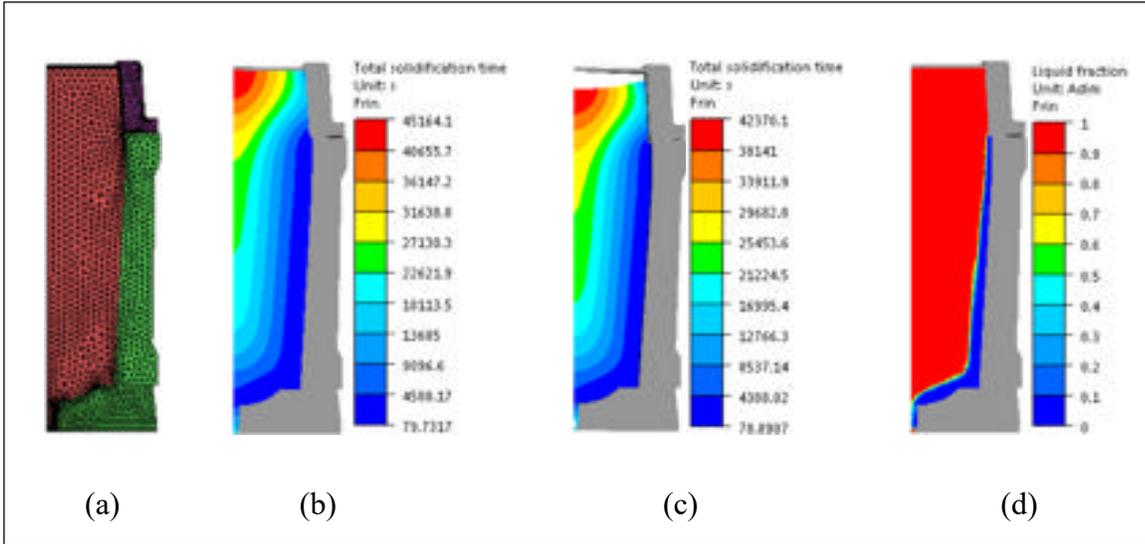
Figure 2.5 15° model (15M1). (a) Mesh image with 17626 elements (15-60 mm) (b) Predicted solidification time in thermic calculation mode (12 h 33 min) (c) Predicted solidification time in thermomechanic calculation mode (11 h 46 min) (d) Liquid fraction pattern at the end of filling stage.
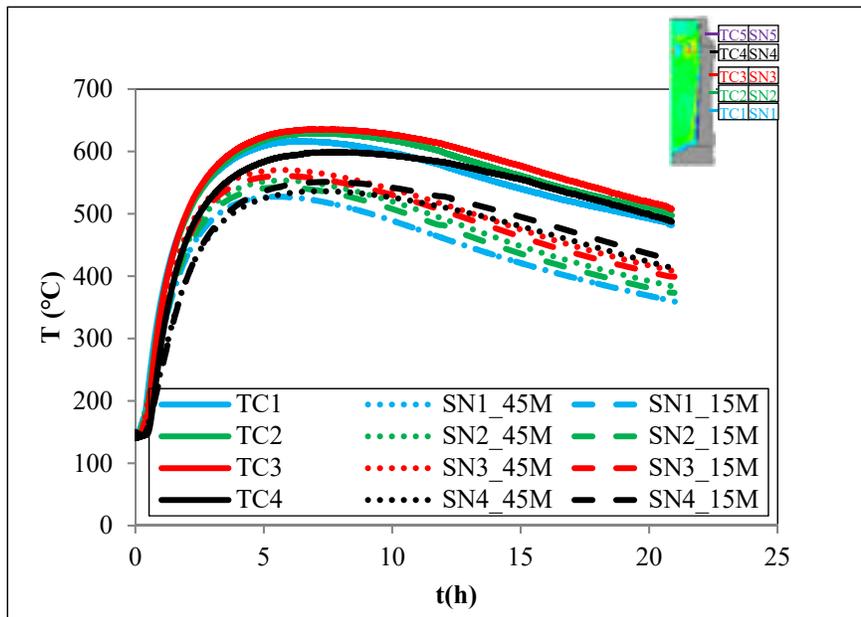
Figure 2.6 Variation of temperature on the mold outside surface for the 45° and 15° models.
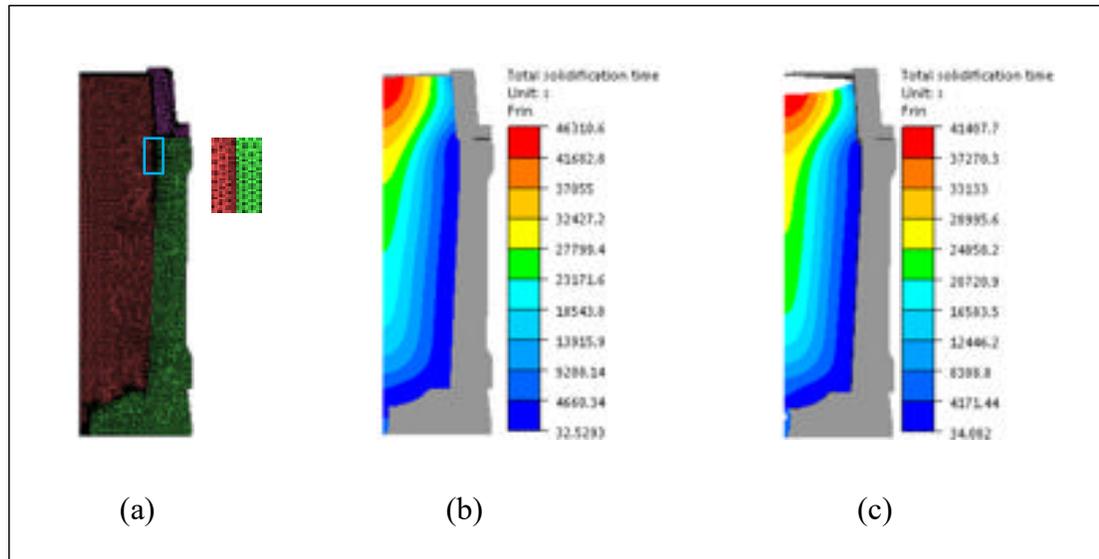
Figure 2.7 15°C model with 46872 elements (grid size of 10-40 mm) (15M2). (a) Mesh image (b) Predicted solidification time with thermic calculation (12 h 52 min) (c) Predicted solidification time with thermomechanic calculation (11 h 30 min).
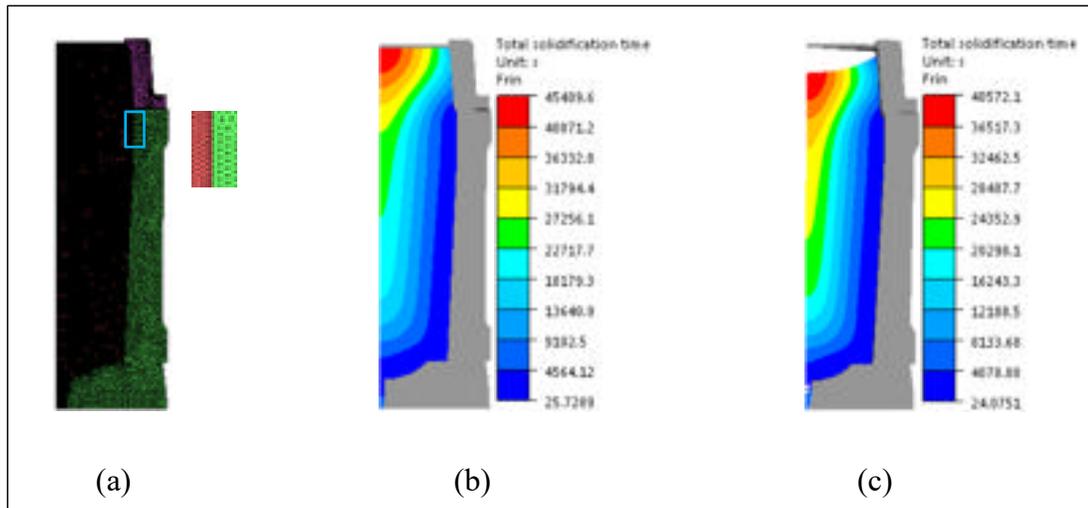
Figure 2.8 15° model with 244216 elements (grid size of 8-30) (15M3). (a) Mesh image (b) Predicted solidification time with thermic calculation (12 h 37 min) (c) Predicted solidification time with thermomechanic calculation (11 h 16 min).

Table 2-2 Tested models and meshes.

Name	45° Model	15° Model		
	45M	15M1	15M2	15M3
Number of nodes in the steel part	6921	4316	10770	49960
Number of elements in the steel part	31877	17626	46872	244216
Total number of nodes in the casting system	25679	14209	41192	80382
Total number of elements in the casting system	112351	56895	182103	379447

Furthermore, macrosegregation calculations in thermomechanic mode (solute distribution, thermal conduction, natural convection and thermomechanical shrinkage are all taken into account) were repeated three times for both established meshes (Figures 2.9 and 2.10). The modeling was performed for the steel in study, using the determined parameters presented in the following sections in this chapter, under the casting condition of ingot n°1 (Table 1-2). It was seen that solidification time deviated 1.2 % for the 35 mm mesh, and the result deviation range got to 0.4 % for the 25 mm mesh case. This finding indicates that over 5 times finer mesh decreased the result deviation range to a limited extent.

It should be noted that the increase of the mesh refinement from 35 mm to 25 mm is too computational expensive. The computation time for macrosegregation can be controlled within 2 days for the former, while it gets to a couple of weeks for the latter. Considering the acceptable stability and small deviation range arising from the mesh size effect, it can be said that the 15° model with medium mesh size (model 15M2 with average grid size of 35 mm with 46872 elements) can provide a compromise between computational accuracy and efficiency. Therefore, the 35mm mesh 15° model was deemed as the base for all the rest simulations.
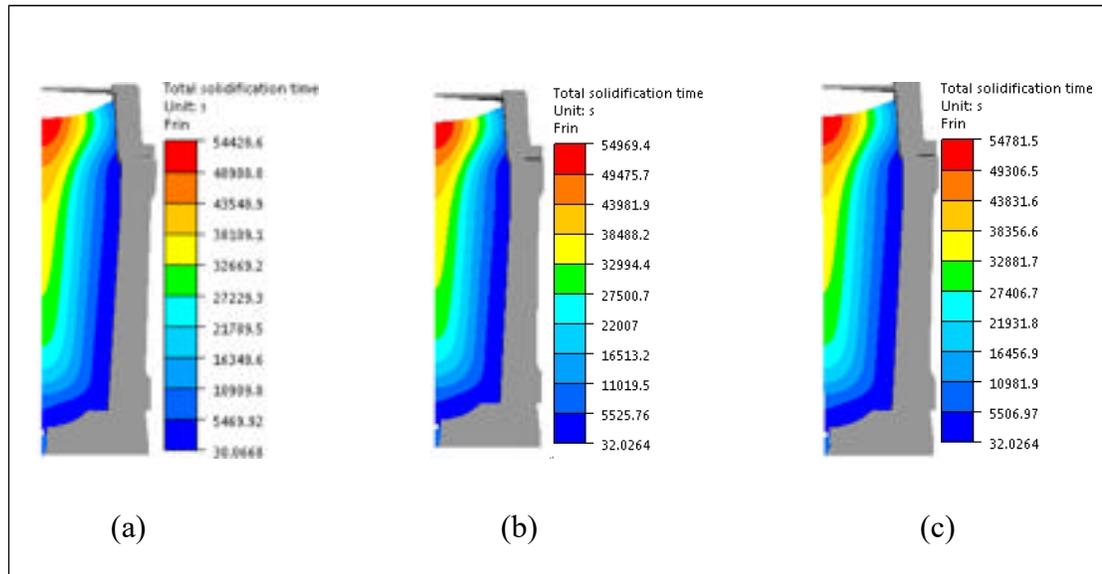
Figure 2.9 Three solidification times predicted by the 15° model with 46872 elements (10-40 mm grid size) (15M2) with macrosegregation simulation of the steel in study in thermomechanic calculation mode. (a)15 h 07 min (b) 15 h 16 min (c) 15 h 13 min.
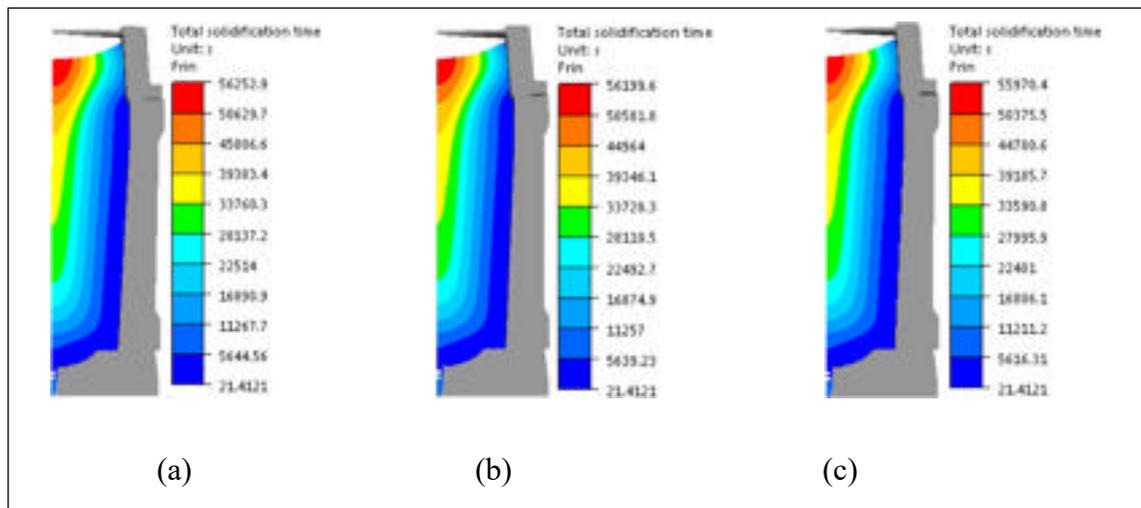
Figure 2.10 Three solidification times predicted by the 15° model with 244216 elements (8-30 mm grid size) (15M3) with macrosegregation simulation of the studied steel in thermomechanic calculation mode. (a)15 h 38 min (b) 15 h 37min (c) 15 h 33 min.

2.4 Determination of material properties

Macrosegregation models depend significantly on the input parameters fed into them. Typical input parameters are temperature dependent, reflecting thermodynamic, thermomechanic and thermodiffusion behaviors. Slight variations in such values have been found to influence (often significantly) model results (Schneider et Beckermann, 1995; Wu, Ludwig et Fjeld, 2010). So, all steel properties were cautiously determined or selected.

As shown in Figure 2.11, four different materials are concerned for the casting system in study: the steel casting, the cast iron hot-top, mold and base, the insulating refractory tiles, and the exothermic board at the top. The property determinations of all the four types of materials are given in detail in the following context.
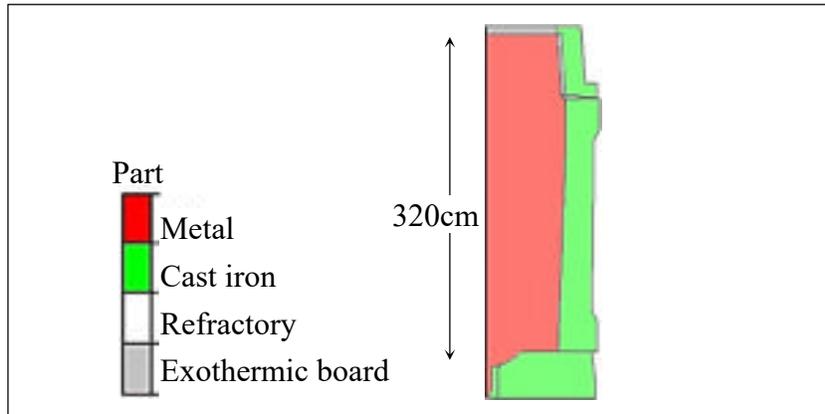
Figure 2.11 Established model made of different materials.

2.4.1 Steel thermodynamic properties

The temperature dependence of the density (ρ), solid fraction (f_s) and the specific heat capacity (C_p) of steel were determined by means of the computational thermodynamics program Thermo-Calc® classic version R with the TCS Fe-containing slag database

(Andersson et al., 2002). The thermal conductivity of the steel (λ) was assumed to follow the model below as a function of temperature and phase fraction (Miettinen, 1997).

$$
\begin{cases}
\lambda = f_\alpha \lambda_\alpha + f_\delta \lambda_\delta + f_\gamma \lambda_\gamma + f_L \lambda_L \\
\lambda_\alpha = (80.91 - 9.9269 \times 10^{-2} T + 4.613 \times 10^{-5} T^2)\left(1 - a_1 \left(C_{pct}\right)^{a_2}\right) \\
\lambda_\delta = (20.14 - 9.313 \times 10^{-3} T)\left(1 - a_1 \left(C_{pct}\right)^{a_2}\right) \\
\lambda_\gamma = 21.6 + 8.35 \times 10^{-3} T \\
\lambda_L = 39 \\
a_1 = 0.425 - 4.385 \times 10^{-4} T \\
a_1 = 0.209 + 1.09 \times 10^{-3} T
\end{cases}
\tag{2.19}
$$

where f_δ, f_γ and f_L are the volume fractions of δ-ferrite, γ-austenite and liquid, respectively, determined using Thermo-Calc®, T is the temperature in °C, ω_0^C is the nominal weight percent of carbon in the steel.

The applicability of the software Thermo-Calc® and Miettinen's model was verified before applying them to the investigated steel. First, the solid fraction of AISI steel 316, the density of pure iron, the specific heat capacity of AISI steel 1040, and the thermal conductivity coefficient of AISI steel 1020 were calculated using Thermo-Calc®/Miettinen's model. The obtained values were found to generally agree with the corresponding experimental behaviors gathered from the literatures ((Mills, 2002) for 316 steel and pure iron, (Physical constants et al., 1953) for 1040 and (Thermo properties et al.) for 1026 steels). The software and the model were then used to calculate the thermodynamic properties of the investigated steel. The curves used for verifying the applicability of the above approach, as well as the determined thermodynamic properties of the studied steel as a function of temperature, are plotted in Figure 2.12.
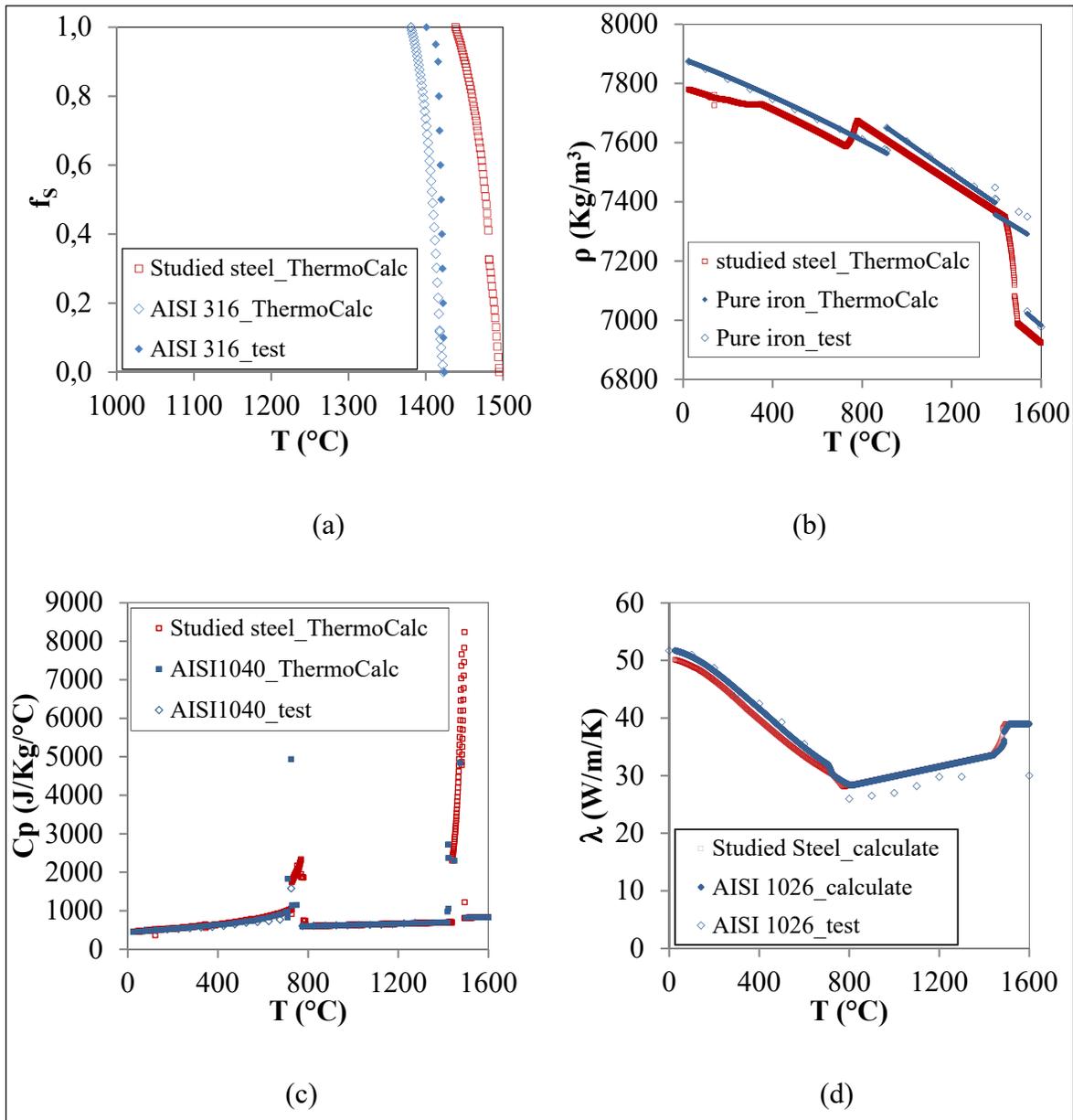
Figure 2.12 Temperature dependence of thermodynamic parameters of the studied steel. (a) Solid fraction (b) Density (c) Specific heat capacity (d) Thermal conductivity coefficient.

2.4.2   Steel thermomechanical properties

Thermomechanical behaviors of studied steel were determined experimentally by means of room and high temperature tensile tests. Cylindrical specimens were from the regions with

the uniform chemical compositions similar to the nominal one (the square region framed with dashed lines with segregation ratio = 0 in Figure 2.13a) and safe from solute enriched A-segregated bands (black bands in the macrograph, as seen in Figure 2.13b, of the square region framed in dashed lines in Figure 2.13a). They were machined parallel to the radial direction of the ingot (as shown in Figures 2.13a and b), with a diameter of 10mm, a length of 122 mm and the gauge length of 22 mm, as illustrated in Figure 2.13c.
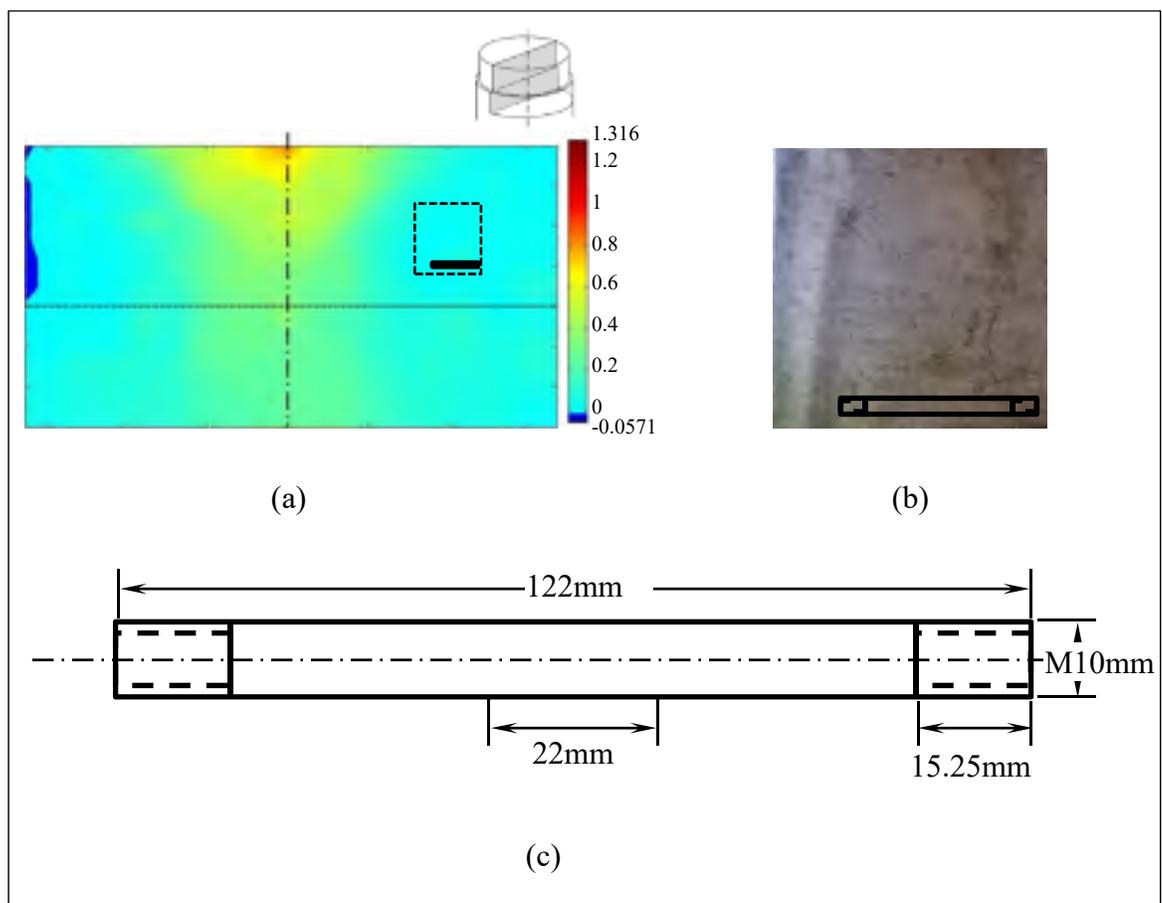
Figure 2.13 Source and geometry of tensile specimens for tensile tests. (a) Segregation ratio pattern of carbon on the longitudinal section of the hot-top and upper section of ingot n° 1 (b) Macrograph of the square region framed in dashed lines in segregation ratio pattern with solute-enriched black A-segregation bands (c) Specimen geometry for tensile tests according to ASTM A370 standard.

The testing conditions were determined based on the predictions from the macrosegregation simulation in thermomechanic calculation mode for the steel 25CrMo4 using the 15° model (15M2). For temperature range determination, temperature pattern was examined at the end of solidification, as given in Figure 2.14. The lowest temperature occurred at the right corner of the ingot bottom and got to 630 °C. Given the pouring temperature for the studied ingots (1557-1576 °C) and the limit capability of the available testing equipment, the tensile temperature range was decided to be 20-1300 °C.
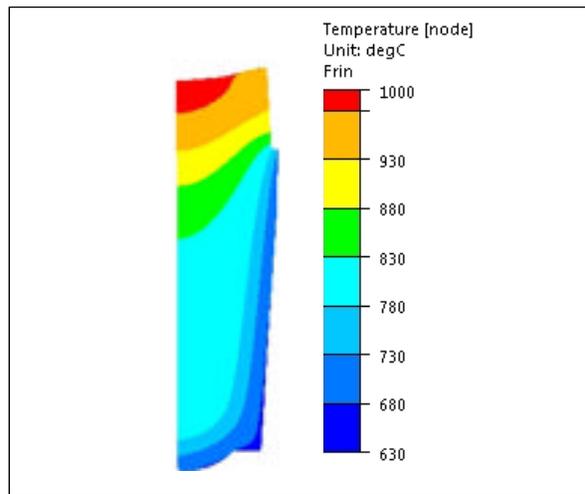
Figure 2.14 Temperature field predicted
by macrosegregation simulation for the
steel 25CrMo4 using 15M2 model.

For determination of testing strain rates and strain extent, the predicted strain rate pattern was quantitatively analyzed. As shown in Figure 2.15a, 15 points were selected along the diagonal line from the bottom right corner to the top center of the entire casting to examine the evolution of strain rates from the pouring moment till the end of solidification. It can be seen in Figure 2.15b that intense strain rates were concentrated in the early stage of casting. Through zooming in the plot in the first hour (Figure 2.15c) and in the range below 0.005/s (2.15d), 10^{-3} and 10^{-4} /s were determined to be the two strain rates for test due to their representativity for most analyzed positions.
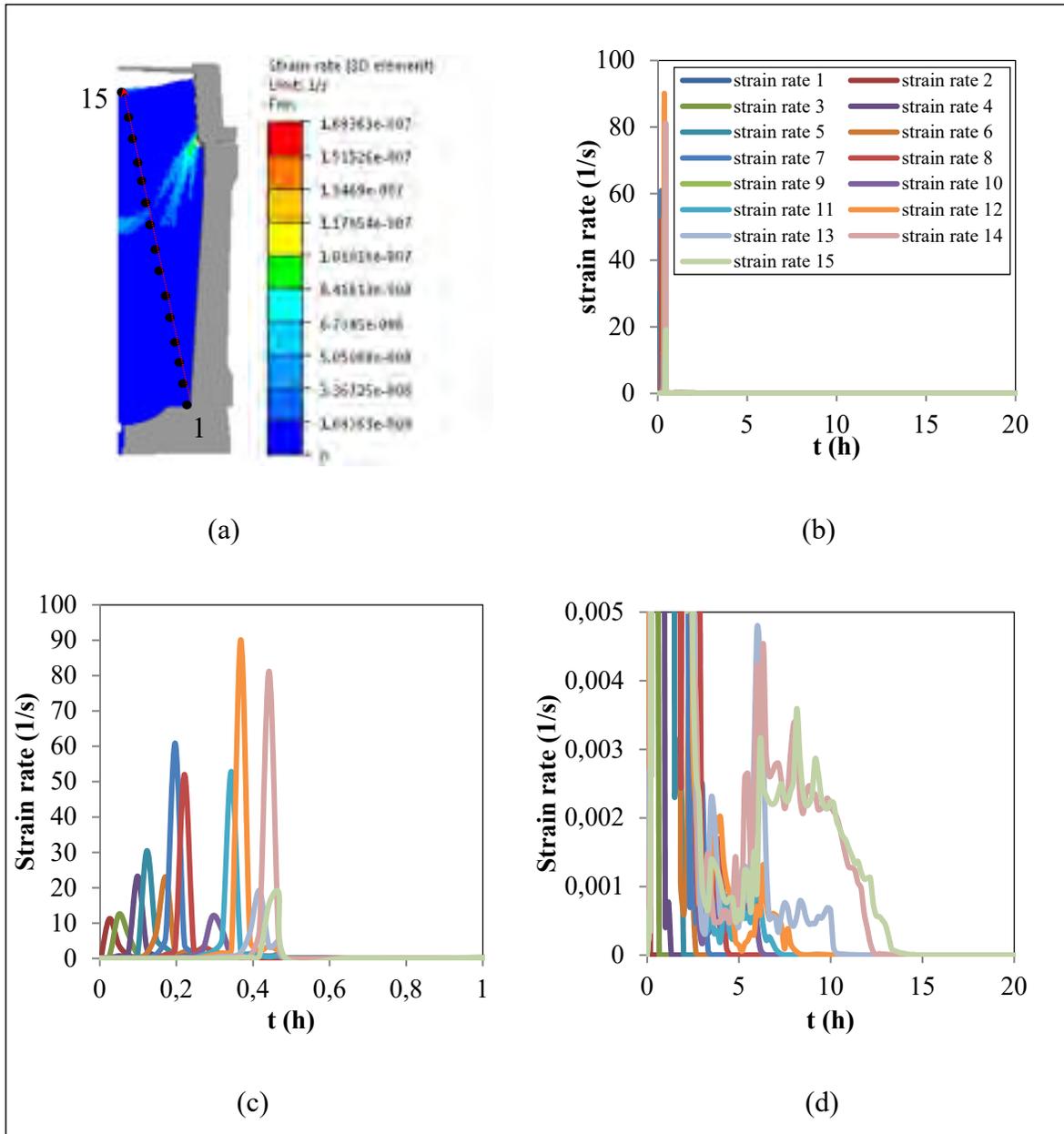
Figure 2.15 Strain rate analyses on the 15° model (15M2) with thermomechanical macorsegregation simulation of steel 25CrMo4 along the diagonal line of the ingot. (a) Strain rate pattern and the 15 analyzed points (b) Strain rate evolution during the casting process on the 15 selected points (c) Enlarged strain rate plot in the first hour (d) Enlarged strain rate plot below the 0.005 strain region.
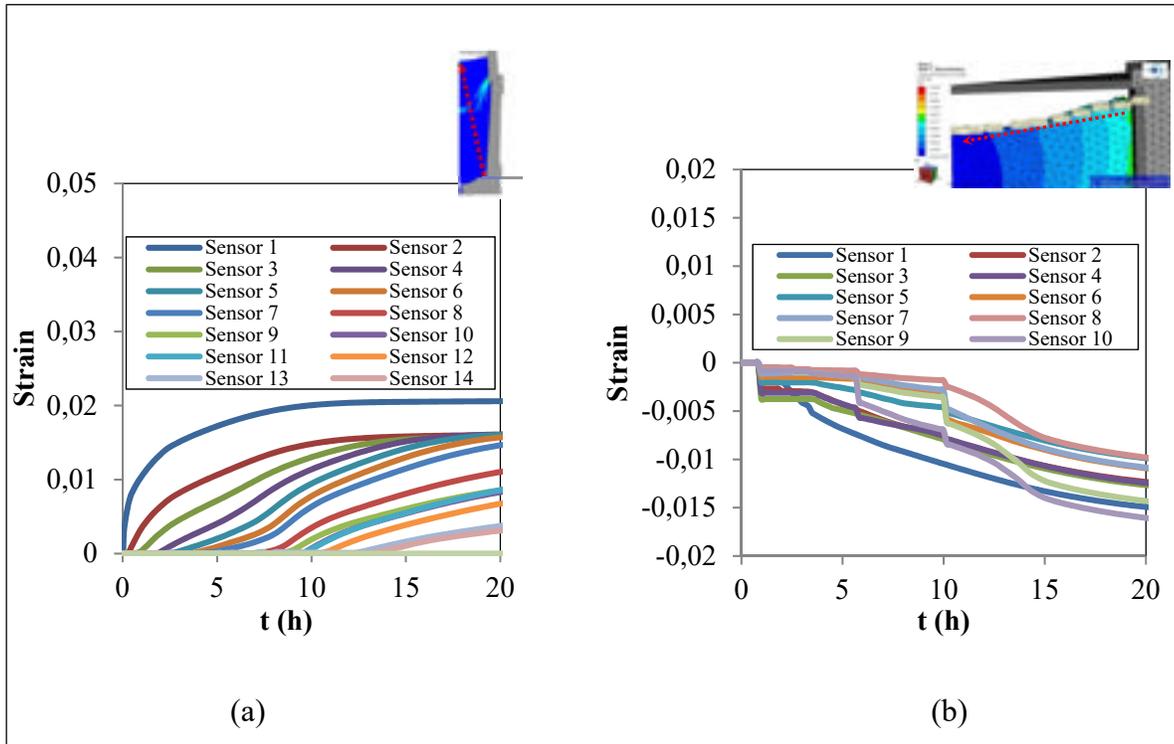
Figure 2.16 Effective strains subjected by the ingot during the casting process. (a) Radial strains on 15 points along the diagonal line (b) Vertical strains on 10 points on the ingot top skin.
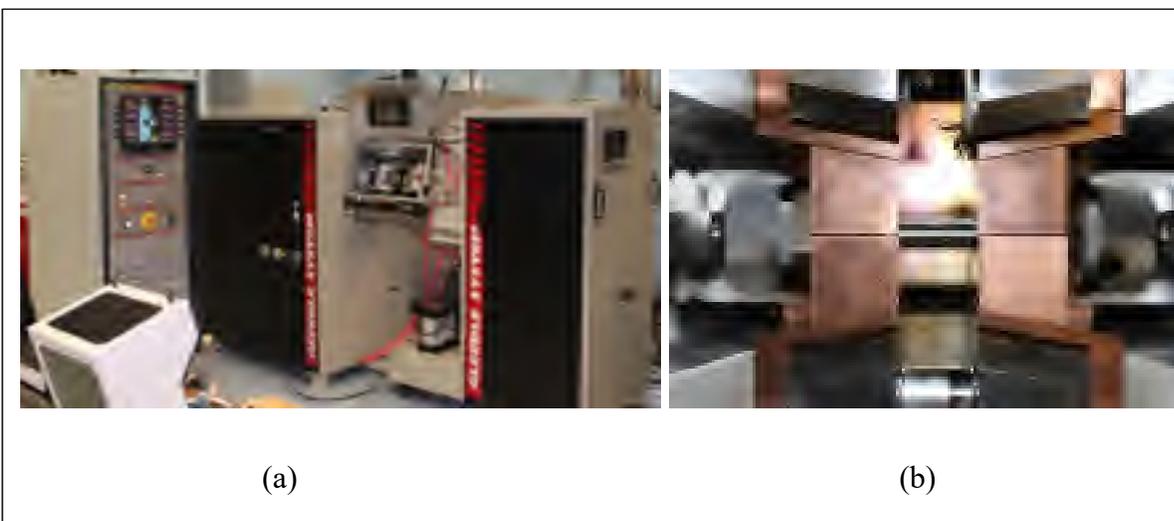
Figure 2.17 Tension test machine and chamber. (a) Gleeble^{TM} 3800 (b) Test chamber with specimen installed.
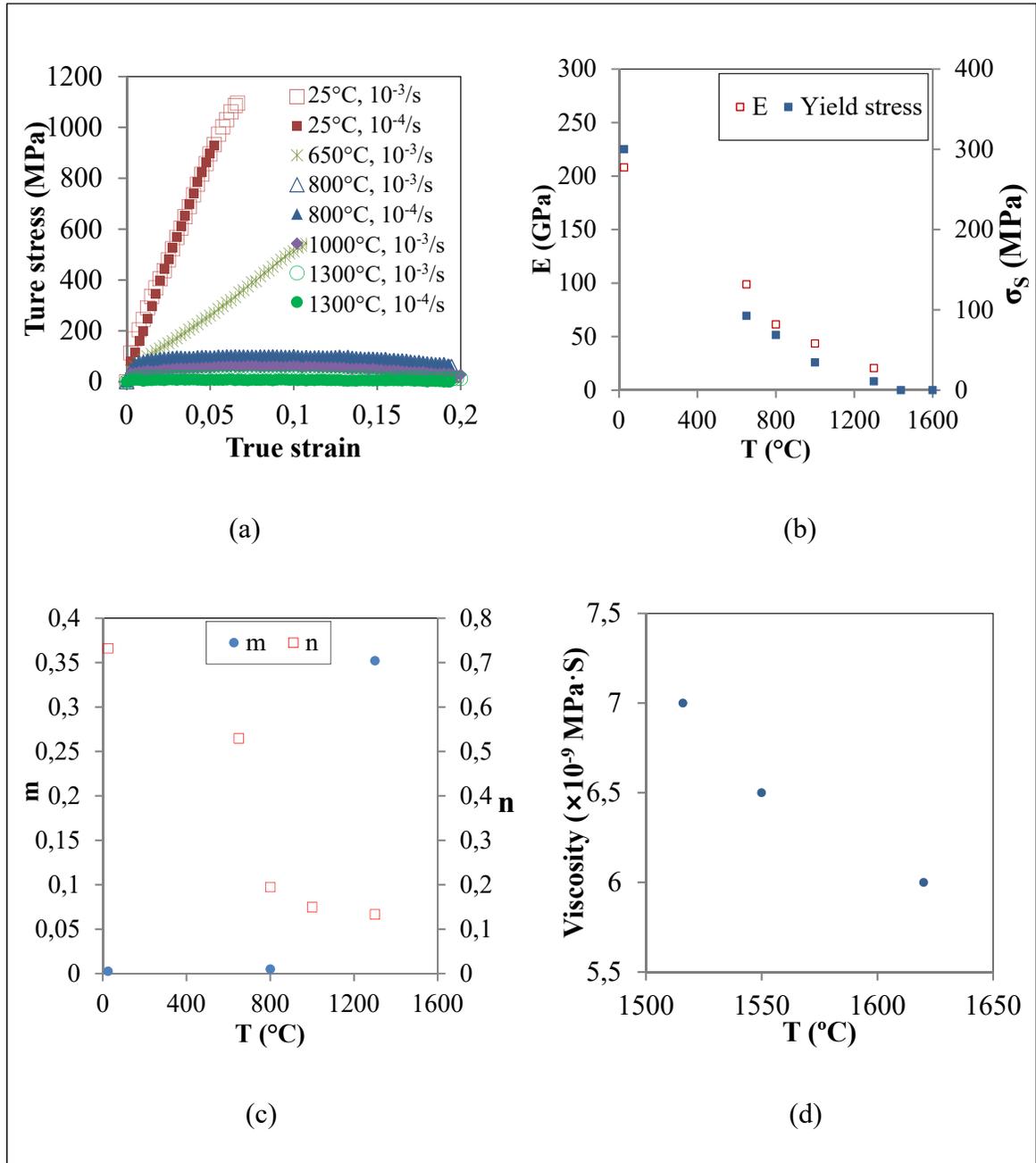
Figure 2.18 Temperature dependence of thermo-mechanical properties of the studied steel. (a) True stress and strain curves (b)Young's modulus (E) and yield stress (σ_s) (c) Stain rate sensitivity (m) and strain hardening coefficient (n) (d) Dynamic viscosity (Barfield et Kitchener, 1955).

Radial effective strains were analyzed on the same 15 points located along the diagonal line. Results in Figure 2.16a showed that the largest radial strain occurred at the bottom corner of

the casting and got to 0.02. The effective strain in the vertical direction was examined using 10 sensors lying on the top surface of the casting, as shown in the right corner of Figure 2.16b. The largest vertical strain was accumulated at the top center of the casting, and the value got to less than 0.02, as seen in Figure 2.16b. Based on above analyses, tensile tests were performed in vacuum in Gleeble^{TM} 3800 Thermomechanical Simulator (Figure 2.17) at temperatures of 25, 650, 800, 1000 and 1300 °C and strain rates of 10^{-3} and 10^{-4}/s.

During the testing process, samples were first heated at the rate of 0.5 °C/s till the respective target temperatures, and then maintained for 15 min so as to get homogeneous temperature over the specimen before being tensioned till the fracture. Sample temperatures were controlled using S-type thermocouples installed in the gauge center of the specimen. During hot tensile test, the temperature difference between the programmed and the actual sample was within ± 1 °C.

The experimentally obtained room and high temperature true stress-strain curves were plotted in Figure 2.18a. Based on these curves, the thermomechanical behaviors, such as yield stress σ_s, Young's modulus E, strain hardening exponent n and strain-rate sensibility coefficient m and their variations as a function of temperature were determined and given in Figure 2.18. Dynamic viscosity and its temperature dependence were also given in the same figure, which are from the literature for 0.36 wt.% C steel (Barfield et Kitchener, 1955).

2.4.3 Steel thermodiffusion properties

The steel thermodiffusion properties employed in the simulations are presented in Table 2-3. The equilibrium partition coefficient k and the slopes of liquidus line m_l were calculated for each element based on linearized binary phase diagrams with respect of iron using Thermo-Calc$^{®}$, as exampled in Figure 2.19. The solutal expansion coefficient β_i and diffusion coefficient in the liquid of each element D were found in (Duan et al., 2016; Schneider et Beckermann, 1995; Dong et al., 2017).
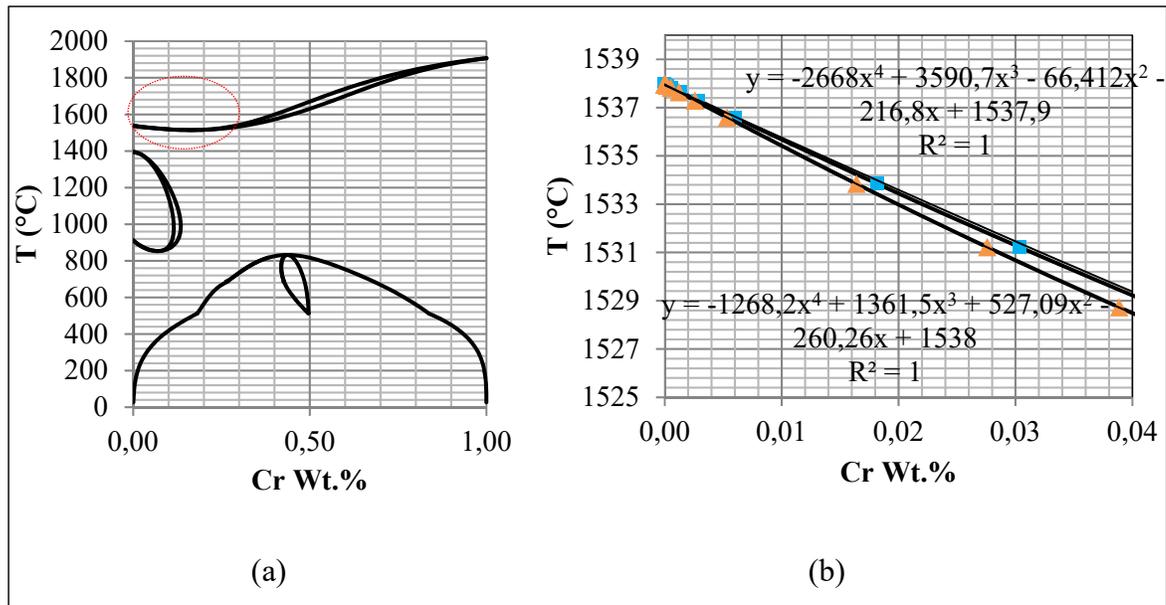
Figure 2.19 Linearized binary phase diagrams with respect to iron using Thermo-Calc®
and the enlarged region for the studied steel.

Table 2-3 Thermodiffusion properties for each solutal element.

Elements	Symbol	Unit	C	Si	Mn	S	Cr	Mo	P	Ni	Reference
Liquidus slope	m_l	K/wt.%	-80.6	-15.7	-5.35	-6.83	-1.66	-2.53	-67.52	-4.82	
Solute partition coefficient	K		0.3664	0.7	0.7545	0.0252	0.94	0.837	0.308	0.8474	
Solutal expansion coefficient	βi	$\times 10^{-2}$/wt.%	1.4164	1.19	0.192	1.23	0.397	-0.192	1.15	-0.069	Duan et al., 2016; Schneider et Beckermann, 1995
Diffusion coefficient	D	mm²/s	0.02	0.0038	0.0028	0.0042	0.0049	0.0025	0.0016	0.0012	Dong et al., 2017

2.4.4   Other parameters

The thermophysical properties of all other materials are listed in Table 2-4. They were
obtained from Thermo-Calc® calculations (Andersson, 2002), Thercast® material database

(TherCast 8.2®, 2012), literature (Duan et al., 2016; Schneider et Beckermann, 1995), experimental measurement, or from the industry.

Table 2-4 Other parameters of the calculation and of the alloys.

	Property	Symbol	Unit	Value	Reference
Steel	Reference density	ρ_0	kg/m³	6.99×10^{-6}	Andersson, 2002
	Melting temperature of pure iron*	T_m	°C	1538	Andersson, 2002
	Reference temperature (liquidus)	T_{ref}	°C	1495.3	Andersson, 2002
	Thermal expansion coefficient	β_T	/K	1.07×10^{-4}	Duan et al., 2016
	Latent heat of fusion	L_f	kJ/kg	266.8	Schneider et Beckermann, 1995
	Emissivity	ε_T		0.8	TherCast 8.2®, 2012
Cast iron	Density	ρ	kg/m³	7000	TherCast 8.2®, 2012
	Thermal conductivity	λ	W/m/K	30	TherCast 8.2®, 2012
Refractory	Density	ρ	kg/m³	2353	TherCast 8.2®, 2012
	Thermal conductivity	λ	W/m/K	1.2	TherCast 8.2®, 2012
Exothermic refractory	Density	ρ	kg/m³	600	-
	Enthalpy of reaction	ΔH	kJ/kg	8373.6	-
	Thermal conductivity	λ	W/m/K	0.2	-
Initial conditions	Steel pouring temperature	T_0	°C	1570	-
	Initial temperature of molds, powders and refractory	T_{mold}	°C	50	-
	Filling time	t_F	min	30	-
	Exterior environmental temperature	T_{ext}	°C	20	-

<p style="text-align:center;">CHAPITRE 3</p>

ARTICLE 1 ON THE IMPACT OF MICROSEGREGATION MODEL ON THE THERMOPHYSICAL AND SOLIDIFICATION BEHAVIORS OF A LARGE SIZE STEEL INGOT

Chunping Zhang[1]✉ , Mohammad Jahazi[1], Paloma Isabel Gallego[2]

[1]Mechanical engineering department, École de technologie supérieure, 1100 Notre-Dame Street West, Montreal, Quebec H3C1K3, Canada
[2]Finkle-Steel Sorel, 100 McGarthy Street, Saint-Joseph-de-Sorel, QC J3R 3M8, Canada

3.1 Abstract

The impact of microsegregation models on thermophysical properties and solidification behaviors of a medium-carbon high strength steel was investigated. The examined microsegregation models include the classical equilibrium lever-rule, the extreme non-equilibrium Scheil-Gulliver, as well as other treatments in the intermediate regime proposed by Brody and Flemings, Clyne and Kurz, Kobayashi and Ohnaka. Based on the comparative analyses performed on three representative regions with varied secondary dendrite arm spacing sizes, the classical equilibrium Lever rule and non-equilibrium Scheil scheme were employed to determine the thermophysical features of the studied steel, using the experimentally verified models from literature. The evaluated thermophysical properties include effective thermal conductivity, specific heat capacity and density. The calculated thermophysical data were used for three-dimensional simulation of the casting and solidification process of a 40 metric ton steel ingot, using FEM code Thercast®. The simulations captured the full filling, the thermo-mechanical phenomena and macro-scale solute transport in the cast ingot. The results demonstrated that Lever rule turned out to be the most reasonable depiction of the physical behavior of steel in study in large-size cast ingot and appropriate for the relevant macrosegregation simulation study. The determination of the model was validated using the experimentally measured top cavity dimension, the

62

thermal profiles on the mold outside surface by means of thermocouples, and the carbon distribution patterns via mass spectrometer analysis.

Keywords: steel, large size ingot, Finite Element simulation, thermo-physical properties, microsegregation model, solidification behavior, macrosegregation

3.2 Introduction

Ingot casting is the only method for the production of large size mono-block medium-carbon high-strength steels to meet the increasing demands from the energy and transportation industries. Solidification of large-size ingots generates non-homogeneous distribution of the alloying elements at the scale of the product, called macrosegregation. From a practical viewpoint, the nature and extent of the macrosegregation (Pickering, 2013), accompanied with the ratio of the columnar to equiaxed structure (Wolczynski, Ivanwa et Kwapisinski, 2018), determines the quality of the final product. The presence of macrosegregation results in inconsistent transformation products (i.e. martensite, bainite) during subsequent hot working and further plastic deformation (Wolczynski, Ivanwa et Kwapisinski, 2019), and causes nonuniformity in mechanical properties of the finished product. To elucidate the controlling mechanisms of the formation and development of macrosegregation, extensive studies have been conducted using finite element modeling (FEM), the most economical approach. However, the predictive reliability of the solute transport model significantly depends on the accuracy of the prescribed thermophysical properties. The latter is closely associated with dendritic microsegregation models (Guan et al., 2018; Fridber, Torndahl et Hillert, 1969). It is the microsegregation of elements on the dendritic scale that leads to the enrichment and paucity of the liquid and macroscale segregation of chemical species, through thermosolutal convection currents in the course of ingot solidification. Therefore, the selection of microsegregation model is of utmost significance for the accuracy of any macrosegregation predictions (Guan et al., 2018).

So far, due to the enormous computation burden, the microsegregation models used in the macroscopic solute transport works have largely been based on the classical equilibrium Lever rule model (infinite diffusion in solid) and non-equilibrium Scheil treatment (null

diffusion in solid) (Smith et Hashemi, 2006; Scheil et Metallk, 1942; Xiong et Kuznetsov, 2001; Schaffnit et al., 2015; Kozeschinik, Rindler et Buchmayr, 2007). In reality, microsegregation in steels often falls into the intermediate area between the two extreme cases, which are characterized by incomplete solute diffusion in the solid. That is due to the mixture of interstitial and substitutional elements present in steel and the range of solidification times given by various casting processes (Pickering, 2013). Moreover, simple microsegregation models often assume a fixed dendrite arm spacing (Won et Thomas, 2001). It is known that there is an important variation of dendrite arm spacing in a large-size cast ingot, resulting from large temperature and concentration difference present in the system (Vandersluis et Ravindran, 2017). It appears that an increase in the dendritic arm spacing increases the permeability of the mushy zone (Kurz et Fischer, 1989), and thus can influence the thermophysical features. Hence, the selection of appropriate microsegregation models in different regions in the casting system of interest may be well dependent on the local temperature, concentration and the resulting dendrite arm spacing. Therefore, there is a need to make a sensitivity analysis to assess the influence of microsegregation models on thermophysical features, and their dependence on local dendritic arm spacings at various locations of the cast ingot.

The objective of the present work is to investigate the effect of microsegregation model selection on thermophysical properties and solidification behavior of a medium-carbon high strength steel. For this, notable analytical or semi-analytical models of solute redistribution problem will first be considered. These include the ideal equilibrium lever-rule (Smith et Hashemi, 2006), the extreme non-equilibrium Scheil-Gulliver treatment (Scheil et Metallk, 1942), as well as other analyses in the intermediate regime between the two extreme cases, such as those of Brody and Flemings (Flemings, 1974), Clyne and Kurz (Clyne et Kurz, 1985), Kobayashi and Ohnaka (Kobayashi, 1988).

These microsegregation models were then applied to determine thermophysical properties in three regions of a 40 MT (metric ton) cast high strength steel ingot. The three specified regions (each occupying 4.5×6.5 cm^2) were selected on the centerline cross section along the radius of the ingot 30cm below the hot-top/ingot body interface. They were located in the

ingot wall side, radial midway and center, with varied typical SDAS (secondary dendrite arm spacing), representing typical dendritic structures which formed in the initial, intermediate and final stages of the solidification process. The calculated thermophysical properties were used for three-dimensional simulations of the solidification process of the 40 MT steel ingot, using Thercast® 8.2 FEM code (TherCast 8.2®, 2012). The simulations were carried out for each of the microsegregation models, and captured the full filling, the thermo-mechanical phenomena and macro-scale solute transport in the casting ingot. The reliability of the model was validated using the experimentally measured top cavity dimension, the thermal profile on the outside of the mold surface using thermocouples, and the carbon distribution profile via mass spectrometer analysis. On the basis of the obtained results, the microsegregation model that best predicts macrosegregation was identified. The present work demonstrates the importance of the solid back diffusion in the solidification behavior of large size ingot. The findings could contribute to a better understand of the underlying mechanisms responsible for the occurrence of macrsegregation in the casting process of large size ingot.

3.3 Microsegregation models

In the dendritic solidification process, solute diffusion in the liquid, which is at the origin of microsegregation, is complete. Hence, interdendritic microsegregation models are formulated by dealing with the diffusion in the solid phase, described by the relationship between the solute concentration at the advancing solid/liquid interface, ω_s, and the solid fraction, f_s. Transient solute transfer by diffusion in the solid depends on the value of the dimensionless back-diffusion Fourier number α (Wan et Thomas, 2001):

$$\alpha = D_s t_f / l^2 \tag{3.1}$$

Here, D_s is the diffusivity of solute element in the solid phase (µm/s), t_f is the diffusion time (local solidification time) (s) and l is the length scale of the microsegregation domain (usually taken as half of secondary dendrite arm spacing d_2) (µm).

For a high value of α, the solid-mass diffusivity of carbon is assumed to be so intense that the composition is always uniform within each phase (i.e. the system is always in

thermodynamic equilibrium). Then the solidification behavior is described by the classical Lever rule (Smith et Hashemi, 2006). For a small α, the diffusion in the solid can be ignored, which is opposite to the Lever rule and described by Scheil-Gulliver or Scheil equation (Scheil et Metallk, 1942). The reality, however, is expected to lie somewhere between the above two extremes, depending on the importance of solid-state diffusion. Therefore, various models have been put forward to quantify the effect of solid-state diffusion for the intermediate states between the Scheil and Lever rule cases. For them, the following assumptions are made (Clyne et Kurz, 1985):

(i) Straight liquidus and solidus lines of the concerned phase diagram (i.e. a constant partition coefficient k connecting the slope of solidus and liquidus together)

(ii) A constant diffusion coefficient

(iii) A plate-like or cylindrical dendrite geometry

(iv) A single phase in the solid (an abrupt occurrence of δ-ferrite/γ-austenite transformation)

(v) A parabolic ($v = \sqrt{t/t_f}$) or linear local solid/liquid interface advance velocity ($v = L/t_f$)

Brody-Flemings presented a decreasing parabolic model, based on one-dimensional solute redistribution, for the solid/liquid interface advance (Flemings, 1974). Clyne-Kurz model modified the Brody-Flemings equations by introducing a parameter, $\Omega(\alpha)$, to be substituted for α, in order to limit the errors introduced by the geometrical simplifications. Kobayashi and Ohnaka proposed an extended mathematical model, incorporating a thermal model of solidification into the analysis, and solved more rigorously the Brody-Flemings model (Kobayashi, 1988). The equations regarding all above microsegregation models are summarized in Table 3-1.

In the above table, ω_0 is the original composition (%wt.), k is the partition coefficient, T is the system temperature (K), T_l is the liquidus temperature (K), T_f is the melting temperature for pure iron (K). For Brody-Flemings and Kobayashi-Ohnaka models,

$$\Omega = \alpha\left\{1 - exp\left(-\frac{1}{\alpha}\right)\right\} - \frac{1}{2}\,exp\left(-\frac{1}{2\alpha}\right) \tag{3.2}$$

$$\eta = (k - 1)(1 + 2\alpha)/(1 + 2\alpha - 2\alpha k) \qquad (3.3)$$

Table 3-1 Microsegregation models and equations.

Microsegregation model	Solute concentration at the solid/liquid interface ω_S	Solid fraction f_S	Reference
Lever rule	$\omega_s = k\omega_0 / \{(1 - f_s) + kf_S\}$	$f_s = \{1/(1 - k)\}\{(T_l - T) / (T_f - T)\}$	Smith et Hashemi, 2006
Scheil-Gulliver Model	$\omega_s = k\omega_0(1 - f_s)^{k-1}$	$f_s = 1 - \{(T_f - T) / (T_f - T_l)\}^{1/(k-1)}$	Scheil et Metallk, 1942
Brody-Flemings model	$\omega_s = k\omega_0\{1 - (1 - 2\alpha k)f_s\}^{(k-1)/(1-2\alpha k)}$	$f_s = \left[\dfrac{1}{(1 - 2\alpha k)}\right]\{1 - [(T_f - T)/(T_f - T_l)]^{(1-2\alpha k)/(k-1)}\}$	Flemings, 1974
Clyne-Kurz model	$\omega_s = k\omega_0\{1 - (1 - 2\Omega k)f_s\}^{(k-1)/(1-2\Omega k)}$	$f_s = \left[\dfrac{1}{(1 - 2\Omega k)}\right]\{1 - [(T_f - T)/(T_f - T_l)]^{(1-2\Omega k)/(k-1)}\}$	Clyne et Kurz, 1985
Kobayashi-Ohnaka Model	$\omega_s = k\omega_0\{1 - [1 - 2\alpha k /(1 + 2\alpha)]f_s\}^\eta$	$f_s = \left[\dfrac{(1 + 2\alpha)}{(1 + 2\alpha - 2\alpha k)}\right]\{1 - [(T_f - T)/(T_f - T_l)]^{1/\eta}\}$	Kobayashi, 1988

3.4   Material and methods

3.4.1   Experimental and modeling processes

A 40 metric tons (MT) cylindrical shape steel ingot was cast at 1570 °C with a filling time of 30 min. During the casting process, the molten steel, with the chemical composition listed in Table 3-2, was bottom poured into a big-end-up cast iron mold 250 cm in height, 150 cm in mean diameter, and hot-topped above 70 cm in height.

Table 3-2 Chemical composition of the investigated steel and regions (wt.%).

	C	Si	Mn	S	Cr	Mo	P	Ni	Fe
Nominal	0.36	0.4	0.85	0.0023	1.82	0.45	0.01	0.16	Balance
Region 1	0.37	0.4	0.86	0.001	1.92	0.44	0.013	0.17	Balance
Region 2	0.38	0.4	0.86	0.001	1.93	0.45	0.014	0.17	Balance
Region 3	0.44	0.42	0.86	0.001	1.89	0.44	0.015	0.17	Balance

After solidification and stripping out, as shown in Figure 1a, the centerline cross section (the grey face in Figure 3.1b) of the hot-top and 30 cm thick section of the ingot's main body were chemically characterized using the Thermo Scientific ARL^{TM} 4460 mass spectrometer. Then three regions were selected along the radius of the ingot in the section 30 cm below the hot-top/ingot body interface. They were located in the ingot wall side, radial midway and center (Regions 1, 2 and 3 in Figure 3.1), representing the solidified regions in the initial, intermediate and final stages of the solidification process. This section was chosen to reduce the effect of defects encountered in the hot-top, which could influence dendrite evolutions (Rutskii, et al., 2017). The axial faces of the three regions were first chemically characterized with the Thermo Scientific ARL^{TM} 4460 mass spectrometer. They were then polished and etched in Oberhoffer's solution (100 cm^3 H2O + 100 cm^3 alcohol + 3 cm^3 HCl + 0.2 g CuCl$_2$ * 2H$_2$O + 3 g FeCl$_3$ * 6H$_2$ + 0.1 g SnCl$_2$ * 2H$_2$O) for metallographic examination using a binocular microscope. Secondary dendrite arm spacing (SDAS, d_2) was measured on the obtained micrographs using ImageJ software (Abramoff, Magalhaes et Ram, 2004). The

determined SDAS was an average value of repeated measurements in at least 5 different areas.
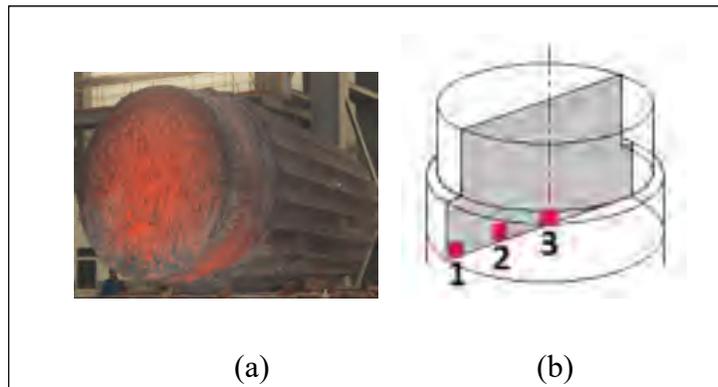
Figure 3.1 (a) The 40 MT cast ingot after stripping
out of the mold (b) Three regions subjected to
chemical and microstructure characterizations.

In the simulation work, a 3D model was constructed using the commercial finite element (FE) code Thercast® (TherCast 8.2®, 2012) based on accurate axisymmetric geometries of the above-mentioned steel ingot and casting tools in the experiment. The boundary conditions were set to reproduce actual casting practice. The FE modelings of the casting and solidification processes of the 40MT steel ingot were stopped when the entire casting completely solidified (i.e. around 700 °C for all the calculated micromodels). For both the experiments and simulations, temperature evolutions on the outside surface of the mold were monitored using thermocouples (TC, for experimental process) and sensors (SN, for modeling) at specific locations 2.5 cm from the mold exterior surface, for comparison and validation purposes, as shown in Figure 3.2. The floating or settling of equiaxed crystals in the melt and the thermomechanical deformation of the mold were not considered in the model to reduce computational cost. Other details related to macrosegregation model establishment and experimental processes could be found in our previous publications (Zhang et al., 2018; Zhang et al., 2018).
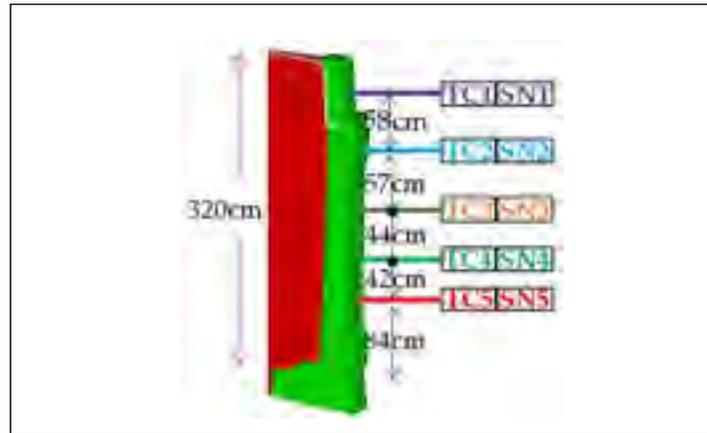
Figure 3.2 The used 3D model and the installation
positions of thermocouples (TC) for experiment
and sensors (SN) for simulation

3.4.2 Determination of Fourier number α

The Fourier numbers α for the three representative regions were determined via Equation (3.1), which relates the diffusivity of carbon in austenite D_s (in cm^2/s) to the local solidification time t_f (in s) and the local measured SDAS d_2 (in μm). The diffusivity of carbon in austenite was taken as a mean diffusivity over the freezing interval from the expression (Meng et Thomas, 2003):

$$D_s = D_0 \times \exp(-\frac{Q}{RT}) \tag{3.4}$$

Here, D_0 is the frequency factor of 0.0761 cm^2/s, Q is the diffusion activation energy of 32160 cal/mol, R is gas constant of 1.987 cal/mol·K, and T is the temperature in Kelvin.

The local solidification time t_f (in s) was determined using Won's empirical expression for low-alloy steels with 0.15 wt.% $< \omega_C <$ 0.6 wt.% (Won et Thomas, 2001):

$$d_2(\mu m) = 143.9 \times C_R^{-0.3616} \times \omega_C^{(0.5501 - 1.996\,\omega_C)}$$

$$= 143.9 \times \left(\frac{T_l - T_s}{t_f}\right)^{-0.3616} \times \omega_C^{(0.5501 - 1.996\,\omega_C)} \tag{3.5}$$

Where C_R is the cooling rate (°C/s) and ω_C is the carbon content (wt.% C). The liquidus T_l (°C) and solidus T_s (°C) of each region were calculated in terms of local chemical composition using the computational thermodynamics program Thermo-Calc® with TCFE7 steel/Fe-alloy database (Andersson et al., 2002).

3.4.3   Determination of thermodynamic properties

The temperature dependence of solid fraction (f_s) was determined using the equations correlated to different microsegregation models, as given in Table 3-1. The effective thermal conductivity (λ), specific heat capacity (C_P) and density (ρ) of the heterogeneous mixture of δ-ferrite, γ-austenite and liquid in the mushy state of the studied regions were calculated with the phase fractions and properties of each phase in the mushy state from the equations in references (Meng et Thomas, 2003; Mietinen et Louhenkilpi, 1994).

The effective thermal conductivity (λ) was calculated as a function of temperature (T), carbon content (ω_C) and phase fraction (f), following Meng's equations (Meng et Thomas, 2003). The model was proposed by applying regression analysis to the experimental thermal conductivity data compilation.

$$\begin{cases} \lambda = f_\alpha \lambda_\alpha + f_\delta \lambda_\delta + f_\gamma \lambda_\gamma + f_l \lambda_l \\ \lambda_\alpha = (80.91 - 9.9269 \times 10^{-2}T + 4.613 \times 10^{-5}T^2)(1 - a_1(\omega_C)^{a_2}) \\ \lambda_\delta = (20.14 - 9.313 \times 10^{-3}T)(1 - a_1(\omega_C)^{a_2}) \\ \lambda_\gamma = 21.6 + 8.35 \times 10^{-3}T \\ \lambda_l = 39 \\ a_1 = 0.425 - 4.385 \times 10^{-4}T \\ a_2 = 0.209 + 1.09 \times 10^{-3}T \end{cases} \tag{3.6}$$

Where f_α, f_δ, f_γ and f_l are the volume fractions of α-ferrite, δ-ferrite, γ-austenite and liquid, respectively.

The density (ρ in kg/m³) was expressed as a heterogeneous phase mixture containing liquid (l), ferrite (α/δ) and austenite (γ) (Mietinen et Louhenkilpi, 1994):

$$\begin{cases}
\rho = \dfrac{1}{\dfrac{f_l}{\rho_l} + \dfrac{f_\alpha}{\rho_\alpha} + \dfrac{f_\delta}{\rho_\delta} + \dfrac{f_\gamma}{\rho_\gamma}} \\[4mm]
\rho_l = 8319.49 - 0.835T + (-83.19 + 0.00835T)\omega_C + (-53.58 + 0.00515T)\omega_{Si} \\
\qquad + (-17.21 + 0.00135T)\omega_{Mn} + (-14.77 + 0.00535T)\omega_{Cr} \\
\qquad + (10.21 + 0.00835T)\omega_{Mo} + (12.72 - 0.00325T)\omega_{Ni} \\
\rho_\alpha = \rho_\delta = 7875.96 - 0.297T - 5.62 \times 10^{-5}T^2 + (-206.35 + 0.00778T + 1.472 \times 10^{-6}T^2)\omega_C \\
\qquad - 36.86\omega_{Si} - 7.24\omega_{Mn} + (-8.58 + 1.229 \times 10^{-3}T + 0.852 \times 10^{-7}T^2 + 0.018367\omega_{Cr})\omega_{Cr} \\
\qquad + 30.78\omega_{Mo} + (-0.22 - 0.47 \times 10^{-3}T - 1.855 \times 10^{-7}T^2 + 0.104608\omega_{Ni})\omega_{Ni} \\
\rho_\gamma = 8099.79 - 0.506T + (-118.26 + 0.00739T)\omega_C - 68.24\omega_{Si} - 6.01\omega_{Mn} \\
\qquad + (-7.59 + 3.422 \times 10^{-3}T - 5.388 \times 10^{-7}T^2 - 0.014271\omega_{Cr})\omega_{Cr} + 12.45\omega_{Mo} \\
\qquad + (1.54 + 2.267 \times 10^{-3}T - 11.26 \times 10^{-7}T^2 + 0.062642\omega_{Ni})\omega_{Ni}
\end{cases} \quad (3.7)$$

Where temperature T is in °C, and solute contents are given in %wt.

In the same way, specific heat was determined using the following equations (Meng et Thomas, 2003):

$$\begin{cases}
C_p = C_{p\alpha}f_\alpha + C_{p\delta}f_\delta + C_{p\gamma}f_\gamma + C_{pl}f_l \\[2mm]
C_{p\alpha} = \begin{cases}
504.8146 - 0.1311139T - 5.1875834 \times 10^6 T^{-2} + 4.486659 \times 10^{-4}T^2 \; (for\ T \leq 800K) \\
-4720.324 + 4.583364T + 1.109483 \times 10^9 T^{-2} \; (for\ 800K < T \leq 1000K) \\
-11501.07 + 12.476362T \; (for\ 1000K < T \leq 1042K) \\
34871.21 - 32.0268T \; (for\ 1042K < T \leq 1060K) \\
-10068.18 + 5.9868T + 5.217657 \times 10^9 T \; (for\ 1060K < T \leq 1184K)
\end{cases} \\[2mm]
C_{p\delta} = 441.3942 + 0.17744236T \\
C_{p\gamma} = 429.8495 + 0.1497802T \\
C_{pl} = 824.6157
\end{cases} \quad (3.8)$$

Where temperature T is in K.

3.5   Results and discussions

3.5.1   SDAS and back-diffusion parameter

The measured chemical compositions of the three investigated regions (as shown in Figure 3.1) are listed in Table 3-2. As compared with the nominal composition, all the three regions show positive segregation. The carbon concentration presents a linear increase in the radial direction from the ingot periphery to the center, attesting that the liquid-solid interface set off

from the mold wall and then advanced inwards to the later solidifying regions. Other elements take on the same trend, but to a weaker extent. Based on chemical compositions, the solidus and liquidus temperatures, corresponding to each position, were determined and given in Table 3-3. It can be seen that stronger segregated regions are accompanied with lower phase transformation temperatures, including the liquidus and solidus. The temperature difference between liquidus and solidus present, in contrast, a progressive augmentation with the increase of segregation intensity and SDAS.

Figure 3.3 presents the optical micrographs observed on the three selected regions. Analyses on these micrographs revealed SDAS values (d_2) of 366 μm in the periphery of the ingot, 474 μm in the ½ radius position and 536 μm in the ingot center. A scheme was added to Figure 3.3b to illustrate the method to determine the SDAS values. Based on the measured SDAS, local solidification time for each case was calculated using Equation (3.5). The results were added to Table 3-3. It can be seen that the evolution of solidification time with the SDAS is in agreement with the reports in the literature that higher SDAS is correlated with longer solidification time (Campbell, 2011).

Table 3-3 Calculated parameters for the investigated regions.

Region	T_S (°C)	T_L (°C)	d_2 (μm)	t_f (s)	α
1	1428.5	1493.1	366	509	10.57
2	1426.5	1492.8	474	1017	12.60
3	1414.2	1486.7	536	1307	12.66

With the measured SDAS (d_2), the determined diffusion coefficient D_s based on Equation (3.4) and the calculated local solidification time (t_f), Fourier number α values were calculated using Equation (3.1) and given in Table 3-3. It was revealed that with the increase of the dendritic arm spacing and the local freezing time from the ingot wall side chill zone to the center, the value of Fourier number α increased along the radius of the 40MT ingot.
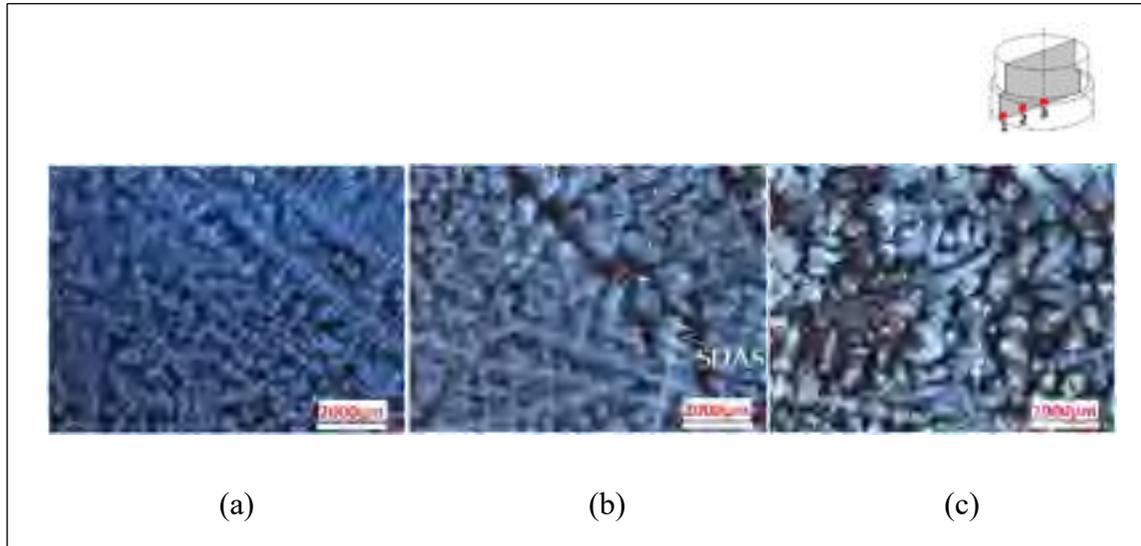
Figure 3.3 Micrographs of the three studied regions on the axial face along the section of 30cm below the hot-top/casting body separation interface. (a) Region 1 in the periphery (d_2 = 366 µm) (b) Region 2 in the ½ radius position (d_2 = 474 µm) (c) Region 3 in the center (d_2 = 536 µm).

3.5.2   Impact of microsegregation model on thermophysical properties

Figure 3.4 gives the dependence of local solid fraction within the mushy zone on local temperature for the three investigated regions in the steel ingot. The entire ranges of Fourier numbers (3 values) were all investigated based on different microsegregation models given in Table 3-1. It can be seen that for the Lever-rule, the decrease of the liquidus and the increase of solidus-liquidus difference (as indicated in Table 3-3), with the increase of SDAS and the resultant α value in the ingot radial direction, were reflected in the movement of the predicted curves to the lower temperature and their larger inclination.
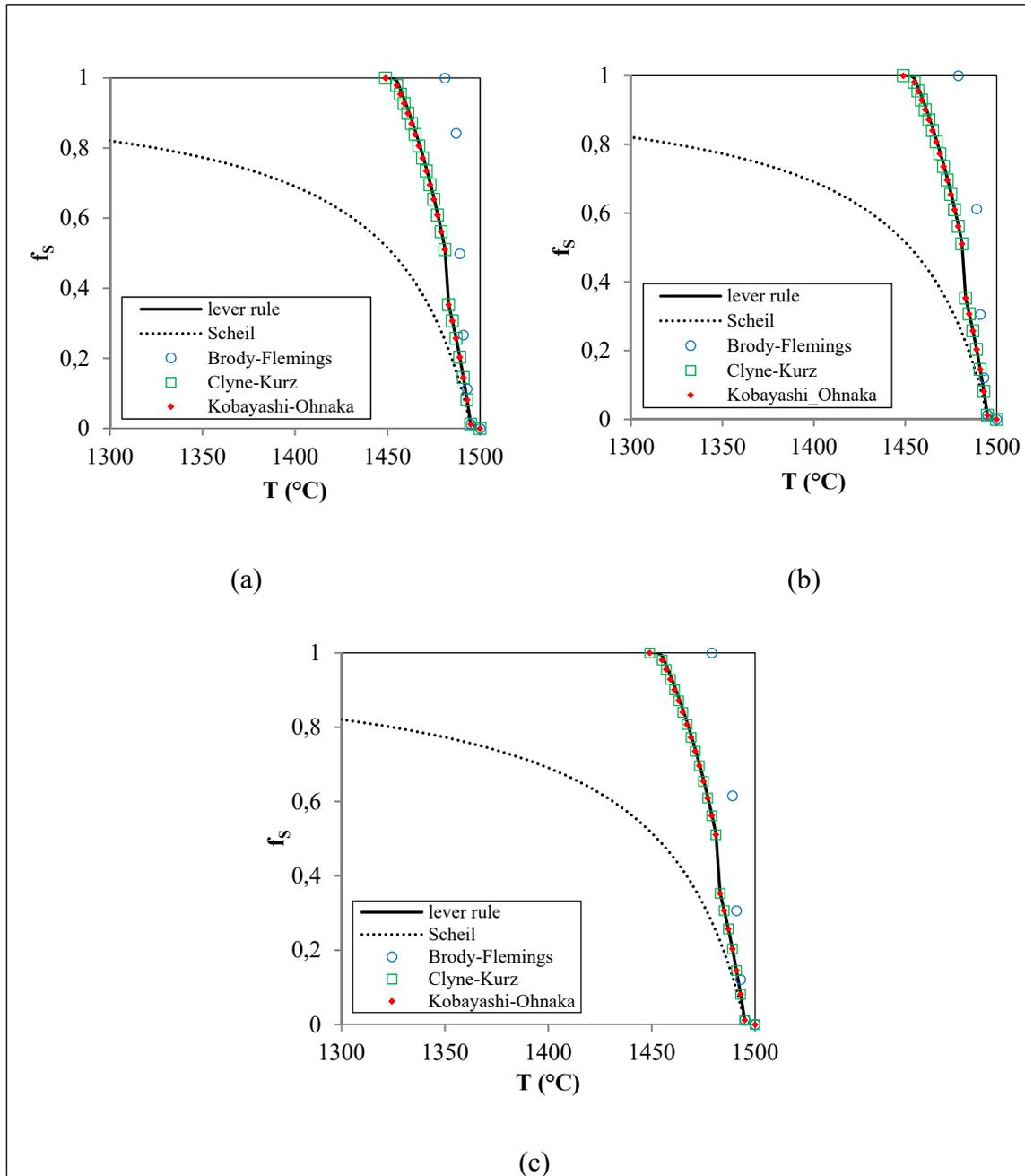
Figure 3.4 Predicted solid fraction/temperature curves for the Regions 1-3 according to the classical limiting cases and the intermediate models over a range of Fourier number values. (a) $\alpha = 10.57$ (ingot wall side) (b) $\alpha = 12.60$ (mid-radius region) (c) $\alpha = 12.66$ (ingot center).
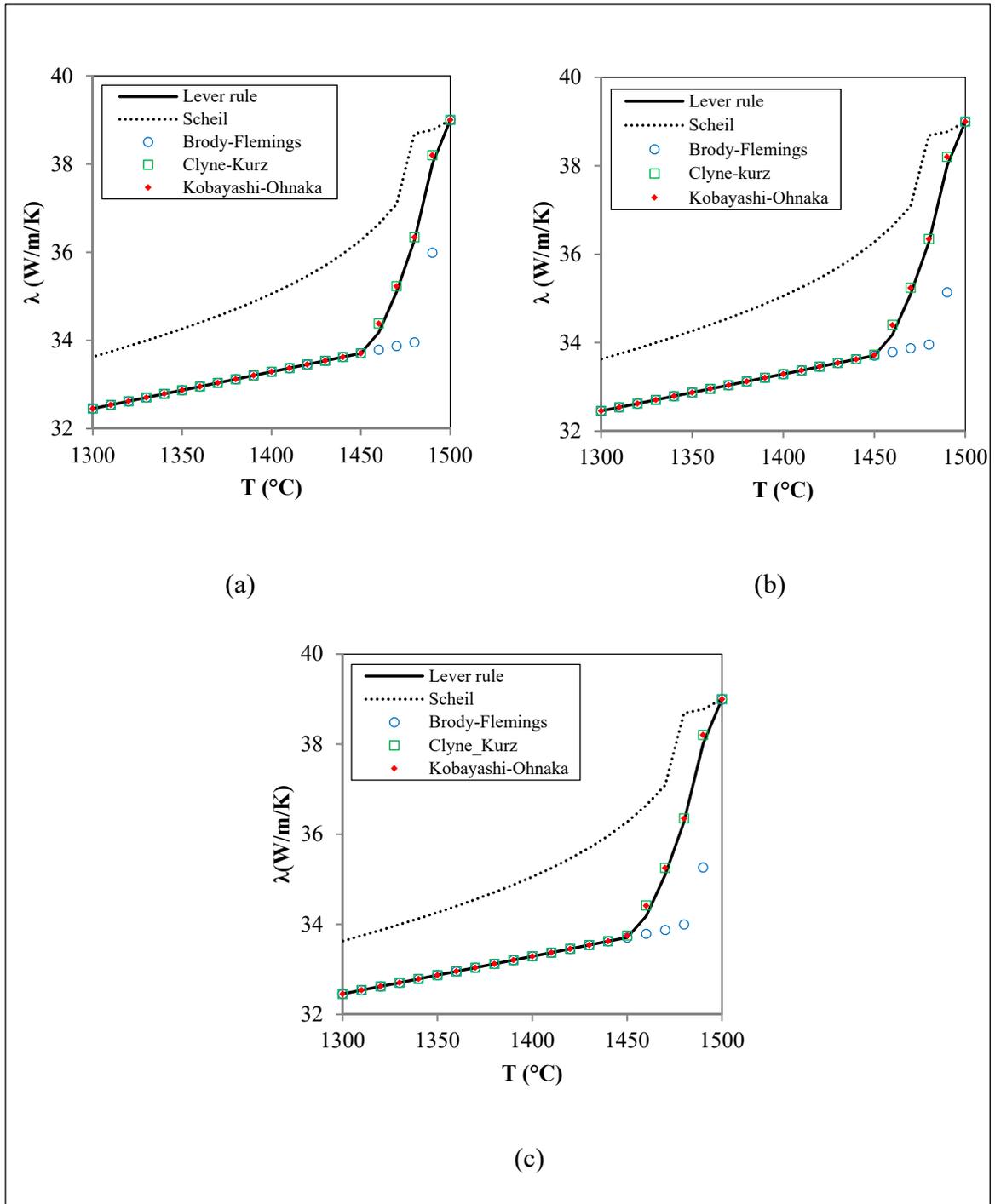
Figure 3.5 Temperature dependence of thermal conductivity for the steel in study according to different microsegregation solidification models for the three cases. (a) α = 10.57(ingot wall side) (b) α = 12.60 (mid-radius region) (c) α = 12.66 (ingot center).

Figure 3.6 Temperature dependence of specific heat for the steel in study according to different microsegregation solidification models for the three cases. (a) $\alpha = 10.57$ (ingot wall side) (b) $\alpha = 12.60$ (mid-radius region) (c) $\alpha = 12.66$ (ingot center).
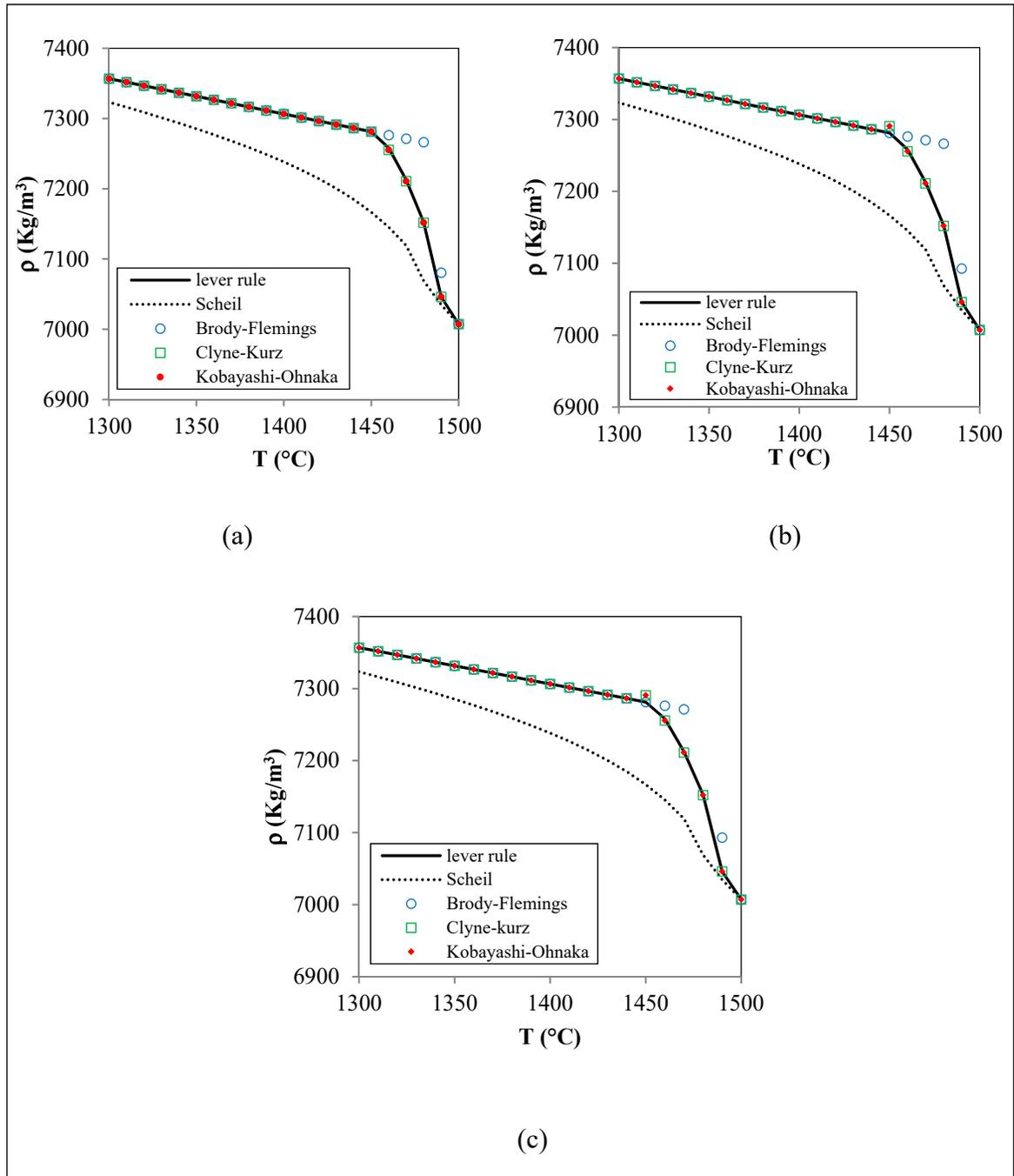
Figure 3.7 Temperature dependence of density for the steel in study according to different microsegregation solidification models for the three cases. (a) α = 10.57(ingot wall side) (b) α = 12.60 (mid-radius region) (c) α = 12.66 (ingot center).

In addition, for all the three examined regions, the freezing zones predicted using Scheil model were much larger than the predictions from other microsegregation models. This is probably due to the assumption in Scheil's formulation that with a perfectly mixed liquid and no diffusion in the solid phase, solidification does not occur until reaching the eutectic temperature. The predictions given using Brody-Flemings model appear physically impossible, since the temperature at which solidification is complete lies above the equilibrium solidus. Similar errors predicted by Brody-Flemings equations have also been reported by others (Clyne et Kurz, 1985; Kobayashi, 1988). It is worth emphasizing here that Flemings approach has been successfully applied to cases where no solid material enters or leaves the volume element during solidification; the elementary domain for establishing the balances was defined on the undeformed solid skeleton of the mushy zone (Pickering, 2013). Thus, it appears probable that the approximate equations derived by Brody-Flemings do not have the physical justification. And it is necessary to use a more realistic model for solute microsegregation/redistribution.

The data presented in Figure 3.4 also reveal that for all the three Fourier number cases, the phase transformations predicted using Clyne-Kurz and Kobayashi-Ohnaka equations are similar to each other. They also nearly coincide with the Lever rule curves, whether before or after the δ/γ transformation during the cooling process. This finding indicates that the Lever rule may be regarded as a better approximation for the diffusion behavior in the solid in the large-size cast ingot.

Different segregation levels and SDAS sizes resulted in the change of the kinetics of phase transformations, and generated variations in the thermophysical properties of the formed phases. Figure 3.5 presents the temperature dependence of the effective thermal conductivity on the dendritic solidification model. The variations of specific heat and density as a function of temperature are given in Figures 3.6 and 3.7. For the three examined regions, Lever rule predicts significant increase of the thermal conductivity of the mushy zone as a function of temperature. The evolution of the specific heat follows the same trend while that of the density goes in the opposite direction.

It must be noted that all the changes in the dynamic thermophysical properties arose after the phase transformation during the cooling process. Hence, similar changes in the thermophysical properties are also expected to be observed in the evolution of solid phase. For instance, for all the three regions, the predictions from Brody-Flemings equations appeared questionable, and the variations in Clyne-Kurz and Kobayashi-Ohnaka curves were indistinguishable from those given by the Lever rule.

Based on the above analyses, Lever rule can be regarded as a suitable approximation for the diffusion behavior in the solid in an industrial scale ingot, whether in the initial solidification stage or in the intermediate and late solidification phases. Therefore, the dynamic physical properties of the studied steel were calculated using Lever rule. The determined data were used to simulate the solidification behavior of the industrial scale 40 MT steel ingot. FE simulation using Scheil equations were also performed for comparison purposes.

3.5.3   Impact of microsegregation model on solidification behavior

The thermophysical properties of the studied steel, determined using Lever rule and Scheil scheme, were adopted for the computation of the thermomechanical behavior and solutal distribution during the solidification process of the 40 MT steel cast ingot. Figure 3.8 displays the temperature patterns (left figures) combined with liquid fraction fields (right figures), predicted using Lever rule and Scheil models, at times of 0.5 h (end of filling stage), 5.5 h, 10.5 h and 15.5 h. The results show that the solid diffusion plays a great role in the solidification behavior of the large-size steel ingot.

For the temperature fields, at the end of the filling operation (Figures 3.8a and e), a long inclined 1550 ºC isothermal curve was obtained by the application of the Lever rule, which was different from the relatively flattened and short one in the calculation with Scheil equation. The high temperature area in the bulk liquid (the red region above the 1550 ºC isotherm) in the Lever rule case was smaller than that from Scheil. This finding indicates the occurrence of a delayed heat dissipation in the superheated molten steel under Scheil conditions. With the solidification proceeding, at any given solidification moment, the

movement of any isotherm in Scheil predictions always lagged behind the corresponding one predicted using Lever rule. This feature is indicative of a solidification delay in Scheil due to the absence of solid diffusion.

Predicted temperature variations on the mold's outside surface as a function of time, monitored using sensors (SN), were compared with experimental readings of thermocouples (TC) placed at five specified positions (as illustrated on the top right corner in Figure 3.9). A better agreement can be seen, in Figure 3.9, between the values predicted using Lever rule model and the measured profiles.

In the liquid fraction patterns (right figures) in Figure 3.7, it can be seen that for both treatments, during the solidification process, three phases coexisted in the mold cavity: a full solid region (blue region), a solid + liquid mushy zone (multicolor region) and a full liquid zone (red region). In metals, the mushy zone is bounded by liquid and solid (or eutectic isotherms) and usually has a dendritic crystalline structure. In the liquid fraction fields in Figure 3.7, it was noted that Scheil predictions were accompanied by larger mushy zones due to the occurrence of solidification at eutectic temperature. These larger mushy regions resulted from the larger temperature difference between the liquidus and solidus, leading to smaller solid/liquid partition coefficients. This would allow more solutes to be rejected from the solidifying dendrites in the mushy region and to form higher microsegregation levels (Schneider et Beckermann, 1995). As a result, thermo-solutal convection currents present in the mushy region would carry the larger quantity of solutes away from the site of rejection, resulting in higher intensity of macrosegregation.
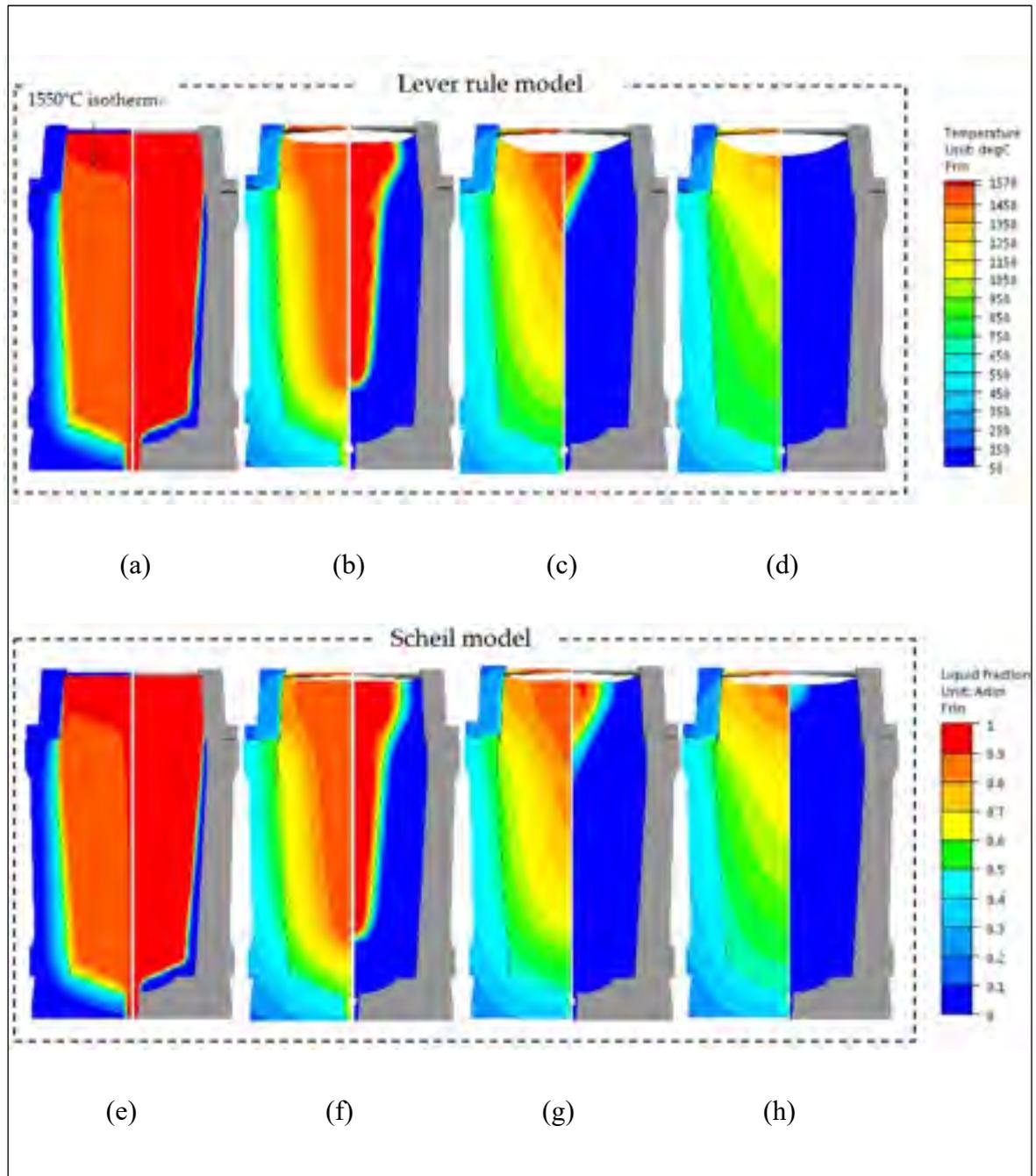
Figure 3.8 Temperature field (left figures) combined with liquid fraction patterns (right figures) predicted using Lever rule and Scheil models in the solidification process. (a, e) 0.5h (end of filling) (b, f) 5.5h (c, g) 10.5h (d, h) 15.5h.
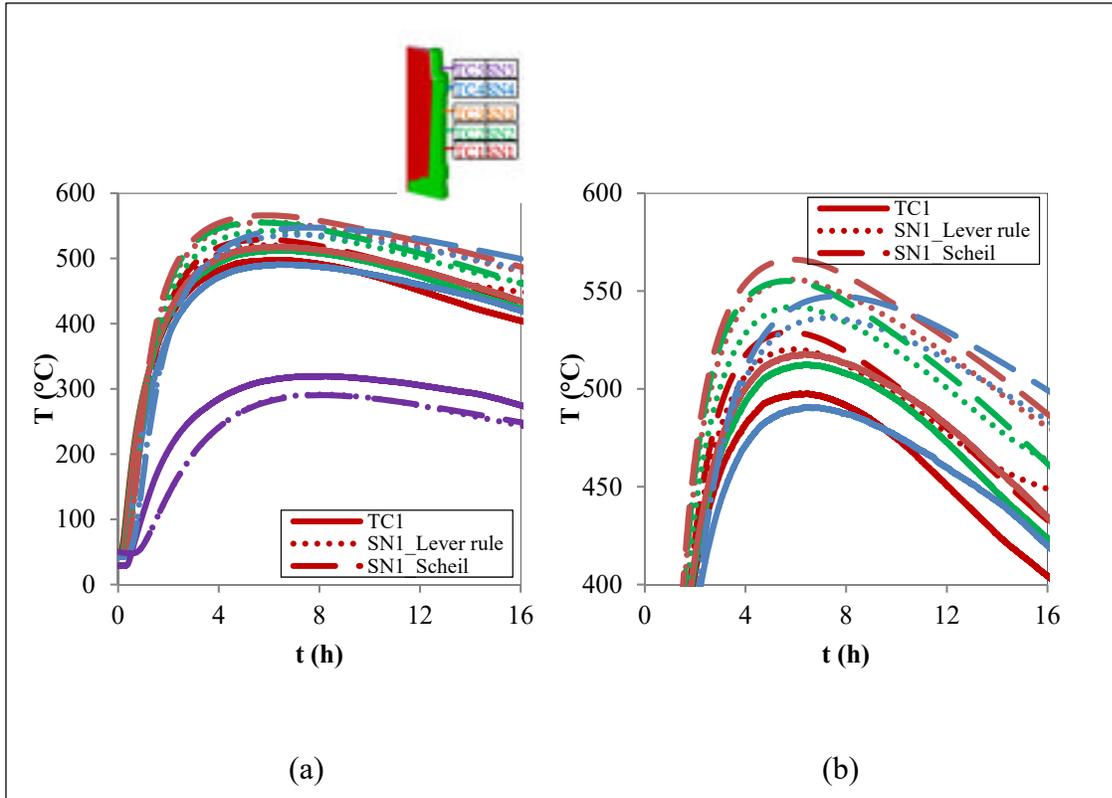
Figure 3.9 Temperature profiles on 5 specified positions on the outside surface of the mold. (a) Temperature profiles for all 5 monitored positions (b) Temperature profiles in the higher temperature regions for the first four monitored positions.

In the liquid fraction patterns (right figures) in Figure 3.8, it can be seen that for both treatments, during the solidification process, three phases coexisted in the mold cavity: a full solid region (blue region), a solid + liquid mushy zone (multicolor region) and a full liquid zone (red region). In metals, the mushy zone is bounded by liquid and solid (or eutectic isotherms) and usually has a dendritic crystalline structure. In the liquid fraction fields in Figure 3.8, it was noted that Scheil predictions were accompanied by larger mushy zones due to the occurrence of solidification at eutectic temperature. These larger mushy regions resulted from the larger temperature difference between the liquidus and solidus, leading to smaller solid/liquid partition coefficients. This would allow more solutes to be rejected from the solidifying dendrites in the mushy region and to form higher microsegregation levels

(Schneider et Beckermann, 1995). As a result, thermo-solutal convection currents present in the mushy region would carry the larger quantity of solutes away from the site of rejection, resulting in higher intensity of macrosegregation.

Further comparative analyses of liquid fraction fields in Figure 3.8 revealed similar solidification delay tendency in the calculations with null diffusion in the solid (Scheil model), as observed above in temperature patterns. For instance, for the Scheil case, after the pouring operation, the solid front was always closer to the hot-top wall side in the hot-top part (Figures 3.8f, g and h); at 15.5 h, a mushy zone were still remained, which was in contrast to the complete solidification for Lever rule.
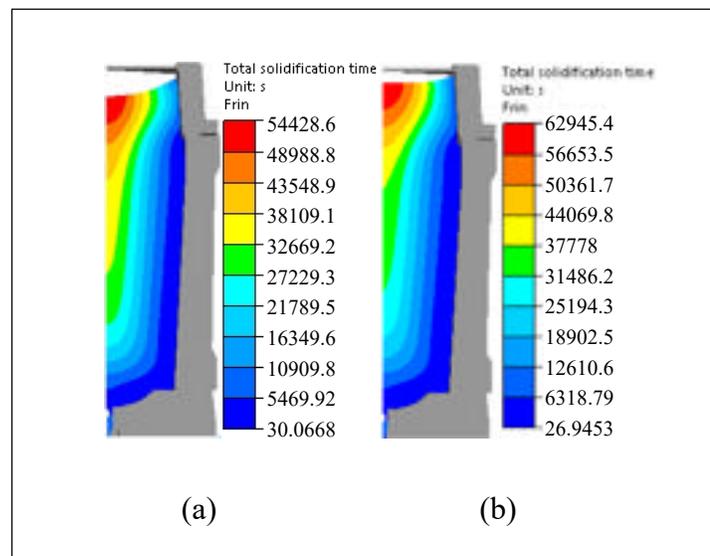
Figure 3.10 Total solidification time (s) for simulations based on microsegregation models. (a) Lever rule (b) Scheil.

The solidification delay in Scheil predictions was also reflected in the difference in the solidification times predicted using the two models. With Lever rule, 54428 s (15 h 07 min) was needed for complete solute redistribution, while based on Scheil model, the solidification of the ingot did not end until 62945 s (17 h 29 min in Figure 3.10). The approximate 15h for the 40MT ingot to complete solidification was in good accordance with the casting time in the actual manufacturing practice. It should be noted that the delay in solidification would

allow more time for solute-rich interdendritic liquid to redistribute in the steel. This tendency would permit the formation of more carbide and aggravate macroscopic solute segregation.

Furthermore, the extents in the top shrinkage predicted by the two approaches were also different. The top shrinkage predicted using Lever rule reached 26 cm (≈ 8% vertical contraction measured from the original fill height) at the end of solidification, while for the Scheil case, the top contraction arrived at 10 cm (3.2% vertical contraction) when solidification was finished. Thus, the smaller top shrinkage (as seen in Figure 3.8) and the resulting larger ingot final volume should be the root cause for the substantial increase in the solidification time for the simulation using Scheil rule. It should be noted that the Lever rule's predicted top shrinkage depth at the centerline of about 26cm agreed closely with the cavity dimensions measured on the experimental obtained ingot.
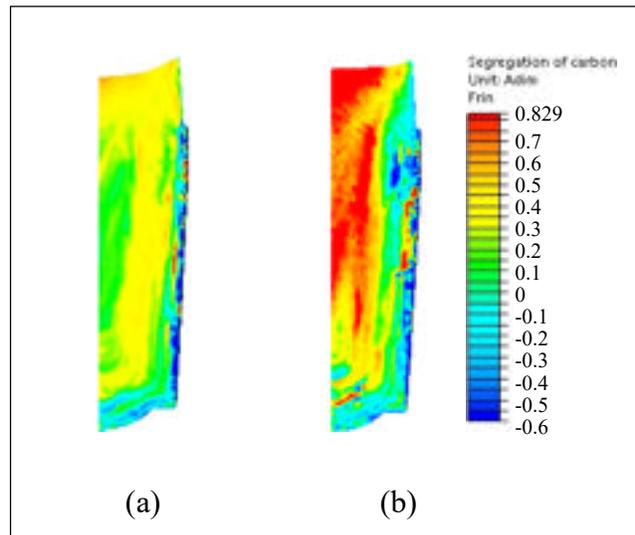
Figure 3.11 Predicted segregation pattern of carbon. (a) Lever rule (b) Scheil.

Macrosegregation patterns of carbon predicted in the simulations using the two microsegregation treatments are provided in Figure 3.11. For both cases, the carbon concentrations in the hot-top, in the head of the ingot and in the mid-radius region of the ingot body were higher than the nominal one (0.36 wt.%), indicating the occurrence of positive segregation in these regions. However, under the combined action of larger mushy

zone and longer solidification time, higher macrosegregation extent and intensity could be predicted in these regions in the calculations using Scheil model.
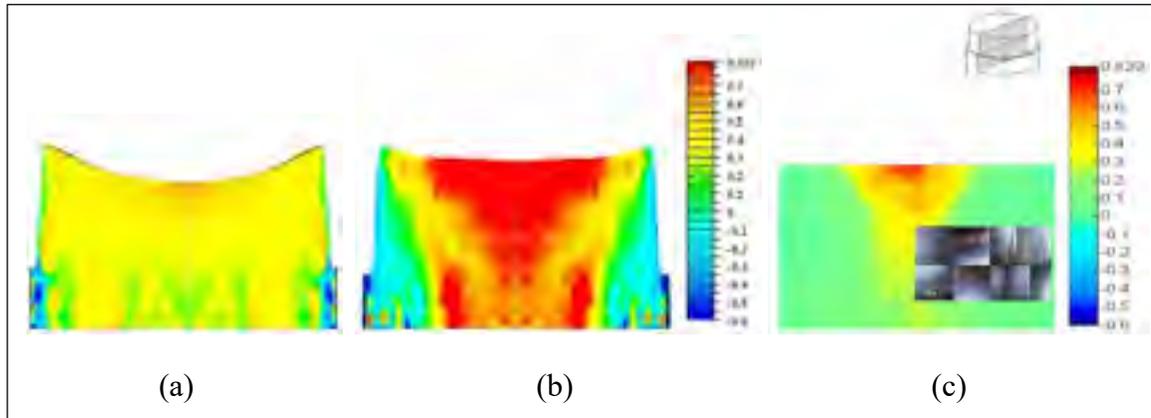
Figure 3.12 Segregation pattern of carbon on the axial surface of the hot-top and upper section of ingot. (a) Lever rule (b) Scheil (c) Mass spectrometer measurements with macrostructure around the hot-top/ingot junction.

The chemical predictions were compared with experimental measurements on the centerline section of hot-top and the upper part of the ingot, as displayed in Figure 3.12. The chemical profile was obtained based on the compilation of measurements over 250 pieces of 4.5×6.5 cm^2 samples, using Thermo Scientific ARL^{TM} 4460 mass spectrometer. The experimentally obtained segregation ratio pattern is symmetric about the ingot central axis, with a positive gradient in solute concentration over the ingot's radius from the periphery to the center and along the ingot axis from the lower to the upper region. Such features are similar to the recently obtained macrosegregation pattern for a 15-ton steel forging ingot (Wolcznski, 2018). It can be seen that the general carbon pattern in the experiment was well reproduced and a fair agreement was obtained between experimental measurements and Lever rule numerical results. The predicted solute-enriched zone between the center and ingot wall in Figure 3.11a matched well the area enclosed by the two black solute-enriched bands in Figure 3.11c. In contrast, some apparent discrepancies were present between experimental results and Scheil predictions. As it can be seen, the extent of segregation is numerically overestimated in Scheil case (Figure 3.11b) due to the neglect on solid back diffusion. This

finding indicates that the degree of the error in the Scheil analysis could be reduced by including back diffusion in the solid in the calculations.

To further examine the segregation ratio in the solute-rich band, new experimental measurements with a sampling density of 0.9×0.9 cm^2 were carried out on the axial section at 30cm below the hot-top/ingot body interface. It can be seen in Figure 3.13 that the segregation intensity inside the solute-rich bands got to 0.34, in agreement with the value predicted using Lever rule in the corresponding regions. This finding further demonstrates the applicability of Lever rule to approach the realistic microsegregation behavior in the course of casting and solidification of large size ingots.

Based on the above analyses, it can be seen that the extent of segregation is numerically overestimated in Scheil case (Figure 3.12b) because solid back diffusion is not considered. This finding indicates that the degree of the error in the Scheil analysis could be reduced by including back diffusion in the solid in the calculations.

(a)   (b)
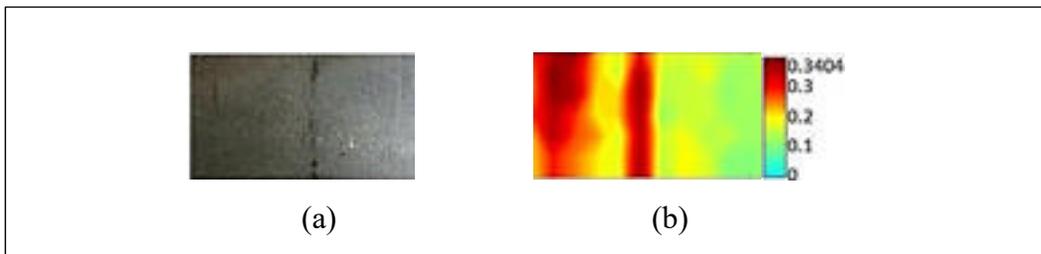
Figure 3.13 Macrograph around positive segregated bands on the longitudinal section at 30 cm below the hot-top/ingot body interface and the corresponding segregation ratio patterns of carbon. (a) Macrograph with black solute-enriched bands (b) Mass spectroscopy measurements of the carbon segregation ratio pattern with sampling density of 0.9×0.9 cm^2.

It should be mentioned that a better approximation may be obtained if using other models considering both solidification and transformation with predicted behaviors situated between the Lever Rule and Scheil's theory, such as the solute microsegregation/redistribution model recently proposed by Wolczynski (Wolczynski, 2015). Wolczynshi's model has been justified/substantiated since solidification path is located on liquidus line, microsegregation path on solidus line and redistribution path between both lines of a given phase diagram.

Moreover, the newly proposed model was applied to the study of steel solidification (Himemiya et Wolcsynski, 2002). Considering the model complexity, the high computation cost for a 40-ton ingot, and the unavailability of all nucleation and transformation parameters, the above-mentioned model was not considered in the present study and will be applied to the future work.

3.6   Conclusions

In the present work, the impact of microsegregation models on thermophysical properties and solidification behavior of a medium-carbon high strength steel was studied. The examined microsegregation models include the ideal equilibrium Lever rule, the extreme non-equilibrium Scheil-Gulliver and the schemes proposed by Brody-Flemings, Clyne-Kurz, Kobayashi-Ohnaka, which are characterized by incomplete solution diffusion in the solid. Based on the comparative analyses on representative regions, and the 3D simulations of the casting and solidification process of a large-size steel ingot, the following conclusions can be drawn:

1) For a large-size steel ingot, Lever rule can be regarded as a better approximation for the diffusion behavior in the solid, whether in the initial solidification stage or in the intermediate and late solidification phases.

2) The validity of Lever rule for reasonable depiction of the physical behaviors which take place in the casting course of large size steel ingot was demonstrated with a good agreement of the simulation predictions with experimental measurements.

The application of recently introduced models that provide a more accurate description of solute microsegregation and redistribution would be an interesting addition for future studies on the solidification of large size ingots.

3.7   Author contributions

Conceptualization, M. J. and C. Z.; methodology, C. Z.; software, C. Z.; validation, C. Z.; formal analysis, C. Z.; investigation, C. Z. and P. I. G.; resources, M. J. and P. I. G.; data curation, C. Z.; writing—original draft preparation, C. Z.; writing—review and editing, M. J.;

visualization, C. Z.; supervision, M. J.; project administration, M. J.; funding acquisition, M. J.

3.10 Conflicts of interest

The authors declare no conflict of interest. The funders had no role in the design of the study; in the collection, analyses, or interpretation of data; in the writing of the manuscript, or in the decision to publish the results.

ARTICLE 2 INFLUENCE OF THERMOMECHANICAL SHRINKAGE ON MACROSEGREGATION DURING SOLIDIFICATION OF A LARGE-SIZED HIGH-STRENGTH STEEL INGOT

C. Zhang[1, ✉], D. Shahriari[1], A. Loucif[1], H. Melkonyan[2], M. Jahazi[1]

[1]Mechanical engineering department, École de Technologie Supérieure, 1100 Notre-Dame Street West, Montreal, Quebec H3C1K3, Canada
[2]Finkl-Steel-Sorel, 100 McCarthy Street, Saint-Joseph-de-Sorel, Quebec J3R 3M8, Canada

4.1 Abstract

Finite element modeling (FEM) validated by experimental work was used to simulate the influence of thermomechanical shrinkage on macrosegregation of alloying elements in a large size ingot of high strength steel. The full algorithms of the filling and solidification process for thermohydraulic and thermomechanic analyses were developed and implemented in the 3D FEM code Thercast®. Material properties were determined by a combination of experimental works, thermodynamic software Thermo-Calc®, a database and literature source. It was predicted that thermomechanical shrinkage decreased the temperature gradients, advanced the initiation of solidification and reduced the solidification time. The above changes resulted in less severe segregation along the centerline, in the zone next to the ingot surface, in the upper section of the ingot and in the hot-top. Thermomechanic model predictions were proved to agree better with experimental results than the thermohydraulic one. The obtained results were interpreted in the framework of the theories on diffusion and solidification of alloyed systems. These findings contribute to a better understanding of the impact of thermomechanical shrinkage in ingot cooling process. They could also be used in industry to improve the quality of large size ingot production and the productivity of high value-added steels or other alloys.

Keywords: large size ingot, steel, Finite Element modeling, solidification, thermomechanical shrinkage, macrosegregation

4.2 Introduction

Ingot casting is the only method for the production of heavy mono-block forgings of multi-component special steels to meet the increased demands from the power-generation industry. Macrosegregation, as a compositional heterogeneity at the scale of the product, is one of the most significant defects occurring during the solidification process. Often post casting operations such as homogenization are sufficient to remove the extent and severity of macrosegregation in small size ingots; however, in the case of large size ingots (more than 1.5 m diameter), it proves difficult to be removed by subsequent thermo-mechanical treatments, and could pose quality problems (ASM Handbook, 2002; Loucif et al., 2018).

Due to the significant cost and difficulties for large scale experimental trials, extensive efforts have been devoted to the development of numerical models for the prediction of macrosegregation in heavy ingots (Fleming et Nereo, 1967). Im et al. (Im, kim et Lee, 2001) simulated the casting process from the filling stage to solidification using a two-dimensional model, and pointed out the necessity to carry out a coupled filling and solidification analysis because the mixed residual and natural convection flow resulting from the filling stage exert an important effect on solidification. Sang et al. (Sang et al., 2010) numerically studied the possibility of simulating solidification conditions in a large ingot using a relatively small ingot as reference. Li et al. (Li et al., 2012) used a three-phase mixed columnar-equiaxed solidification model to study the formation of columnar and equiaxed zones and segregation patterns in a 2.45-ton steel ingot. Combeau et al. (Combeau et al, 2009; Combeau et al., 2012) developed a 2D multiphase model tackling the natural convection flow together with the motion and growth of equiaxed grains to study the development of macrosegregation in a 3.3-ton and a 65-ton steel ingot, and successfully predicted bottom negative segregation zone. Wu and Ludwig (Wu et Ludwig, 2009) modified an equiaxed solidification model to study the globular and dendritic grain growth, and molded non-uniform solute distribution in the interdendritic melt region as well as the species exchange between the extra- and interdendritic melts by the mechanisms of species diffusion and grain growth. However, in

the above analyses, the solid is assumed as a rigid, fixed and stationary phase (i.e. thermomechanical shrinkage is ignored). Such assumptions result in inaccuracies because changes in the composition and mechanical properties of the solidified phase are not taken into consideration (Beckermann, 2002).

Solidification shrinkage and the deformation of the solid skeleton have been numerically studied on several metallic systems, such as Al-Cu (Chiang et Tsai, 1992; Gao et al., 2017), Pb-Sn (Heinrich et Poirier, 2004), and steel (Ehlen et al., 2003; Lan et Zhang, 2014). Gao et al. (Gao et al., 2017) established a theoretical model based on the analysis of the redistribution behaviors of gas and alloying elements for predicting porosity formation and segregation in as-solidified Al-4.5 wt.% Cu alloys. The results showed that porosity formation in the mushy zone slightly relieved the solute enrichment in the interdendritic liquid, and consequently reduced the solute segregation. Lan and Zhang (Lan et Zhang, 2014) developed a 3D FEM model coupled with natural convection, solute and interfacial heat transfer behavior to predict shrinkage porosity and macrosegregation in a 3.3 ton steel ingot. They found that macrosegregation and shrinkage porosity occurred together in the hot top of the ingot. Other researchers studied the effect of solid deformation on velocity flow (Chiang et Tsai, 1992; Heinrich et Poirier, 2004), temperature field (Ehlen et al., 2003), and macrosegregation in specified zones (Heinrich et Poirier, 2004; Ehlen et al., 2003). However, their influence on the final and global segregation patterns is still unclear. In addition, in most of the above works, important variables, such as solidification contraction ratio (Ehlen et al., 2003), casting speed (Chiang et Tsai, 1992; Gao et al., 2017), feeding length (Lan et Zhang, 2014), or the flow velocity (Heinrich et Poirier, 2004), were considered constant due to the unavailability of material temperature-dependent thermomechanical parameters (Ehlen et al., 2003), or appropriate modeling tools (Reikher et al, 2010). Finally, few simulation results have been compared with experimental observations performed under controlled conditions (Heinrich et Poirier, 2004).

In the present work, the influence of solidification shrinkage and solid deformation was studied using 3D finite element simulations of mold-filling and solidification in a 40 MT (metric ton) ingot of a high-strength steel. Specifically, a thermohydraulic model (TH) was

first developed to study heat and solute transport coupled with flow driven by thermosolutal convection (buoyancy-driven flow). Then a thermomechanic model (TM) was developed where thermosolutal transport induced by the combined effects of buoyancy- and shrinkage-induced flow was considered. The numerical studies were realized in the finite element code Thercast® using a two-phase (liquid-solid) multiscale solidification model. Material parameters were determined by physical simulations, directly done in laboratory, using thermodynamic software Thermo-Calc®, from literature, or from Thercast® material database. The thermal boundary conditions for each case were set to be close to the actual industrial operational conditions used for casting of large size ingots. The evolution of solid shrinkage, air gap formation, temperature, solid fraction and melt velocity fields throughout the filling and cooling stages were investigated. The prediction capabilities of the two models were validated with chemical, thermal and dimensional experimental measurements.

For a comprehensive analysis of the solidification process, detailed information on grain nucleation, growth, morphology transition, and their interactions with macrosegregation evolution is required. Considering the model complexity, the high computation cost for a 40 MT ingot and the unavailability of all nucleation and transition parameters, these phenomena were not included in the present model.

4.3   Experimental setup, process and model geometry

The studied material is a modified P20 steel with the nominal chemical composition listed in Table 4-1. The ingot had a cylindrical shape with 250 cm in height and 150 cm in mean diameter and was cast in a big-end-up cast iron mold. The interior surface of the mold was corrugated, as shown in Figure 4.1a, to increase the perimeter in relation to the cross-sectional area of the ingot for increasing cooling rate and minimizing possible cracking of the ingot during solidification. The mold was hot topped above in 70 cm in height with insulating refractory tiles lined inside, and a layer of insulating exothermic refractory board was over laid on the melt top, as shown in Figure 4.1b. To ensure higher ingot surface quality and low turbulence, the molten steel was bottom poured into the mold at 1570 °C with a superheat of 75 °C. The filling time was 30 min. The temperature of the outside of the mold was monitored continuously throughout the casting procedure using 5 Chromel-Alumel

thermocouples (TC, type K) located in specified positions, as presented in Figure 4.1b. Each thermocouple was cemented into holes drilled 2.5 cm into the mold from the exterior surface. Temperature measurements from each thermocouple were made every 90 seconds from the start of the steel pouring until the ingot was removed from the mold.

Table 4-1 Nominal chemical composition of the studied modified P20 steel (wt.%).

C	Si	Mn	S	Cr	Mo	P	Ni	Fe
0.36	0.4	0.85	0.0023	1.82	0.45	0.01	0.16	balance

(a)   (b)   (c)
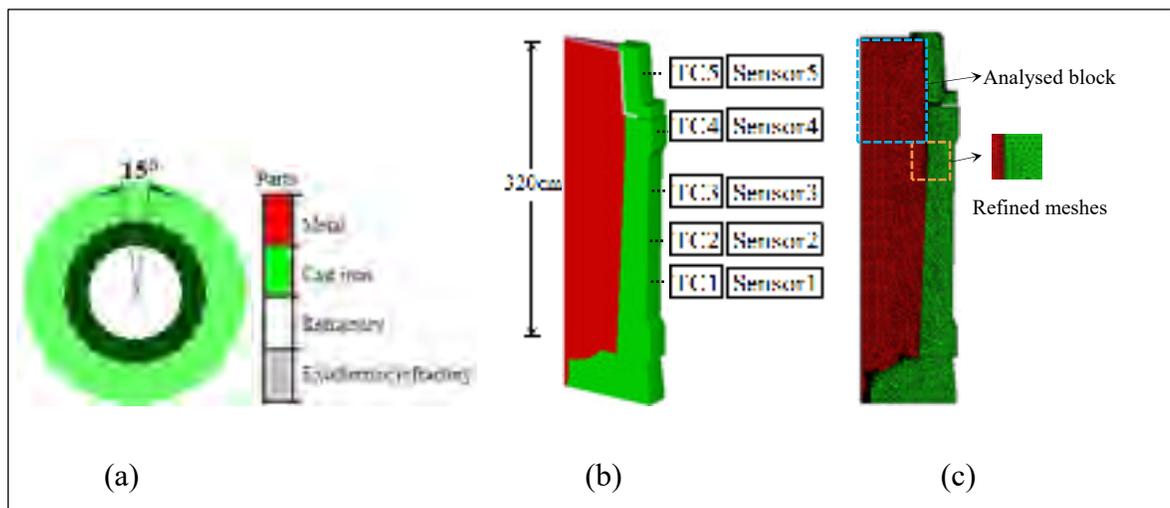
Figure 4.1 Casting system and established model. (a) Top view image of the mold (b) Main elements and corresponding materials in the 15° model with sensors placed in the same positions as the thermocouples (TCs) (c) Mesh distribution of the 15° model.

A block comprised of the hot-top and 30cm of the ingot's main body was transversely cut off for the investigation, as the one framed in blue in Figure 4.1c. Then, two plates (130 × 70 × 1.5 cm³) were sliced on each side of the axial plane, as illustrated in Figure 4.2. The axial face of one slice (the gray face in the figure) was prepared by grinding and etched in a 50% HCl solution at 50 °C to reveal macrosegregation patterns. The other slice was sectioned at regularly spaced intervals into 250 samples (6.5 × 4.5 × 1.5 cm³). All the faces in the

centerline plane along the longitudinal axis (the gray face) were grinded, and then chemically mapped using the Thermo Scientific ARL^{TM} 4460 mass spectrometer.
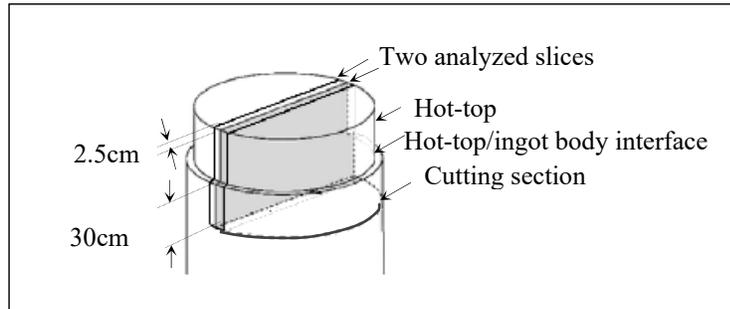
Figure 4.2 Cutting diagram for chemical and macrostructure analyses.

The chemical composition of each specimen was obtained by averaging out 3 random spectrometer measurements in order to increase accuracy. Then the segregation ratio for each solute element, R^i, was calculated using the relation, $R^i = (\omega^i - \omega_0^i)/\omega_0^i$ (Duan et al., 2016). Here, ω^i is the local concentration and ω_0^i is the nominal concentration value. A positive/negative R^i value corresponds to positive/negative segregation. Segregation ratio patterns of different elements in the longitudinal section of the studied block were then reconstructed by interpolation using MATLAB$^®$ (MATLAB, 2012b). This was done by filling the areas between the isolines using constant colors corresponding to the local segregation intensities.

The configuration of the model is displayed in Figure 4.1b. Due to the symmetry conditions, as shown in Figure 4.1a, only 15° of the 40MT ingot was modelled. Five sensors were installed at the positions identical to those of the five K type thermocouples. 3D linear tetrahedral elements were used for the spatial discretization of the part and mold components. An average grid of 35 mm was selected based on a mesh size optimization analysis. Meshes on the ingot surfaces in contact with molds were refined to approach the true solution, as shown in Figure 4.1c. Boundary conditions were defined according to the actual industrial practice. For both investigated models, calculations were taken to the moment when the entire casting comes to complete solidification (i.e. around 1400 °C).

4.4 Mathematical formulation

The 3D simulations of mold filling and solidification were performed in the finite element code Thercast®, based on a volume-averaged solid-liquid two-phase model (TherCast 8.2®, 2012). An Arbitrary Lagrangian-Eulerian (ALE) formulation was used for computing the thermal convection in the liquid pool and mushy zone, and for managing the evolution of metal volume and mass in the mold as a function of time during the filling phase. In contrast, a Lagrangian method was employed for calculating the deformation in solid regions. Sedimentation of equiaxed grains and the deformation of molds were not taken into account in the modeling. In order to simplify the numerical models and reduce the computational cost without altering the accuracy of the results, several assumptions were made:

1) The liquid was assumed incompressible Newtonian and the fluid flow laminar.

2) The mushy region was considered as an isotropic porous solid medium saturated with liquid.

3) Microscopic diffusion of carbon in the solid was assumed to be complete (Lever rule behavior).

4) Local temperature was considered as a function of the liquid concentration composition ω_l^i and the liquidus slope m_l^i:

$$T = T_m + \sum_{i=1}^{N} m_l^i \, \omega_l^i \tag{4.1}$$

where T_m is the melting temperature of the pure iron and N is the number of solute elements in the steel.

5) The heat flux was determined by the law of Fourier and given by the sum of natural convection and radiation contribution:

$$q = -\lambda \nabla T \cdot \mathbf{n} = h(T - T_{ext}) + \varepsilon_T \sigma_T (T^4 - T_{ext}^4) \tag{4.2}$$

where $\mathbf{n}$ denotes the outward normal unit vector, h (W/m/°C) is the heat transfer coefficient and T_{ext} is the external temperature (temperature of the mold), ε_T is the steel emissivity (assumed to be 0.8), σ_T is the Stephan-Boltzmann constant (= 5.776×10^{-8} W/m^2/K). The value of heat transfer coefficient h depends on time or on the interface temperature between the part and the mold, simulating the casting/mold contact or loss of contact (formation of air gap) during the cooling of the metal.

6) The solute flux was determined by Fick's law:

$$j = -D_l^i \nabla \omega_l^i \tag{4.3}$$

Where D_l^i is the diffusion coefficient of the chemical element i in the liquid.

7) In the liquid phase, the gravity-driven natural convection loops were created by local density variations (TherCast 8.2®, 2012). These convective flows are mainly of two types: i) thermal convection flows induced by thermal expansion and temperature gradients, and ii) solutal convection flows induced by solutal expansion and concentration gradients:

$$\rho_l = \rho_0 \left(1 - \beta_T (T - T_{ref}) - \sum_{i=1}^{n} \beta_{\omega^i} \left(\omega_l^i - \omega_0^i \right) \right) \tag{4.4}$$

Here, ρ_l is the density of the liquid, ρ_0 is the reference density taken at the reference temperature T_{ref} (imposed equal to the liquidus temperature), β_T and β_i are the thermal and solutal expansion coefficients, respectively, T is the temperature, ω_l^i is the solute concentration in liquid, and ω_0^i is the initial solute concentration mass fraction for solute element i.

For the TH model (thermohydraulic model), a constant alloy density was considered during solidification (i.e. $\rho = \rho_l$) so that the solid was assumed to be rigid and stationary. In contrast, for the TM model (thermomechanic model), the density evolved as a function of liquid and solid phases, i.e. $\rho = f_l \rho_l + f_s \rho_s$.

Based on the above assumptions, the analysis of fluid flow, temperature, and solute distribution in a solidifying material amounts to the coupled solution of the equations stating the conservation of mass, momentum, energy and solute. For the TM model, a coupled computation of the stress fields is also performed. The detailed derivation of associated auxiliary equations can be found in reference (TherCast 8.2®, 2012) and they will not be repeated here. The variables and their definitions mentioned above and hereinafter are listed in Appendix 4.1.

4.5   Determination of material properties

Most of the input parameters used in the modeling of macrosegregation are temperature dependent, reflecting thermodynamic, thermomechanic, and thermodiffusion behaviors.

Slight variations in such values have been found to influence, often significantly, model results. Schneider et al. (Schneider et Beckermann, 1995) found that two different sets of data for partition coefficients and liquidus temperature led to completely opposite simulation results for the solidification of the same steel. Wu et al. (Wu, Ludwig et Fjeld, 2010) pointed out that the poorly estimated nucleation or thermal parameters resulted in major discrepancy in the prediction of columnar-to-equiaxed transition (CET) region. Therefore, significant care must be taken for the selection of these parameters. In the following, the approaches used in the present investigation are presented.

4.5.1 Steel thermodynamic properties

The temperature dependence of the density (ρ), solid fraction (f_s) and the specific heat capacity (C_p) were determined by means of the computational thermodynamic software, Thermo-Calc® with TCFE7 Steels/Fe-alloys database (Andersson et al., 2002). The thermal conductivity (λ) of the steel was assumed to follow Miettinen's model below as a function of temperature and phase fraction (Miettinen, 1997):

$$
\begin{cases}
\lambda = f_\alpha \lambda_\alpha + f_\delta \lambda_\delta + f_\gamma \lambda_\gamma + f_l \lambda_l \\
\lambda_\alpha = (80.91 - 9.9269 \times 10^{-2}T + 4.613 \times 10^{-5}T^2)(1 - a_1(\omega_0^C)^{a_2}) \\
\lambda_\delta = (20.14 - 9.313 \times 10^{-3}T)(1 - a_1(\omega_0^C)^{a_2}) \\
\lambda_\gamma = 21.6 + 8.35 \times 10^{-3}T \\
\lambda_l = 39 \\
a_1 = 0.425 - 4.385 \times 10^{-4}T \\
a_2 = 0.209 + 1.09 \times 10^{-3}T
\end{cases}
\tag{4.5}
$$

where f_δ, f_γ and f_l are the volume fractions of δ-ferrite, γ-austenite and liquid, respectively, determined using Thermo-Calc®, T is the temperature in °C, ω_0^C is the nominal weight percent of carbon in the steel.

The applicability of the software Thermo-Calc® and Miettinen's model was verified before applying them to the investigated steel. First, the solid fraction of AISI steel 316, the density of pure iron, the specific heat capacity of AISI steel 1040, and the thermal conductivity coefficient of AISI steel 1020 were calculated using Thermo-Calc®/ Miettinen's model.

When the obtained values were found to generally agree with the corresponding experimental behaviors gathered from the literatures ((Mills, 2002) for 316 steel and pure iron, (Physical constants et al.) for 1040 and (thermo properties of metals et al.) for 1026 steels), the software and the model were used to calculate the thermodynamic properties of the investigated steel. The curves used for verifying the applicability of the above approach, as well as the determined thermodynamic properties of the studied steel as a function of temperature, are plotted in Figure 4.3.

4.5.2   Steel thermomechanical properties

Yield stress (σ_s), Young's modulus (E), strain hardening exponent (n), strain-rate sensitivity coefficient (m) and their variations with temperature were extracted from experimental tensile stress-strain curves and given in Figure 4.4. For tensile tests, cylindrical specimens were machined with a diameter of 1cm and a length of 12.2 cm with the gauge length of 2.2 cm. Tensile tests were performed using Gleeble^{TM} 3800 Thermomechanical Simulator at temperatures of 25, 650, 800, 1000 and 1300 °C and strain rates of 10^{-3} and 10^{-4} /s.

4.5.3   Steel thermodiffusion properties

The steel thermodiffusion properties employed in the simulations are presented in Table 4-2. The equilibrium partition coefficient (k) and the slopes of liquidus line (m_l) were calculated for each element i based on linearized binary phase diagrams with respect to iron, using Thermo-Calc$^®$ (Andersson et al., 2002). The solutal expansion (β_i) and the diffusion coefficient in the liquid (D) of each element were extracted from references (Duan et al., 2016; Schneider et Beckermann, 1995; Dong et al., 2017).
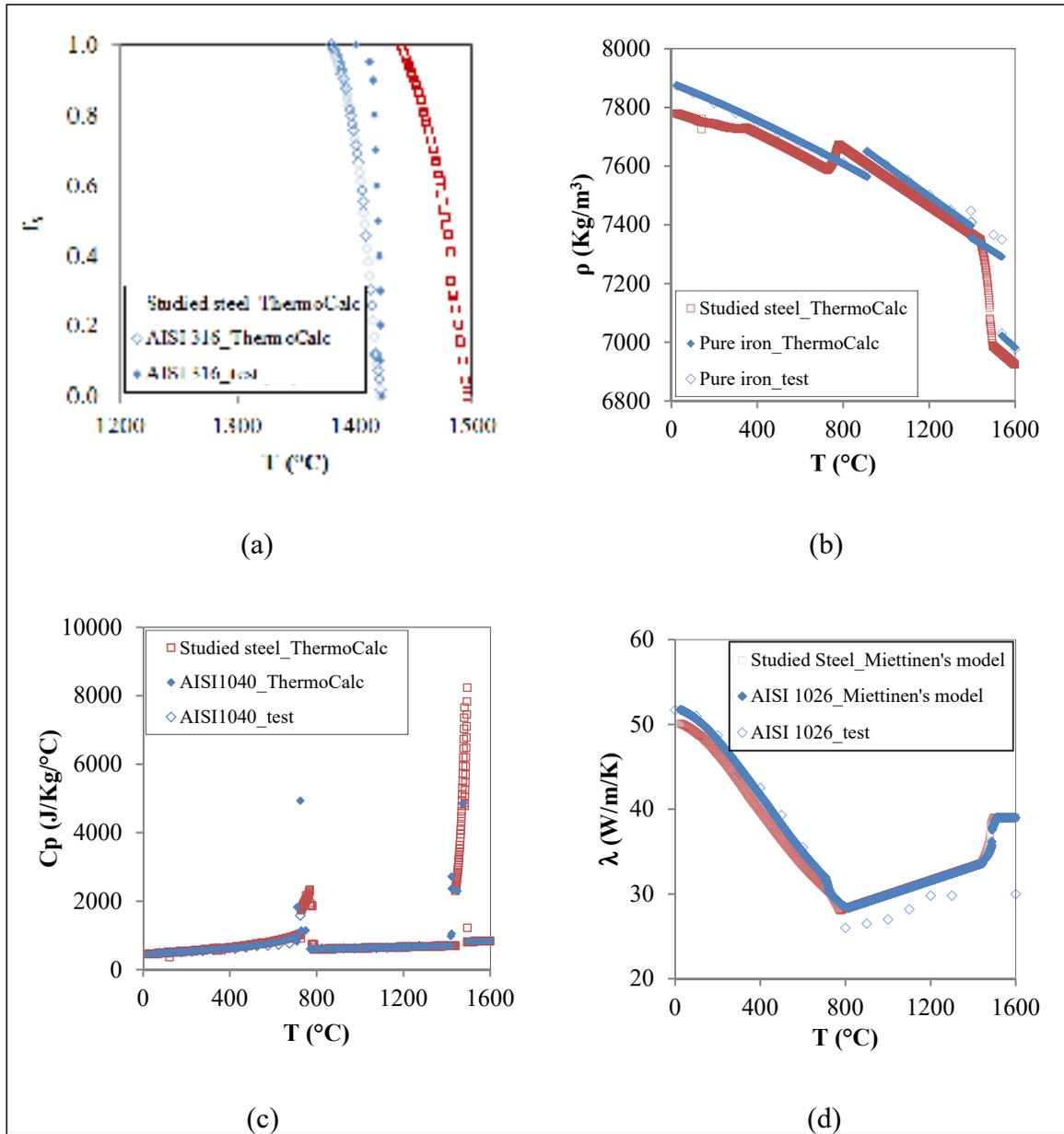
Figure 4.3 Temperature dependence of thermodynamic parameters of the studied steel, as well as the calculated and reported properties of pure iron and AISI commercial steels for verifying the applicability of the used software/model. (a) Solid fraction (b) Density (c) Specific heat capacity (d) Thermal conductivity coefficient.

(a)   (b)
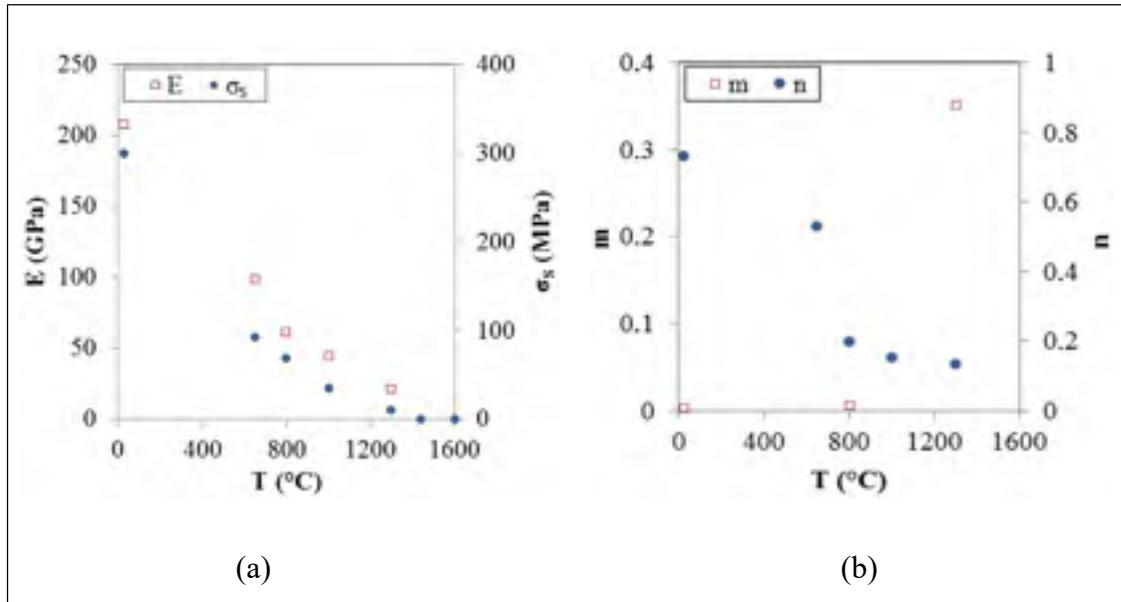
Figure 4.4 Temperature dependence of thermomechanical properties of the studied steel. (a) Young's modulus and yield stress (b) Stain rate sensitivity and strain hardening coefficient.

Table 4-2 Thermodiffusion properties for each solutal element.

Elements	Symbol	Unit	C	Si	Mn	S	Cr	Mo	P	Ni	Reference
Liquidus slope	m_l^i	K/wt.%	-80.6	-15.7	-5.35	-6.83	-1.66	-2.53	-67.52	-4.82	Andersson et al., 2002
Solute partition coefficient	k^i		0.3664	0.7	0.7545	0.0252	0.94	0.837	0.308	0.8474	Andersson et al., 2002
Solutal expansion coefficient	β_{ω^i}	$\times 10^{-2}$/wt.%	1.4164	1.19	0.192	1.23	0.397	-0.192	1.15	-0.069	Duan et al., 2016; Schneider et Beckermann, 1995
Diffusion coefficient	D^i	mm²/s	0.02	0.0038	0.0028	0.0042	0.0049	0.0025	0.0016	0.0012	Dong et al., 2017

4.5.4 Other parameters

The thermophysical properties of all other materials and initial modeling parameters are listed in Table 4-3. They were obtained from Thermo-Calc® calculations (Andersson et al., 2002), Thercast® material database (TherCast 8.2®, 2012), literature (Duan et al., 2016; Schneider et Beckermann, 1995), experimental measurement, or from the industry. It should be mentioned that the numerical parameters given in Table 4-3 are for the 15° casting system.

Table 4-3 Other parameters of the calculation and of the alloys.

	Property	Symbol	Unit	Value	Reference
Steel	Reference density	ρ_0	kg/m^3	6.99×10^{-6}	Andersson et al., 2002
	Melting temperature of pure iron*	T_m	°C	1538	Andersson et al., 2002
	Reference temperature (liquidus)	T_{ref}	°C	1495.3	Andersson et al., 2002
	Thermal expansion coefficient	β_T	/K	1.07×10^{-4}	Duan et al., 2016
	Latent heat of fusion	L_f	KJ/Kg	266.8	Schneider et Beckermann, 1995
	Emissivity	ε_T		0.8	TherCast 8.2®, 2012
Cast iron	Density	ρ	kg/m^3	7000	TherCast 8.2®, 2012
	Thermal conductivity	λ	W/m/K	30	TherCast 8.2®, 2012
Refractory	Density	ρ	kg/m^3	2353	TherCast 8.2®, 2012
	Thermal conductivity	λ	W/m/K	1.2	TherCast 8.2®, 2012

Table 4-3 Other parameters of the calculation and of the alloys (continued).

	Property	Symbol	Unit	Value	Reference
Exothermic refractory	Density	ρ	kg/m^3	600	-
	Enthalpy of reaction	ΔH	KJ/kg	8373.6	-
	Thermal conductivity	λ	W/m/K	0.2	-
Initial conditions	Steel pouring temperature	T_0	°C	1570	-
	Initial temperature of molds, powders and refractory	T_{mold}	°C	50	-
	Filling time	t_F	min	30	-
	Exterior environmental temperature	T_{ext}	°C	20	-
Numerical parameters	Number of nodes in the steel part	-	-	10770	-
	Number of elements in the steel part	-	-	46872	-
	Total number of nodes in the casting system	-	-	41192	-
	Total number of elements in the casting system	-	-	182103	-

*Melting temperature of pure iron was used to calculate local temperature as a function of the liquid chemical composition, using Equation (4.1).

4.6   Results and discussions

4.6.1   Top shrinkage and air-gap formation

In contrast to the TH model where no shrinkage and solid contraction are considered, both these phenomena are analyzed in the TM model. To this end, 4 points were selected (as

presented on the upper right corner of Figure 4.5a) to examine the evolution of top shrinkage and lateral air-gap formation as the solidification proceeds. The time dependent vertical displacements of Point 1 (at the top center of the hot-top), and the radial displacements of Points 2 (at the top periphery of hot-top), 3 (at the hot-top/ingot junction skin), and 4 (at the ingot bottom periphery) were monitored. As reported by Point 1 in Figure 4.5a, the top shrinkage began to appear at the end of the filling stage. Then it developed at a constant rate because of liquid → solid phase change so that after 10h, a vertical displacement of 21 cm had taken place. After that, the shrinkage rate slowed down, probably because the contribution of solid deformation caused by the temperature decrease became dominant. Once the bulk metal was completely solidified (15 h 7 min later after pouring), the top shrinkage was close to its final position. The predicted shrinkage depth at the centerline (measured from the original fill height) of about 26 cm ($\approx$8% vertical contraction) agreed closely with the cavity dimensions measured on the ingot.

The initiation and development of air gap at different heights of the ingot are also reported in Figure 4.5a. It can be seen that no radial displacement appeared on Point 2 before 5 h and on Point 3 before 0.5 h. Such absence of air gap in the hot-top in the early solidification phase could be due to the poor thermal conductivity of the refractory tiles impeding the heat loss in the hot-top. Radial displacements on Point 3 were found to take place at the end of filling, while on Point 4, it occurred at almost the first pouring moment, indicating that the air gap was created below the hot-top/ingot interface section before the end of filling. This early occurrence of air gap could be the result of the ingot solidification shrinkage resulting from the no continuous temperature distribution at the casting/mold interface. The slopes of the radial displacement curves followed by Points 3 and 4 were found to decrease with the time, indicating the gradual decrease in the development rate of the air gap probably owing to the increase of the solid fraction. This different initiation time and growth of the radial shrinkage resulted in a staircase distribution of the air gap size along the ingot skin at the end of solidification: 0.84 cm at the top on Point 2 ($\approx$ 1.2 % radial shrinkage), 1.06cm at the hot-top/ingot intersection on Point 3 ($\approx$ 1.4 % radial shrinkage), and 1.5cm at the bottom on Point

4 ($\approx$ 2.2 % radial shrinkage). This predicted air gap values matched well with the radial contraction measurements for the ingot.

The combination of the shrinkage at the top of the ingot and the formation of the radial air gap detached the casting away from the top and the mold walls, leading to a volume reduction, as shown in Figure 4.5b. The volume reduction of ingot body + hot-top and its variation with time were obtained by measuring the ratio between the instantaneous longitudinal cross-section area of ingot body + hot-top and their initial value before solidification. The shrinkage also resulted in the variation of global shape, as shown in Figure 4.6, and the change of heat transfer mode from purely conduction to convection and radiation. All the above changes gave rise to different features in the temperature gradient, liquid fraction distribution, fluid flow field, solidification time, and macrosegregation pattern, compared to those predicted with the TH model, as discussed below.

(a)   (b)
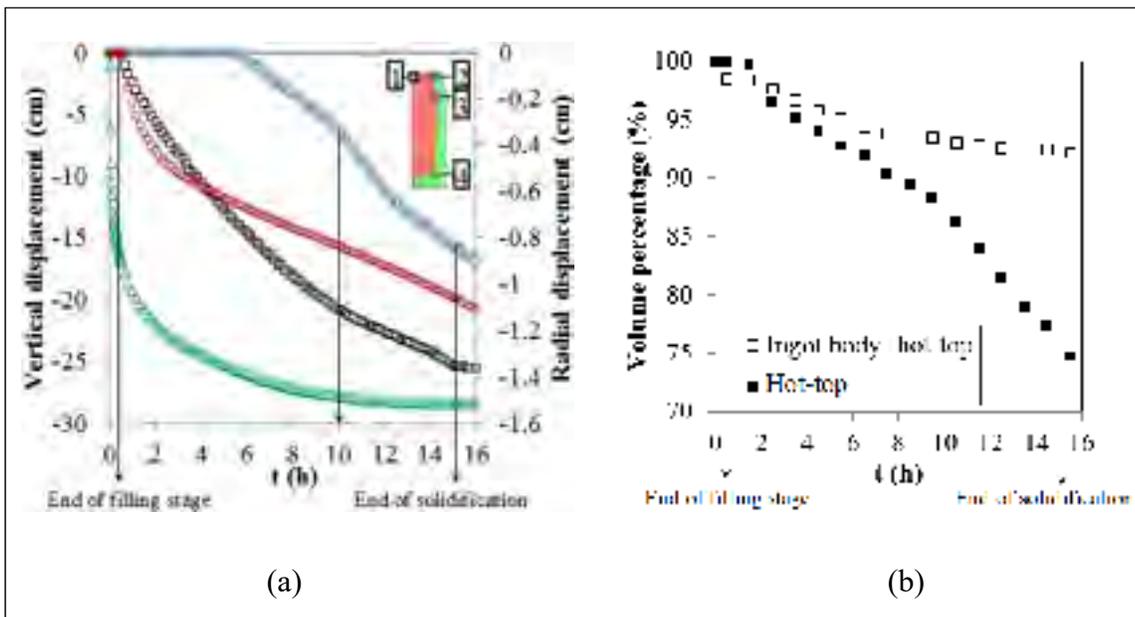
Figure 4.5 Predictions of thermomechanic model (TM). (a) Vertical displacement of Point 1, and radial displacements of Points 2, 3 and 4 with time (b) Evolution of ingot volume with time.

4.6.2   Temperature gradient

Temperature gradient patterns at times of 0.5 h (end of filling) 5.5 h, 10.5 h and 15.5 h after pouring are shown in Figure 4.6. The left four figures correspond to the predictions using the TH model and the right four ones are from the TM model. For the TH case, the interface between the ingot and the mold was marked artificially with dashed lines. Two common features can be seen for the thermohydraulic and thermomechanic predictions: (1) at the end of the filling stage, a slight horizontal temperature gradient was developed close to the mold chill wall and a vertical one next to the mold base (Figures 4.6a and 4.6e); (2) as solidification proceeded, the horizontal isotherms became inclined and the spacing between the adjacent isotherms widened. The above evolution of temperature isotherms are similar to those reported by Im et al. for pure heat conduction analysis (Im, Kim et Lee, 2001).
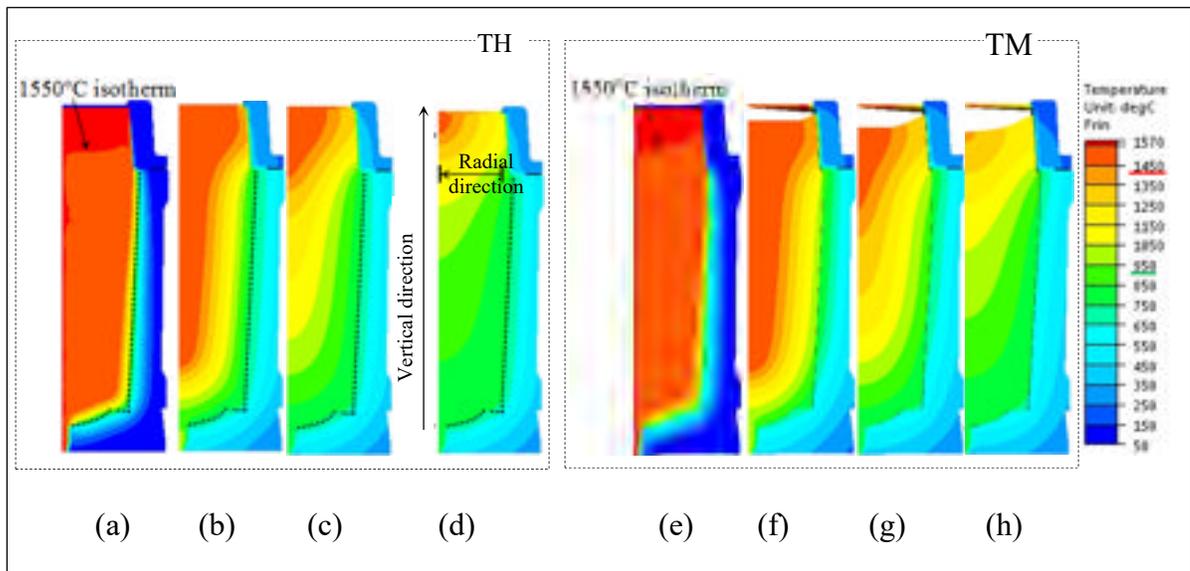
Figure 4.6 Temperature fields predicted by thermohydraulic (TH, left) and thermomechanic models (TM, right). (a, e) 0.5 h (end of filling) (b, f) 5.5 h (c, g) 10.5 h (d, h) 15.5 h after pouring.

However, at the end of the filling stage, the TM model presents an inclined isotherm of 1550 °C (Figure 4.6e), in contrast to a horizontal one in the TH model (Figure 4.6a). This

inclination could be attributed to the variation in volumetric contraction that occurs along the ingot skin from the bottom to the hot-top/ingot body interface section. Furthermore, as shown in Figures 4.6b-d and 4.6f-h, in the late solidification stage (i.e. above 10 h after pouring), the vertical and radial temperature gradients predicted by the TM model were smaller than those from the TH model. Above 15 h after pouring, as shown in Figures 4.6d and h, the vertical temperature gradient along the ingot axis reached 1.96 °C/cm for the TM model and 2.12 °C/cm for the TH model; the radial gradient along the hot-top/ingot body interface section was 4.21 °C/cm for the TM model and 5.09 °C/cm for the TH model.

Examinations of individual isotherms revealed that when considering the mechanical properties of the solid (i.e. TM model), *smaller* thermal gradients were predicted. Figure 4.7 shows the evolution of isotherms of 1450 °C and 950 °C with time in the vertical direction along the ingot axis (Figure 4.7a) and in the radial direction along the hot-top/ingot body interface section (Figure 4.7b). It can be seen that at any given solidification moment, the distances between the two isotherms predicted by the TM model are larger than those in the TH case.
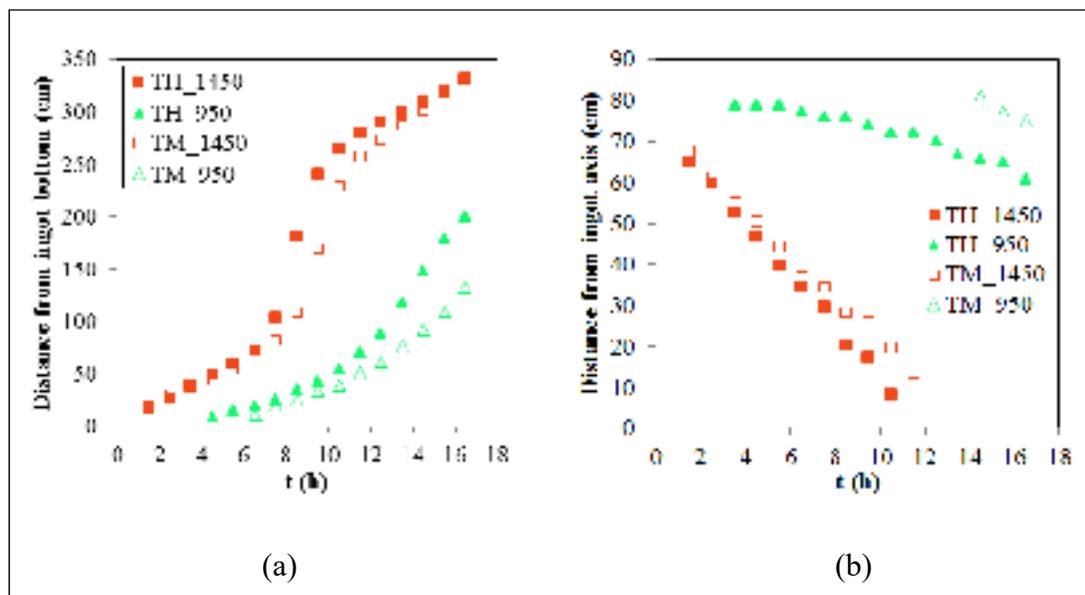
Figure 4.7 Movement of 1450 °C and 950 °C isotherms with time. (a)
In the vertical direction (b) In the radial direction.

4.6.3 Liquid fraction and solidification time

Liquid fraction patterns at times of 0.5 h (end of filling) 1.5 h, 10.5 h and 15.5 h after pouring are shown in Figure 4.8 for both models. It can be seen in Figures 4.8a and e that at the start of solidification, the liquid fraction predicted by the two models is very similar, presenting no distinct action of the mechanical deformation. A metal shell, occupying about 7 % of the total mass, formed next to the chill mold wall in the ingot body. Its formation could be associated with the rapid extraction of the initial superheat of the melt from the cold mold, as also reported by Schneider and Beckermann (Schneider et Beckermann, 1995).

Furthermore, a comparison of Figures 4.8c and d with 4.8g and h shows that when shrinkage and the mechanical properties of the solid are considered (TM model), solidification proceeds slower before the complete solidification of the ingot body: it takes 10 h in the TH model to reach a total solid ingot body, but 11 h with the TM model; solidification proceeds quicker and ends earlier after entire solidification of the ingot body.
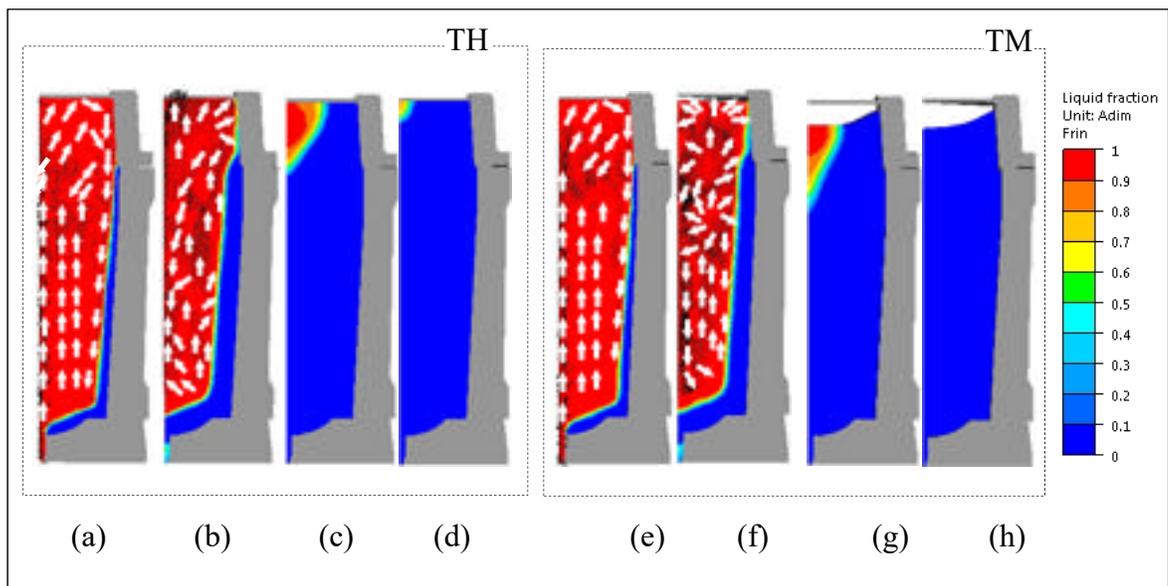
Figure 4.8 Liquid fraction and liquid flow patterns predicted by thermohydraulic (TH, left) and thermomechanic resolution (TM, right). (a, e) 0.5 h (end of filling) (b, f) 1.5 h (c, g) 10.5 h (d, h) 15.5 h after pouring.

Examination of the variation of solid volumetric fraction with time proved the nonuniform solidification rate over the solidification interval. As shown in Figure 4.9, the solid fraction predicted by the TM model was similar to the one with the TH model for the first 3 hours, but became lower between the 4 and 10 hours (before complete solidification of ingot body), and turned higher after it, until the end of the solidification process. The lower solid fraction in the second phase could be related to the slower heat-extraction rate due to the formation of the air gap and its insulating effect, as also reported by Chiang and Tsai (Chiang et Tsai, 1992), as well as the downward pulling of the solidification front owing to the formation of the shrinkage cavity at the top. The significant hot-top volumetric contraction in the third phase, as presented in Figure 4.5b, could be at the origin of the observed higher solidification rate of the ingot in the second phase.
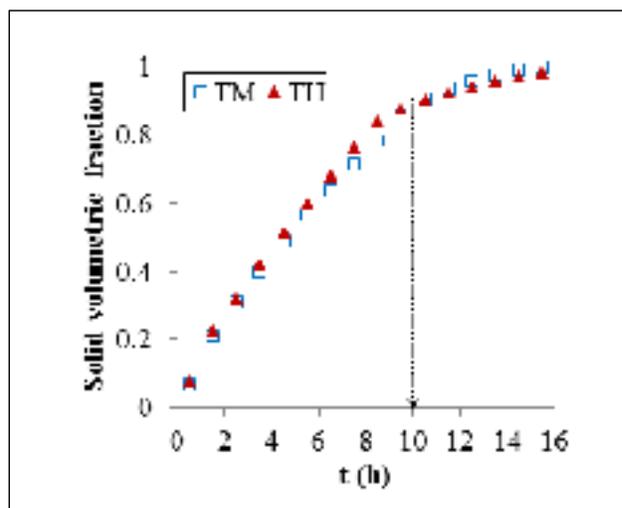
Figure 4.9 Evolution of solid volumetric
fraction with time.

The acceleration in the solidification process caused by thermomechanic deformation was also proved by the solidification time analyses, as shown in Figure 4.10. For both models, it was predicted that the solidification of the initial superheated melt was initiated almost immediately (8s) after pouring, in the region next to the chill zone, because of the sensible heat loss from the cold mold. The maximum initiation time for the triggering of solidification in the TM model was predicted to be 5 h 18 min. This value is 23 min shorter than in the TH

model. The total solidification time of 15 h 7 min (54429 s, see Figure 4.10b) obtained with the TM model is 1 h 47 min shorter than when using the purely conduction TH model (16 h 54 min, as shown in Figure 4.10a). The faster solidification process could be the result of the reduction of ingot body and hot-top volume (as shown in Figure 4.5b), which could prevail over the insulating function of the air gap in the cooling stage.
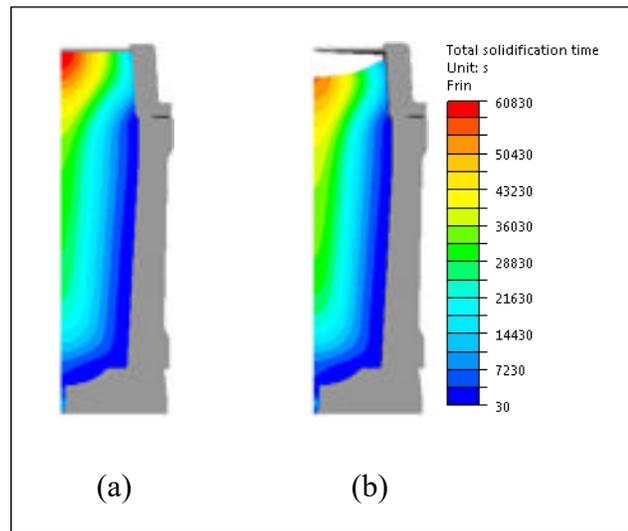
Figure 4.10 Total solidification time patterns.
(a) Thermohydraulic model (TH) (b)
Thermomechanic model (TM).

4.6.4 Macrosegregation pattern

As shown in Figure 4.11, large scale compositional variations were closely associated with the convective flow, and influenced by the above-mentioned changes of temperature gradient and solidification rate. At the start of solidification, the first solid particles formed in the upper part of the ingot body in the TH model (shown by red spots in Figure 4.11a), while in the TM model, they were formed in the hot-top (shown by red spots in Figure 4.11e). These different positions could be related to different residual flow modes in the two models, as seen in Figures 4.8a and e. In the TH model (Figure 4.8a), during mold filling, liquid bulk first moved upward along the centerline, then flowed downward along the solidification front

affected by the local mold configuration. It then diverged toward the less dense core under the influence of lateral thermal gradient, creating clockwise vortex in the upper part where the first solid particles start to form in the melt. In the TM model (Figure 4.8e), the residual flow driven clockwise vortex was moved upwards due to the radial shrinkage. Therefore, the first particles were formed in the hot-top rather than in the upper part of the ingot. Furthermore, this downward and diverged flow would pass through the low-f_i mushy zone, remelt and consequently channel the mushy zone. This process could be responsible for the formation of positive segregated bands close to the chill zone (Qian et al., 2015), as observed in Figures 4.11b-d and 4.11f-h.
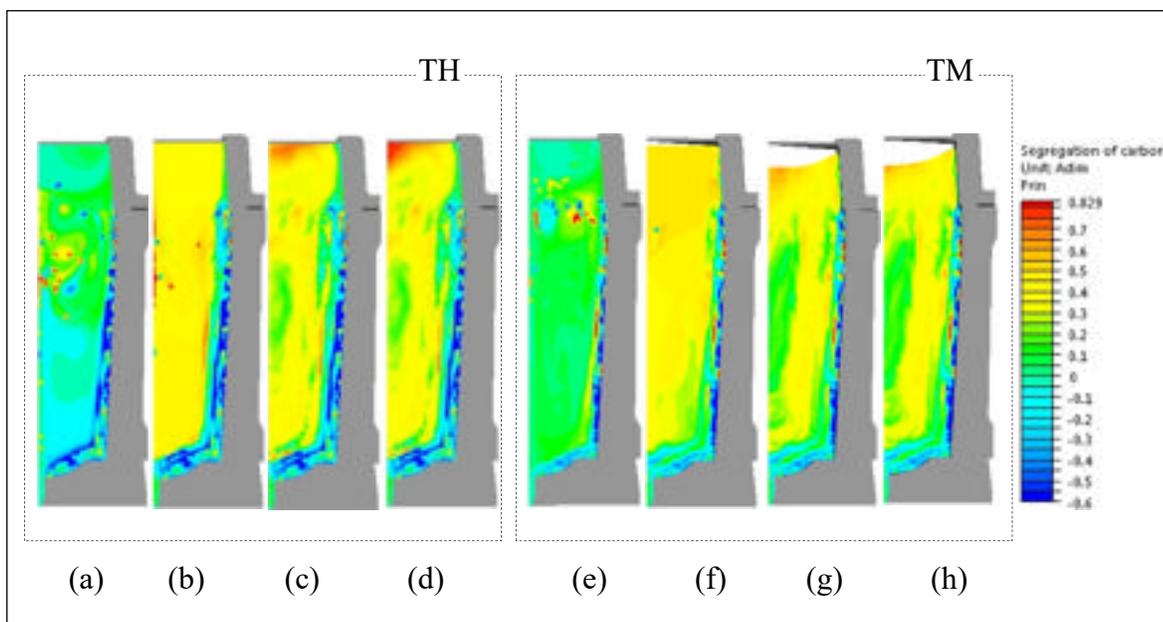
Figure 4.11 Carbon segregation ratio patterns predicted with thermohydraulic (TH, left) and thermomechanic models (TM, right). (a, e) 0.5 h (end of filling) (b, f) 1.5 h (c, g) 10.5 h (d, h) 15.5 h after pouring.

During later solidification phase, as compared between Figures 4.11b and f, lower concentrations of solutes along the ingot axis and the solidification front were predicted by the TM model. This finding could be associated with the natural convection flow prevailing in the later stages of solidification under the action of local density variation, as seen in Figures 4.8b and f. In the TH model (Figure 4.8b), natural convective flow counteracted the

downward flow, resulting in the inversion of the initial clockwise movement. In contrast, in the TM model (Figure 4.8f), mechanical shrinkage disordered this convective flow, and therefore impeded the directed distribution of the rejected solutes and weakened the accumulation trend of solutes along the centerline and in the solidification front. In addition, this lower positive segregation intensity could also originate from the smaller density variations due to the lower temperature gradient resulting from thermomechanic shrinkage.

Ten hours after the filling stage, when the ingot body was almost totally solidified, as illustrated in Figures 4.11c and g, positive segregated zones formed in the center upper region and negative segregated zones at the bottom. Solute-enriched segregation zones were also formed between the center and the ingot wall, as clearly revealed in Figures 4.11c, d, g and h. They extended nearly over the entire length of the ingot, inclined with respect to the ingot boundaries with a pattern similar to those calculated numerically by Schneider and Beckermann (Schneider et Beckermann, 1995). Finally, it should be noted that as shown in Figure 4.11d, large spatial variations in composition are predicted with the TH model. Sang et al. (Sang et al., 2010) also reported similar observations and related it to pure convection-induced flows that are assumed in the thermohydraulic modeling. In contrast, the macrosegregation in the upper section of the ingot and in the hot-top predicted by TM model was comparatively less severe, as seen in Figure 4.11h. The milder segregation finds its origin in the accelerated solidification in the casting process due to ingot volume contraction as discussed above.

4.6.5   Validation of models

Temperature profiles on the mold outer surface and the chemical distribution pattern on the longitudinal cross-section of the investigated block were used for the validation of the established models. Predicted temperature variations on the mold's outer surface as a function of time were compared with measured values of thermocouples (TC) placed at 5 characteristic positions (as illustrated in Figure 4.1b). As shown in Figure 4.12, at first, the temperatures sharply increased one after another, reflecting the successive contact between the melt and mold during pouring. Then, the increasing tendency was slowed down because

of the heat loss from the mold wall. Temperatures began to decrease about 6 hours after reaching their individual temperature peaks. Owing to the low conductivity of the insulating tiles inside the hot-top mold, the increasing tendency was slowed and the lowest peak temperature value was recorded by TC5. All these features were reproduced by the sensors of the TM model. A very good correlation can be seen between the predicted values by the TM model and the measured values. The 20 – 50 °C difference could be attributed to the uncertainty in the exact values of the thermal conductivity of the cast iron mold and the refractory tiles used in the computations. In contrast, the mold surface temperature evolutions predicted by the TH model predictions did not agree well with TC measurements.
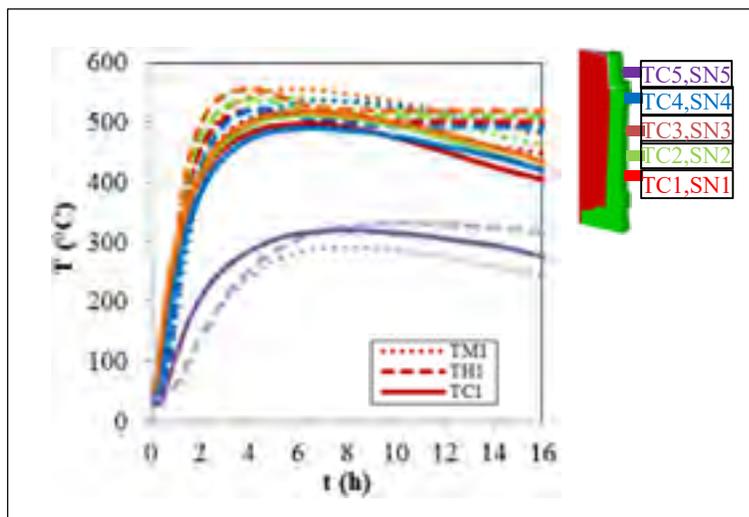
Figure 4.12 Temperature readings for thermocouples (TC) and the temperature predictions from simulations with thermomechanical (TM) and thermohydraulic models (TH).

Carbon segregation ratio profiles along the ingot centerline were quantitatively compared between simulation results and experimental measurements, as given in Figure 4.13a. The y-axis was set as the distance from the hot-top/ingot interface section. It can be noted that the thermomechanic chemical predictions matched better the experimental results in the hot-top as well as in the upper part of the ingot. The strong carbon positive segregation at the top

center of the hot-top and the lower segregation intensity in the ingot were well reproduced. For the TH model, at the top center of the hot-top, the carbon concentrations were overestimated and in the upper part of the ingot, the segregation severity varied dramatically from the test results.

Chemical variation examination along the transverse cutting section, 30 cm below the hot-top/ingot separation interface, confirmed the better predictability of the TM model, as shown in Figure 4.13b. The positive solute bands between the center and the ingot wall were predicted by both models. But the same regions were not detected by experimental measurements. This difference could be related to the fact that measured sampling points were not sufficient for inspection of finer segregation structures.
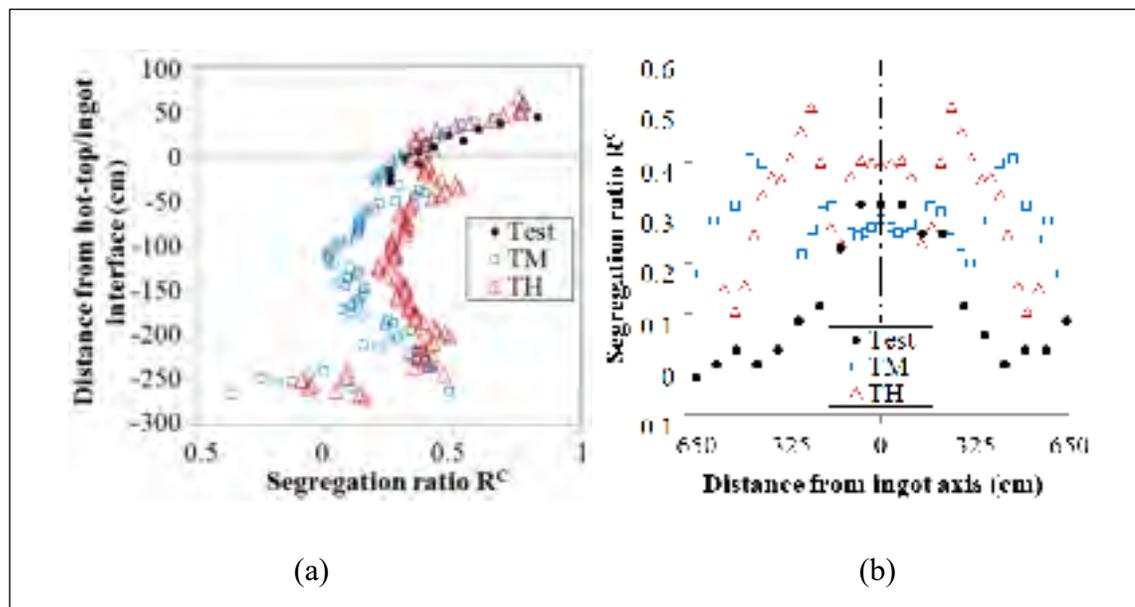
Figure 4.13 Evolution of macrosegregation ratio of carbon at the end of solidification. (a) Along the ingot centerline (b) Along the cutting section with 30cm below the hot-top/ingot body interface.

Macrosegregation ratio patterns of carbon predicted by both models were compared with mass spectrometer measurements and the results are presented in Figure 4.14. As shown in Figures 4.14a and b, the solute-enriched zone between the center and the ingot wall predicted by TM model matched better the area enclosed by the two black solute-enriched bands in

Figure 4.14c. However, it was not possible to capture enough details about the size and the number of positively segregated channels with any of the two models. Indeed, in order to attain a high spatial resolution in a relatively small scale (a few centimeters), a very high grid resolution is required, which was not the case in the present study.

It can be seen that the TM model predictions agree better with experimental results than the TH model. Based on the above discussions, this is probably due to the fact that the TM model considered solid deformation features during solidification, which is ignored by the TH model. These features include the formation of the shrinkage cavity at the top and the air gap between casting shell and mold. They result in the reduction of global volume and the change of heat transfer mode from purely conduction to convection and radiation. These changes correspond to characteristics closer to the actual solidification phenomena, in the temperature gradient, liquid fraction distribution, fluid flow field, solidification time, and macrosegregation pattern, compared to those predicted with the TH model. As a result, a better agreement with experimental measurements was obtained by the TM model.
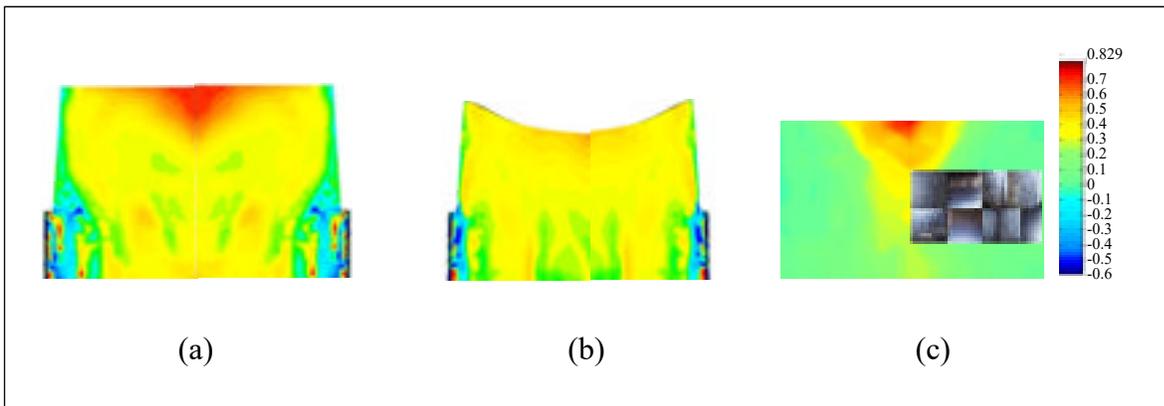
Figure 4.14 Segregation ratio patterns of carbon on the axial surface of longitudinal section. (a) Thermohydraulic model (TH) (b) Thermomechanic model (TM) (c) Mass spectrometer measurements with macrostructure around the hot-top/ingot junction.

4.7   Conclusions

In the present work, the effect of liquid contraction, solid shrinkage and air gap formation on macrosegregation patterns during casting and solidification of large size steel ingots was investigated. A thermohydraulic model (TH), based on natural convection, and a thermomechanic model (TM), considering both convection and solidification shrinkage, were developed and the obtained simulation results were validated with experimental measurements. The following conclusions can be drawn from the present study:

1) Temperature gradients, liquid flow pattern and macrosegregation patterns in the casting are primarily dominated by buoyancy effects (i.e. natural convection).

2) The formation of the shrinkage cavity at the top and the air gap between casting shell and mold modified the inclination of isotherms and solidification front, the iso-f_l area, the initiation of solidification and the total time for solidification.

3) The divergence and the disorder in the fluid flow generated by volume change influences the solutal redistribution in the melt and impacts the final macrosegregation patterns.

4) The model accounting for the combined influence of buoyancy and shrinkage (the TM model) presents a better quantitative and qualitative match with the thermal, chemical and dimensional experimental results, when compared with the case neglecting shrinkage effect and air gap formation (the TH model).

This study permits to better understand the impact of thermomechanical shrinkage in ingot cooling process and could be used in industry to improve the quality of large size ingot production and the productivity of high value-added steels or other alloys.

As a preliminary result for the coupling prediction of segregation and shrinkage, more effort is still needed, like the determination of actual mold material properties, the improvement of grid resolution and additional development to describe grain nucleation, growth and the morphology transition between globular and dendritic grains during solidification. To realize the possible prediction of mesosegregation and grain structure formation and transition, particularly in large size ingots, there is still a long way to go.

116

4.8 Acknowledgements

Appendix Nomenclature

Table 4-4 Nomenclature

Parameters	Symbols	Parameters	Symbols
Segregation ratio of solute i	R^i	Reference temperature (liquidus) (°C)	T_{ref}
Local concentration of solute i	ω^i	Solutal expansion coefficient of solute i ($\times 10^{-2}$/wt.%)	β_i
Nominal concentration of solute i (wt.%)	ω_0^i	Liquid fraction	f_l
Temperature (°C)	T	Solid fraction	f_s
Melting temperature of pure iron (°C)	T_m	Solid density (kg/m^3)	ρ_s
Liquidus slope of solute i (K/wt.%)	m_l^i	Density (kg/m^3)	ρ
Concentration of solute i in the liquid	ω_l^i	Specific heat capacity (J/Kg/(°C))	C_P
Number of solute elements	N	Volume fraction of δ-ferrite	f_δ
Heat flux	q	Volume fraction of γ-austenite	f_γ
Thermal conductivity (W/m/K)	λ	Yield stress (MPa)	σ_s
Heat transfer coefficient (W/m/°C)	η	Young's modulus (GPa)	E
Emissivity	ε_T	Strain hardening exponent	n
Stephan-Boltzmann constant (= 5.776×10^{-8} W/m^2/K)	σ_T	Strain-rate sensitivity coefficient	m

Table 4-4 Nomenclature (continued).

Parameters	Symbols	Parameters	Symbols
Exterior environmental temperature (°C)	T_{ext}	Solute partition coefficient of solute element i	k^i
Solute flux	j	Latent heat of fusion (KJ/Kg)	L_f
Diffusion coefficient of solute i in the liquid (mm^2/s)	D_l^i	Enthalpy of reaction (KJ/kg)	ΔH
Density of liquid (kg/m^3)	ρ_l	Steel pouring temperature (°C)	T_0
Reference density (kg/m^3)	ρ_0	Initial temperature of molds, powders and refractory (°C)	T_{mold}
Thermal expansion coefficient (/K)	β_T	Filling time (min)	t_F

ARTICLE 3 ON THE EFFECT OF FILLING RATE ON POSITIVE MACROSEGREGATION PATTERNS IN LARGE SIZE CAST STEEL INGOTS

Chunping Zhang[1,✉], Abdelhalim Loucif[1], Mohammad Jahazi[1], Rami Tremblay[2], Louis-Philippe Lapierre Boire[2]

[1] Department de Mechanical Engineering, École de technologie supérieur, 1100 Notre-Dame Street West, Montreal, Quebec H3C 1K3, Canada
[2] Finkl-Steel-Sorel, 100 McCarthy Street, Saint-Joseph-de-Sorel, Quebec J3R 3M8, Canada

5.1   Abstract

The effect of filling velocity on positive macrosegregation in large size steel ingots was studied. Macrosegregation and macro/microstructures were characterized on the hot-tops and a portion of the upper section of two ingots. The measurements revealed that segregation features in the two ingots varied as a function of the alloying elements, and that the severity of positive macrosegregation in the casting body was reduced when the filling rate was increased. It was also found that at the higher filling rate, grain morphologies in the first solidified zones of the ingot changed from columnar to equiaxe, and secondary dendrite arm spacing (SDAS) became slightly smaller in the intermediate and final solidified zones. The experimental findings were analyzed in the framework of diffusion and convection-controlled solidification, as well as liquid metal flow theories. The solute dependence of segregation features was related to the difference in the solid-liquid partition coefficient and diffusion capability of each element in the liquid iron. Calculation of Reynolds numbers (Re) during the filling process, for both ingots, showed that higher filling velocity caused more instable movement of the liquid metal in the initial solidification stage, resulting in the modification of grain morphology, as well as accelerated solidification rate.

Keywords: medium-carbon low-alloy steel, large size ingot, hot-top, filling rate, positive macrosegregation

5.2 Introduction

Ingot casting is the only method for the production of large size mono-block high-strength steels used in the energy and transportation industries. Various forms of casting defects, however, may stem from the liquid metal filling stage, and then remain during the solidification process. Among them, macrosegregation, defined as chemical heterogeneity on the scale of the entire ingot, is one of the most important, particularly in high alloyed steels. Such compositional variation over large distances results in local changes in mechanical properties, which may lead to reduced ingot quality and sometimes even to ingot rejection (Majka, Matlock et Krauss, 2002; Loucif et al., 2018). While the severity of macrosegregation could be significantly reduced in small to medium size ingots through subsequent homogenization and forging operations; the situation is more complex when it comes to large size ingots. Therefore, a better understanding of macrosegregation mechanisms, with the aim to control its extent in heavy castings, is an important scientific challenge with direct industrial implications. This is particularly true when it comes to high value-added products, such as large size casting of high strength steels used for turbine shaft applications.

Macrosegregation patterns in heavy low-alloy steel ingots is often characterized by intense positive segregation in the upper part, negative segregation at the bottom, and A- and V-type segregates in the body (Pickering et al, 2015). The pioneering work of Flemings et al., developed in the 1960s (Flemings, 2000; Beckermann, 2002), set the theoretical bases for studying the mechanisms of macrosegregation. Since then, intensive research has been underway, and some critical process parameters have been identified and used as 'countermeasures' to produce sound ingots with improved quality and limited macrosegregation (Combeau et al., 2009; Pikkarainen et al., 2016; Galkin et al., 2013; Dub et al., 2014). Specially, stringent control of the superheat (Pikkarainen et al., 2016), accelerating the solidification process in the mold (Galkin et al., 2013), and improving ingot dimensions and configurations (Dub et al., 2014) have been investigated experimentally and numerically by researchers.

In recent years, the influence of filling process parameters has been studied by several researchers. Lee et al. (Lee, Mok et Hong, 1999) numerically studied the velocity, stress, and temperature fields of pure metal during mold filling and the solidification process, showing the important effect of the filling process on fluid flow and heat transfer at the early stages of the casting process. Im et al. (Im, Kim et Lee, 2001) modeled the effects of wall temperature and filling flow on solidification and pointed out that the residual flow due to the filling stage had an important effect on flow characteristics and the liquid metal solidified more slowly in higher flow situations. Ravindran et al. (Ravindran et lewis, 1998) presented a model to investigate the effect of mold filling on cold shuts formation and metal front migration, and incorporated inter-dendritic flow models to simulate the effect of solidification on the filling patterns and temperature fields. Yadav et al. (Yadav et al., 2009) modeled the filling and solidification of a Pb-15 wt% Sn alloy in a small side-cooled cavity (50×60 mm^2) and investigated melt superheat and filling velocity on the evolution of mushy regions and macrosegregation. It was found that residual flow due to filling effects significantly affected the shape of the mushy zone and delayed the development of solutal convection, resulting in less intense macrosegregation near the cold wall and a farther distance of A-segregates from the cold wall. Kermanpur et al. (Kermanpur et al., 2010) simulated a 6-ton Cr-Mo low alloy steel to study the effect of bottom pouring rate and mold dimensions on solidification behavior and crack susceptibility during subsequent hot forging. Results showed that pouring the melt at a constant rate with a lower mold slenderness ratio would improve the riser efficiency and thereby possibly reduce crack susceptibility during subsequent hot forging. However, the effect of filling velocity on macrosegregation in large size steel ingots has not yet been reported, either numerically or experimentally.

In the present work, the effect of the filling rate on positive macrosegregation patterns in two large size cast ingots was studied. Various experimental techniques were used to examine the chemical composition, macro- and microstructure evolution of the hot-top and a portion of the upper section of the ingot. The results were analyzed in the framework of diffusion and convection-controlled solidification, as well as liquid metal flow theories. The obtained results are expected to contribute to a better understanding of macrosegregation mechanisms in large size ingots. The results could also be used as an input data in numerical simulation

codes which still suffer from lack of accurate determination of material characteristics (Pickering, 2013).

5.3   Materials and experimental process

Two 40 metric ton (MT) cylindrical shape steel ingots, 250 cm in height and 150 cm in mean diameter, were cast in big-end-up cast iron molds using identical conditions, except for the filling rate. The hot-top, as an extension of the ingot that was 70 cm in height, was made in the mold lined inside with insulating tiles. During the production process, molten steel with the nominal composition listed in Table 5-1 was first produced by melting scrap material in an electric arc furnace, and then teemed into a ladle before ladle refining and vacuum degassing in an argon atmosphere. Then it was smoothly bottom poured into the mold at 1570 °C, until the mold was filled to the top of the insulating tiles. Two filling times were used: the first ingot named LFR, with a filling rate of about 0.0018 m/s (30 min for the 40 MT ingot), and the second one, HFR, with a filling rate of about 0.0024 m/s (22 min). The liquidus temperature for the current material was determined to be 1495 °C, using the thermodynamic software Thermo-Calc® (Thermo-Calc Software, 2012). Based on this value, the initial superheat (the excess temperature above the melting point) for both ingots was determined to be 75 °C.

Table 5-1 Nominal chemical composition of the investigated steel (wt.%).

C	Mn	Cr	P	S	Si	Ni	Mo	Fe
0.36	0.85	1.82	0.01	0.0023	0.4	0.16	0.45	balance

After solidification, a block comprised of the hot-top and 30 cm thick section of the ingot's main body was transversely cut off for investigation. Then, two plates (130 × 70 × 1.5 cm³) were sliced on each side of the axial plane. One slice was sectioned at regularly spaced intervals into over 250 samples (6.5 × 4.5 × 1.5 cm³). All the faces in the centerline plane along the longitudinal axis were ground, and then chemically mapped using the Thermo Scientific ARL™ Optical Emission Spectrometer. The axial face of the other slice was prepared by grinding and macroetched in a 50% HCl solution at 50 °C to reveal

macrosegregation patterns. Some selected regions were metallographically prepared and etched in Oberhoffer's etchant, and then optically observed using a binocular microscope.

It should be noted that hot-tops are commonly used in the ingot casting industry in order to provide a reservoir of molten steel for feeding the shrinkage zone as the ingot solidifies (Majka, Matlock et Krauss, 2002). They are generally cut off from the ingot body after solidification. However, there is a growing interest in reserving at least part of the hot-top for further use (Qian et al., 2015). Thus, in the present study, positive segregation in the hot-top was also characterized, along with the upper section of the casting body to evaluate and validate such possibility. It is clear that, if successful, the findings could result in significant material and energy saving in the ingot casting industry.

The chemical composition of each specimen was obtained by averaging out 3 random spectrometer measurements and calculated using the relation (Duan et al., 2016):

$$R^i = \left(\omega^i - \omega_0^i\right)/\omega_0^i \tag{5.1}$$

Here, R^i is the segregation ratio for solute element i, ω^i is the solute's local concentration and ω_0^i is its nominal concentration value. A positive R^i value corresponds to positive segregation, and conversely, a negative R^i to negative segregation. Segregation ratio patterns of different elements in the longitudinal section of the entire block were then reconstructed using MATLAB® (MATLAB, 2012b) by filling the areas between the isolines using constant colors corresponding to the local segregation intensities.

5.4 Results and discussions

5.4.1 General macrosegregation patterns

The chemical distribution patterns of the principal alloying elements on the axial plane in the two ingots are shown in Figure 5.1. The observed section is illustrated in grey in the upper right corner of the figure. The patterns on the left are for LFR and those on the right are for HFR. Regions with no segregation ($R^i = 0$) are colored with light blue, negative segregation

($R^i < 0$) with dark blue, and the hot-top/casting body separation position is marked with a black dashed line. It can be seen that all the solute segregation ratio maps appear symmetric about the ingot central axis, even though minor differences are present. A gradient in solute concentration is observed over the ingot's radius from the periphery to the center and from the lower to the upper region. This indicates that the slow rise in concentration of solute in the solid was the result of bulk liquid becoming progressively concentrated in solute elements.

A weak difference from nominal composition (negative segregation) is observed in the region next to the surface layer of the hot-tops. This difference could be attributed to the increased local solidification time due to the presence of the refractory lining in the hot-top wall. The presence of the refractory lining decreases the cooling rate, as compared to the mold wall, and therefore reduces the segregation in these regions (Duan et al., 2016). On top of this, some concentration islands were observed, which can be associated with possible segregation channels.

It is also noted in Figure 5.1 that segregation features in the two ingots were found to vary as a function of alloying elements. Carbon is the element with the highest segregation ratio. The most intense positive segregation ratio of carbon, manganese, and chromium in both ingots was found to be sequenced in decreasing order, and reached 1.316, 0.225, and 0.212, respectively. The above sequence is consistent with the descending order of the solid-liquid partition coefficient k (the ratio of the solute content in the solid C_s compared to the solute content in the liquid C_l in equilibrium, $k = C_s / C_l$) of each solute. This coefficient was determined for each element based on linearized binary phase diagrams, with respect to iron calculated using Thermo-Calc® (Thermo-Calc Software, Pittsburgh, PA, USA, Andersson et al. 2002), and the results are shown in Figure 5.2a. The smaller the partition coefficient of a solute element, the more solute the solid will reject into the liquid during solidification, and the more intense the resulting segregation will be (Schneider et Beckermann, 1995). Although the k value of manganese lies between carbon and chromium, as seen in Figure 5.2a, its slightly lower diffusion coefficient in the liquid iron (as displayed in Figure 5.2b (Miettinen, 1997) results in a similar positive segregation pattern to chromium. In addition,

as shown in Figure 5.1, the most intense segregations of all the solutes (the red color in the maps) in LFR were observed at the top center of the hot-top, in contrast to the lower locations of positive segregates of manganese and chromium in HFR.
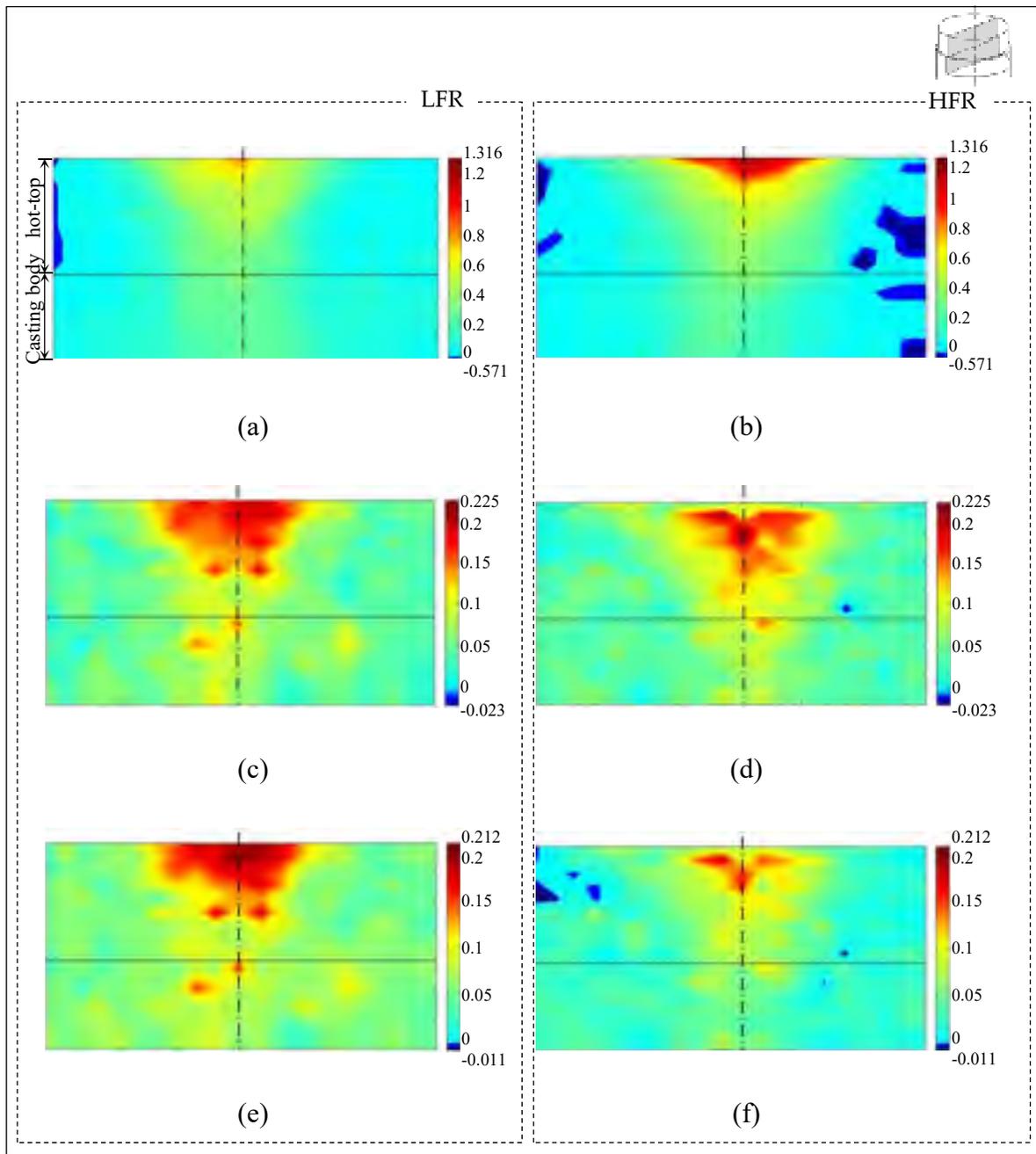
Figure 5.1 Segregation ratio patterns in the two ingots (LFR and HFR) for the three analyzed solutes. (a, b) C (c, d) Mn (e, f) Cr.
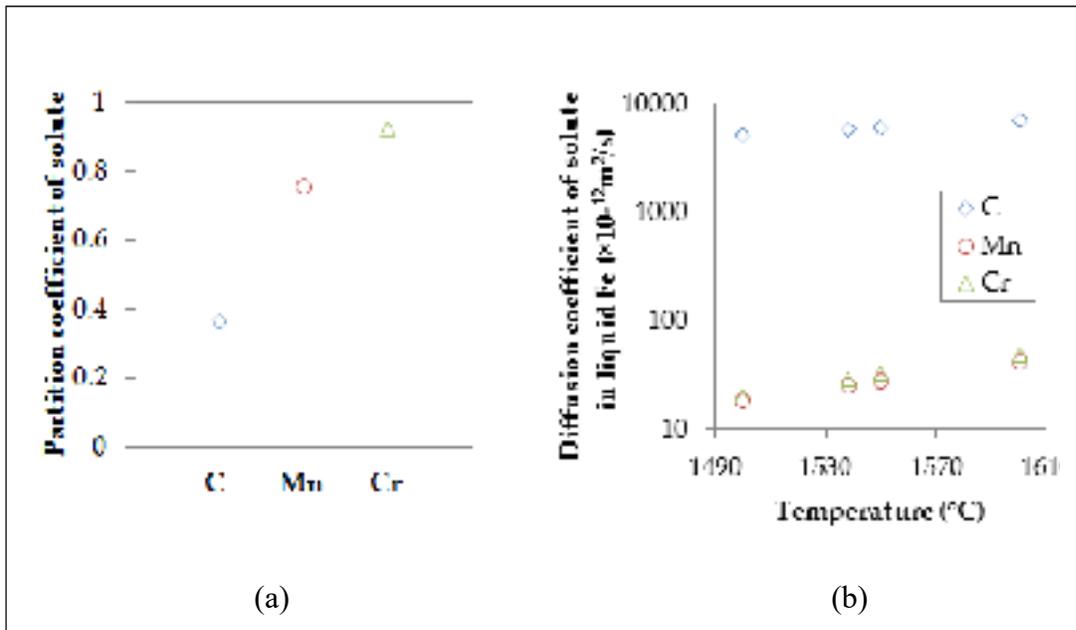
Figure 5.2 Partition coefficients of different alloying elements and diffusion coefficients of different solutes in liquid iron. (a) Partition coefficients of different alloying elements determined based on linearized binary phase diagrams with respect to iron (b) Evolution of diffusion coefficients of solutes in liquid iron as a function of temperature.

5.4.2   Effect of filling rate on segregation severity

Frequency distribution of segregation ratios were examined in the hot-top and the upper section of the casting body for the two investigated ingots. The results are plotted in histograms in Figure 5.3. It can be seen in Figure 5.3a that in the hot-top of ingot HFR, the intensity of positive segregation of all the analyzed elements is more pronounced (histograms with $R^i > 0$), especially in higher segregation regions ($R^i > 0.1$); solute concentrations close to the nominal composition are less so (histograms in the region $R^i = 0$). In contrast, in the upper section of the casting body of ingot HFR (Figure 5.3b), the positive segregation is less intense (histograms with $R^i > 0$) and more solutes are present with concentrations near the nominal composition ($R^i = 0$).

The above-mentioned tendency, *more severe* segregation in the hot-top of HFR and *less severe* segregation in the casting body of HFR, was more remarkable when the evolution of

carbon and manganese was examined along the central axis, as shown in Figures 5.4a and b. The axial concentration examination of chromium presented *less severe* segregation in both the casting body and the hot-top of HFR, as shown in Figure 5.4c. Moreover, it can be seen that in both ingots, the axial concentrations of carbon present a stepped monotonic increase from the cutting section to the top center of the hot-top. In contrast, positive segregation of manganese and chromium were found to increase progressively in a fluctuating way. The fluctuation was more distinct in HFR. The most intense positive segregation regions of manganese and chromium in HFR were found to lie about 5cm below the corresponding regions in the low filling rate case, LFR.
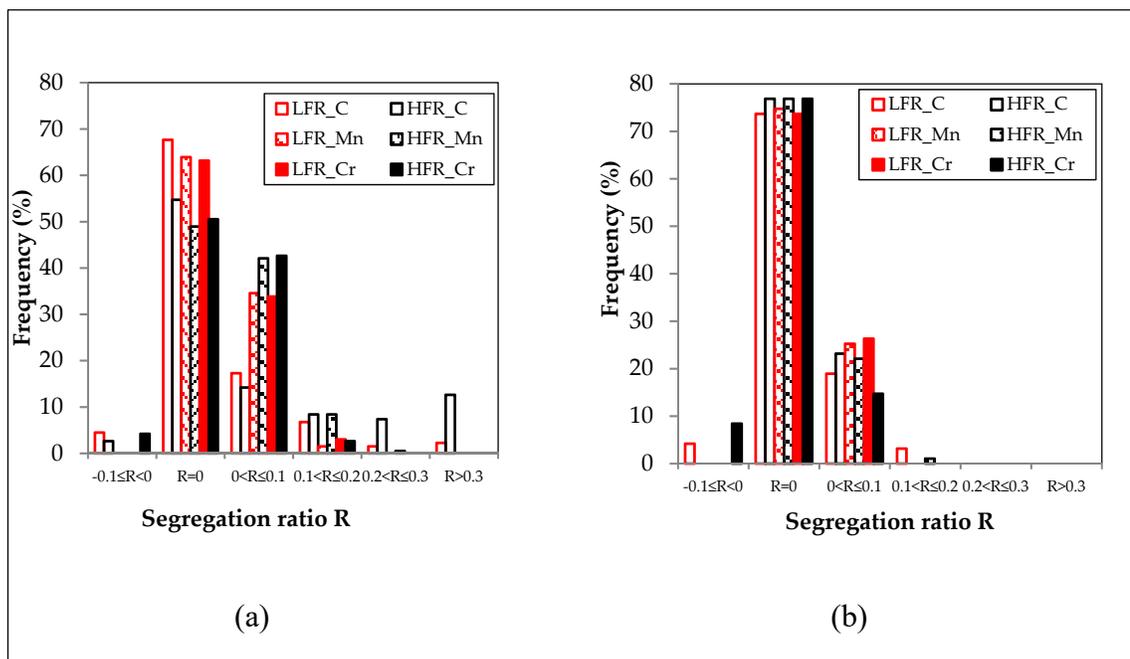
Figure 5.3 Frequency distribution of segregation ratios. (a) In the hot-top (b) In the upper section of ingot body.

An examination of the concentration distribution along the cutting line of the two ingots (i.e., 30 cm below the hot-top/casting body interface), as shown in Figure 5.5, revealed that the concentration profiles of all the three solutes in the casting body of HFR are below the LFR case and closer to the nominal composition ($R^i = 0$), presenting less severe segregation.
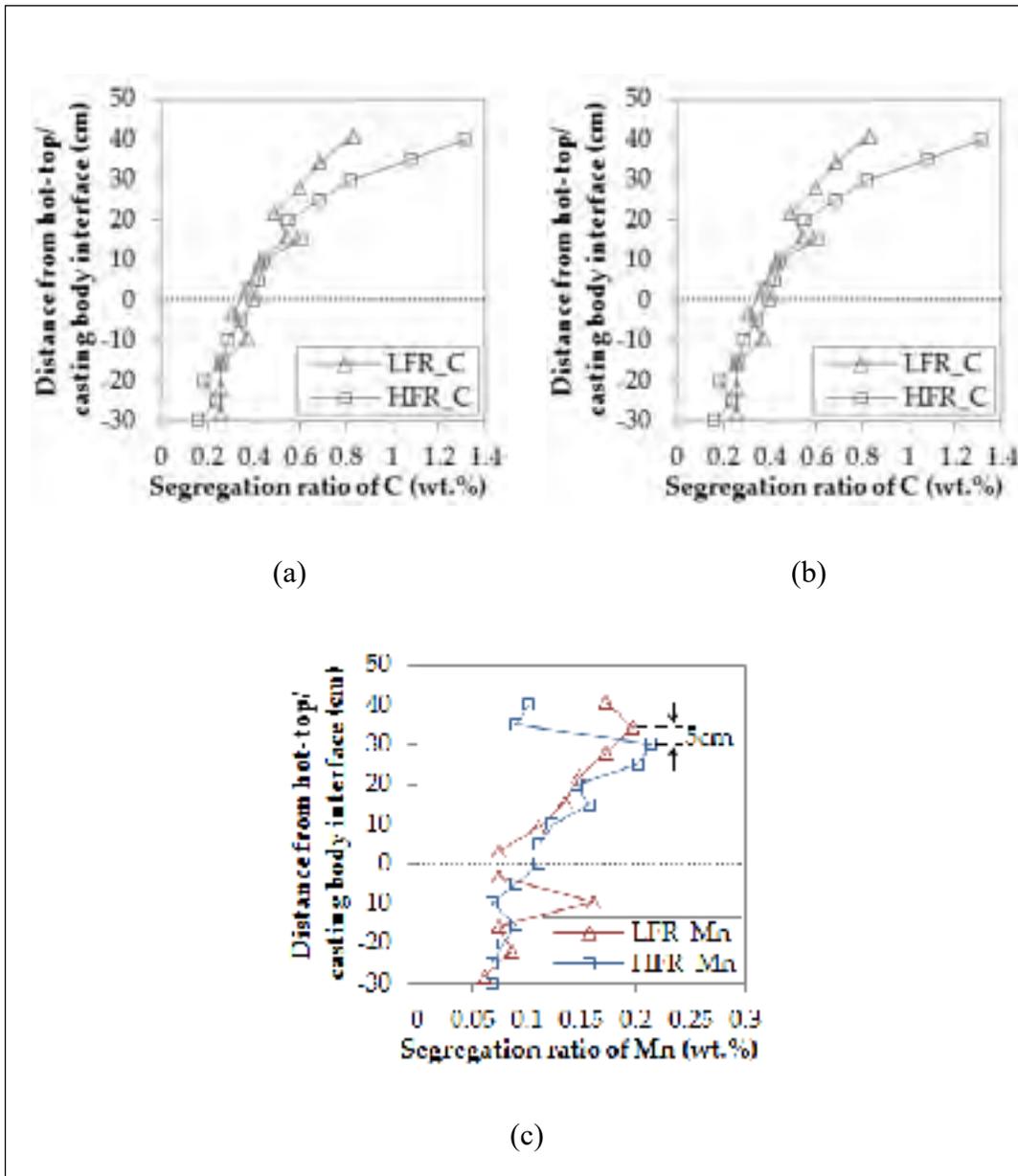
Figure 5.4 Segregation ratio profiles along the ingot central axis of the two ingots.
(a) Carbon (b) Manganese (c) Chromium.

The above results indicate that the filling velocity has a clear influence on the resultant macrosegregation, at least in the studied zones, of large size ingots. The obtained results confirm the observations of Yadav et al. (Yadav et al. 2009) in small size ingots, despite

the fact that in large size ingots the filling time is very short compared to the total solidification time.
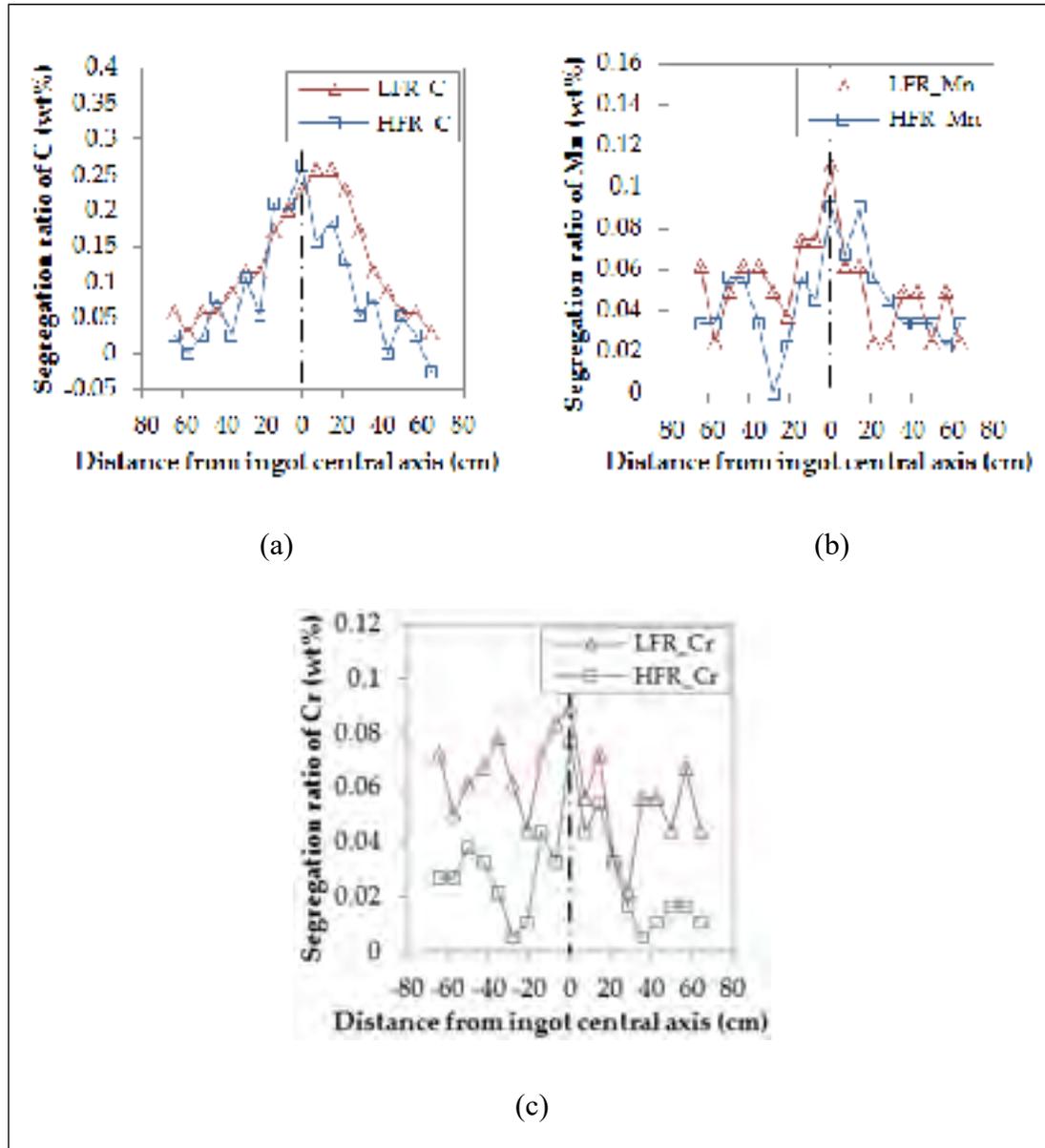
Figure 5.5 Segregation ratio profiles along the bottom of the cutting section of the two ingots. (a) Carbon (b) Manganese (c) Chromium.

5.4.3　Effect of filling rate on fluid flow and solidification time

Considering the large size of the ingots, the solid percentage formed at the end of filling was not expected to induce changes in the melt density, temperature, and viscosity. Thus, the influence of filling velocity on the flows of the liquid steel during the filling stage (considered as isothermal flow of a single phase material) was analyzed using the dimensionless Reynolds number (Re) (Marx et al., 2014; Reikher et Barkhudarov, 2007). The proposed approach is similar to the ones used by Marx et al. (Marx et al., 2014) and Wu et al. (Wu et al., 2010) for physical modelling of liquid melt flow in steel ingots:

$$Re = \frac{\rho v d}{\mu} \tag{5.2}$$

In the above equation, ρ represents the density of the fluid (kg/m^3), v the fluid flow velocity (m/s), d the characteristic length (m), and μ the dynamic viscosity of the fluid (Pa·s).

The density and the dynamic viscosity of the investigated steel at the filling temperature, 1570°C, were determined using Thermo-Calc® (Thermo-Calc Software, Pittsburgh, PA, USA, Andersson et al., 2002) and JMatPro® (Sente Software Ltd., Guildford, Surrey, UK, 2005), respectively. The mean filling speed was taken as the characteristic velocity and the average diameter of the cylinder mold cavity as characteristic length. After calculation with all the determined parameters, Reynolds numbers of 3208 for LFR and 4375 for HFR during the pouring process were obtained. The higher value of Re$_{HFR}$ indicates that more flow instabilities and movements were produced inside the mold under HFR condition. This flow instability is expected to result in some residual flow up to the initial stage of solidification under HFR condition.

Macroetch analysis of the zones near the surface of the ingot (first solidified zones), as reported in Figure 5.6, revealed columnar grains in the casting body of LFR (Figure 5.6a) and equiaxed grains in the same position of HFR (Figure 5.6b). The examined region is encircled in red in the upper right corner of Figure 5.6. Schematic views of the grain morphologies are also provided for clarification (due to the large size of the blocks and the grains, it is difficult

to capture high quality images with uniform light and shade in one single picture). Campbell (Campbell, 2011) found that a dampened fluid flow promotes columnar growth, while an unsteady liquid movement promotes the development of equiaxed grain structure (Willers et al. 2005). The presence of the equiaxed grain morphology in the first solidified zone in HFR is probably indicative of the presence of higher liquid instabilities at the start of solidification, as also predicted by the Reynolds number calculations.
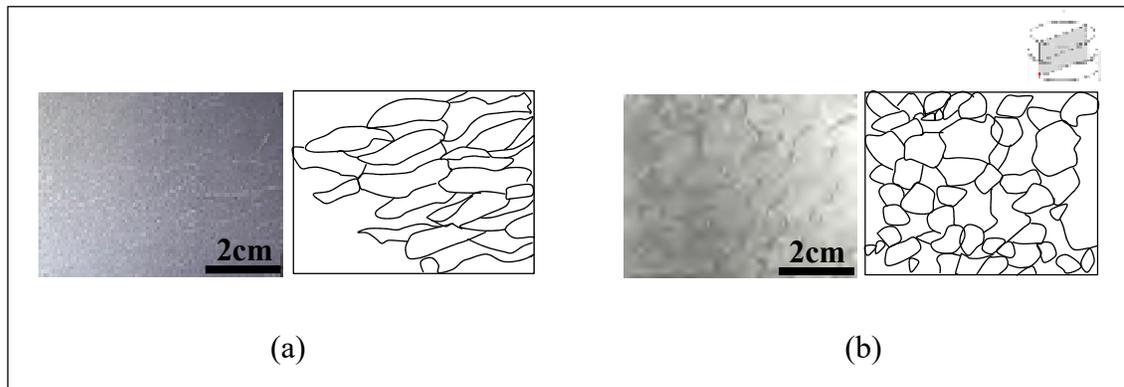
Figure 5.6 Grain morphologies in the bordering zones (the chill walls are on the left).
(a) LFR, (b) HFR.

Several researchers have examined the mutual influence of residual flow and solidification on the thermal and solutal behaviors of the ingot. Zhao et al. (Zhao et al., 2007) and Zhu et al. (Zhu et al., 2008) reported that the presence of residual flow can homogenize the temperature and solute field in the bulk liquid at the early stages of solidification, while Wang et al. (Wang et al., 2007; Wang, Yang et Tang, 2008) and Aboutalebi (Aboutalebi, 1994) related it to a decrease of temperature gradient in the pool of liquid. The lower temperature gradient can prolong the thermal convection time in the cavity and delay the development of solutal convection (Liu et al., 2011), because of better mixing of solute ahead of the liquidus front and thus decreased density gradients (Zhang, Bao et Wang, 2016). Others reported that delayed solutal convection can significantly affect the distribution of solutes (Vives et Perry, 1986; Hachani et al., 2012; Liu, Liu et Kang, 2008), and hence affect

the evolution of macrosegregation patterns during the intermediate and final stages of solidification. Therefore, more intense movement of the liquid metal in the initial solidification stage, caused by higher filling velocity, is probably the source for the observed reduced solute segregation in the casting body in the HFR ingot as compared to LFR.
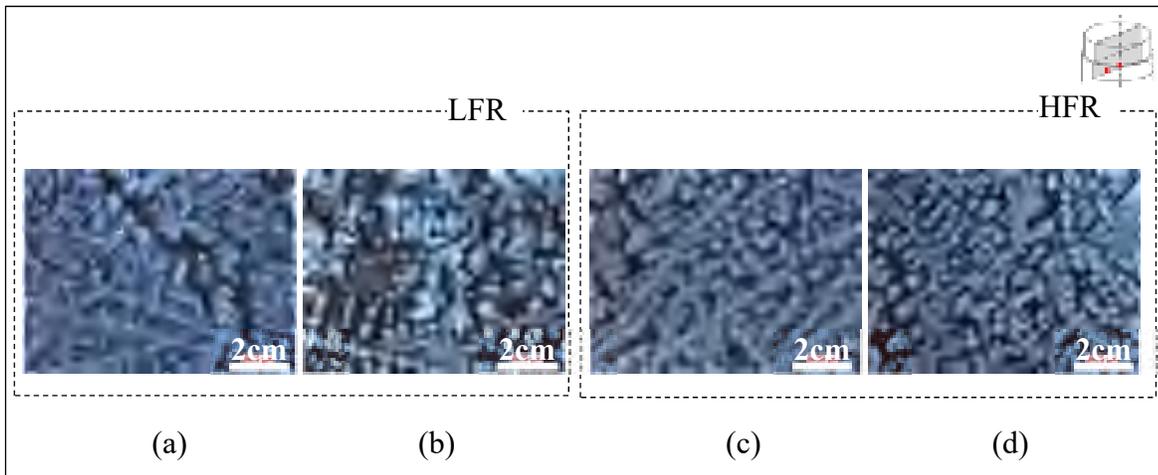
Figure 5.7 Micrographs along the bottom of the cutting section (30 cm below the hot-top/casting body separation position) of ingots LFR (left) and HFR (right). (a, c) In the 1/2 radius position from the center (b, d) In the center.

In addition, secondary dendrite arm spacing (SDAS) measurements along the cutting section of the LFR ingot revealed SDAS values as large as 474 μm in the 1/2 radius position from the center and 536 μm in the ingot center. The two observed regions solidified in the intermediate or final stage of the solidification process. The SDAS values were also in the same range for the HFR ingot but slightly smaller (470 μm and 530 μm, respectively, in the corresponding regions), as presented in Figure 5.7. Lower SDAS values are generally correlated with shorter solidification times (Campbell, 2011). Furthermore, as reported by Vives et al. (Vives et Perry, 1986), higher filling rates result in increased dissipation rate of the melt superheat with the mold and accelerated solidification rate due to the higher strength of convection. Therefore, the findings of the shorter solidification time resulting from higher filling velocity could result in less time available for solutes to transport, and could be another source for the lower segregation intensity in the casting body of HFR. It should be noted that further experimental work on measuring the SDAS values in different locations of

the ingots will contribute to confirm and better quantify the differences in the SDAS values for each condition.

The shorter solidification time and the lower diffusion coefficient of the solutes are probably the main sources for the observed lower location (~ 5 cm) of the positive manganese and chromium concentration cores in HFR (as reported in Figures 5.1 and 5.4). Besides, no sufficient diffusion time could be the origin for the observed higher fluctuations in the concentrations of manganese and chromium in the radial and axial distributions in HFR (as seen in Figures 5.4 and 5.5). The reduced segregation in the casting body of HFR, produced under fast filling conditions, is probably the root cause for the higher segregation intensity observed in the hot-top of HFR. Indeed, a lower segregation level in the casting body results in more partitioning of solutes into the melt and their accumulation towards the end of solidification in the upper part of the hot-top (Flemings, 2000). The axial less severe segregation of chromium in both the casting body and the hot-top of HFR could be due to less available time for the diffusion of the solute.

5.5   Conclusions

The effect of filling rate on positive macrosegregation characteristics in large size steel ingots was studied based on the analysis of the hot-top and a small portion of the main ingot body. The following conclusions can be drawn:

1) General macrosegregation patterns presented the solute dependence of segregation features, which was related to the difference in the solid-liquid partition coefficient and diffusion capability of each element in the liquid iron.

2) Frequency distribution of segregation ratios, as well as the axial and horizontal concentration evolutions, presented less severe segregation in the casting body of the ingot with the higher filling rate.

3) One source of the reduced solute segregation in the casting body in the higher filling rate case is the presence of higher liquid instabilities at the start of solidification, which was predicted by the Reynolds number calculations during the filling process, and confirmed by macroetch grain morphology observations in the first solidified zones.

134

4) Another source for the lower segregation intensity in the casting body of higher filling rate case is the shorter solidification time, resulting in less time available for solutes to transport, which was revealed by the secondary dendrite arm spacing (SDAS) measurements along the cutting section of the ingot in the regions solidified in the intermediate and final stages of the solidification process.

Therefore, the alleviation of solute segregation in the upper section of the casting body resulting from the accelerated filling process could be due to a combination of the more intense movement of the liquid metal, caused by higher kinetic energy of the liquid metal in the initial solidification stage, and shorter solidification time that reduces the available time for the segregation to build up.

5.6 Author contributions

Conceptualization, M. J. and C. Z.; Methodology, C. Z.; Software, C. Z. and A. L.; Validation, C. Z.; Formal Analysis, C. Z.; Investigation, C. Z. and R. T.; Resources, R. T., M. J. and L.-P. L.; Data Curation, C. Z.; Writing - Original Draft Preparation, C. Z; Writing-Review & Editing, M. J. and A. L.; Visualization, C. Z.; Supervision, M. J.; Project Administration, M. J.; Funding Acquisition, M. J.

5.7 Acknowledgments

5.8 Conflicts of interest

The authors declare no conflict of interest.

ARTICLE 4 SIMULATION AND EXPERIMENTAL VALIDATION OF THE IMPACT OF FILLING RATE ON MACROSEGREGATION IN LARGE-SIZE STEEL INGOTS

Chunping Zhang[1, ✉], Abdelhalim Loucif[1], Mohammad Jahazi[1]

[1]Department of Mechanical Engineering, École de technologie supérieur, 1100 Notre-Dame Street West, Montreal, Quebec H3C 1K3, Canada

6.1   Abstract

In order to study the influence of casting parameters on macrosegregation in a 40-metric ton (MT) ingot of a high-strength low-carbon steel, a combination of Finite Element (FE) simulation and experimental validation was used. The development of a two phase (liquid-solid) multiscale 3D model and the modeling of the filling and solidification processes were realized using the FE code Thercast®. The residual flows induced by pouring jet, the thermosolutal convection and the thermomechanical deformation of the phases were taken into consideration. In the present paper, the impact of filling rate (with filling times of 38, 30 and 22 min), representing the variables encountered in industry during casting of large size ingots, were examined. The evolution of solute transport, as well as its associated phenomena throughout the filling and cooling stages, were investigated. It was found that increasing the filling rate (i.e. shortening the filling time) resulted in reduced macrosegregation in the upper section and the mid-radius regions of the ingot. The reliability of the established model was verified by experimental temperature and chemical composition measurements. The beneficial effect of the higher filling rate on the alleviation of macrosegregation was quantitatively validated against experimental characterizations. The results were analyzed in terms of heat and mass transfer theories.

Keywords: Finite Element modeling, large-size ingot, steel, filling rate, macrosegregation

136

6.2   Introduction

In recent years, there is an increasing demand for large size forged steel ingots in energy and transportation industries (Scarabello, Ghiotti et Bruschi, 2010). The occurrence of macrosegregation in the ingots poses quality problems, as it creates chemical compositions different from the nominal one, resulting in inhomogeneous metallurgical and mechanical properties. Unfortunately, to date, macrosegregation cannot be fully eliminated by homogenization treatments, even after very long holding times (Loucif et al., 2018; Pickering, 2013). Therefore, measures, such as optimizing process parameters (Zulaida et Suryana, 2016), 'adjusting' the chemical composition (Su et al., 2018), or modifying the geometry of the mold and the hot-top (Qian et al. 2015), must be taken to minimize the severity of the phenomenon (Zulaida and Suryana, 2016; Su et al., 2018; Qian et al., 2015). However, this requires a better understanding of the fundamental mechanisms that govern the impact of each of the above parameters. Considering that a fully experimental-based approach is very costly and time-consuming, numerical simulation is a valuable tool. Simulation study is not only beneficial cost wise but also allows to quantify the impact of each parameter in a more rigorous way, so that input parameters can be determined accurately (Pickering, 2013).

It has been reported that macrosegregation starts from the very early stages of mold filling and then expands through the entire solidification process. Therefore, minimization of macrosegregation starts from a stringent control of the mold filling operation. During the pouring process, filling rate needs to be carefully controlled, since too fast pouring can raise turbulence, while the opposite can result in early solidification before the mold filling finishes (Campbell, 2011). Im et al. (Im, Kim et Lee, 2011) numerically modeled the effect of filling flow on solidification of an aluminum alloy, and pointed out the important effect of the residual flow on flow characteristics and solidification speed. Lee et al. (Lee, Mok et Hong, 1999) studied fluid flow, temperature and thermal stress fields during mold filling and solidification process of pure aluminum. Based on the numerical results, they found the significant influence of filling process on fluid flow, metal front migration and heat transfer at the early stages of casting process. Kermanpur et al. (Kermanpur et al., 2010) simulated

the effect of bottom pouring rate and mold dimensions on solidification behavior of a low alloy steel (6-metric ton (MT)). They showed that pouring at a constant rate with a lower mold slenderness ratio would improve the riser efficiency, and reduce crack susceptibility during subsequent hot forging. Ravindran and Lewis (Ravindran et Lewis, 1998) developed a computational model to investigate the effect of mold filling on cold shuts formation, and the effect of solidification on the filling pattern and temperature field. Yadav et al. (Yadav et al., 2009) modeled the filling and solidification of a Pb-Sn alloy in a small side-cooled cavity (50 × 60 mm^2). They found that residual flow due to filling effects significantly affected the shape of the mushy zone, delayed the development of solutal convection, resulting in less intense macrosegregation near the cold wall, and a farther distance of A-segregates from the cold wall. Zhang et al. performed an experimental study on the effect of filling rate in a large size steel ingot, and reported that increased filling rates help to alleviate the severity of positive macrosegregation in the upper section of the casting (Zhang et al., 2018). The more intense movement of the liquid metal in the initial solidification stage, and shorter solidification time were deduced to be the two root causes for the observed behavior. However, the effect of filling rate on global macrosegregation in large size ingots and the relevant mechanisms still need further investigation.

The aim of the present work is to perform comprehensive numerical analyses about the influence of filling rate on macrosegregation of a 40MT ingot in a high-strength low-carbon steel alloy. A 3-D thermomechanic solidification model was used, which was constructed in the FEM code Thercast® (TherCast 8.2®, 2012). Three filling rates were investigated, representing the variables encountered in industry during casting of large size ingots. The flows induced by pouring jet, the thermosolutal convection and the thermomechanical deformation of the phases were all taken into consideration. The predicted macrosegregation patterns were compared with the experimental chemical measurements reported by Zhang et al. (Zhang et al., 2018). The study helps to have a better understanding of formation mechanisms of macrosegregation in large size ingots.

6.3   Model establishment

The 40MT model used in the study is composed of a cylindrical ingot 250 cm in height and 150 cm in average diameter. The ingot is cast in big-end-up cast iron mold with a hot-top 70 cm in height laid above. The hot-top part is lined inside with insulating refractory tiles, and an insulating exothermic refractory board is over laid on the melt top, as shown in Figure 6.1a. 3D linear tetrahedral elements, with an average grid of 35 mm, were used for the spatial discretization of the part and mold components.

The chemical composition of the investigated steel is given in Table 5-1. For the simulations, the liquid steel is bottom poured into the mold at 1570 °C (with a superheat of 75 °C). Three filling rates of 0.084, 0.107 and 0.145 m/min (filling times of 38, 30 and 22 min) are investigated. Therefore, the modeled cases are identified in the rest of the manuscript as 38M, 30M and 22M. After the pouring operation, the steel melt cools naturally inside the mold until complete solidification of the ingot (i.e. around 1400 °C).

The segregation ratio patterns of carbon predicted by 30M and 22M, on the centerline plane in the upper block of the ingot (30 cm's upper section of the ingot main body + hot-top), were compared with those from two experimentally cast 40MT ingots in the studied steel, 30E and 22E, from Zhang et al. (Zhang et al., 2018). The two experimentally obtained ingots were cast at 1570°C with average filling rates of 0.107 m/min (for 30E with filling time of 30 min) and 0.145 m/min (for 22E with filling time of 22 min), respectively. They were fabricated in a casting system identical to the model used in the present study. The chemical mapping of carbon distribution on the longitudinal sections of 30E and 22E was determined using Thermo Scientific ARLTM 4460 mass spectrometer. Patterns of carbon segregation ratio, R^C, were constructed based on the relation: $R^C = (\omega^C - \omega_0^C)/\omega_0^C$, where ω^C is the local carbon concentration and ω_0^C is its nominal concentration value.
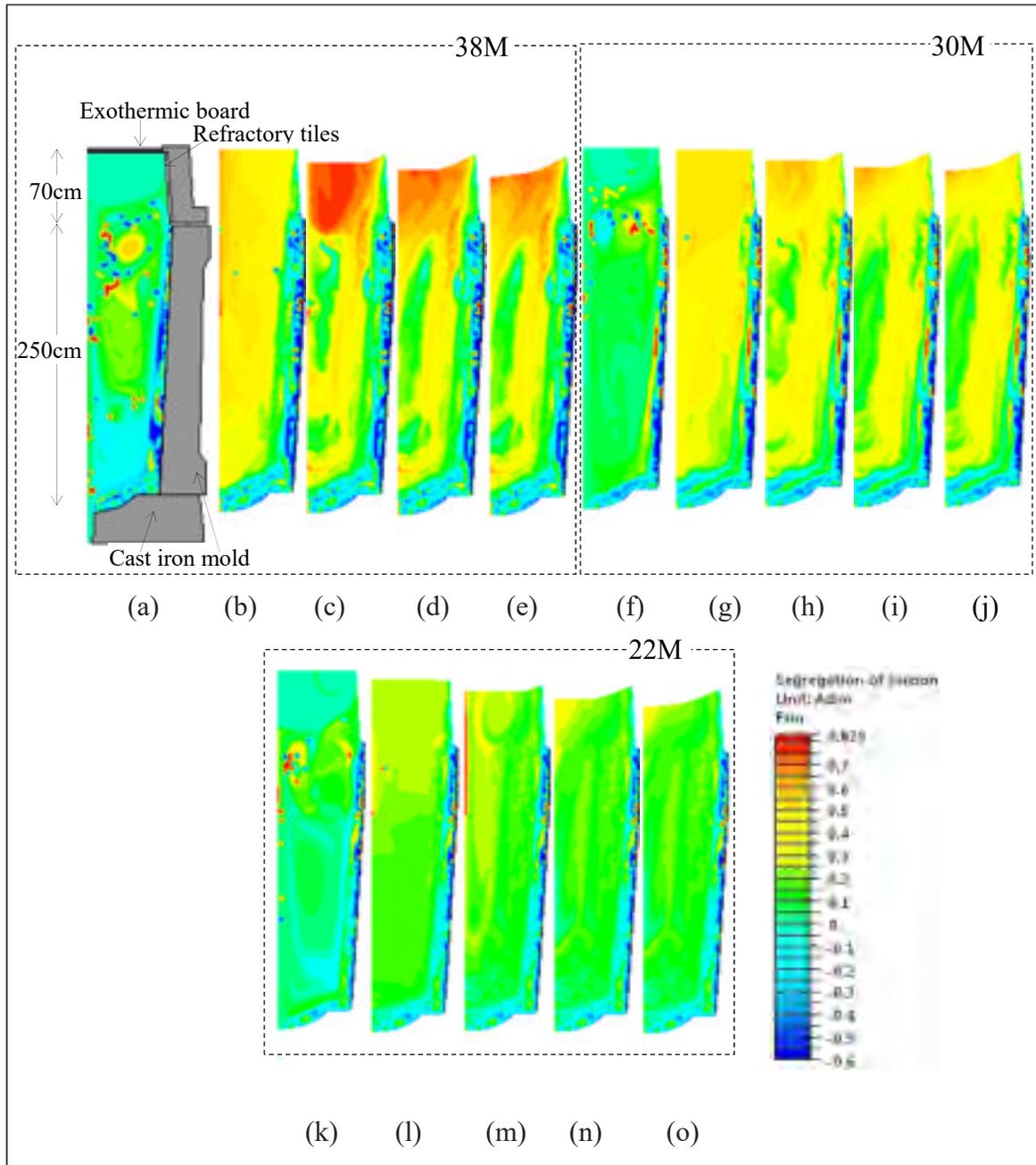
Figure 6.1 Predicted macrosegregation ratio patterns of carbon in the solidification process. (a, f, k) End of filling (b, g, l) 1.5 h (c, h, m) 5.5 h (d, i, n) 10.5 h (e, j, o) End of solidification.

The three-dimensional simulations of mold filling and solidification were realized in the finite element (FE) code Thercast®, based on volume-averaged solid-liquid two-phase thermomechanical models (Thercast 8.2®, 2012). An Arbitrary Lagrangian-Eulerian (ALE) formulation was used, for computing the thermal convection in the liquid pool and mushy zone, and for managing the time-dependent evolution of metal volume and mass in the mold during the filling phase. A Lagrangian method was employed for calculating the deformation in the solid regions. The analysis of fluid flow, temperature, and solute distribution in a solidifying material amounts to the coupled solution of the equations, stating the conservation of mass, momentum, energy and solute. Sedimentation of equiaxed grains and mold deformation were not taken into account in the modeling, either because they are not considered in the FE code or to reduce the computation time. All the material parameters used for the simulations in the present study are from Zhang et al. (Zhang et al., 2018).

6.4　　　Results and discussions

6.4.1　　　Macrosegregation ratio patterns and verification

Figure 6.1 shows the evolution of segregation ratio patterns of carbon on the longitudinal section in the casting process for the three cases. It can be seen that the variation of filling rate gave rise to different large-scale compositional distribution from the pouring moment till the end of solidification. At the end of pouring operation, in 38M, the first segregated particles (red and blue spots in Figure 6.1a) formed in a large area in the ingot body. For 30M (Figure 6.1f) and 22M (Figure 6.1k), fewer particles were distributed in smaller regions. Solutal gradient began to appear in 38M, but it tended to be smaller with the increase of filling rate. At 1.5 h after pouring, in 38M (Figure 6.1b), solute rejecting occurred in the bulk liquid; a solutal gradient was observed in the radial and vertical directions of the entire casting. In 30M (Figure 6.1g) and 22M (Figure 6.1l), in contrast, the radial and vertical solutal gradients were much less in intensity and extent.

As the solidification proceeded, a positive segregated zone in the upper center region and a negative one at the bottom of the ingot formed progressively for all the three studied cases, as

presented in Figures 6.1c, h and m. The weakest accumulation of solutes occurred at the highest filling rate (that is, in 22M), and was maintained till the end of solidification, as seen in Figures 6.1e, j and o. Furthermore, the carbon macrosegregation ratio patterns revealed that solute-enriched bands formed between the ingot axis and the mold wall for all the three cases (Figures 6.1c-e, h-j and m-o). They extended nearly over the entire height of the ingots, inclined with respect to the ingot periphery. The segregation intensity in these mid-radius solute-enriched bands became lower as the filling rate was increased.
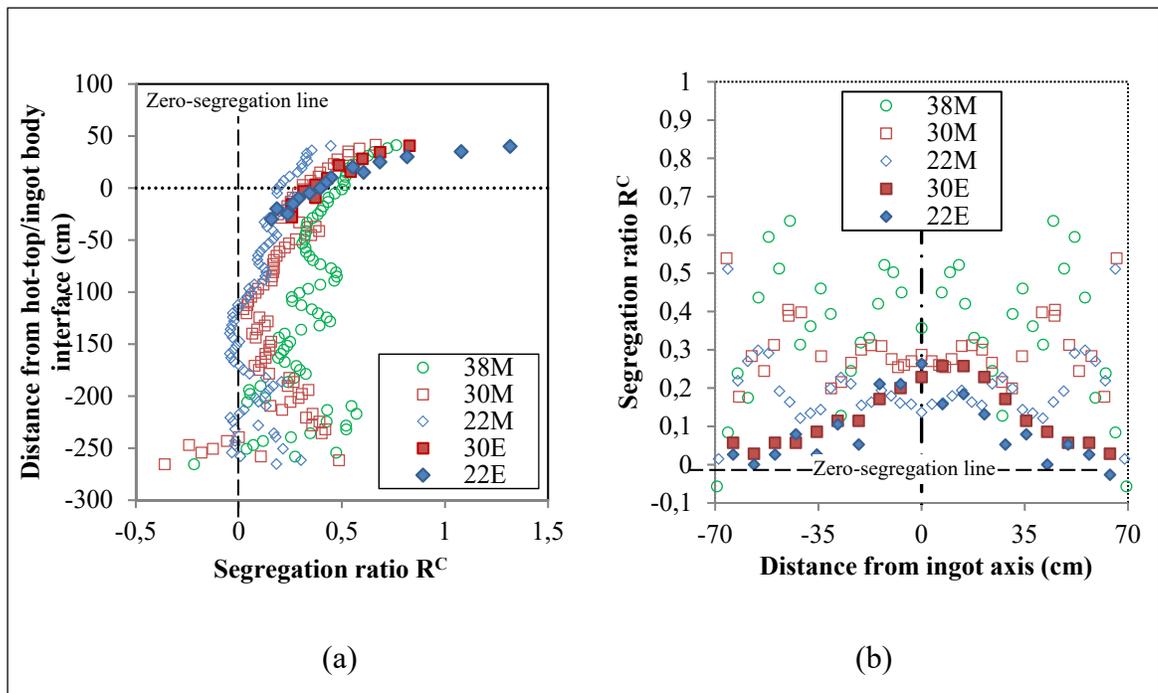
Figure 6.2 Evolution of macrosegregation ratio of carbon at the end of solidification. (a) Along the ingot centerline (b) Along the cutting section with 30cm below the hot-top/ingot body interface.

The final carbon segregation ratio profiles along the ingot centerline are compared among the three cases in Figure 6.2a, where the y-axis was set to be the distance from the hot-top/ingot body interface. In the figure, it can be seen that with increasing filling rate, the centerline segregation ratio profiles moved closer to the zero-segregation ratio line. Quantitative examination indicated that the axial carbon segregation ratio intensity in 38M was 14.7 %

and 25.7 %, in average, greater than that in 30M and 22M, respectively. The horizontal carbon segregation ratio variations were also examined along the section located at 30 cm below the hot-top/ingot body separation interface and the results are reported in Figure 6.2b. It can be seen that similar to the vertical case, the segregation severity decreased with the increase in the filling rate. In addition, the segregation ratio inside the mid-radius positively segregated bands in 38M was found to be, largely, 10.5 % and 22.7 % greater than that in 30M and 22M.

In Figures 6.2 and 6.3, comparisons are made between the carbon segregation profiles obtained from simulation and experimental measurements. In the case of 30 minutes pouring time, the predicted carbon segregation intensity in the mid-radius region is relatively greater than the measured ones (Figures 6.2b, 6.3a and b), with an exception of the region located at the top center of the hot-top. For the 22 minutes pouring time condition, the segregation intensity in regions other than the top center of the hot-top are very similar (Figures 6.3c and d). Furthermore, the experimental results show that segregation severity in the top center of the hot-top increased with reducing the pouring time (i.e. increased filling rate), which is in contrast to the predictions, as shown in Figures 6.2a and 6.3. The above observations are in agreement with the findings of Lesoult (Lesoult, 2005), who reported that neglecting the sedimentation of free equiaxed grains and solid fragments could result in underestimation of the positive segregation intensity at the top of the ingot and overestimation of the solutes concentrations at the bottom of the ingot.
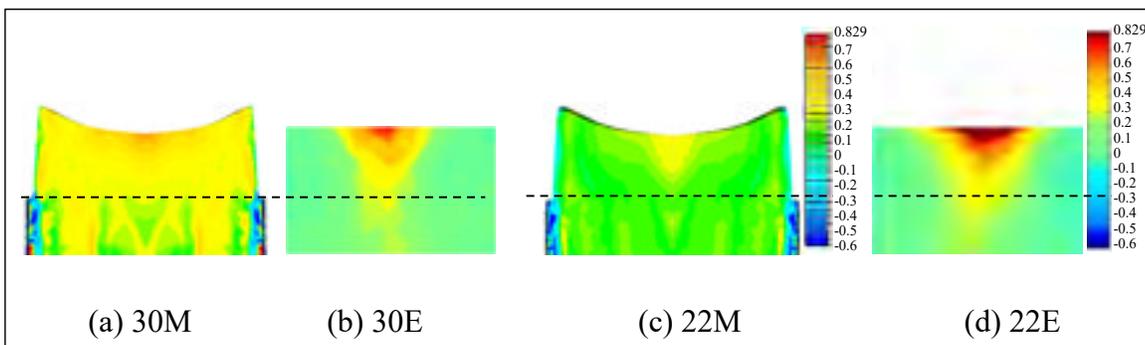
Figure 6.3 Segregation ratio patterns of carbon on the axial surface of longitudinal section of 30M, 22M and 30E, 22E. (a, c) Model prediction (b, d) Mass spectrometer measurements and macrostructures.

The relatively higher positive segregation in the regions between the center and the mold wall predicted by simulation could be related to the sensitivity of the measurement method. Indeed, the mass spectrometer results are a compilation of over 250 measurements on 4.5×6.5 cm^2 small samples; such dense sampling provided an acceptable accuracy of the provided values. However, despite the above fact, the measured sampling points were probably not sufficient for inspection of finer segregation structures. To validate such possibility, new experimental measurements with a sampling density of 0.9×0.9 cm^2 were carried out and illustrative examples are shown in Figure 6.4. It can be seen that the segregation intensity inside the solute-rich bands decreased by 17.2 % in average with the increase of the filling rate from 0.107 m/min (30E) to 0.145 m/min (22E). This finding confirms the above-mentioned predictions of the alleviation of segregation inside the positively segregated bands with the higher filling rate.
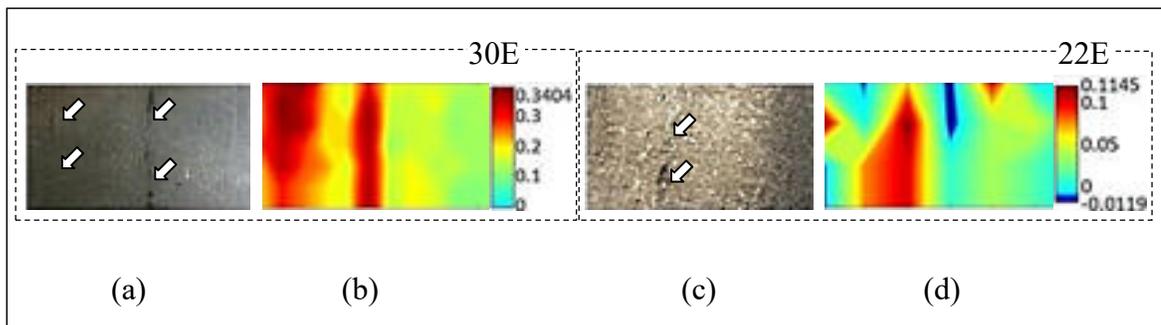
Figure 6.4 Macrographs around positive segregated bands on the longitudinal section at 30 cm below the hot-top/ingot body interface and the corresponding segregation ratio patterns of carbon. (a, c) Macrograph with black solute-enriched bands (pointed by arrows) (b, d) Mass spectroscopy measurements of the carbon segregation ratio pattern with sampling density of 0.9×0.9 cm^2.

Based on the above results, it can be said that higher filling rates generate lower macrosegregation intensity in the ingot body, in the centerline and in the mid-radius solute-enriched bands. This finding is of importance from a practical point of view for reducing the extent of macrosegregation in large size ingots. This also indicates that the solidification process of the ingot body induced by different filling rate plays a key role on the compositional variations, as will be discussed in the following sections.

6.4.2 Liquid movement

As reported in Figure 6.5, different filling rates created varied liquid movement during the casting processes. In the course of mold filling, as seen in Figures 6.5a, f, and k, higher filling rate led to higher rising velocity of the liquid level in the mold cavity. The ingot axial up-flow, the melt surface lateral flow toward the mold wall, and the clockwise vortex on the melt surface took place for all three cases. Such features have been reported to be due to the combined effect of the pouring jet, the inertia effect of the residual flow, and its impact on the mold wall (Zhang, Bao et Wang, 2016). However, in the present study, higher filling rate decreased the size of the melt surface vortex, pushed the vortex towards the outer radius, and created farther descending fluid flow along the melt front. Particularly, under the highest filling rate condition (i.e. 22M), the incoming melt from the center impinged on the lateral flow from the impact action of the mold wall, creating a hump on the molten steel surface (Figure 6.5k). The varied liquid flow features indicate larger momentum produced by higher filling rate. This predicted higher kinetic energy in the bulk liquid with increased filling rate agrees with the reported results based on Reynolds number calculation (Zhang et al., 2018). Higher fluid instability, as reported by Campbell (Campbell, 2011), is not convenient for the formation of first particles. Thus, fewer segregated particles formed in smaller area at the end of filling operation in the case of higher filling rate, as observed in Figures 1a, e and i, should originate from the higher instability in the bulk liquid.

At the end of filling operation, as seen in Figures 6.5b, g and l, all the above-mentioned features were still present for the three conditions. In addition, the centerline up-flow stream began to branch from the ingot axis, taking on an open umbrella shape. Higher filling rate went along with larger deviation angle, passing from 15º for 38M to 30º for 30M, and then 45º for 22M. Given that the up-flow branching commenced when the bulk liquid touched the top-laid board, this axial flow deviation should be due to the impact of the up-flow liquid on the top board. The increase of the deviation angle for the higher filling rate case should arise from the higher kinetic energy and the resultant stronger impact force of the pouring jet to the mold top. Examination of the simulation results in Figures 6.5b, g and l showed that the fluid

streams deviated laterally only in the ingot body and forced the superheated fluid to flow more strongly towards the mold wall, affecting the radial thermal gradient in the ingot body.
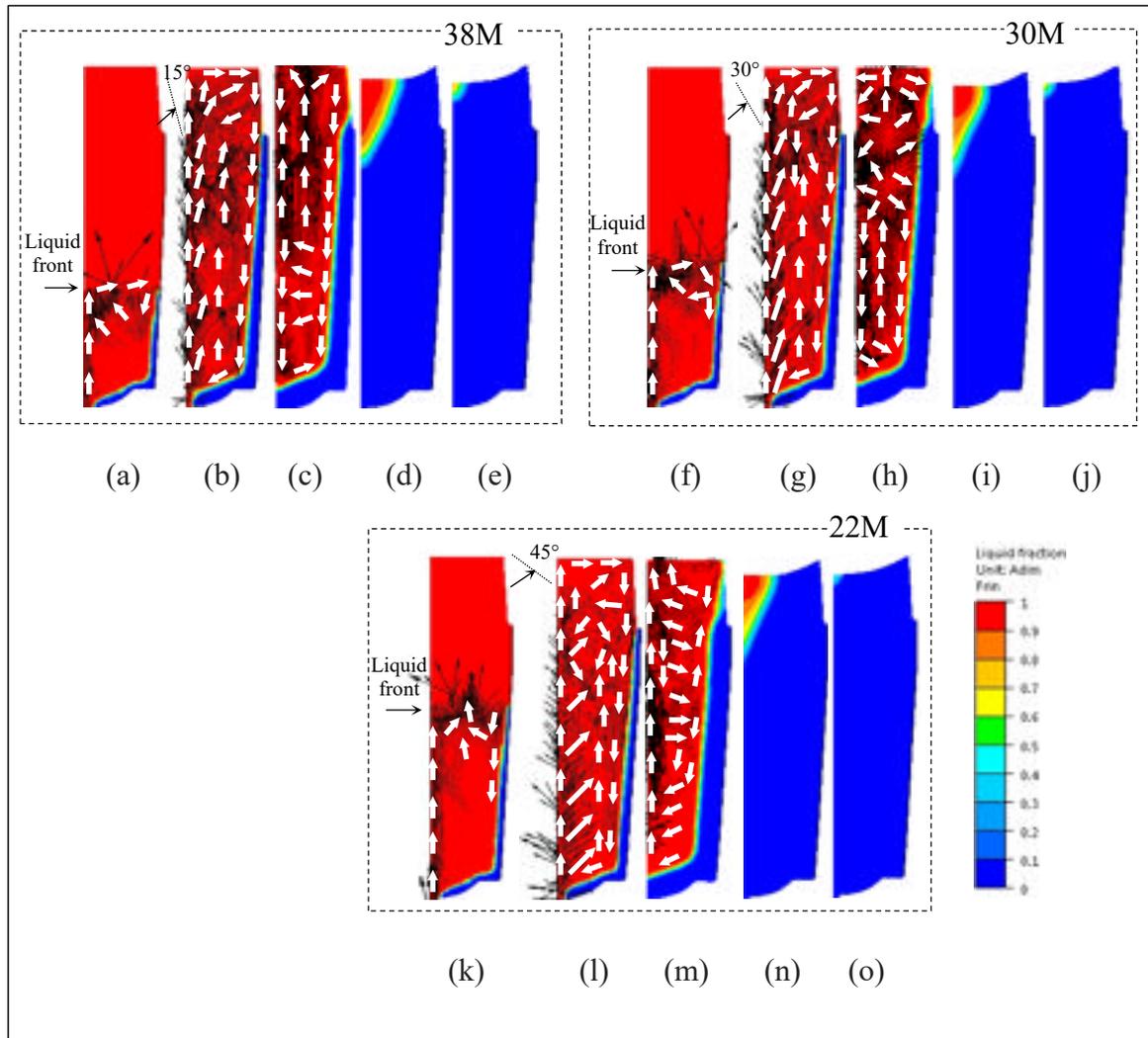
Figure 6.5 Liquid fraction patterns combined with velocity vectors predicted by 38M, 30M and 22M. (a, f, h) 12 min after pouring (b, g, l) End of filling (c, h, m) 1.5 h (d, i, n) 10.5 h (e, j, o) 14.5 h after pouring.

At 1.5h, Figures 6.5c, h and m, a clear difference can be seen between the three studied cases. At the lowest filling rate (38M, Figure 6.5c), slight trails of clockwise vortex in the hot-top and the disappearance of the deviated streams in the ingot body suggests the reduction and diminution in the residual flow. A downward flow was remarked, moving from

the upper hot region to the bottom cold zone along the centerline in the lower part of the ingot, demonstrating the development of thermal convection, as reported by Yadav et al. (Yadav et al., 2009). Furthermore, lateral streams from the periphery (denser region) to the center (less dense region) was observed in the lower part of the ingot body, which could be related to the development of solutal convection under the action of density gradient, as reported by Zhang et al. (Zhang, Bao et Wang, 2016). All the above features indicate the dominance of natural convection as the main heat transfer mode for the 38M condition. At the intermediate filling rate of 30M, Fig. 5h, clockwise flows were present in the hot-top and in the middle part of the ingot, indicating that the residual flow was still active. A strong stream moved downwards along the ingot axis, displaying the trails of thermal convection. A large counterclockwise vortex formed in the region around the hot-top/ingot body interface, which could be caused by the counteraction with the thermal convection from the center hot region to the cold mold zone (Yadav et al., 2009). Such characteristics of the 30M condition are indicative of a sort of transition state from the residual to thermal dominant flow. At the highest filling rate (22M, Figure 6.5m), important axial up-flow, strong lateral deviated streams in the ingot body, and large clockwise movement in the hot-top are all still observed, which correspond to the features of a strong residual flow. The above features in the liquid movement indicate that higher filling rate gave rise to preponderance of residual flow over longer times and the delayed occurrence of thermal and then solutal convections in the early stages of the solidification process.

On the basis of the above findings, it could be said that the significant difference in solutal distributions in the early solidification stage, as shown in Figures 6.1b, g and l, should result from the varied liquid movement created by different filling rates. The decrease of the centerline solutal gradient in higher filling rate case is probably due to the larger deviation from the centerline up-flow stream, which weakened the solutal accumulation along the ingot axis. The stronger residual flow, its longer dominant time and the delayed development of thermosolutal convection could be identified as the root causes of the smaller solutal gradient. In agreement with the findings of Qian et al. (Qian et al, 2015), the less ordered down-stream movement of the liquid metal along the solidification front next to the mold wall is the main cause for the less severe segregation in the mid-radius band in the smaller

filling rate case, as shown in Figures 6.1 and 6.2b. This stream would pass through the lower liquid fraction (small-f_l), remelt and consequently channel the mushy zone, thereby influencing the mass transfer and the formation of the positive segregated bands close to the chill zone.

6.4.3   Solidification speed

Further examination of Figure 6.5 revealed that the solidification speed was affected by mold filling rate. From Figures 6.5a, f and k, it can be seen that for all the three cases, solidification took place at the mold bottom corner before the end of pouring stage. Then, the solid skin grew inward and upward due to the rapid extraction of the initial superheat from the cold mold wall. However, it was noted that the solid shell heights next to the mold wall increased with the increase of filling rate. This could be due to the larger liquid level rising velocity, which brought hot melt in contact with the larger cold inner surface of the mold in a given time, and ultimately led to the formation of a higher solid shell.

In addition, a comparison among Figures 6.5b, g and l revealed that increasing the filling rate resulted in the formation of a thinner solid layer along the cold wall at the end of the filling process. The solid shell thicknesses next to the mold wall had an average value of 1.7, 1.6 and 1.5 cm for 38M, 30M and 22M, and occupied about 7.5 %, 7 % and 6.5 % of the total mass, respectively. This finding is in agreement with those reported by Im et al. (Im, Kim et Lee, 2001), who pointed out the association of higher residual flow with the decrease of the local solidification rate during the initial stages of solidification. This delay in solidification could be related to the continuous supply of hot molten steel to the wall side due to the longer action of lateral residual flow after filling. It must be noted that no solid layers formed in the hot-top for all the studied cases. This can be related to the insulation of the side refractory tiles laid inside the mold.

However, it was found that the solidification rate increased with the filling rate after the initial step of the solidification process. For instance, at 1.5 h after pouring (see Figures 6.5c, h and m), the solid shell in the hot-top grew shorter (i.e. larger liquid fraction) in 38M than in

30M and 22M. Furthermore, after 10.5 h, when the ingot solidification was very advanced, as seen in Figures 6.5d, i and n, the largest liquid fraction and deepest liquid pool (largest red area) were found in the smallest filling rate case (i.e. 38M). After 14.5 h, when the solidification was almost complete, as seen in Figures 6.5e, j and o, solidification advanced farther in 22M.

Analysis of the total solidification time confirmed the acceleration tendency of the solidification process under higher filling rate condition. It was predicted that it took 15 h 21 min (55312 s) for 38M to complete the solidification, as shown in Figure 6.6. This time was 14min longer than 30M (54428 s) and 26min than 22M (53735 s). In a previous report, the authors, based on experimental measurements, showed that the secondary dendritic spacing decreased with increasing filling rate (Zhang et al., 2018); thereby, confirming the predicted tendency of the decrease of the solidification time with the increase of filling rate.
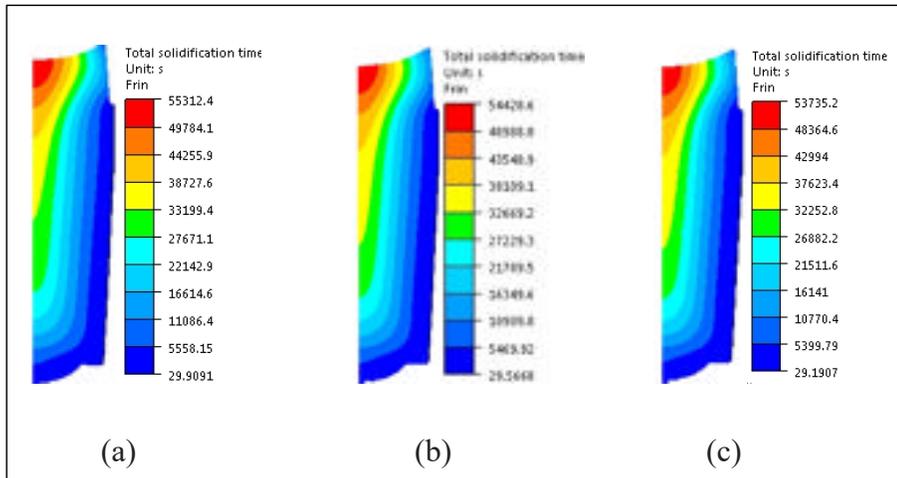
Figure 6.6 Predicted solidification time. (a) 38M (b) 30M (c) 22M.

The increase in the solidification process for increased filling rates could be interpreted in terms of the casting volume evolution. To carry out the analysis of the variation of the casting volume, four specific locations on the casting surface were monitored for the three cases, as illustrated on the upper right corner of Figure 6.7a: Point 1 (at the ingot bottom skin,

in blue), Point2 (at the hot-top/ingot junction skin, in green), and Point3 (at the top skin of hot-top, in red) were checked for radial contraction (air gap formation). Finally, Point 4 (at the top center of the hot-top, in black) was monitored for the vertical shrinkage.
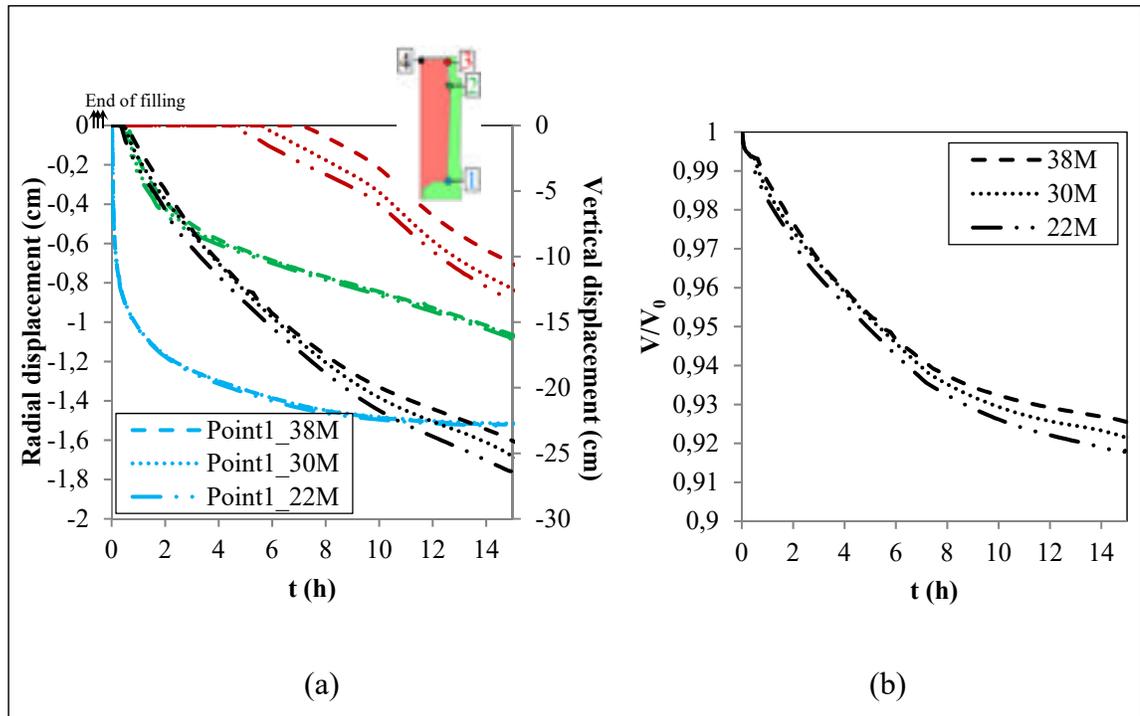
Figure 6.7 Time-dependent displacements of ingot surface and volume change. (a) Time-dependent displacement of Points 1-4 in the radial and axial directions (b) Time-dependent of instantaneous volume to the initial volume of the castings.

As seen in Figure 6.7a, on Point1, no difference on the radial contraction was observed for the three case studies, which could be due to the negligible difference on the arrival time of hot melt from one case to another. On Point2, the growth rate of the radial air gap for 22M was the least in the first 4 hours, and then it came to coincide with the other two cases. The lag in the air gap development in higher filling rate case in the first hours could be correlated with the stronger lateral residual flow and its longer dominance time. On Point3, higher filling rate advanced the initiation of the radial air gap. The advance tendency was maintained till the completion of the solidification. In the end, the lateral contraction on Point3 reached 0.7, 0.8 and 0.9 cm for 38M, 30M and 22M, respectively. On Point4, higher filling rate led to earlier start of the top contraction and larger extent of contraction. At the

end of solidification, the vertical top contractions on Point4 reached 24.3, 25.2 and 26.3 cm for 38M, 30M and 22M, respectively. This increased depth of shrinkage cavity with increasing filling rate was in agreement with the findings of Zhang and Bao in a recent publication (Zhang, Bao et Wang, 2016).

Based on the analyses of radial and axial shrinkage on the casting surface, it can be said that higher filling rate brought about a larger decrease in the casting volume. The final casting volume for 38M reached 92.5 % of the total mold vacant volume, while it was 92.1 % and 91.7 % for 30M and 22M, respectively, as plotted in Figure 6.7b. Thus, the acceleration in the solidification process in the higher filling rate case has probably its origin in a larger volume contraction. Therefore, the more rapid solidification process and thus less available time for solutal diffusion should be another source for the weaker accumulation of solutes and less severe segregation intensity.

6.4.4 Temperature field

The global temperature fields predicted by the three simulations are shown in Figure 6.8. At the end of filling, as displayed in Figures 6.8a, d and g, more liquid (the red regions above the 1550 ºC isotherm) was left for the higher filling rate condition (i.e. 30M and 22M). This finding further confirms the effect of smaller superheat dissipation rate due to stronger residual flow in higher filling rate case in the first hours. The slower superheat extraction under higher filling rate condition resulted in slightly thinner temperature gradient regions next to the mold chill wall and the base.

Further analysis of Figure 6.8 indicated that independent of filling rate, the horizontal isotherms tended to incline more and more as the solidification proceeded, and the spacing between the adjacent isotherms widened. However, in the intermediate stage of solidification (Figures 6.8b, e and h), the temperature regions next to the hot-top wall, enclosed by isotherms of 1450 and 1350 °C, was wider at higher filling rate (i.e. smaller temperature gradient). After 10.5h, in Figures 6.8c, f and i, the 1350 °C isotherm in 22M moved farther

away from the isotherm 1250 °C, which is next to the wall side, indicating smaller temperature gradient under higher filling rate conditions.
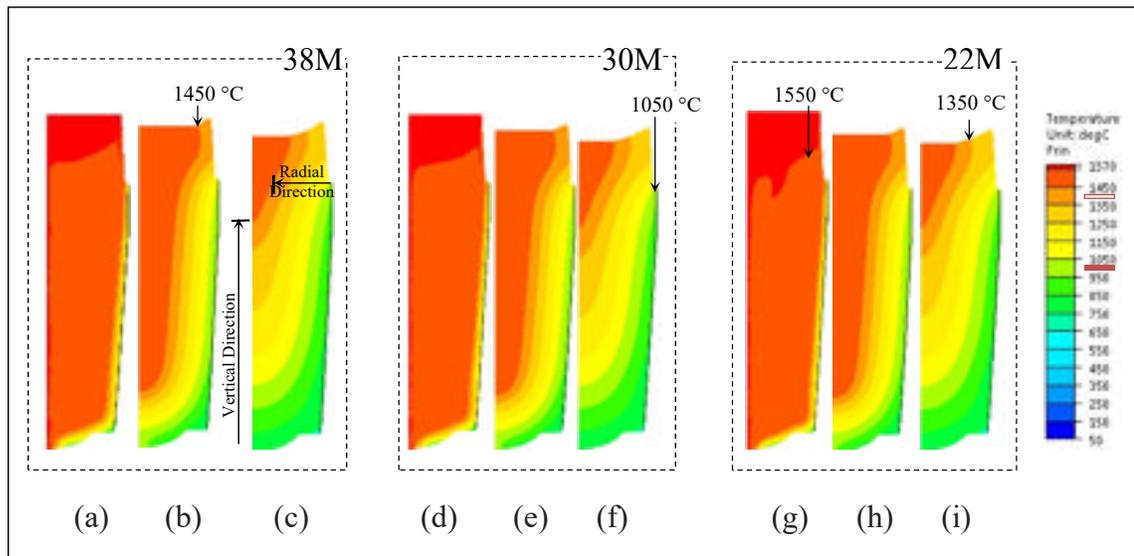
Figure 6.8 Temperature fields predicted by 38M (left group), 30M (middle group) and 22M (right group). (a, d, g) End of filling (b, e, h) 5.5h (c, f, i) 10.5h after pouring.

Figure 6.9 shows a comparative analysis of the influence of filling rate on the evolution of temperature gradient in the ingot. Time dependent movement of isotherms 1450 °C and 1050 °C, which are of practical importance in the large size ingot casting process, were examined on two different locations: in the radial direction, along the hot-top/ingot body interface section, and in the vertical direction, along the ingot axis. The two investigated isotherms are identified in Figure 6.8.

In the radial direction (Figure 6.9a), under higher filling rate condition, the two isotherms were found to be closer to the ingot axis, indicating more significant radial growth of the solidified shell, confirming the above-mentioned solidification acceleration phenomenon. It can also be seen that for the highest filling rate (22M), the radial distance between the two investigated isotherms kept larger, and the tendency became more remarkable in the later solidification stages. This larger distance between fixed isotherms indicates that smaller

thermal gradient is expected to be produced when higher mold filling rates are used. The vertical displacement of the same two isotherms, in Figure 6.9b, further supports the findings that smaller temperature gradient are produced for higher filling rate conditions, particularly in the later solidification phase. Similar findings on the decrease of thermal gradient at higher filling rates have been reported by Aboutalebi (Aboutalebi, 1994) and more recently by Wang et al. (Wang et al., 2007; Wang, Yang et Tang, 2008). However, they are different from those of Prescotte and Incropera (Prescott and F.P. Incropera, 1995) who did not observe a noticeable change on vertical thermal gradient when inlet pouring conditions were changed. The difference could be due to the fact that contributions from thermomechanical deformation were not considered in their study. It must be noted that the smaller temperature gradient in the case with higher filling rate can also contribute to reduced solute segregation in the casting body of the ingot, as observed in Figures 6.1 and 6.2. The lower temperature gradient occurred concomitantly with decreased density gradient, and hence delayed the development of solutal convection, inhibiting the solutal distribution in the solidification process, in agreement with reports from other works (C. Zhang et al., 2018; Zhang et al., 2018; Vives et Perry, 1986; Hachani et al., 2012; Liu, Liu et Kang, 2008).

6.5   Conclusions

In the present work, the effect of filling rate on macrosegregation in large size steel ingots was investigated using FE modeling and experimental validation. A thermomechanic model, considering both convection and solidification shrinkage, was developed. The entire filling and casting processes of three ingots with different filling rates were simulated. The evolution of macrosegregation patterns, as well as the associated phenomena, including the evolution of the fluid flow, solidification speed, and temperature gradient, was analyzed. The findings of the study, as summarized below, are expected to contribute to a better understanding of the macrosegregation formation mechanism in ingot casting process of high strength steels:
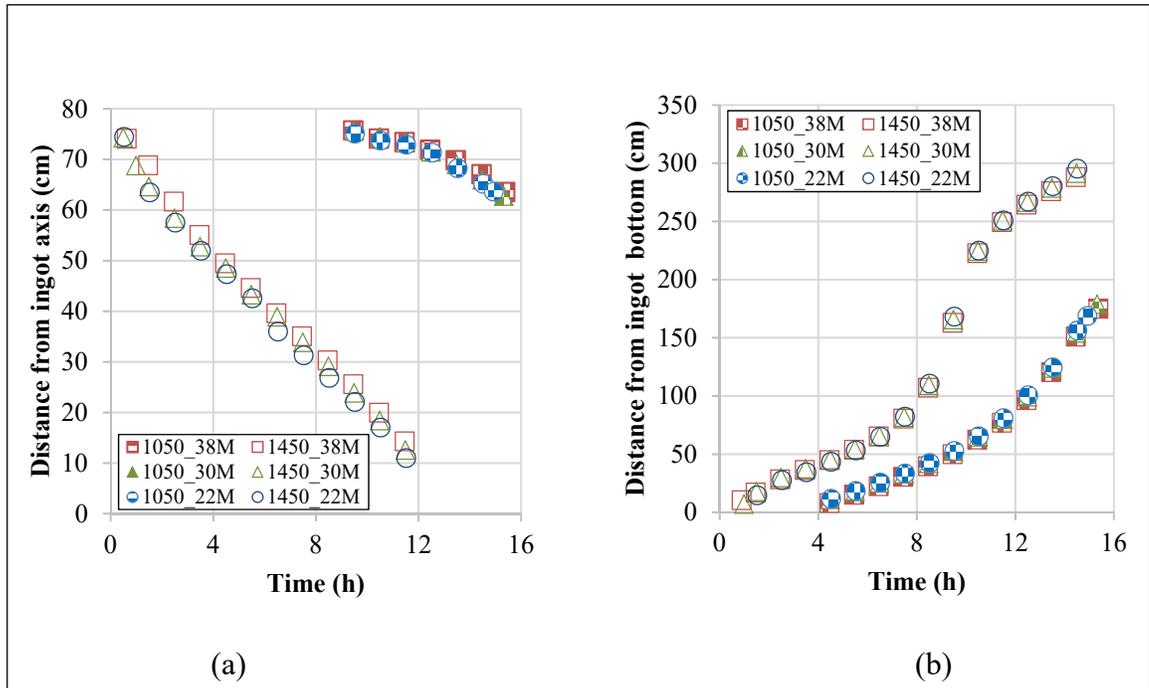
Figure 6.9 Time-dependent displacement of isotherms 1450 °C and 1050 °C during the casting process predicted by 38M, 30M and 22M. (a) In the radial direction (b) In the vertical direction.

Higher filling rate helps to decrease the segregation severity in the upper section of the ingot body, along the centerline, and in the region between the ingot centerline and the mold wall.

A good agreement was obtained between the model predictions and experimental results, demonstrating the validity of the developed model and its application for other casting conditions.

The lower intensity of the segregation in the ingot with higher filling rate could be attributed to three sources:

1) the accelerated solidification process;

2) the decreased temperature gradient;

3) the more instable liquid movement: the increased fluid flow instability in the filling process, the prolonged action of the residual (particularly the lateral flow) and the delayed development of thermosolutal convection.

All these findings could be used in industry, to improve the quality of large-size ingot production made of high value-added steels, or other alloys which are prone to macrosegregation.

6.6　Acknowledgements

ARTICLE 5 SIMULATION AND EXPERIMENTAL VALIDATION OF THE EFFECT OF SUPERHEAT ON MACROSEGREGATION IN LARGE-SIZE STEEL INGOTS

Chunping Zhang[1,✉], Mohammad Jahazi[1], Rami Tremblay[2]

[1]Department of Mechanical Engineering, École de technologie supérieur, 1100 Notre-Dame Street West, Montreal, Quebec H3C 1K3, Canada
[2] Finkl Steel-Sorel, 100 McCarthy Street, Saint-Joseph-de-Sorel, Quebec J3R 3M8, Canada

7.1   Abstract

A 3D model was employed to study the effect of melt initial superheat on the macrosegregation formation using FE modeling and experimentation methods. The casting process of three ingots with the initial melt superheats of 75 °C, 65 °C and 55 °C were simulated. The three cases represented three variables encountered in industry during casting of large size ingots. For the above three studied cases, all other casting conditions were kept the same. Results showed that the variation of initial melt superheat gave rise to changes in temperature pattern, liquid flow field, solidification speed, and thermomechanical contraction. Under the combined actions of all these changes, lower superheat tended to alleviate the segregation intensity in the upper part of the ingot body, in the hot-top, and in the solute-rich bands between the ingot centerline and periphery. The beneficial effect of lower superheat on alleviation of segregation severity was confirmed by experimental chemical measurement results. The results were analyzed in terms of heat and mass transfer theories and allow for a better understanding of the underlying mechanisms responsible for the occurrence of macrosegregation in ingot casting process. The findings should be helpful for the casting process design of a given ingot of high value-added steels or other alloys.

Keywords: Finite Element modeling, large-size ingot, steel, superheat, macrosegregation

7.2   Introduction

During casting in industry, non-equilibrium conditions prevail, resulting in chemical heterogeneities on the scale of the entire ingot and the formation of so-called macrosegregation (Pickering, 2013). Macrosegregation of solutes is one of the most significant casting defects in large size ingots (Becker et Shipley, 2002), as it is difficult to alleviate and completely remove using any subsequent practical heat treatment and mechanical process (Loucif et al., 2018; Scarabello, Ghiotti et Bruschi, 2013).

In order to achieve high quality large-size cast ingots, a better understanding of the influence of chemical composition and process parameters is needed in order to be able to take measures for minimizing the extent and intensity of macrosegregation. The measures commonly taken include control of chemical compositions (reduction of Mn and Si contents) (Suzuki et Taniguchi, 1981), improvement in mold geometry (Dub et al., 2014; Lesoult, 2005), optimisation of casting process (control of melt temperature, mold preheating temperature, filling rate) (Pikkarainen et al., 2016; Zhang et al., 2018), employment of engineering solution (intensive rapid cooling, mechanical vibration and electromagnetic stirring) (Galkin et al., 2013; Zhang, Cui et lu, 2003), and application of multipouring technique (sequential pouring of molten steel from multiple ladles with different concentrations of alloying elements) (Tu, shen et Liu, 2015). Among the above strategies, superheat control is one of the simplest methods to implement. Superheat is excess of the casting temperature above the liquidus (Campbell, 2011). Despite numerous studies on the impact of superheat on macrosegregation, the function of superheat is, however, still unclear or even controversial, and far from conclusive.

Liu et al. numerically studied the formation mechanism of macrosegregation in a 3.3 t steel ingot and ascribed the reduced height of bottom negative segregation cone with higher superheat to the variations of flow field (Liu et al., 2011). Pikkarainen et al. investigated the continuous casting of low-alloyed steel, and found that a higher superheat caused smaller segregation in the central fine equiaxed dendritic structures, while a low superheat brought about negative segregation due to sedimentation of globulites and higher segregation in the central coarse globular structures (Pikkarainen, et al., 2016). Zhong et al. studied the

permanent mold casting of a ferrite-based alloy, and pointed out that with superheat increasing, coarser equiaxed dendritic grains formed and secondary dendritic arm spacing increased, but carbon segregation became less intense (Zhong et al., 2012). EI-Bealy and Hammouda modeled the solidification of Al-Cu ingots, and reported that with increasing superheat, the magnitude of convection velocities increased, the grain size of equiaxed crystals decreased and macrosegregation decreased (EI-Bealy et Hammouda, 2007).

In contrast, Mäkinen and Uoti declared that low superheat favored an equiaxed structure, which can minimize the severity of centerline macrosegregation in continuous casting of low-alloyed copper billets (Mäkinen et Uoti, 2006). Sun et al. reported that a lower melt superheat and a higher nucleation density decreased the severity of macrosegregation by weakening the flotation of grains (Sun et al., 2016). Guan et al. demonstrated that V-shaped segregation decreased with decreasing superheat in continuous casting blooms (Guan et al., 2018). Choudhary and Ganguly observed that low superheat favored the surviving of equiaxed crystals, which ejected solutes uniformly within the mushy zone, resulting in a reduction in segregation (Choudhary et Ganguly, 2007). Yadav et al. simulated the filling and solidification process of side-cooled Pb-Sn alloy, and pointed out that when superheat was low, considerable amount of solidification occurred during filling of the cavity, causing some positive segregation near the wall, and then negative segregation subsequently formed due to the slowing-down of the solidification rate resulting from the continuous supply of hotter melt by convection (Yadav et al., 2009). Eskin et al. performed experimental and numerical investigations of the direct-chill (DC) casting of an Al-Cu alloy, and observed coarsened structure, increased probability of bleed-outs, increased severity of subsurface segregation, and unaffected macrosegregation in the rest of the billet with increased casting temperature (Eskin, Savran et Katgerman, 2005).

Based on the above conflicting findings on the effect of melt superheat on macrosegregation, we are urged to turn to experimental and simulation investigations for an answer. The objective of the present study is to investigate the impact of melt initial superheat on macrosegregation in a production scale ingot (40 metric ton (MT)) of a low-alloy high strength steel. A 3D two phase (liquid-solid) multiscale thermomechanical solidification

model was used and the simulations were performed in the finite element code Thercast® (TherCast 8.2®, 2012). The mold filling and solidification processes of 3 ingots with different melt superheats were simulated. The evolution of solute transport as well as its associated phenomena throughout the filling and cooling stages, including the bulk liquid flows, the thermal/solutal convection and the thermomechanical deformation of the phases were all investigated. The dimensional tolerance and surface finish, however, were not examined due to their less importance compared to the global macrosegregation profile for the quality of the ingot and also due to the later performance of reheating and forging on the as-cast ingot in industry. The predictions were compared with the chemical measurements on two experimentally obtained 40 MT steel as-cast ingots. The findings will contribute to a better understanding of the macrosegregation formation mechanisms in ingot casting process. They could also be used in industry to improve the quality of large-sized ingot production and the productivity of high value-added steels or other alloys, which are prone to macrosegregation.

7.3   Model establishment and experimental process

The used model is a casting system, as shown in Figure 7.1a, composed of a cylindrical ingot (250 cm in height and 150 cm in average diameter) in big-end-up cast iron mold with an above hot-top 70cm in height. The hot-top part is lined inside with insulating refractory tiles, and an exothermic refractory board is laid above on the melt top. 3D linear tetrahedral elements, with an average grid of 35 mm, were used for the spatial discretization of the part and mold components.

The chemical composition of the steel in study is given in Table 5-1. For the simulations, the liquid steel is bottom poured into the mold at different temperatures with a filling time of 30 min. Three superheats of 75 °C (pouring melt temperature of 1570 °C), 65 °C (pouring melt temperature of 1560 °C) and 55 °C (pouring melt temperature of 1550 °C) were investigated. The three simulated superheat cases represented three variables encountered in industry for casting large-size ingots. The three simulated cases were identified, in the rest of this manuscript, as 75M (for superheat of 75 °C), 65M (for superheat of 65 °C), 55M (for superheat of 55 °C), reflecting their respective superheat.

The predicted carbon segregation ratio profiles were compared with the chemical measurements from two experimental obtained 40MT steel ingots. One is the 75E (cast at initial melt superheat of 75 °C, pouring melt temperature of 1570 °C), and the other is 62E (cast at the initial melt superheat of 62 ºC, pouring melt temperature of 1557 ºC). The compositional determination for the experimentally obtained ingots was conducted on 4.5 × 6.5 cm^2 small samples, using Thermo Scientific ARL$^{\mathrm{TM}}$ 4460 mass spectrometer. Segregation ratio of carbon (for both experiment measurements and simulation predictions) on each sampling, R_C, was determined based on the relation: $R^C = (\omega^C - \omega_0^C)/ \omega_0^C$, where ω^C is the local carbon concentration and ω_0^C is its nominal concentration value (Duan et al. 2016). A positive/negative R^C value corresponds to positive/negative segregation. For all the above simulated and experimentally obtained cases, all casting conditions were kept the same expect for initial melt superheat. The material parameters for the FE simulations were all from Zhang et al. (Zhang et al., 2018).

7.4   Results and discussions

7.4.1   Macrosegregation patterns and verification

Figure 7.1 reports the evolution of macrosegregation pattern of carbon in the casting process for the three initial superheat cases 75M, 65M and 55M. As featured in the figure, different initial melt superheat produced varied large-scale compositional distribution from the mold pouring moment till the end of solidification. At the end of the filling operation, as compared among Figures 7.1a, e and i, in the lowest superheat case (55M with 55 °C superheat), more first segregated particles (red and blue spots) formed in a larger region. As the solidification proceeded, as reported in Figures 7.1b, f and j, the weakest accumulation of solutes occurred in the lowest initial superheat case (i.e. 55M). This feature was reflected in the upper section of the ingot, in the hot-top and in the mid-radius solute-enriched bands. Such trend was maintained until the completion of solidification, as seen in the rest figures of Figure 7.1. The predicted smaller extent of segregation at lower superheat is in agreement with the findings reported by Mäkinen and Uoti (Mäkinen et Uoti, 2006), Sun et al. (Sun et al., 2016), as well as Choudhary and Ganguly (Ghoudhary et Granguly, 2007).
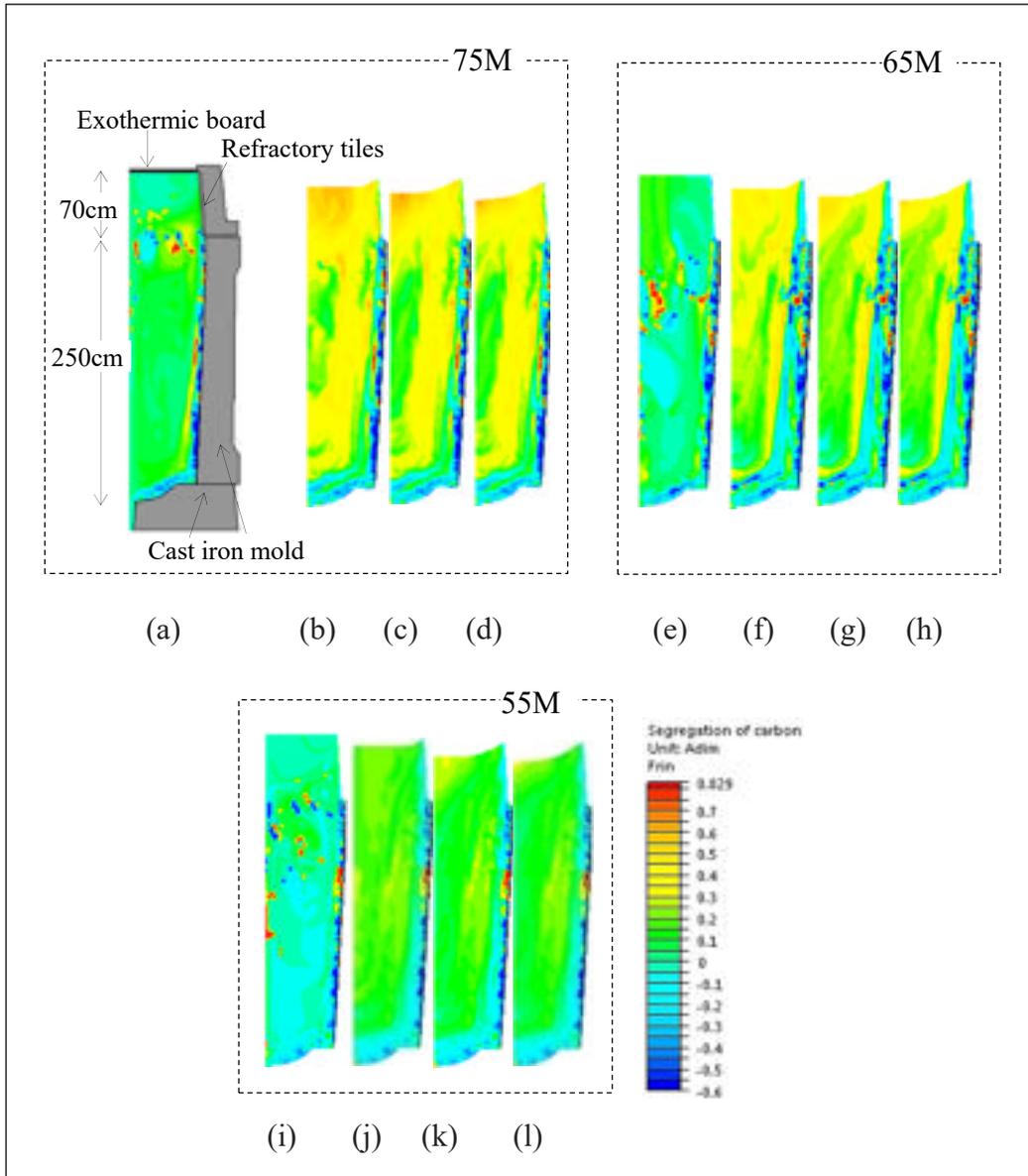
Figure 7.1 Segregation ratio patterns of carbon during the casting process predicted by 75M (upper left group), 65M (upper right group), and 55M (lower group). (a, e, i) 0.5 h (end of filling), (b, f, j) 5.5 h, (c, g, k) 10.5 h and (d, h, l) End of solidification.

The comparison among the three cases on the final segregation ratio profiles of carbon along the ingot central axis was plotted in Figure 7.2a. It can be seen that with the decrease of the superheat by 10 °C (from the case 75M to 65M, or from 65M to 55M), the segregation ratio intensity was generally alleviated by about 9 % in the upper half of the ingot body and in the

hot-top. Similar effect of lower superheat on alleviation of macrosegregation was also observed in the horizontal direction on the section located 30 cm below the hot-top/ingot body separation interface, as presented in Figure 7.2b. The segregation ratio intensity inside the mid-radius positive-segregated bands in 55M was found to be, in average, 10% and 20% lower than that in 65M and 75M, respectively.
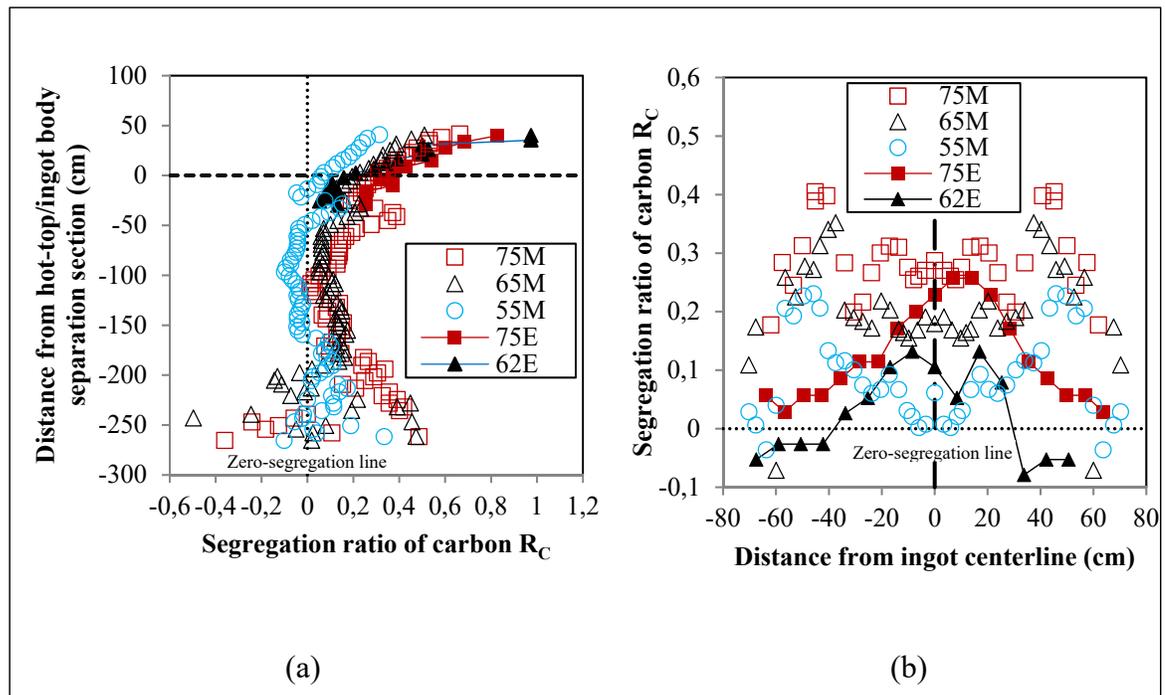
Figure 7.2 Predicted and measured segregation ratio profiles of carbon at the end of solidification. (a) In the vertical direction along the ingot centerline (b) In the horizontal direction along the section at 30cm below the hot-top/ingot body separation interface.

The carbon segregation profiles of experimentally cast ingots 75E (75 °C initial superheat) and 62E (62 °C initial superheat) were also reported in Figure 7.2. In Figure 7.2a, the centerline carbon segregation distribution curve from lower superheat case (i.e. 62E) was located closer to the zero-segregation line than that from 75E, demonstrating the decrease of the segregation intensity when initial melt superheat was decreased. Particularly, the measured centerline carbon profile from 62E lied between the predicted profile from 65M (under 65 °C superheat condition) and that from 55M (with 55 °C initial superheat), yet

closer to that from 65M. The above features were also remarked in the regions in the vicinity of the ingot axis in Figure 7.2b. The good agreement of the chemical predictions with the experimental measurements, in both vertical and radial directions, verified the beneficial effect of the decreasing initial superheat on the decrease of macrosegregation intensity.

Furthermore, in Figure 7.2a, the experimental results showed that the segregation intensity in the top center of the hot-top increased with lowering the melt superheat, which was in contrast to the simulation predictions. The above observations are in agreement with the findings of Lesoult (Lesoult, 2005), who reported the underestimation of positive segregation severity at the top of the ingot and the resulting overestimation of solutes concentrations at the bottom of the ingot due to the neglecting of the sedimentation of free equiaxed grains and solid fragments in modeling.
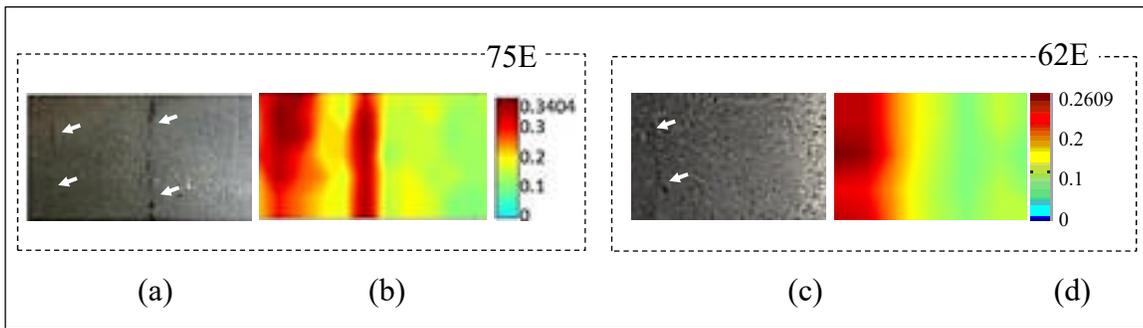
Figure 7.3 Characterizations in mid-radius position on the section 30 cm below the hot-top/ingot body interface for the experimentally obtained ingots 75E and 62E. (a, c) Macrograph with solute-rich black bands illustrated with white arrows, (b, d) Segregation ratio pattern of carbon measured using mass spectrometer with sampling density of 0.9×0.9 cm^2.

In addition, in Figure 7.2b, the measured positive segregation intensities in the regions between the ingot centerline and the periphery were lower than the predicted ones, which could be due to the measurement sampling method (a compilation of over 250 measurements on 4.5×6.5 cm^2 small samples). New experimental measurements with a sampling density of 0.9×0.9 cm^2 revealed an 8% decrease in segregation intensity inside the solute-rich bands with the decrease of the initial melt superheat from 75 °C (75E, as seen in Figures 7.3a and

b) to 62 °C (62E, Figures 7.3c and 3b). These experimental results confirmed the above-mentioned predictive reasonability that the segregation inside the mid-radius solute-rich bands was alleviated with the initial melt superheat decreased.

Based on the above results, it can be said that lower initial melt superheat helped to decrease the macrosegregation severity in the upper part of the ingot body, in the centerline and in the solute-enriched bands between the ingot centerline and surface. This finding indicates that the varied solidification behavior in the ingot induced by different initial superheat exerts a significant impact on the compositional distributions, as will be discussed in the following sections.

7.4.2   Temperature gradient

The predicted temperature fields at times of 0.5 h (end of filling), 5.5 h and 10.5 h after pouring are given in the left half of each pattern in Figure 7.4. At the end of the filling phase (Figures 7.4a, d and g), at the lowest initial melt temperature condition (55M), the 1550 °C isotherm became longer and more inclined towards the hot-top upper skin region and smaller liquid area (the red regions above the 1550 °C isotherm) was left. These features indicate that the acceleration of energy loss was induced by decreasing initial melt temperature, which could be resulted from the less thermal energy provided by the less hot melt.

In the intermediate and later solidification stages, as displayed in Figures 7.4b, c, e, f and compared with Figures 7.4h, i, the distances between adjacent isotherms, whether vertically or radially, tended to be larger under lower superheat condition. For instance, at 5.5h, in the case with smaller superheat, the 1450 °C isotherm moved farther away from the 1350 °C one next to the hot-top wall side, as compared among Figures 7.4b, e and h. Similar tendency was also observed at 10.5 h between 1350 °C and 1250 °C isotherms (Figures 7.4c, f and i). The above characteristics are indicative of the production of smaller temperature gradient when lowering initial melt temperature.
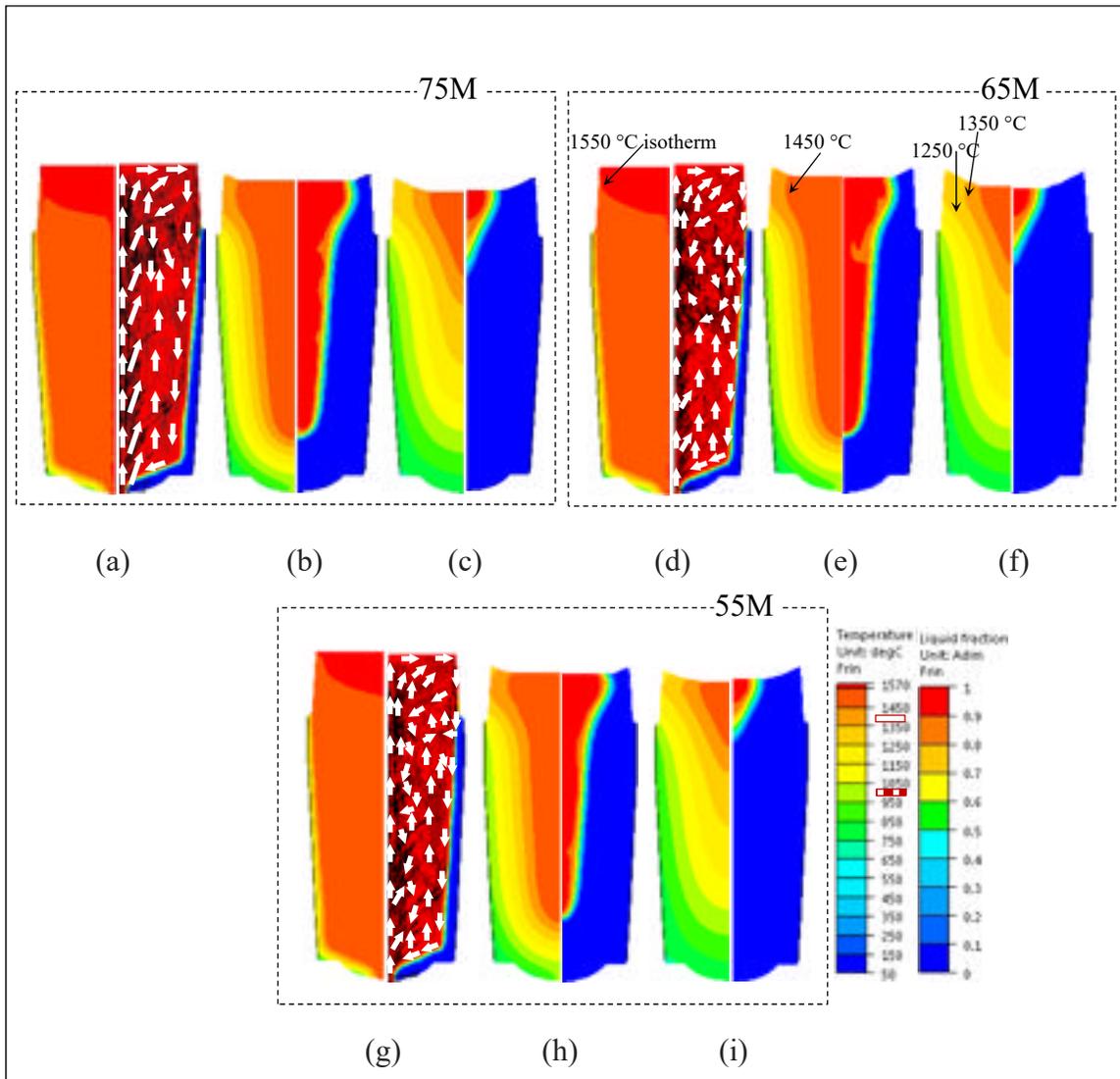
Figure 7.4 Temperature field (left figures) and liquid fraction patterns combined with velocity vectors (right figures) predicted by 75M, 65M and 55M. (a, d, g) 0.5 h (end of filling) (b, e, h) 5.5 h (c, f, i) 10.5 h after pouring.

Figure 7.5 plots the displacements of 1450 °C and 1050 °C isotherms (as identified in the Figure 7.4 color bar) as a function of time during the solidification process, for the three studied cases. It can be seen that for the lower superheat case, in the radial direction on the hot-top/ingot body separation section (Figure 7.5a), the two investigated isotherms were located closer to the ingot axis; in the vertical direction along the ingot centerline (Figure 7.5b), they lay farther from the ingot bottom. These observations confirmed the above-

mentioned acceleration of energy loss under lower superheat condition. Furthermore, it was noted that in the lowest superheat case (55M), the distance between the two examined isotherms, both radially and vertically, kept larger. Quantitative examination revealed that 10 °C superheat decrease brought about 2 cm enlargement in the two isothermal curves distance in the radial direction on the hot-top/ingot body separation section (Figure 7.6a) and about 3.2 cm broadening in the vertical direction along the ingot centerline (Figure 7.6b). The quantitative results evidenced the creation of smaller thermal gradient when lower initial melt temperatures were used.

The smaller temperature gradient in the case with lower initial melt superheat should be the root cause for their milder segregation in the steel casting, as observed in Figures 7.1 and 7.2. Based on the reports from others (zhang, Bao et Wang, 2016), smaller thermal gradient coexists with decreased density gradient, which leads to delayed development of solutal convection, inhibiting the accumulation of solutes in the solidification process.

(a)

(b)
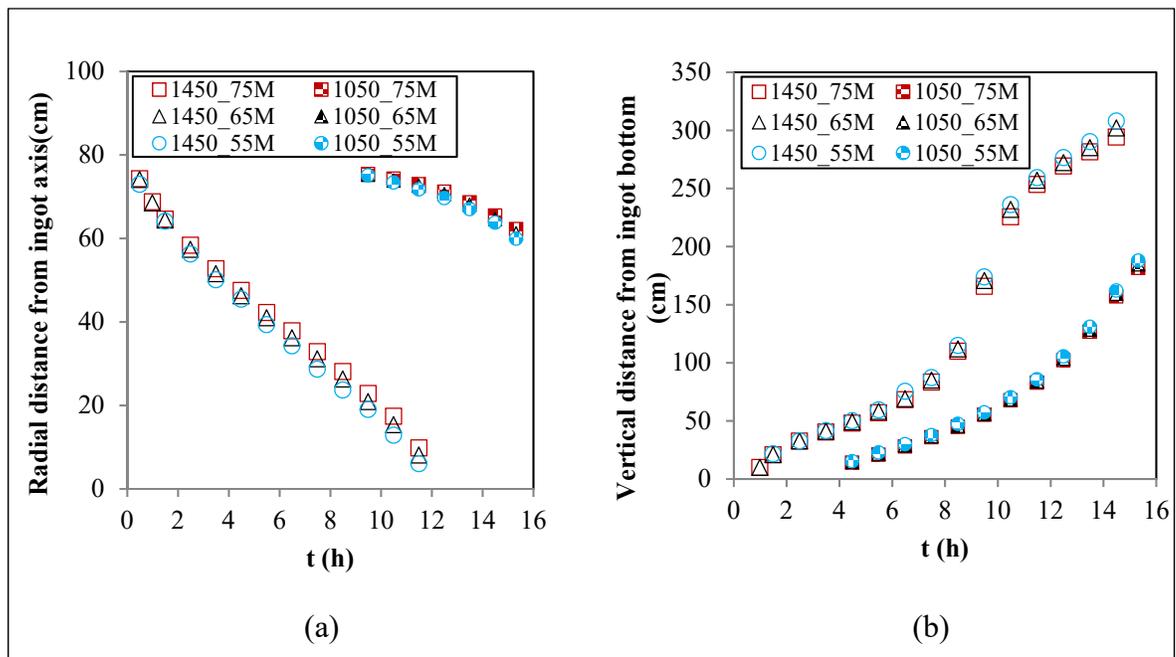
Figure 7.5 Movement of 1450 °C and 1050 °C isotherms with time. (a) In the radial direction (b) In the vertical direction.

7.4.3   Liquid flow and solidification speed

Liquid fraction field combined with velocity vectors were reported in the right half of the patterns in Figure 7.4. As seen in Figures 7.4a, d and g, clockwise and counterclockwise cells coexisted in the bulk liquid in the intermediate (65M) and lowest superheat cases (55M). These features were in contrast to 75M, in which only clockwise vortex existed in the upper part where the first solid particles started to form in the melt. More inversion of clockwise movement was observed inside the ingot body in lower superheat case, counteracting the orderly liquid bulk flow. The occurrence and multiplication of counterclockwise streams in the early solidification stage could arise from the earlier dominance of natural convection flow, induced by the earlier triggering and quicker development of radial temperature gradient in lower initial superheat cases, as observed and discussed in section 3.1. The greater destabilization of the bulk liquid flow could be the origin of first solid particles scattering in wider regions at the initial period of solidification in the simulations with lower superheat.

Further analyses on the liquid fraction evolution revealed that thicker solid shell was always observed next to the chill wall in the hot-top at lower superheat condition, as also reported by Yadav et al. (Yadav et al., 2009). In addition, at 10.5 h after pouring (Figures 7.4c, f and i), less liquid (red zone areas) was left in the calculations with smaller initial superheat. These features suggested that smaller initial melt superheat increased the solidification rate and quickened up the solidification process.

The solidification acceleration caused by the reduction of superheat was also revealed by the solidification time analysis results, as presented in Figure 7.7. It was predicted that smaller initial superheat advanced the completion of the solidification by a few seconds in the first solidified region at the bottom corner of the ingot. The predicted total solidification time for 55M (53103s with 55 °C as the initial melt superheat) was 11 min and 22 min, respectively, shorter than the time needed for 65M (53757 s with 65 °C as the initial superheat) and 75M (54428 s with 75 °C as the initial superheat).
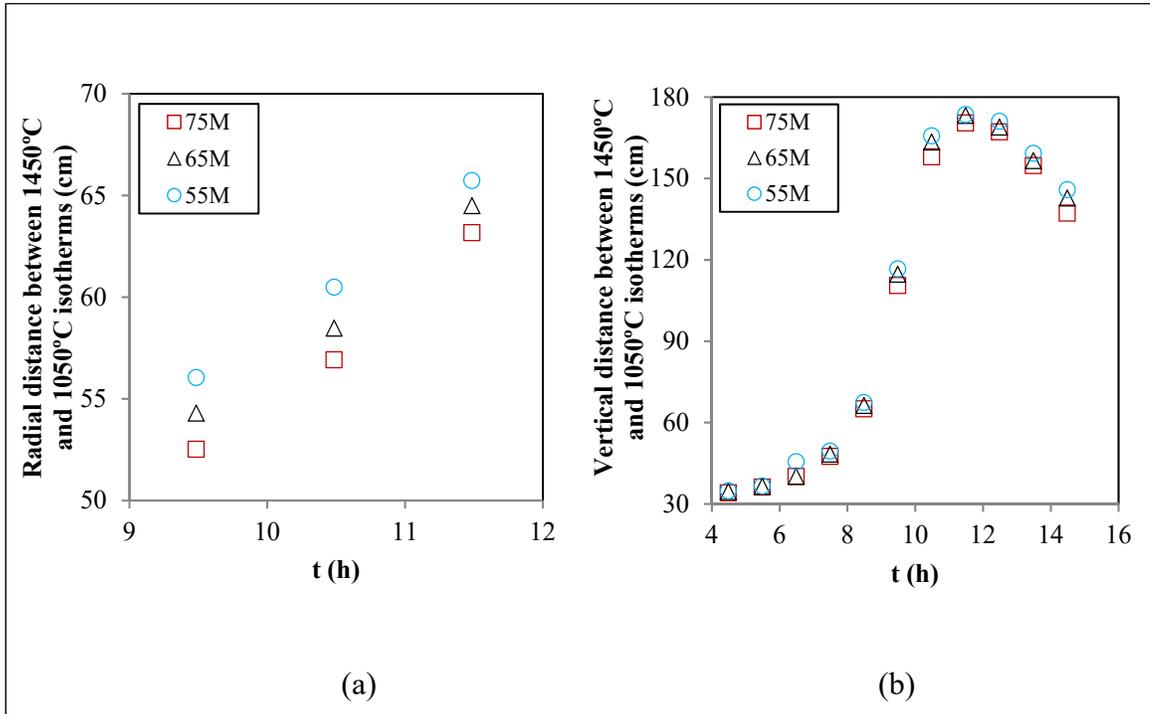
Figure 7.6 Distance between 1450 °C and 1050 °C isotherms with time. (a) In the radial direction (b) In the vertical direction.
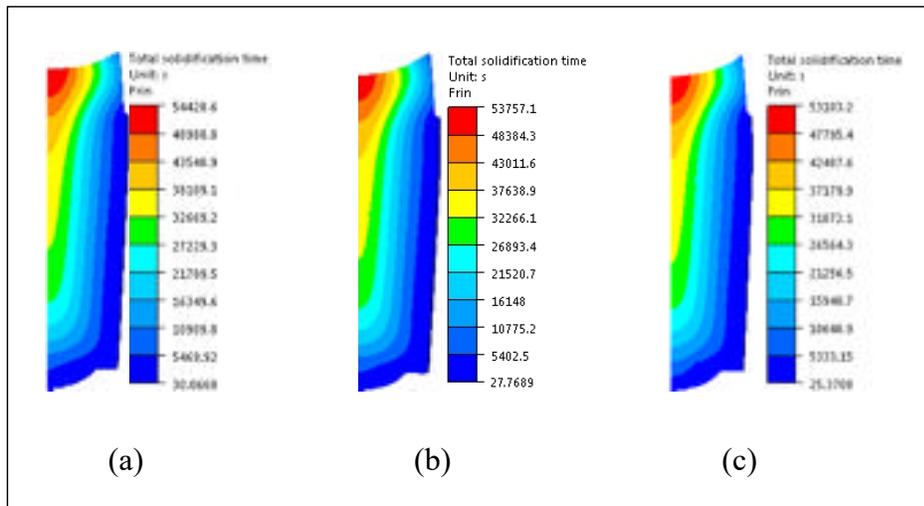
Figure 7.7 Predicted total solidification times. (a) 75M (b) 65M (c) 55M.

The faster solidification process in lower initial superheat case could be associated with its larger casting volume contraction, as reported in Figure 7.8. Figure 7.8a plotted the evolution of lateral air gap formation and the top shrinkage during the casting process on four selected points (as illustrated on the upper right corner of Figure 7.8a). The radial displacements on Point1 (at the ingot bottom skin in blue), Point2 (at the hot-top/ingot body junction skin in green), Point3 (at the top skin of hot-top in red), and the vertical displacement on Point4 (at the top center of the hot-top in black), were monitored during the whole filling and solidification processes. As seen in the figure, lower initial superheat resulted in earlier creation of the radial air gap on Point3 and larger air gap size on Points 2 and 3, indicating wider air gap from the bottom to the top along the casting height. When it comes to the top shrinkage examination on Point4, lower initial superheat was in line with quicker development of top contraction and larger shrinkage degree.
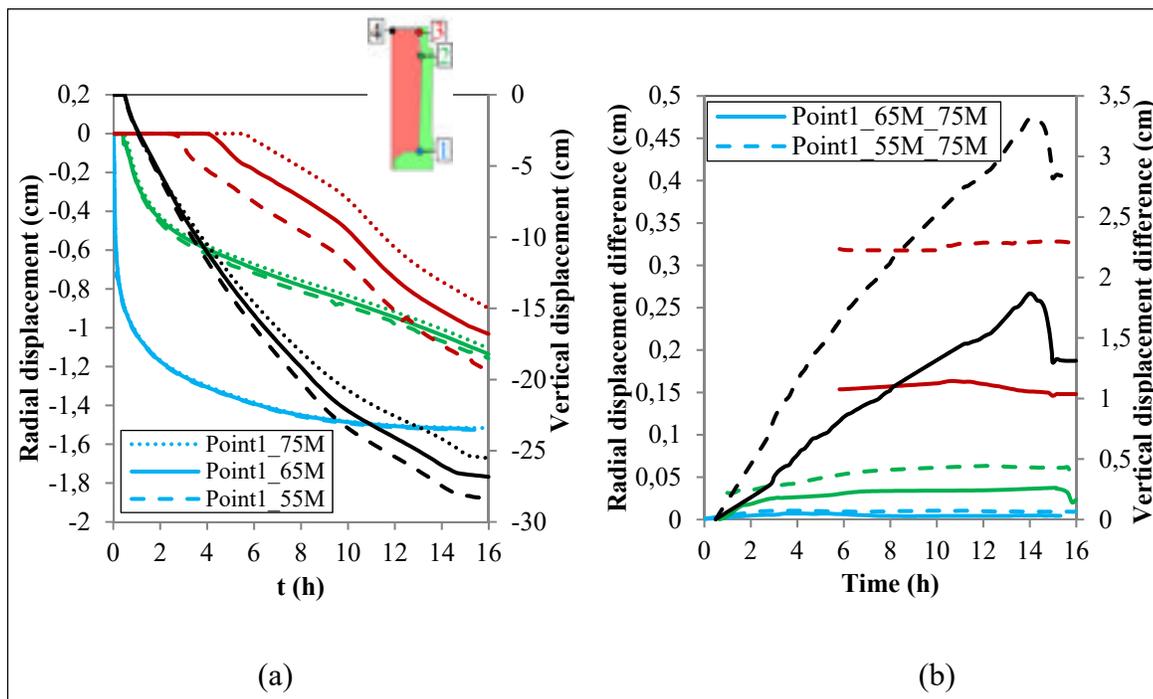
Figure 7.8 Examination of ingot volume contraction in the solidification process of three superheat cases. (a) Predicted time-dependent displacements of Points 1-3 in the radial direction and Point4 in the axial direction (b) Displacement differences between 65M/55M and 75M on Points 1-3 in the radial direction and Point4 in the axial direction

Figure 7.8b quantified the radial and vertical shrinkage differences on the same examined point among the three studied cases. It can be noted that at 16h, the difference in the radial air gap width on Point3 between 65M and 75M was 0.15 cm, while it got to 0.33 cm between 55M and 75M on the same point. The variation in the vertical shrinkage on Point4 between 65M and 75M and that between 55M and 75M reached 1.3 cm and 2.8 cm, respectively.

The above analyses of the time-dependent radial and vertical displacements of the casting skin presented that the reduction of the initial superheat led to the increase of the air gap and top shrinkage sizes. The combination of the larger shrinkage at the top of the casting and the wider radial air gap detached the casting away from the top and the mold walls, leading to a bigger volume reduction. This higher volume reduction in the lower superheat case should be the origin of its higher solidification speed and faster solidification process.

The milder segregation in lower superheat cases could find its origin in three aspects, as discussed above: 1) the weaker solutal convection induced by the lower density gradient resulting from the lower temperature gradient in the bulk liquid; 2) the more disordered thermal convection flow, which could impede the directed distribution of the rejected solutes; and 3) the accelerated solidification in the casting process due to greater ingot volume reduction, which could result in less time available for solutes to transport. The combined action of the three sources weakened the accumulation of species, resulting in minimized segregation intensity.

7.5   Conclusions

In the present work, the effect of melt initial superheat on the macrosegregation pattern of a 40MT steel ingot was investigated. A thermomechanic model considering both convection and solidification shrinkage was developed. The whole filling and casting processes of three ingots with different superheats were simulated. The evolution of macrosegregation patterns, as well as the associated phenomena, including the evolution of the temperature gradient, solidification speed, top shrinkage, air gap formation, and fluid flow, were all analyzed. The following conclusions can be drawn from the experimental and simulation results:

170

1) Lower superheat tended to advance the initiation and quicken up the development of temperature gradient in the early solidification stage, and also decrease the temperature gradient, both radially and vertically, in the later solidification phase.

2) Lower superheat led to greater top shrinkage and lateral air gap size, which resulted in larger volume reduction and less solidification time.

3) Lower superheat gave rise to earlier dominance of thermal convection, weaker solutal convection, and alleviated segregation in the upper part of the ingot body, in the hot-top, and in the mid-radius solute-rich bands.

The established model and the predictions have been verified with the chemical experimental measurements. The findings are expected to contribute to a better understanding of the macrosegregation formation mechanisms in ingot casting process. The decrease of the superheat should be a practical method for the casting process design of a given ingot of high value-added steels or other alloys.

7.6   Acknowledgements

7.7   Funding

CHAPITRE 8

ARTICLE 6 MACROSEGREGATION IN LARGE-SIZE STEEL INGOTS: MODELIG AND EXPERIMENTAL VALIDATION OF IMPACT OF MOLD INITIAL TEMPERATURE

Chunping Zhang[1,✉], Mohammad Jahazi[1]

[1]École de technologie supérieure, Department of Mechanical Engineering, 1100 Notre-Dame Street West, Montréal, Québec H3C1K3, Canada

8.1   Abstract

Ingot casting is the main technique for the production of high strength special steels. The initial mold temperature, as a casting parameter, is often fixed at or close to room temperature in industrial practice. However, ingots are often cast inside pits close to a wall or other ingots due to space limitation. These spatial constraints could result in variable mold temperatures, thereby affecting the heat and mass transfer, the solidification kinetics and eventually macrosegregation. However, its impact on macrosegregation in large size steel ingots is still not clear and needs to be quantified. In the present work, three initial mold temperature conditions, representing the most commonly encountered industrial conditions, were considered. The flows induced by pouring jet, the thermosolutal convection and the thermomechanical deformation of the phases were all taken into consideration. The results indicated that a higher mold temperature increased the macrosegregation intensity in the upper section of the casting, along the centerline and in the mid-radius solute-enriched bands. The increase was associated with increased temperature gradient in the casting, advance predominance of thermal convection, and the resulting delay in solidification. The thermal predictions of the studied cases were verified with experimental temperature measurements from three industrial size ingots.

Keywords: Finite Element modeling, large size steel ingot, initial mold temperature, macrosegregation

8.2 Introduction

Large size steel ingots often suffer from the occurrence of zones with chemical compositions different from the alloy's nominal one (Pickering, 2013). This phenomenon is called macrosegregation and takes place during the solidification process. The presence of macrosegregation results in inconsistent transformation products (i.e. martensite, bainite) during subsequent hot working, and causes nonuniformity in mechanical properties of the finished product (Zhang et al., 2018). Therefore, it is of great significance to control its extent and severity by stringent selection of casting process parameters, such as melt composition (Zulaida et Suryana, 2016), melt superheat (Su et al., 2018; Pikkarainen et al., 2016), hot-top geometry (Qian et al., 2015) and casting configuration (Dub et al. 2014). This can only be achieved with better understanding of the process parameters and quantification of their impacts (Campbell, 2011).

The initial mold temperature, as a casting parameter, is not specified in production and often fixed at or close to room temperature. In industry, however, ingots are often cast inside pits close to a wall or other ingots due to space limitation. These spatial constraints could result in variable mold temperatures, thereby affecting the solidification kinetics and eventually macrosegregation. Zhang et al. and Li et al. (Zhang et al., 2016; Li et al., 2017) reported that a rise in initial mold temperature coarsens grain size. Li et al. (Li et al., 2017) and Haj et al. (Haj, Bouayad et Alami, 2015) found that a mold at higher temperature condition is accompanied by increased secondary dendrite arm spacing (SDAS) and aggravated shrinkage porosities. Im et al. (Im, Kim et Lee, 2001), Haj et al. (Haj, Bouayad et Alami, 2015) and Li et al. (Li et al., 2017) observed the occurrence of a prolonged solidification time when the initial mold temperature was increased. However, the impact of initial mold temperature on macrosegregation in large size steel ingot is still not clear and needs to be quantified.

In the present work, the sensitivity of macrosegregation to the initial mold temperature was numerically studied. The finite element modeling (FEM) of the bottom pouring, filling and solidification processes of a 40 MT (metric ton) steel ingot was realized using the Finite Element (FE) code Thercast® (TherCast 8.2®, 2012) and in a 3D model. Three mold thermal conditions were examined, representing the variabilities encountered in industry during

casting of large size ingots. The internal thermal field in the casting, the external one in the mold, the residual and natural convection, the solidification velocity and the thermomechanical contraction were considered in the analyses. The predictions were compared with the experimental temperature measurements from three industrial-scale (40 MT) ingots cast at different initial temperature conditions. The results were discussed in the framework of heat transfer, macrosegregation formation and solidification mechanism.

8.3　　　Model establishment

The model used in the study is composed of a cylindrical ingot 250 cm in height and 150 cm in average diameter. The ingot is cast in big-end-up cast iron mold with a hot-top 70 cm in height laid above. The hot-top part is lined inside with insulating refractory tiles, and an insulating exothermic refractory board is over laid on the melt top, as shown in Figure 8.1a. 3D linear tetrahedral elements, with an average grid of 35 mm, were used for the spatial discretization of the part and mold components. The chemical composition of the steel in study is given in Table 5-1.

For the simulations, the liquid steel is bottom poured into the mold at 1570 °C (with a superheat of 75 °C) with a filling time of 30 min. Three initial mold temperatures of 50, 120 and 250 °C were investigated. Therefore, the modeled cases are identified in the rest of the manuscript as 50M, 120M and 250M. The calculations were stopped when the ingot came to complete solidification (i.e. around 1400 °C). For the three models, five sensors (SNs 1-5) were installed in specified positions on the mold outside surface, as presented in Figure 8.1a, to monitor their temperature changes throughout the casting process. Patterns of carbon segregation ratio, R_C, were constructed based on the relation: $R_C = (\omega_l^C - \omega_0^C)/\omega_0^C$, where ω_0^C is the local carbon concentration and ω_0^C is its nominal concentration value, as reported by Duan et al. (Duan et al, 2016).

To verify the established model and examine the thermal predictions, three cylindrical ingots (50E, 80E and 120E), with 250 cm in height and 150 cm in mean diameter, were cast. Ingot 50E was fabricated under the same casting condition as 50M (i.e. at 1570 °C, with a filling time of 30 min, and initial mold temperature of 50 °C). Ingots 80E and 120E were cast at

1576 °C with a filling time of 34 min and with initial mold temperatures of 80 and 120 °C, respectively. Their 80 and 120 °C initial mold temperatures were generated by their respective neighboring ingots. For ingot 50E, the temperature variations on the outside surface of the mold were monitored throughout the casting process using 5 Chromel-Alumel thermocouples (TCs, type K) located in the same emplacements as SNs, as presented in Figure 8.1a. For Ingots 80E and 120E, only TCs 1-4 were set up on the mold outside surfaces. For the three experimental ingots, each thermocouple was cemented into holes drilled 2.5 cm into the mold from the exterior surface. Temperature measurements from each thermocouple were made every 90 seconds from the start of the steel pouring until the ingot was removed from the mold.

The three-dimensional modeling of mold filling and solidification were realized in the FE code Thercast®, based on volume-averaged solid-liquid two-phase thermomechanical models (TherCast 8.2®, 2012). An Arbitrary Lagrangian-Eulerian (ALE) formulation was used, for computing the thermal convection in the liquid pool and mushy zone, and for managing the time-dependent evolution of metal volume and mass in the mold during the filling phase. A Lagrangian method was employed for calculating the deformation in the solid regions. The analyses of fluid flow, temperature, and solute distribution in a solidifying material amount to the coupled solution of the equations, stating the conservation of mass, momentum, energy and solute. Sedimentation of equiaxed grains and mold deformation were not taken into account in the modeling, either because they are not considered in the FE code or to reduce the computation time. All the material parameters used for the simulations in the present study are from Zhang et al. (Zhang et al., 2018).

8.4   Results and discussions

8.4.1   Macrosegregation pattern

The evolution of segregation ratio pattern of carbon on the ingot longitudinal section for the three studied cases is given in Figure 8.1. It can be seen that the large-scale distribution of solutes changed, from the pouring moment till the completion of solidification, as a result of

the variation in mold initial temperature. At the end of pouring operation, in 50M, the first segregated particles (red and blue spots in Figure 8.1a) were formed in a small area around the hot-top/ingot body interface. For 120M (Figure 8.1e) and 250M (Figure 8.1i), more particles were present over larger regions. No solutal gradient appeared in 50M, but it formed in 120M and tended to be larger with increasing the mold temperature. This indicates that an advance development of solutal convection can be expected with the mold temperature rising. At 5.5 h after pouring, in 50M (Figure 8.1b), a solutal gradient was observed in the radial and vertical directions of the entire casting. In 120M (Figure 8.1f) and 250M (Figure 8.1j), the radial and vertical solutal gradients were slightly larger in intensity and extent with the increase of mold temperature.

As the solidification proceeded, a positive segregated zone in the upper center region and a negative one at the bottom of the ingot formed progressively for all the three studied cases, as presented in Figures 8.1c, g and k. The strongest accumulation of solutes occurred in the case with the highest initial mold temperature (that is, in 250M), and the trend was maintained till the end of solidification, as seen in Figures 8.1d, h and l. Furthermore, it was revealed that solute-enriched bands formed between the ingot axis and the mold wall for all the three cases (Figures 8.1c, d, g, h and k, l). They extended nearly over the entire height of the ingots, inclined with respect to the ingot periphery. The segregation intensity in these mid-radius solute-enriched bands appeared higher as the initial mold temperature was increased, but the band tended to be located farther away from the ingot periphery.

The final carbon segregation ratio profiles along the ingot centerline were compared among the three cases in Figure 8.2a, where the y-axis was set to be the distance from the hot-top/ingot body interface. As featured in the figure, the increase of the initial mold temperature gave rise to higher segregation intensity in the upper section of the centerline. Specially, quantitative examination indicated that the axial carbon segregation ratio intensity in 50M was in average about 8.1 % and 14.3 % smaller than the one in 120M and 250M, respectively. Carbon segregation ratio variations in the radial direction were also examined along a section located 30 cm below the hot-top/ingot body separation interface. As reported

in Figure 8.2b, the carbon segregation ratio in the mid-radius solute-enriched bands in 50M was slightly decreased than that in 120M and 250M.

Figure 8.1 Predicted macrosegregation ratio patterns of carbon in the solidification process for three studied cases. (a, e, i) 0.5 h (end of filling) (b, f, j) 5.5 h (c, g, k) 10.5 h (d, h, l) End of solidification.
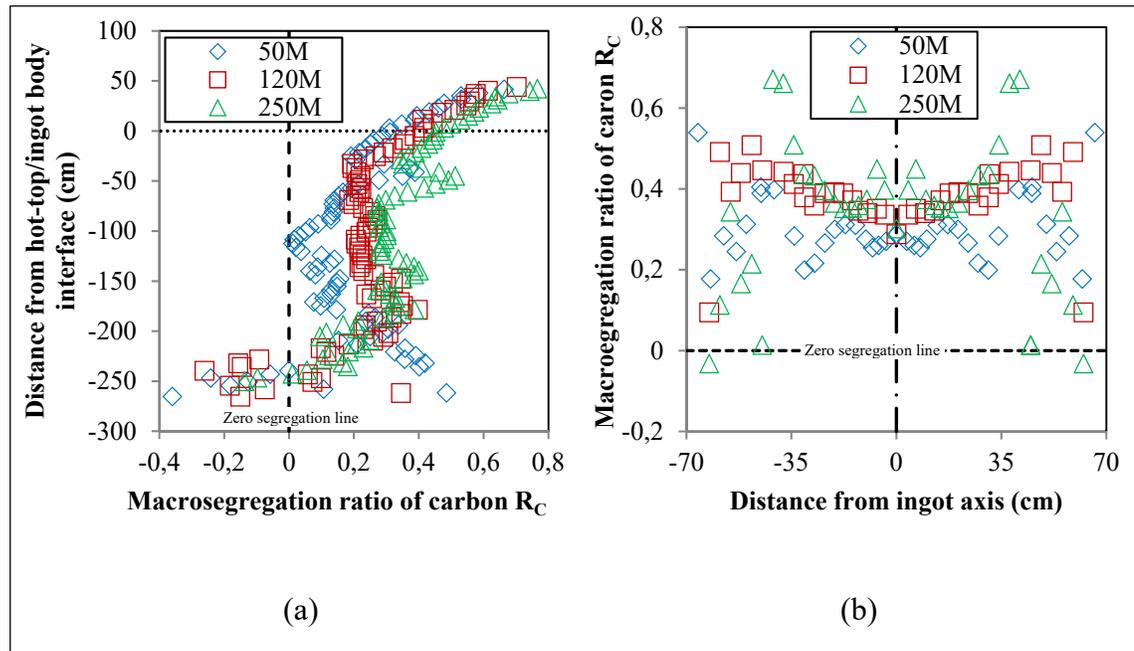
Figure 8.2 Evolution of macrosegregation ratio of carbon at the end of solidification. (a) Along the ingot centerline (b) Along the cutting section 30 cm below the hot-top/ingot body interface.

Based on the above comparative examinations of the macrosegregation patterns under the three different mold thermal conditions, it can be said that initially hotter mold can result in larger macrosegregation intensity in the ingot body, in the upper section of the centerline and in the mid-radius solute-enriched bands. This finding indicates that the solidification process of the ingot body induced by the variation in the mold temperature plays a key role on the compositional distributions, as will be discussed in the following sections.

8.4.2   Temperature field

The temperature fields at different times during the casting process are shown in Figure 8.3. It can be seen that different mold initial temperatures modified the internal temperature field in the casting and the external one in the mold. At the end of the filling stage (Figure 8.3a, d, and g), larger high temperature region (the red regions above the 1550 °C isotherm) was left in the casting with increasing the initial mold temperature, demonstrating its smaller superheat dissipation rate. In addition, for the case with the initial condition of 250 °C (i.e.

250M), a region with larger temperature variation was formed in the mold, from its interior layer throughout the mold thickness, due to the heat transfer from the steel melt and its hotter mold. The delay in heat loss in the hot-top was observed for all the three cases due to the poor conduction of the refractory tiles, but the temperature in the hot-top shell was remarkably higher with the increase in the initial mold temperature.

The final carbon segregation ratio profiles along the ingot centerline were compared among the three cases in Figure 8.2a, where the y-axis was set to be the distance from the hot-top/ingot body interface. As featured in the figure, the increase of the initial mold temperature gave rise to higher segregation intensity in the upper section of the centerline. Specially, quantitative examination indicated that the axial carbon segregation ratio intensity in 50M was in average about 8.1 % and 14.3 % smaller than the one in 120M and 250M, respectively. Carbon segregation ratio variations in the radial direction were also examined along a section located 30 cm below the hot-top/ingot body separation interface. As reported in Figure 8.2b, the carbon segregation ratio in the mid-radius solute-enriched bands in 50M was slightly decreased than that in 120M and 250M.

In the intermediate and later solidification stages, isothermal curves in the casting were displaced later as the initial mold temperature increased. For the 250M ingot, the radial span from the isotherms to the chill mold wall (for instance, the 1450 °C isotherm in Figure 8.3h and the 1350 °C one in Figure 8.3i) remained the smallest. This trend was more remarkable in the hot-top region. The smallest vertical distance between 950 °C isotherm and the ingot base throughout the casting process was also observed with the higher temperature conditions. This later isotherm movement in the radial and vertical directions indicates that a delayed solidification was induced by a rise in initial mold temperature. When it comes to the thermal field in the mold, it was noted that the higher temperature on the interior surface of the mold went always along with the initially hotter mold cases. But the difference in the mold thermal gradient field among the three studied cases tended to fade away with solidification proceeding and assimilate in the latter solidification stage, as reflected in Figures 8.3c, f, i.
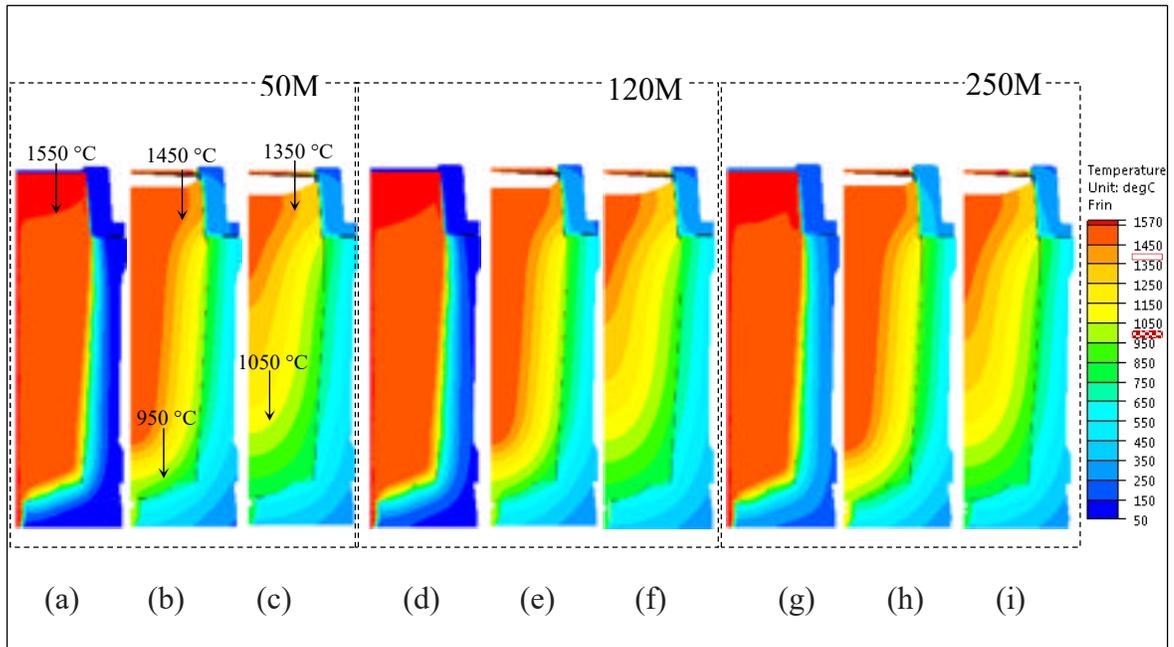
Figure 8.3 Temperature fields predicted by 50M (left group), 120M (middle group) and 250M (right group). (a, d, g) End of filling, (b, e, h) 5.5 h (c, f, i) 10.5 h after pouring.

In order to further quantify the impact of the initial mold temperature condition on the temperature field in the steel casting, time-dependent movements of 1450 °C and 1050 °C isotherms (as identified in Figure 8.3) were monitored. The radial direction was first checked along the hot-top/ingot body interface. As shown in Figure 8.4a, in the radial direction, under higher mold temperature conditions, the two isotherms were located farther from the ingot axis, indicating smaller radial growth of the solidified shell. The radial distance examination between the two investigated isotherms, in Figure 8.4b, revealed the smallest value for the 250 °C initial temperature case. This minimum distance tendency for the hottest mold case became more remarkable in the later solidification stages. For example, after 11 h, the radial distance between the two examined isothermal curves reached 63.2 cm for 50M, in contrast to 61.7 cm for 120M and 58.8 cm for 250M. The smaller distance between fixed isotherms indicated the production of higher thermal gradients when higher initial mold temperature was used. The vertical displacement of the same two isotherms along the ingot centerline axis, Figures 8.5a and b, further supported the findings that higher initial mold temperature

created higher thermal gradients in most solidification stages and overall slowed down the solidification process.
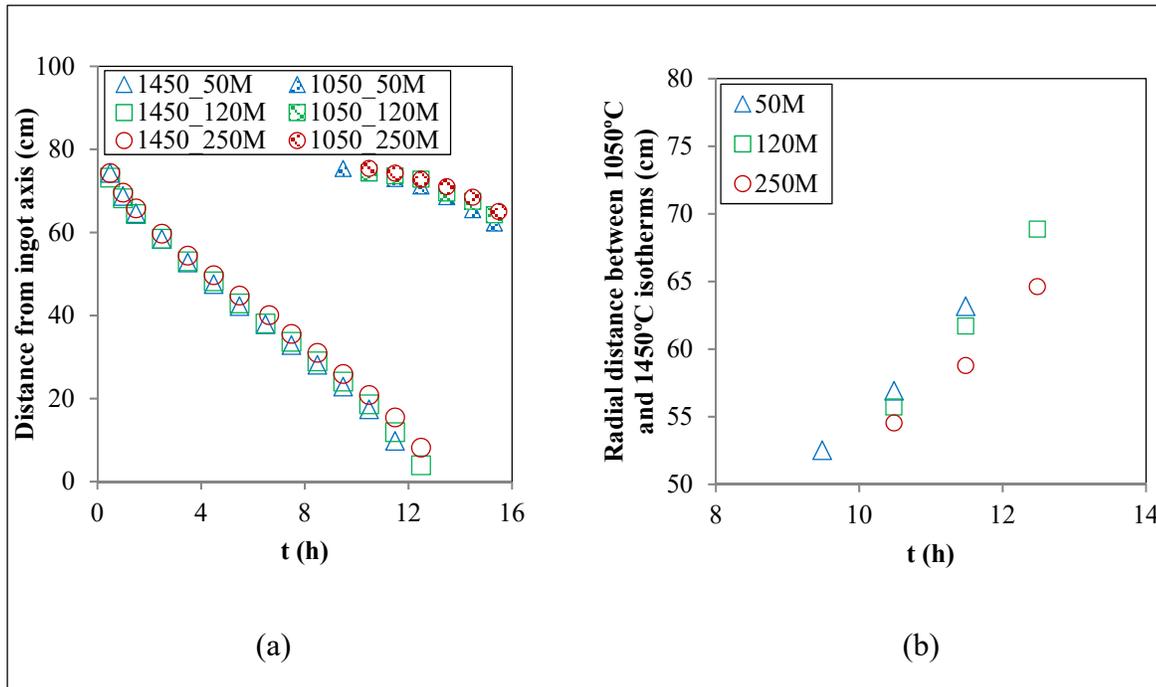
Figure 8.4 Temperature gradient examination in the radial direction along the hot-top/ingot body interface in the cast ingots of 50M, 120M and 250M during the casting process. (a) Time-dependent displacement of 1450 °C and 1050 °C isotherms (b) Time - dependent radial distance between 1450 °C and 1050 °C isotherms.

Figure 8.6a shows a comparative analysis on the temperature variations caught by the sensors installed on the outside surface of the mold. It can be seen that for all the three cases, the mold surface temperature continuously increased from the start of filling until reaching a maximum, and then started to decrease, as also reported by Brookes et al (Brookes, Beckermann et Richards, 2007). The maximum temperatures and the time to reach them were dependent on the initial conditions. For instance, for Sensor1, the temperature increased to its maximum value of 520 °C in 6 hours for 50M, while it reached 533 °C after 5.5h and 557 °C after 5h when the initial mold temperatures were 120 °C (120M) and 250 °C (250M), respectively. An increase in the mold temperature from 50 °C to 120 °C generated an average elevation of the mold surface temperature peak by 11 °C, while a further rise to 250 °C raised

the temperature peak value by about 29 °C on the mold outside surface. Furthermore, the temperature difference on the same sensor, among the three cases, tended to decay as solidification proceeding and came close to each other at the later phase of solidification.
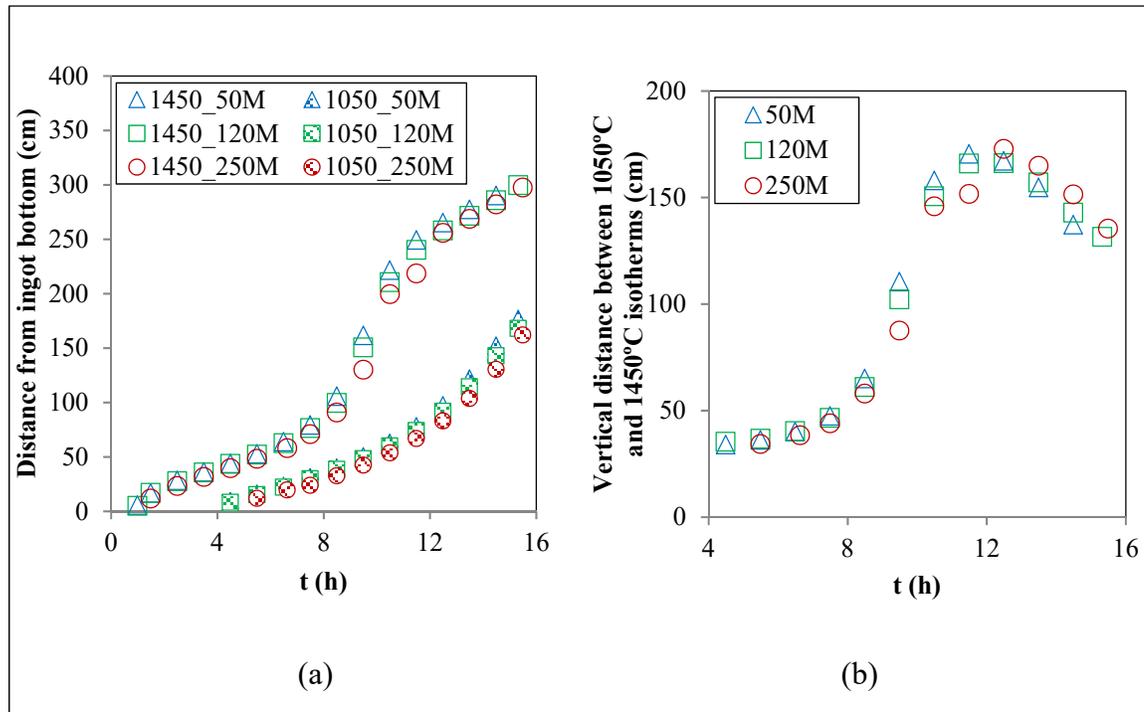
Figure 8.5 Temperature gradient examination in the vertical direction along the ingot centerline axis in the cast ingots of 50M, 120M and 250M during the casting process. (a) Time-dependent displacement of 1450 °C and 1050 °C isotherms (b) Time-dependent vertical distance between 1450 °C and 1050 °C isotherms.

The measured and predicted thermal profiles for the initial mold temperature of 50 °C can be compared between Figures 8.6a and b. A good agreement can be observed, demonstrating the reliability of the model developed in the present study. Furthermore, the above thermal tendency on the mold outside surface (the higher heat peak for initially hotter mold case and the assimilation of thermal gradient in the later solidification stage for the three studied cases) was also observed on ingots 80E and 120E, as plotted in Figure 8.6b. This finding confirms the sensitivity of the temperature field to the initial mold thermal condition.

It must be noted that the larger thermal gradient in the case with higher mold temperature can contribute to increase solute segregation in the casting body, as observed in Figures 8.1 and 8.2. The higher temperature gradient occurred concomitantly with increased density gradient, and hence advanced the development of solutal convection (as observed in Figure 8.1), improving the solutal distribution in the solidification process, as reported by other researchers (Vives et Perry, 1986; Hachani, et al., 2012; Liu, Liu et Kang, 2008).
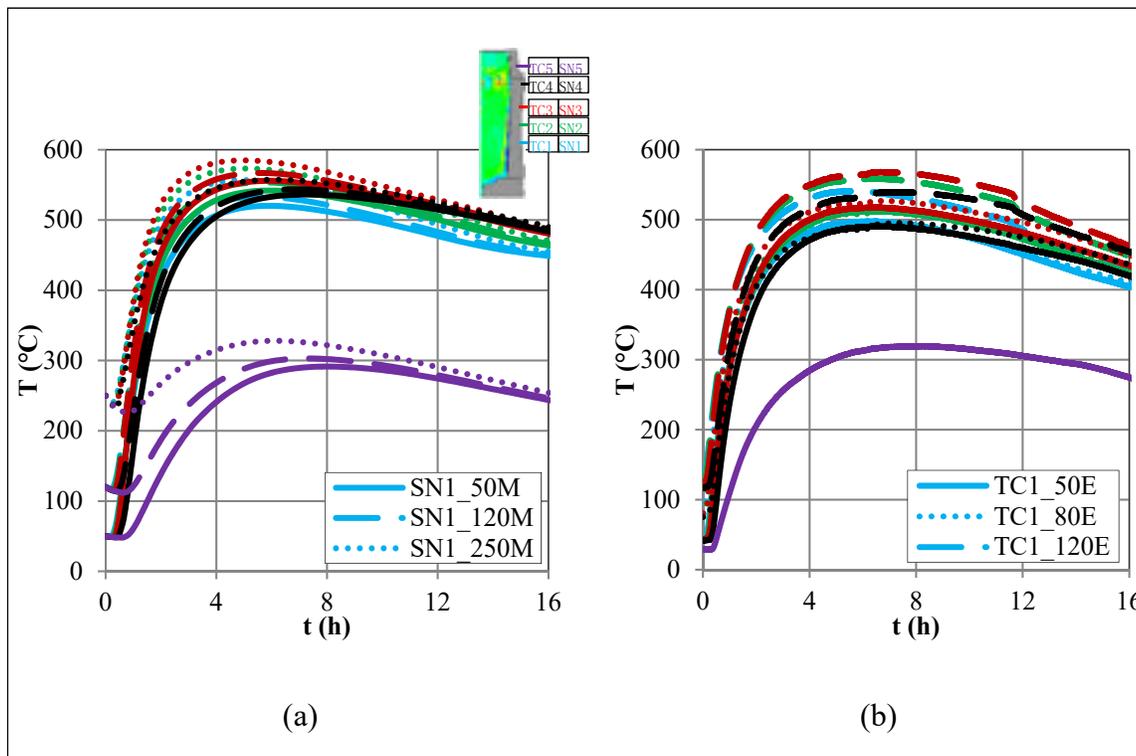
Figure 8.6 Time-dependent displacement of isotherms 1450 °C and 1050 °C during the casting process. (a) In the predictions (b) In the experimental measurement.

8.4.3   Liquid movement

As reported in Figure 8.7a, e, and i, different initial mold temperatures created a clear difference in the liquid movement in the casting. At the end of the filling operation, for the lowest mold temperature (Figure 8.7a), ingot axial up-flow, solidification front down-flow,

and clockwise flows in the hot-top were present, due to the combined effect of the pouring jet and the inertia effect of the residual flow. Similar findings have also been reported by Zhang et al. (Zhang, Bao et Wang, 2016). However, besides the above features, intermediate mold temperature in 120M created axial down-flow moving from the upper hot region to the bottom cold zone, as seen in Figure 8.7b. Based on the report from Yadav et al. (Yadav et al., 2009), the occurrence of axial downward stream are features of thermal convection. Furthermore, in the highest mold temperature case, 250M in Figure 8.7c, a number of clockwise/counterclockwise vortexes were produced and scattered in the ingot body. Such characteristics are indicative of the presence of stronger thermal convection, counteracting the residual flow that goes from the center hot region to the cold mold zone, as also reported by Yadav et al. (Yadav et al., 2009) and more recently by Liu et al. (Liu et al., 2011). The above features in the liquid movement suggests that as the mold initial temperature increases, thermal convection becomes the dominant heat transfer mechanism in the early stages of solidification.

The higher thermal convection is probably responsible for the more segregated particles at the end of filling stage (Figures 8.1a, e, i), and later the larger solutal accumulation in the casting and the mid-radius bands. As reported by Qian et al. (Qian et al., 2015), the down-stream movement of the liquid metal along the solidification front, next to the mold wall, would pass through the lower liquid fraction zones, remelt them and consequently channel the mushy zone, thereby influencing the mass transfer and the formation of the positive segregated bands close to the chill zone. Thus, in the case with hotter mold, the advance arrival of thermal convection and the resultant less ordered solidification front downward residual flow could be the source for the higher segregation intensity in the mid-radius solute-enriched bands and farther location from the mold wall, as shown in Figures 8.1 and 8.2b.

184
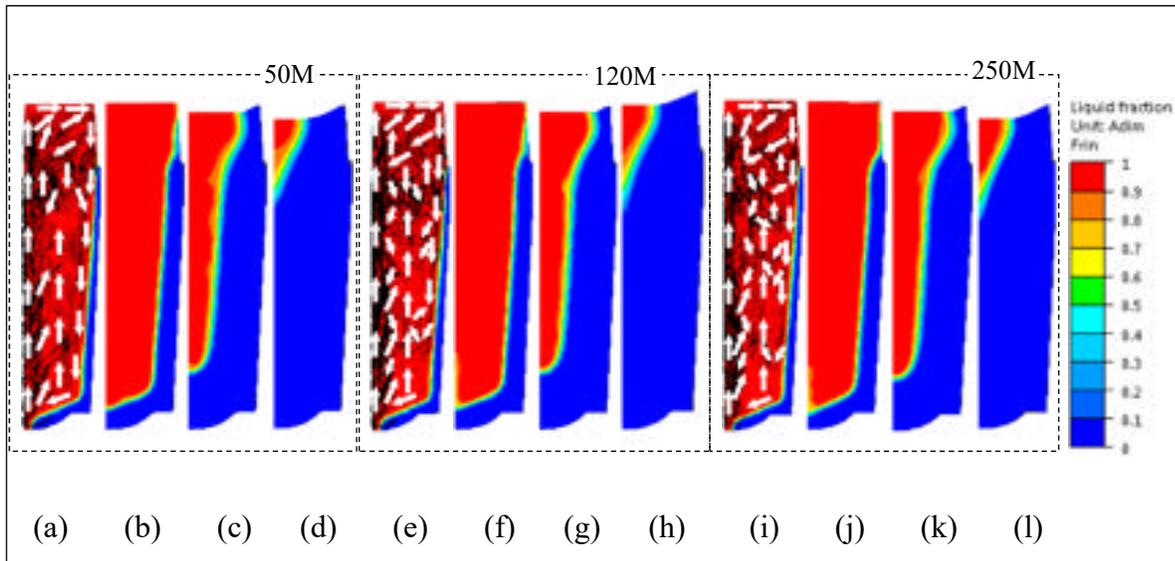
Figure 8.7 Liquid fraction patterns combined with velocity vectors predicted by 50M, 120M and 250M. (a, d, g) 0.5 h (end of filling) (b, e, h)1.5 h (c, f, i) 5.5 h (d, h, l) 10.5 h after pouring.

8.4.4   Solidification speed

Further examination of Figure 8.7 revealed that the solidification speed was decreased as the initial mold temperature increased. From Figures 8.7a, e and i, it was measured that at the end of the filling process, the solid skin thickness next to the mold wall had an average value of 8.15, 7.0, 6.12 cm for 50M, 120M and 250M, respectively, indicating that a delayed solidification was induced when mold temperature was increased. This delayed solidification was maintained until the completion of solidification, which were reflected, in 250M, on the thinner solid layer next to the chill wall (as compared among Figures 8.8b-d, f-h and j-l), as well as the larger liquid fraction and deeper liquid pool (larger red area) in the later solidification stage (Figures 8.8d, h and l). This finding is in agreement with the report from Im et al. (Im, Kim et Lee, 2011), who pointed out the association of the decrease in the solidified fraction with the mold temperature increasing.
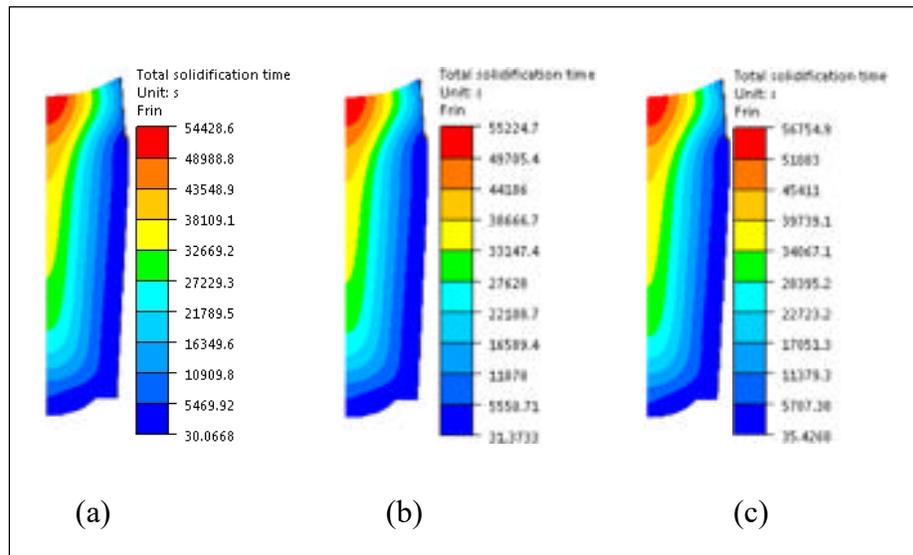
Figure 8.8 Total solidification time (a) 50M (b) 120M (c) 250M.

Analysis of total solidification time confirmed the deceleration of the solidification process under higher mold temperature condition. It was predicted that it took 15 h 07 min (54428 s) for 50M to complete the solidification, as shown in Figure 8.8a. This time was 13 min shorter than 120M (55224 s, Figure 8.8b) and 39 min than 250M (56755 s, Figure 8.8c). This solidification deceleration is in accordance with the observations of the increase in SDAS under higher mold temperature condition from HAJ et al. (Haj, Bouayad et Alami, 2015) and more recently from Li et al. (Li, Li et Gao. 2017).

As reported by Kai and Pehlke (Kai, Robert et Pehlke, 1985), the prolongation of solidification process with increase of mold temperature was related to the variation of heat transfer flux. A temperature discontinuity often exists at the metal/mold interface, or gap. Therefore, the heat transfer across the gap, q, could be computed directly using a simple expression:

$$q = h_{gap}(T_c - T_m) \tag{8.1}$$

where T_c and T_m are the casting surface and mold surface temperatures, respectively. Empirically, the typical value of the gap heat transfer coefficient, h_{gap}, for steel in cast iron mold is 1025 W/m$^2 \cdot$°C (Singer et Evans, 1983). Thus, it can be said that an increase of mold temperature is accompanied with a decrease of heat transfer across the melt/mold interface, resulting in a decreased chilling rate.
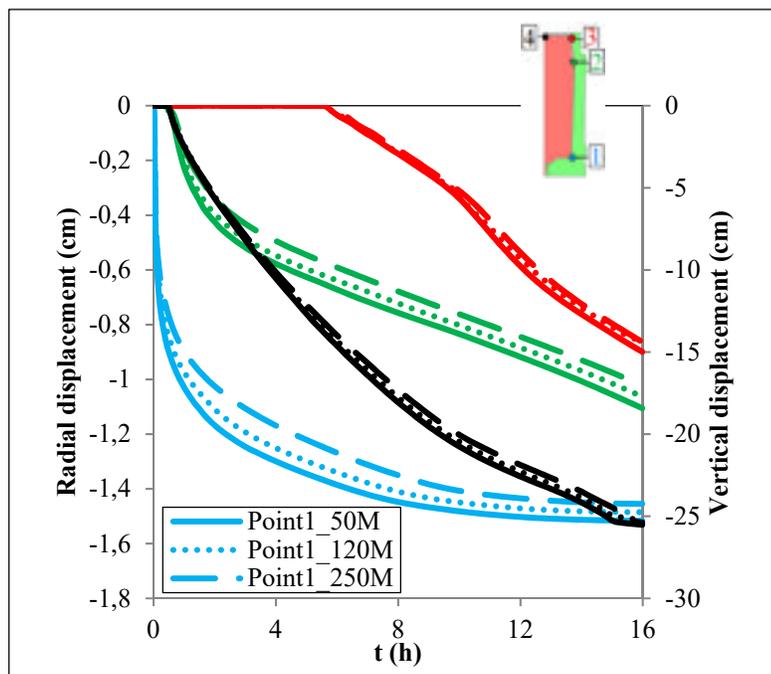
Figure 8.9 Radial displacement of Points 1-3 and vertical displacement of Point 4 in the casting process.

The delay in the solidification process for higher mold initial temperature was also analyzed in terms of the casting volume evolution. To carry out the analysis, four specific locations on the casting surface were monitored for the three cases, as illustrated on the upper right corner of Figure 8.9: Point 1 (at the ingot bottom skin, in blue), Point2 (at the hot-top/ingot junction skin, in green), and Point 3 (at the top skin of hot-top, in red) for radial contraction (air gap formation). Finally, Point 4 (at the top center of the hot-top, in black) was monitored for the vertical shrinkage. As reported in Figure 8.9, higher mold temperature decreased the growth rate of the radial air gap and vertical contraction in the first stages of solidification. For

instance, to form 1 cm air gap at the ingot bottom from the ingot skin (Point 1) against the mold wall, it took 1 h for 50M, 1.3 h for 120M and 1.8 h for 250M, while the formation of a 0.5 cm air gap between Point2 and the mold required 2.8 h, 3.2 h and 4.2 h for 50M, 120M and 250M, respectively.

It was also noted that higher mold temperature brought about the development of smaller air gap and top shrinkage, indicating a smaller decrease in the casting volume. The final casting volume for 50M reached 92.1 % of the total mold vacant volume, while it was 92.3 % and 92.8 % for 120M and 250M, respectively. Thus, the deceleration in the solidification process at higher mold temperature conditions probably originates from a smaller volume contraction. Therefore, the less rapid solidification process in the case with higher initial mold temperature, and thus more available time for solutal diffusion, should be another source for the more accumulation of solutes and more severe segregation intensity.

8.5   Conclusions

In the present work, the effect of initial mold temperature on macrosegregation in large size steel ingots was investigated using FE modeling and experimental validation. A thermomechanic model, considering both convection and solidification shrinkage, was developed. The entire filling and casting processes of three ingots with different mold thermal conditions were simulated. The evolution of macrosegregation patterns, as well as the associated phenomena, including the evolution of temperature gradient in the casting and mold, the fluid flow, solidification speed, and thermomechanical contraction, was analyzed. The findings of the study, as summarized below, are expected to contribute to a better understanding of the macrosegregation formation mechanism in ingot casting process of high strength steels:

1) Higher mold temperature tends to increase the segregation severity in the ingot body, along the centerline, and in the region between the ingot centerline and the mold wall.

2) A good agreement was obtained between the model thermal predictions and experimental temperature measurements, demonstrating the validity of the developed model and its application for other casting conditions.

3) The higher intensity of the segregation in the ingot with higher initial mold temperature could be attributed to three sources:

    a) the increased temperature gradient in the casting;

    b) the advance arrival of natural convection and its longer dominant time;

    c) the decelerated solidification process.

8.6   Acknowledgements

8.7   Funding

CONCLUSIONS

The project aims to develop a reliable model to predict the extent and severity of macrosegregation in a 40MT (metric ton) medium-carbon high strength steel ingot as a function of casting parameters. To realize the objective, a 3-D 15º FEM model (1/24 of the complete casting system) was constructed using the commercial FEM code Thercast®, to calculate the filling and solidification based on volume-averaged solid-liquid two-phase algorithm.

For the accuracy of the model, series of work were conducted to eliminate all possible elements which could introduce uncertainties, using a combined experimental and simulation approaches. The FEM model incorporated all the accurate geometric, structural and configuration features of the constitutional components of actual industrial casting system, with an average grid size of 35mm to discretize the constituent pieces. The boundary conditions were set to well approximate the industrial practice. The input temperature dependent parameters of concerned materials, reflecting their thermodynamic, thermomechanic and thermodiffusion behaviors, were identified by means of combined approaches of computational thermodynamic software Thermo-Calc®, empirical equations, theoretic calculations, industry sources, literature reports, Thercast® material database, as well as experimental room and high-temperature tension tests. Lever rule was decided to be the scheme to depict the diffusion behavior of carbon in the solidification process of the steel ingot. The model was determined to take into account the combined influence of thermosolutal convection and solidification shrinkage effect (with top contraction and air gap formation, i.e. thermomechanic model) for the simulation work. The reasonability of all above selections was verified based on comparative analyses. The reliability of the established model and its applicability to the studied ingot were confirmed based on the good reproduction of experimental measurements on top cavity dimension, the casting duration, the thermal profiles on the outside of the mold surface obtained using thermocouples, and the carbon distribution profile via mass spectrometer analysis.

Using the developed model, qualification and quantification of the impacts of three casting parameters (the filling velocity, the initial melt superheat and the initial mold temperature condition) on the severity and extent of macrosegregation in the studied as-cast ingot were conducted. These casting parameters were determined to be the subject of the current project predominantly in consideration of their common use in industry and the missing and conflicting of relevant data in the literature. For the simulation works, the entire filling and casting processes of the ingot under different casting conditions were calculated. The evolution of macrosegregation patterns, as well as the associated phenomena, including the evolution of temperature gradient in the casting and mold, the fluid flow, the solidification speed, and thermomechanical contraction, was comprehensively analyzed.

In the study about the effect of filling rate with three filling rates examined (0.084, 0.107 and 0.145 m/min with filling times of 38, 30 and 22 min, respectively), following results were indicated: i) higher filling rate helps to decrease the segregation severity in the upper section of the ingot body, along the centerline, and in the region between the ingot centerline and the mold wall; ii) the lower intensity of the segregation in the ingot with higher filling rate could be attributed to the accelerated solidification process, the decreased temperature gradient, and the more instable liquid movement. The more intense instability of fluid motion is attributed to three sources: the increased fluid flow instability in the filling process, the prolonged action of the residual flow (particularly the lateral flow) and the delayed development of thermosolutal convection.

In the investigation of the impact of melt superheat concerning three initial melt superheats of 75, 65 and 55 °C, the results revealed that lower superheat helps to advance the initiation and quicken up the development of temperature gradient in the early solidification stage, and also decrease the temperature gradient, both radially and vertically, in the later solidification phase. As a result, greater top shrinkage and lateral air gap size are generated, which induce larger volume reduction and less solidification time. Under the action of all above elements, lower superheat gives rise to earlier dominance of thermal convection, weaker solute convection, and alleviated segregation in the upper part of the ingot body, in the hot-top, and in the mid-radius solute-rich bands.

When the influence of mold initial temperature conditions was explored (the initial mold temperatures of 50, 120 and 250 °C were examined), the results presented that higher mold temperature tends to increase the segregation severity in the ingot body, along the centerline, and in the region between the ingot centerline and the mold wall. The higher intensity of the segregation in the ingot with higher initial mold temperature could be ascribed to the increased temperature gradient in the casting, the advance arrival of natural convection and its longer dominant time, and the decelerated solidification process.

Furthermore, non-uniform initial temperature condition of the mold can lead to asymmetry in the temperature field, temperature gradient and solidification speed in the casting, along with a delayed solidification process on the side of the mole with a higher temperature. This asymmetry and the solidification lag should influence the distribution of alloying elements.

All above results were verified by the good agreement obtained between the model predictions and experimental characterization results. The increase of the filling operation, the decrease of the melt superheat and the decrease and uniformity of the mold initial temperature condition should be practical methods for the casting process design of a given ingot. The findings are expected to contribute to a better understanding of the macrosegregation formation mechanisms in ingot casting process. All these findings could be used in industry, to improve the quality of large-size ingot production made of high value-added steels, or other alloys which are prone to macrosegregation.

RECOMMENDATIONS

The present project developed a reliable model with respect to a 40 MT medium-carbon high strength low-alloyed steel ingot, with can predict the impact of casting parameters on the extent and severity of macrosegregation. About the model and the future work, the following recommendations are suggested:

1) A lot of data have obtained on the effect of filling rate, melt superheat and mold initial temperature on the solidification behaviors, including the advance of solid front, the change of temperature gradient, the evolution of fluid motion, the extent of solidification shrinkage, the variation of solidification speed, and the formation and development of macrosegregation. It is suggested to conclude the constitutive equations from the obtained data to qualitatively and quantitatively predict the effect of the variation of these production parameters and provide a guide for the future industrial fabrication.

2) The study on the impact of non-uniform initial temperature condition of the mold provides original information about the condition commonly encountered in the industrial manufacture practice. The results revealed an asymmetry in the temperature field, temperature gradient and solidification speed in the casting, and a delayed solidification on the side of the mold with a higher temperature. This asymmetry and the solidification lag should influence the distribution of alloying elements, given that the development of macrosegregation is significantly influenced by the solidification conditions. It is suggested to go further and perform a quantitative prediction on the resulting intensity and pattern of macrosegregation for the future industrial action.

3) It is suggested to perform further analyses on the impact of other parameters using the developed model. For the impact of the mold geometries and dimensions, continuous work can be conducted on the ingot size, the taper ratio of the mold, the length of the riser (hot-top) and the features of corrugations (numbers and angles of flutings) on the interior surface of the mold. For the impact of mold properties, the refractory of the mold components, such as the insulating tiles, and the exothermic capability of the board laid over the top of the ingot, are the elements which should also be considered in industry.

4) The present model is not capable of capturing enough details about the size and the number of positively segregated channels. Therefore, if the prediction of the occurrence of A- or V-segregates is needed, it is recommended to decrease the mesh size in order to attain a high spatial resolution in a relatively small scale (a few centimeters).

.

APPENDIX I

ARTICLE 7 EFFECT OF SEGREGATED ALLOYING ELEMENTS ON THE HIGH STRENGTH STEEL PROPERTIES: APPLICATION TO THE LARGE SIZE INGOT CASTING SIMULATION

Chunping Zhang[1, ✉], Davood Shahriari[1], Abdelhalim Loucif[1], Mohammad Jahazi[1], Louis-Philippe Lapierre-Boire[2] and Rami Tremblay[2]

[1]École de technologie supérieure, 1100 Notre-Dame Street West, Montreal, Quebec H3C 1K3, Canada
[2]Finkl-Steel-Sorel, 100 McCarthy Street, Saint-Joseph-de-Sorel, Quebec J3R 3M8, Canada

AI.1   Abstract

Macrosegregation is one of the most significant defects which exert a determining effect on the properties of heavy ingots. The objective of this work is to study the influence of segregated solute elements on the physical and mechanical properties of a medium carbon high strength steel during large ingot casting process. The solidification process of a 20 Metric Tons (MT) ingot is simulated using Thercast® FEM code. Different segregation levels of solute elements are picked up from a section along the longitudinal axis in the top of the ingot. Input steel data, including physical and mechanical properties, are determined by means of Thermo-Calc®, JMatPro and a material database. Casting parameters are selected according to actual industrial operational conditions used for casting of large size ingots. Thermic and thermomechanic simulations are employed for calculating the solidification time. Results are analyzed in the framework of diffusion-controlled solidification theory and the influence of alloying elements.

Keywords: medium-carbon steel, large size ingot, segregated alloying elements, casting

AI.2 Introduction

For the production of large size mono-block forgings of high-quality multi-component special steels, such as the shaft rotor for steam turbine and the pressure vessels for nuclear reactor, ingot casting is the only method. Macrosegregation, as a compositional heterogeneity, is one of the most significant defects occurring during the solidification process. It influences the thermophysical properties, affects the solidification behavior of casting, deteriorates the microstructure and mechanical properties, proves difficult to remove by subsequent thermo-mechanical treatment, and has haunted the manufacturers over decades.

Macrosegregation can be controlled by optimization of casting metal composition, dimensions of the ingot and casting/solidification processes. Thus, the impact of ingot size (Liu et al., 2011), mold temperature (Zhang et al., 2011), pouring superheat (Pikkarainen et al., 2016), pouring velocity (Zeng et Chen, 2015), cooling rate (Xu, Yin et Nagai, 2006), and steel composition (Shahriari et al., 2015) on the severity of macrosegregation has been investigated extensively. In order to free from the timely and costly 'trial and error' approach, finite element method (FEM) has been used for the simulation of the casting and solidification process. Numerical methods, however, generally use the input data of the fixed initial nominal composition. In reality, the solidification behavior is not only the nominal composition and processing parameters dependent but also varies with individual segregation domains. This study, therefore, was initiated to explore the effect of different segregation levels of solute elements on the material physical and mechanical properties, the solidification and cooling behavior as well as the solidification time so as to approximate the actual solidification process in large size castings. It will be of experimental and industrial significance for the macrosegregation research, the production process design and optimization of ingot manufacturing efficiency.

For this, three-dimensional thermic and thermomechanic simulations of the solidification process of a 20 MT steel ingot were performed using Thercast®8.2 version FEM code (TherCast 8.2®, 2012). Casting parameters were selected according to the actual industrial operational conditions. All the needed data are seldom available in the literature, especially

for the steels like the medium carbon low-alloyed multicomponent steel in study. It is known that even small variations in the composition may have a significant effect on the material physical and mechanical properties. Thus, the input steel data, including physical and mechanical properties, were determined by means of Thermo-Calc® and JMatPro. Modeling results were analyzed in the framework of diffusion-controlled solidification theory and the influence of segregated solute alloying elements. It should be mentioned that mesh size optimization for computation cost minimization and sensitivity analysis of the results have been performed and its selection was based on the analysis results.

AI.3 Material and methods

A cylindrical steel ingot was cast in a cast-iron mold. The steel melt composition is listed in Table AI-1. Molten steel was poured from the mold bottom at about 1570 °C and a layer of exothermic powder was over laid on the melt top. A hot-top, made of cast iron and lined with refractory materials inside, was placed on the top of the steel ingot. After solidification and stripping out, the hot-top with 30 cm's head of the ingot was transversely cut off for the study purpose. A plate with about 2.5 cm in thickness was sliced on one side of the axial plane, as shown in Figure AI.1a. The slice was then sectioned into over 200 samples and faces in the centerline plane along the longitudinal axis of all the samples were subject to grinding, and then chemical mapping using the Thermo Scientific ARL™ 4460 mass spectrometer. The chemical composition of specimen was obtained by averaging out 3 random spectrometer measurements. Segregation maps of different elements in the longitudinal section of the hot-top and 30 cm head of ingot were then reconstructed and macrosegregation patterns were identified.

Typical thermophysical data including the temperature dependence of the density, the specific heat capacity, and the phase transformation temperatures of selected segregated solute levels were determined by means of the computational thermodynamics program Thermo-Calc® classic version R with the TCS Fe-containing slag database (Andersson et al., 2002). Thermomechanical behaviors, such as yield stress, Young's modulus, strain hardening exponent and strain-rate sensibility coefficient and their variations as a function of temperature were developed with the help of JMatPro software, version 9.0 (Sente Software

Ltd., 2005). The simulations of solidification were performed in the finite element code Thercast® by using an Arbitrary Lagrangian-Eulerian (ALE) formulation for computing the thermal convection in liquid pool and mushy zone, and Lagrangian for calculating the deformation in solid regions. The method is applied both to mold filling simulation, where it can provide accurate free surface description, and to the study of thermo-mechanical phenomena occurring in the subsequent cooling down of cast parts: prediction of distortions and stresses.

Table AI-1 Chemical composition of the investigated steel and the four positions in the upper region of the ingot (Wt.%).

	C	Mn	P	S	Si	Ni	Cr	Mo	Cu
Nominal	0.35	0.82	0.007	0.002	0.4	0.15	1.79	0.46	0.13
1	0.33	0.82	0.01	0	0.39	0.17	1.83	0.39	0.13
2	0.6	0.94	0.024	0.002	0.5	0.18	2.1	0.52	0.15
3	0.37	0.86	0.013	0.001	0.4	0.17	1.92	0.44	0.14
4	0.44	0.86	0.015	0.001	0.42	0.17	1.89	0.43	0.14

AI.4   Results and discussions

Solute distribution along the centerline longitudinal axis of the ingot presents sort of symmetry which confirms the formation of type A macrosegregation. The concentrations of all the elements increase continuously from the ingot lower bordering part to the center upper region, attesting that the liquid-solid interface has set off from the mold wall and globally advanced inwards and upwards to the last region to solidify located at the top center due to the efficient thermal protection of the hot-top. Concentrations of most elements in both the hot-top and the head of the ingot are higher than the nominal one, which indicates that positive segregation has taken place in these regions. As seen in Figure AI.2b, the concentration profiles of carbon and chromium along the lines at the top and the bottom of the section in study display all the above-mentioned characteristics. Four representative segregation levels, corresponding to the highest and lowest segregation severity along the ingot centerline and the line next to the mold, were picked up for the analysis. Their chemical

compositions are provided in Table AI-1 also in order to facilitate the comparison with the nominal composition. Their positions in the section are labeled in Figure AI.1a. The numbers given to the four positions are kept consistent hereinafter. The segregation severity level of solute elements in the four studied sites can be sequenced in descending order as 2 > 4 > 3 > 1.
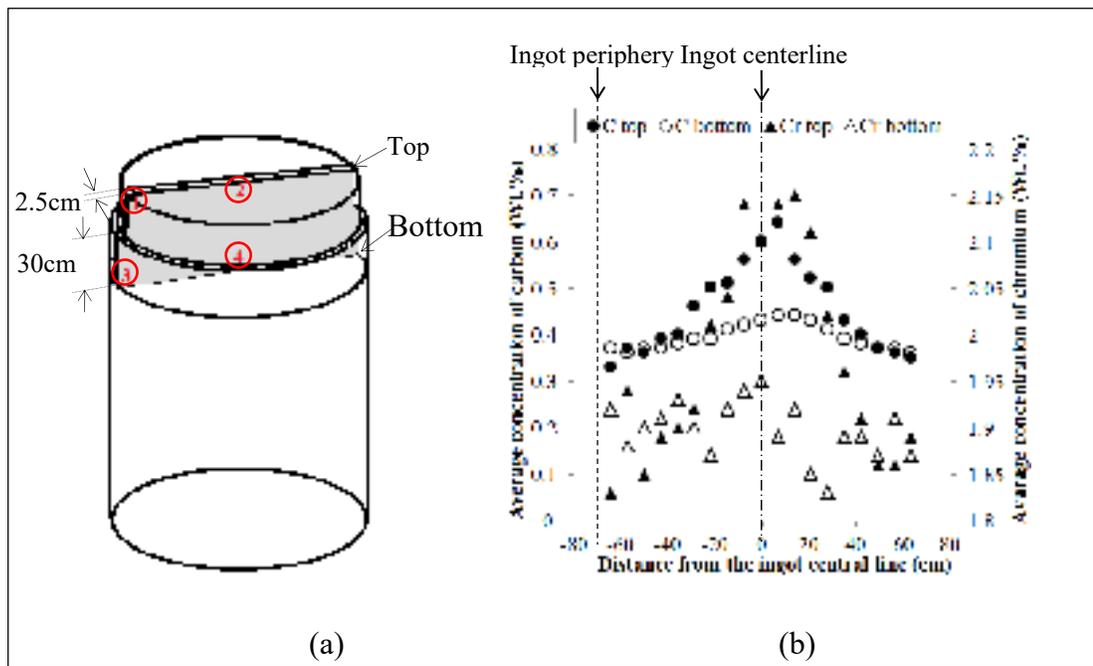
Figure AI.1 Cutting Diagram of the ingot and concentration profiles. a) Cutting diagram of the ingot for chemical analysis and the four analyzed positions (b) Concentration profiles of carbon and chromium along the lines at the top and bottom of the sectioned slice.

AI.4.1   Solidification model description

Considering continuum medium as illustrated in Figure AI.2, different behaviors of the metal are distinguished by the critical temperature T_c, above which a thermo-viscoplastic behavior is considered and below which a thermo-elasto-viscoplastic one (TherCast 8.2®, 2012). In order to take into account the complex behavior of solidifying alloys, a hybrid constitutive mold was used. In the liquid state, the metal was treated as a Newtonian fluid and the Navier-Stokes equation with temperature-dependent terms were employed. When the metal begins to

solidify, the alloy in the mushy state was modeled as a non-Newtonian fluid obeying a Thermo-viscoplastic Norton-Hoff law. In the calculation of the deformation in solid regions using Lagrangian formulation, the computational grid was allowed to move with the material: this was essential to treat the air gap between mold and the casting. The liquid contraction and the solidification shrinkage were taken into consideration when the ALE scheme was applied to compute the thermal convection in liquid pool and mushy zone so as to prevent the mesh from degenerating and allow tracking the free surfaces.

	0 ——— Solid fraction ———→ 1		Temperature
Liquid	Semi-liquid	Semi-solid	Solid
	$T_{liquidus}$	T_c	$T_{solidus}$
Newtonian	Thermo-visco-plastic	Elasto-visco-plastic	Elasto-plastic
Navier-Stokes	Northon-Hoff	Perzyna	
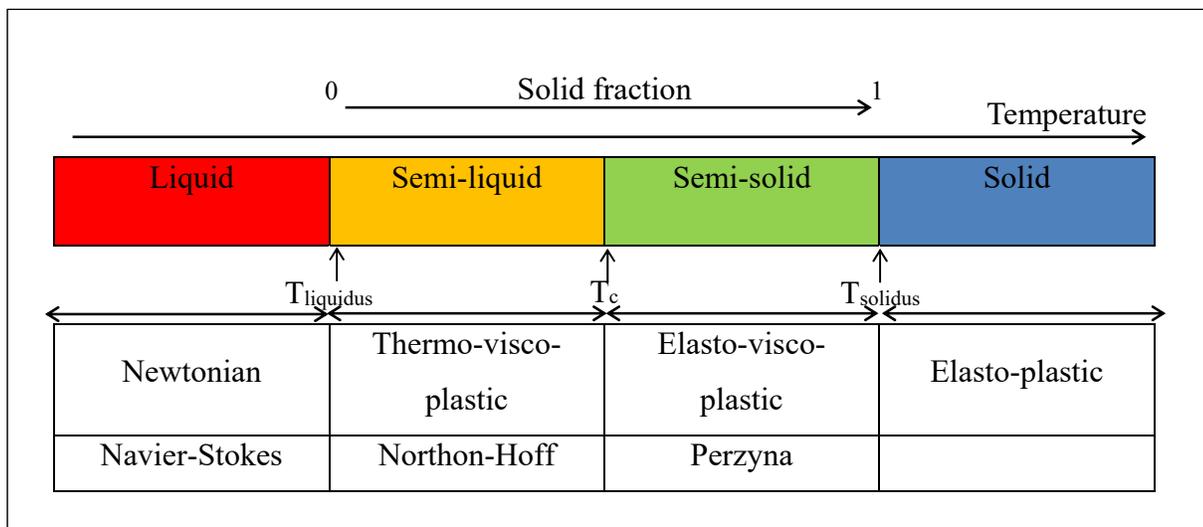
Figure AI.2 Material behaviors depending on its condition in the process of solidification (TherCast 8.2®, 2012).

3D linear tetrahedral elements were used for the discretization of the part and mold components. The unilateral contact condition (loss of contact, that is separation, is accepted) was applied to the boundary between mold and casting. In the resolution stage, a coupled computation of the stress and temperature fields was performed so that equations were solved iteratively using a prescribed time step. Due to the symmetry conditions of the casting system, only one quarter of the 20 MT ingot was modelled, the configuration of which is displayed in Figure AI.3. The mold was considered as non-deformable. The finite element mesh of the solidification system consisted of 1,190,000 elements which were selected based on several mesh refinement studies.
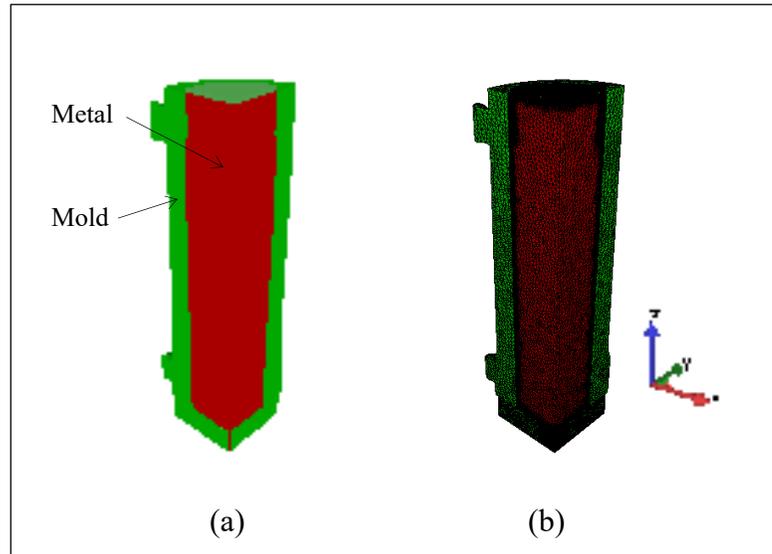
Figure AI.3 (a) Geometry of the cast part (b) Finite
element mesh of the casting and of the mold.

AI.4.2   Effect of segregation levels on physical properties

Different segregation levels result in the change of the kinetics of phase transformations, and then the difference in thermophysical and mechanical properties related to the phases formed. Figures AI.4a and b show the evolution of solid fraction and density with the temperature for the four selected segregated compositions, respectively. As mentioned above, the segregation severity for the four representative positions in descending order is $2 > 4 > 3 > 1$. It can be seen from Figure AI.4 that the evolution of physical properties is in reverse order to the segregation severity level. Lower segregation results in the progressive augmentation of phase transformation temperature, including the solidus, liquidus and the transformation point from delta ferrite (δ) to austenite (γ). In the highest segregation level, the position 2, no δ - γ transformation took place. In addition, lower segregation levels induce smaller temperature differences between the solidus and liquidus, corresponding to slightly higher element liquid/solid partition coefficient. The observed increased density in lower segregation level may be attributed to more alloying elements dissolved. Such tendency in

the density evolution agrees well with the experimental analysis results which indicated low concentration of small porosities in the ingot's center upper region.
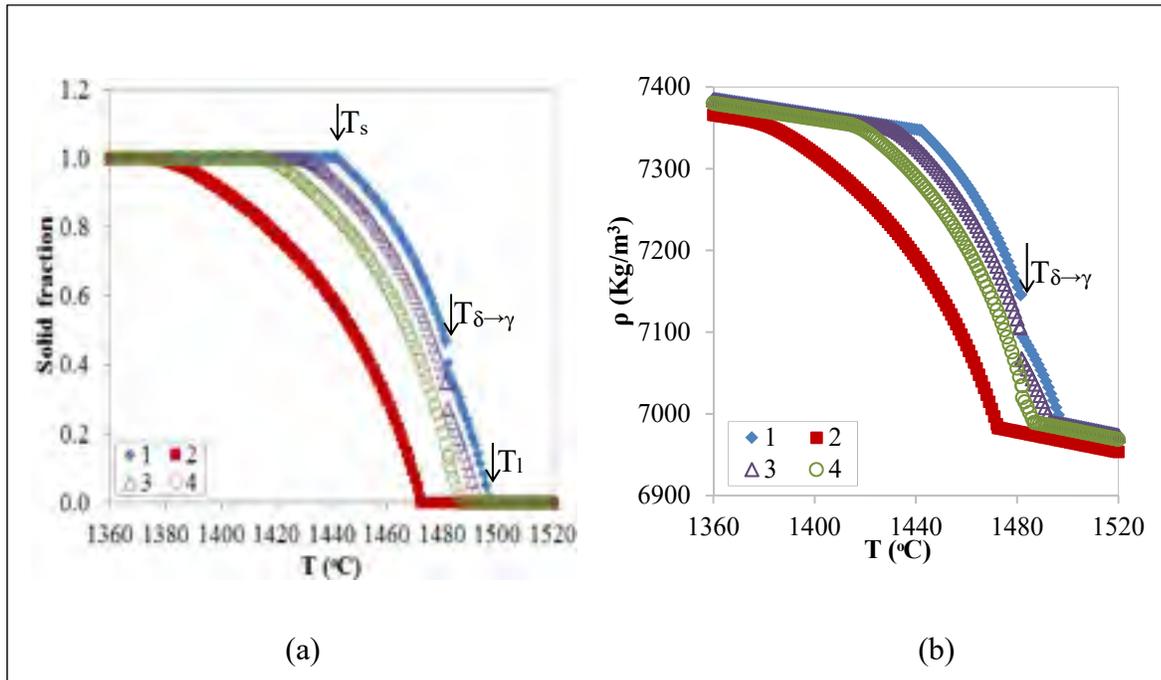
Figure AI.4 Temperature dependence of physical properties for different segregation levels. (a) Solid fraction (b) Density.

The difference in segregation levels, in the meantime, brings about the discrepancy in elastic and plastic behaviors, as observed in Figure AI.5. The evolution of the liquid viscosity displays the same decreasing trend with the increase of the segregation severity. The reported deterioration effect of higher content of alloying elements on toughness and plasticity is in accordance with the calculation results (He, 2015). The reduction of density with the increased severity level of segregation may also be the reason. The solute diffusion coefficient in liquid is discovered, based on Stokes-Einstein equation (Miller, 1924), inversely proportional to solvent viscosity. Thus, the diffusion coefficients in liquid in the four positions can be sequenced as $D2 > D4 > D3 > D1$, in agreement with the segregation severity descending order. All these variations in properties due to different segregation levels affect the heat transfer, convection and radiation modes, as well as stress and

deformation domain during mold filling, cooling down and the progressive solidification of the ingot.
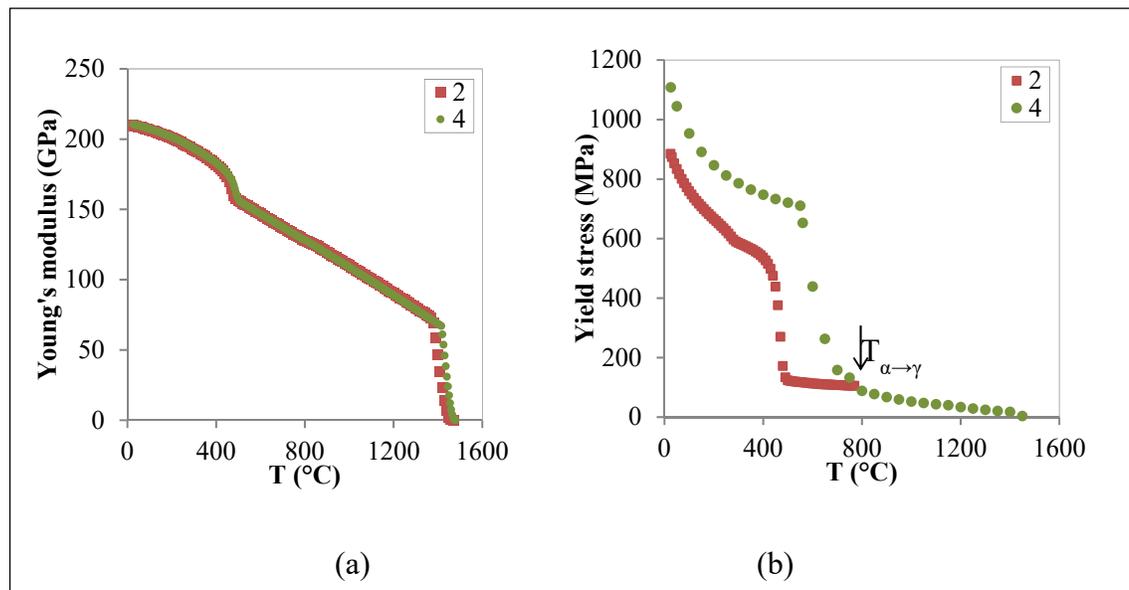
Figure AI.5 Evolution of mechanical properties with segregation severity levels.
Young's modulus (b) Yield Stress

AI.4.3 Effect of segregation levels on solidification time and temperature gradient

The knowledge of solidification time of a large size ingot in the industry is of quite importance in that shorter solidification time will not allow achieving solid state at the center of the ingot and longer time will result in increased segregation levels and porosities. Therefore, solidification time is taken as the simulation result to discuss. Solidification times needed for the four analyzed positions in the casting are different and vary with the segregation severity level. Specifically, solidification time at the center is longer than the one in the mold side, as presented in Figure AI.6. It should be noted that for presentation purposes, the simulation was stopped for a maximum temperature of 1000 °C to make sure that solid state is achieved at the center of the large size ingot. The observed evolution of solidification time with the percent carbon was approximated with a second degree

polynomial function and is illustrated in Figure AI.6, where y is the solidification time and x carbon weight composition. As indicated in the figure, the solidification time attains its peak value at 0.513 wt.% carbon, corresponding to the composition located in the interface between the ingot and the hot-top, which probably concerns the pipe formation and the time for its creation

$$y = -46.474x^2 + 47.661x - 3.3446$$
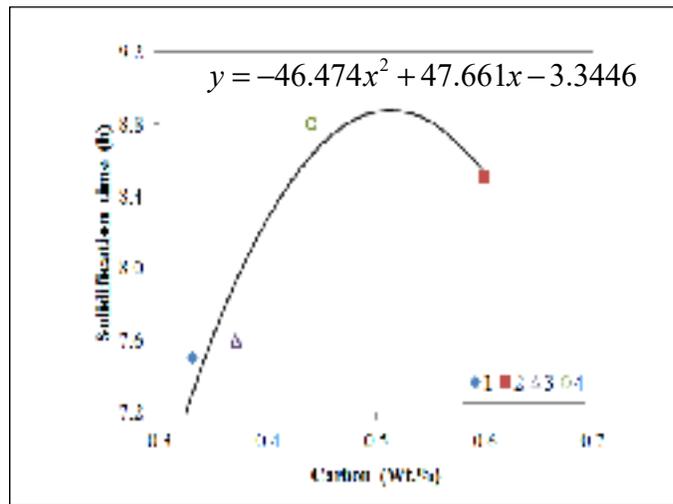
Figure AI.6 Plot of solidificaiton time as a
function of weight percentage of carbon.

Figures AI.7 and AI.8 illustrate respectively the thermic and thermomechanic simulations of the cooling of the cast part with the composition of the position 4 until the solidus temperature, 1414 °C, is reached. It can be seen that the solidification time decreases around 25 minutes, passing from about 8 hours 48 minutes to 8 hours 23 minutes or so when the influence of the solid deformation is taken into account. According to the simulation results, although the last region to solidify is always located at the top center of the hot-top, solid mechanical deformation gives rise to the alteration of thermal gradient, particularly in the interior of the ingot. The free surface can be seen almost flat in Figure AI.8 because of an efficient thermal protection which minimizes the thermal gradient in the hot-top.
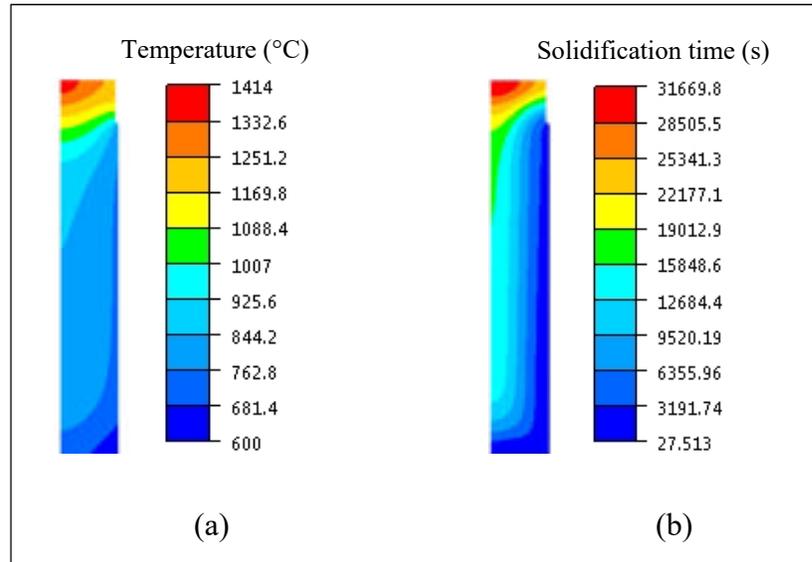
Figure AI.7 Thermic simulation (a) Temperature
distribution (b) Solidification time after 100 %
solidification of position 4.
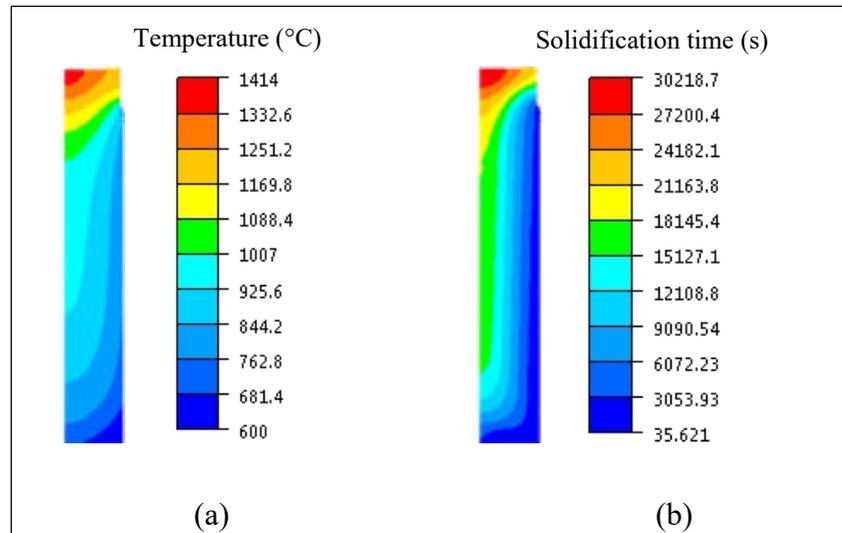
Figure AI.8 Thermomechanic simulation (a) Temperature
distribution (b) Solidification time after 100% solidification
of position 4.

AI.5   Conclusions

This research presented a study on the effect of different segregation levels on the solidification behavior of a 20 MT steel ingot. Comparison analyses of the physical and mechanical properties of representative segregation levels were performed by means of softwares like Thermo-Calc® and JMatPro. Solidification time of varied segregation severities was calculated through thermic and thermomechanic simulations of the mold filling and cooling behavior of steel ingot using Thercast® FEM code. The following main conclusions can be made from this study:

1) The evolution of physical properties and elastic/plastic behaviors is in reverse order to the segregation severity level due to different solute diffusion coefficient in liquid and higher content of alloying elements.

2) By increasing the segregation severity level, solidification time increases. Solid mechanical deformation gives rise to the alteration of thermal gradient and the decrease of solidification time.

AI.6   Acknowledgements

APPENDIX II

ARTICLE 8 EFFECT OF THERMO-PHYSICAL PROPERTIES OF SOLIDIFICATION BEHAVIOR OF LARGE SIZE HIGH STRENGTH STEEL INGOTS

Chunping Zhang✉ , Davood Shahriari[1], Abdelhalim Loucif[1], Mohammad Jahazi[1], Louis-Philippe Lapierre-Boire[2] and Rami Tremblay[2]

[1]École de technologie supérieure, 1100 Notre-Dame Street West, Montreal, Quebec, H3C 1K3, Canada;
[2]Finkl-Steel-Sorel, 100 McCarthy Street, Saint-Joseph-de-Sorel, Quebec, J3R 3M8, Canada

AII.1   Abstract

The impact of different microsegregation models on solidification behavior of large size steel ingots was investigated. The microsegregation models include the ideal equilibrium solidification equation, the extreme Scheil-Gulliver, and the non-equilibrium equations. Different dendritic solidification equations were used to study the evolution of the properties and the cooling process of a 40 Metric Tons (MT) ingot of a medium carbon high strength steel. Material thermophysical properties were determined by means of thermodynamic softwares FactSage® together with various proposed models from the literature and the thermal simulations were done using Thercast® FEM code. The results obtained in this study demonstrate the significant influence of microsegregation model on temperature dependent solid fraction profiles, thermophysical properties, thermal field and solidification time needed for the casting of the large size ingot, which ultimately affect the extent of macrosegregation.

Keywords: steel, large size ingot, casting simulation, thermo-physical properties, equilibrium model, non-equilibrium models

AII.2   Introduction

Macrosegregation, as a compositional heterogeneity, is one of the most significant defects occurring during the solidification process. It exerts a determining effect on the properties of

heavy ingots and has proved difficult to remove. For a broad understanding of the practical processes involving the formation and development of macrosegregation, computer simulation is the most economical and fastest approach. However, reliable prediction of concentration segregation during ingot casting greatly depends on the reliability and precision of the input parameters concerning solute redistribution in the solidification processes. The latter are determined by dendritic microsegregation models (Fridberg, Torndahl et Hillert, 1969). It is the microsegregation of elements on the dendritic scale which ultimately leads to enrichment of the liquid and macroscale advection of species. Therefore, the selection of the microsegregation model will have a direct impact on the outcome of any macrosegregation prediction tool.

The objective of the present work is to investigate the effect of microsegregation model selection on temperature dependent solid fraction profiles, thermophysical properties and solidification behavior of a medium-carbon high strength steel. For this, notable analytical or semi-analytical treatments of solute redistribution problem were summarized, including the ideal equilibrium lever-rule equation (Smith et Hashemi, 2006), the extreme non-equilibrium Scheil-Gulliver treatment (Scheil et Metallk, 1942), as well as other microsegregation models presented by Brody Flemings (Flemings, 1974), Clyne and Kurz (Clyne et Kurz, 1985), Kobayashi and Ohnaka (Kobayashi, 1988), respectively. These microsegregation models were applied to determine thermophysical properties of the steel using thermodynamic softwares FactSage® (Bale, 2017), together with various proposed models from the literature. Three-dimensional thermic simulations of the solidification process of a 40MT steel ingot were performed using Thercast® 8.2 version FEM code [8] with casting parameters selected according to the actual industrial operational conditions.

AII.3   Microsegregation models

In the dendritic solidification process, solute diffusion in the liquid, which is at the origin of microsegregation, is complete. Hence, interdendritic microsegregation models are formulated by dealing with the diffusion in the solid phase, described by the relationship between the solute concentration at the growth solid/liquid interface ω_s and the solid fraction f_S. Solute

diffusion in the solid depends on the value of the dimensionless back-diffusion Fourier number α (Clyne et Kurz, 1985):

$$\alpha = D_S\left(t_f/l^2\right) \tag{AII.1}$$

where D_S is the solute diffusivity in the solid, t_f is the diffusion time (local solidification time) and l is the diffusion distance (half of the dendrite spacing d).

If $\alpha \gg 1$, the diffusion is assumed to be so intense that the composition is always uniform within each phase (i.e. the system is always in thermodynamic equilibrium), then the solidification behavior is described by the classical lever rule written as $\omega_s = k\omega_0/\{(1-f_S)+kf_S\}$, predicting the changing composition of the solid at the solid/liquid interface during solidification (Smith et Hashemi, 2006). Here, ω_0 is the original composition, and k is the partition coefficient. The above equation can also be expressed as the variation of the local solid fraction f_s in terms of the system temperature:

$$f_s = \{1/(1-k)\}\{(T_l - T)/(T_f - T)\} \tag{AII.2}$$

where T_l is the liquidus temperature, T_f is the melting temperature for pure iron.

If $\alpha \ll 1$, the diffusion in the solid can be ignored. Then a complementary limit case to the lever rule can be used, i.e. $\omega_s = k\omega_0(1-f_s)^{k-1}$, or again expressing the local solid fraction at a temperature (Scheil et Metallk, 1942):

$$f_s = 1 - \{(T_f - T)/(T_f - T_l)\}^{1/(k-1)} \tag{AII.3}$$

which is often referred to as the Scheil-Gulliver or Scheil equation.

The actual freezing behavior, however, is expected to lie somewhere between the above two extremes, depending on the importance of solid state diffusion. Therefore, various models have been put forward to quantify the effect of solid state diffusion for the intermediate states between the Scheil and lever rule cases. Under these conditions, the following assumptions are made for the analysis (Clyne et Kurz, 1985): straight liquidus and solidus lines of the

concerned phase diagram (i.e. a constant partition coefficient k), a constant diffusion coefficient, a plate-like or cylindrical dendrite geometry, a single phase in the solid (an abrupt occurrence of δ-ferrite/γ-austenite transformation), and a parabolic ($v = \sqrt{t/t_f}$) or linear local solid/liquid interface advance velocity ($v = L/t_f$).

Brody and Flemings were the first to analyze the solid state diffusion based on a one-dimensional solute redistribution model and presented $\omega_s = k\omega_0\{1 - (1 - 2\alpha k)f_s\}^{(k-1)/(1-2\alpha k)}$ of a decreasing parabolic behavior for the solid/liquid interface advance (Flemings, 1974). The above equation can also be expressed as:

$$f_s = [1/(1 - 2\alpha k)]\left\{1 - [(T_f - T)/(T_f - T_l)]^{(1-2\alpha k)/(k-1)}\right\} \tag{AII.4}$$

Clyne and Kurz modified the Brody-Flemings model by introducing a parameter, $\Omega(\alpha)$, to be substituted for α in Eq.(AII.4) to limit the errors introduced by the geometrical simplifications involved in the Brody-Flemings model (Clyne et Kurz, 1985):

$$\Omega = \alpha\left\{1 - exp\left(-\frac{1}{\alpha}\right)\right\} - \left(\frac{1}{2}\right)exp\left\{-\frac{1}{2\alpha}\right\} \tag{AII.5}$$

Kobayashi proposed an extended mathematical model, incorporating a thermal model of solidification into the analysis, and solved more rigorously Brody-Flemings model with parabolic growth. His equation was found to coincide with the equation derived by Ohnaka on the basis of a profile method (Kobayashi, 1988) $\omega_s = k\omega_0\{1 - [1 - 2\alpha k/(1 + 2\alpha)]f_s\}^\eta$ and:

$$f_s = [(1 + 2\alpha)/(1 + 2\alpha - 2\alpha k)]\left\{1 - [(T_f - T)/(T_f - T_l)]^{1/\eta}\right\} \tag{AII.6}$$

$$\eta = (k - 1)(1 + 2\alpha)/(1 + 2\alpha - 2\alpha k) \tag{AII.7}$$

AII.4   Material and methods

The composition of the investigated steel is listed in Table AII-1. Typical thermophysical data including the liquidus temperature (1492 °C), partition coefficients k_δ (0.82) and k_γ

(0.4053) as well as the δ/γ phase transformation temperatures (1478 °C) were determined by means of the computational thermodynamics program FactSage® version 7.0 (Bale, 2017).

Table AII-1 Chemical composition of the investigated steel (wt.%).

C	Mn	P	S	Si	Ni	Cr	Mo	Cu
0.35	0.82	0.007	0.002	0.4	0.15	1.79	0.46	0.13

It was assumed that the primary dendrite arm spacing d_1 is equal to the secondary dendrite arm spacing d_2. Hence, the Fourier number α was determined via the empirical expression for low-alloyed steels relating the secondary dendrite arm spacing d_2 (in μm) to the constant cooling rate C_R (in °C/s) and the local solidification time t_f (in s) (Suzuki et al., 1968):

$$d_2 = 150 C_R^{-0.385} = 150 \times \left[(T_l - T_s)/t_f\right]^{-0.385} \tag{AII.8}$$

where T_s is the solidus temperature in °C.

The temperature dependence of the effective thermal conductivity λ, specific heat capacity C_P and density ρ of the heterogeneous mixture of δ-ferrite, γ-austenite and liquid in the mushy state of the studied medium carbon high strength steel was calculated with the volume fractions and properties of each phase in the mushy state from the equations in reference (Miettinen et Louhenkilpi, 1994) for density and (Meng et Thomas, 2003) for thermal conductivity and specific heat, respectively.

The thermal simulations of the solidification process of a 40 MT ingot were performed in the finite element code Thercast® with a maximum temperature of 800 °C as the stop signal to make sure that solid state is achieved at the center of the large size ingot. All the details of the models can be found in references (Shahriari et al., 2015; Zhang et al., 2017).

AII.5   Results and discussions

AII.5.1   Effect of microsegregation models on solid fraction profiles

An indication of the determination of Fourier number α for the steel based on Equation (AII.1) is given in Table AII-2, where the diffusivity (in $\mu m^2/s$) of carbon in austenite is taken as a mean diffusivity over the freezing interval from the expression (Gorni et SP, 2015):

$$D_s(m^2/s) = 0.1 \times 10^{-4} \times exp\big(-16321.9/T(K)\big) \qquad (AII.9)$$

Here, only the segregation of carbon is considered. Three cases of dendritic arm spacings were investigated, and assumed to be representative of the structure's size of the ingot wall side, radial midway, and the center. It was found that α values tend to increase from the ingot wall side chill zone to the center. This corresponds to the increase of the dendritic arm spacing and then local freezing time from the surface to the center.

Table AII-2 Calculated solidification parameters for the current steel.

d_2 (μm)	t_f (s)	α
2	0.0009	0.616
20	0.36	2.44
200	142	11.27
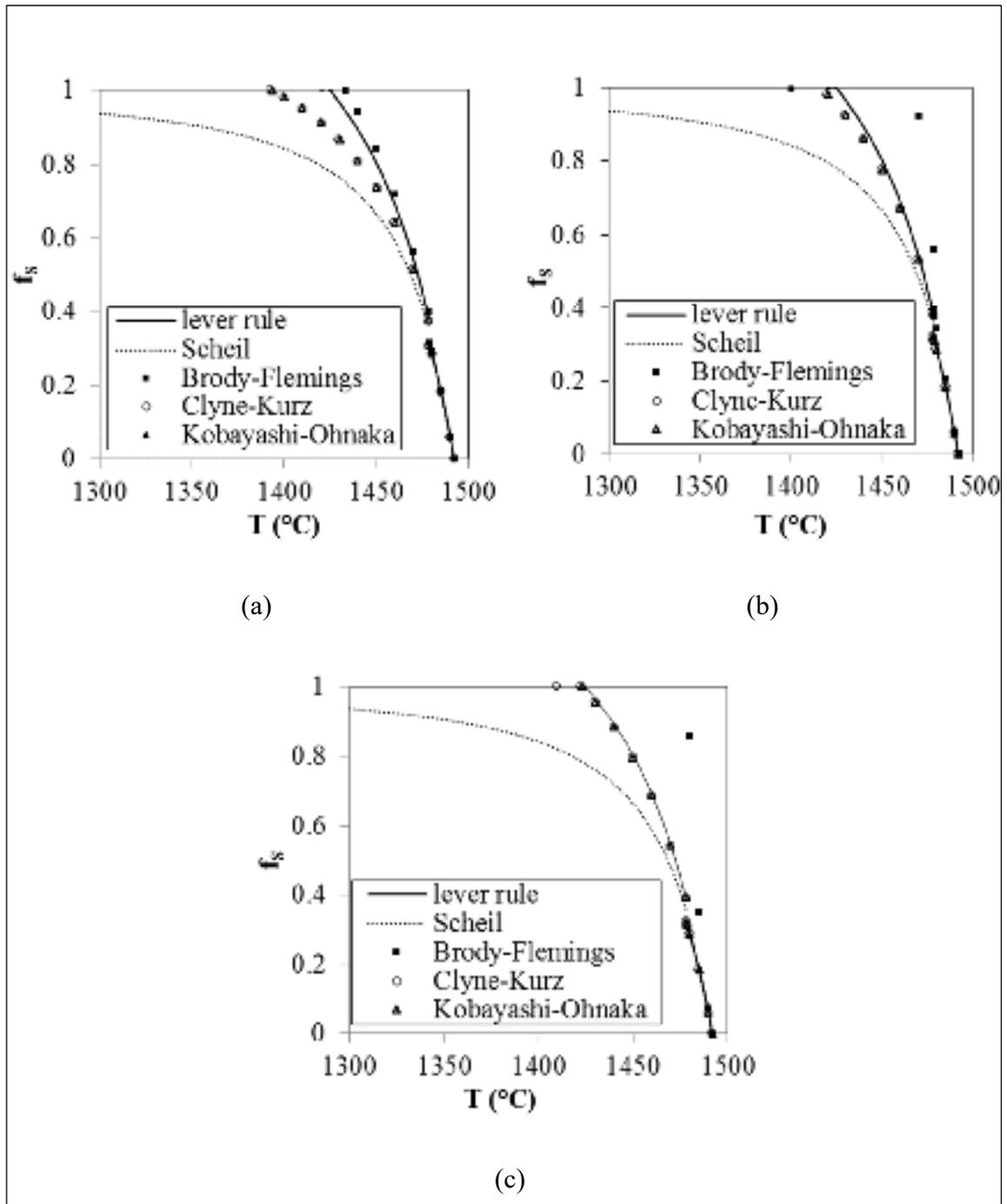
Figure AII.1 Predicted solid fraction/temperature curves for the investigated steel according to the classical limiting cases and the proposed models over a range of Fourier number values (a)$\alpha = 0.616$ (b) $\alpha = 2.44$ (c) $\alpha = 11.27$

Figure AII.1 shows the dependence of local solid fraction within the mushy zone on local temperature for the steel over the investigated range of Fourier number values according to different models (Equations (AII.2 – AII.7)). It is clear that large values of α lead to physically impossible curves predicted by Brody-Flemings in that the temperature at which solidification is complete lies above the equilibrium solidus. Similar errors predicted by Brody-Flemings equations have also been reported by others (Clyne et Kurz, 1985; Kobayashi, 1988). It appears probable that the approximate equations derived by Brody-Flemings cannot be directly applied to large ingot cases. In contrast, the predictions made using Clyne-Kurz and Kobayashi-Ohnaka equations are similar. The latter two models may be regarded as better approximation for the diffusion behavior in the solid. Examination of Figure AII.1 also reveals that as α is increasing from 0.616 (Figure AII.1a) to 11.27 (Figure AII.1c), solute redistribution in the solid phase progressively becomes rather close to the lever rule. All the changes arose after the δ/γ transformation occurrence during the cooling process.

AII.5.2   Effect of microsegregation models on thermophysical properties and solidification behavior

Figure AII.2 shows the variation of material dynamic thermophysical properties as a function of local solid fraction in the mushy zone. Temperature dependent material thermophysical behaviors are found to be significantly influenced by dendritic solidification models.

When different thermophysical properties were used for thermal field computation of the solidification process, it was found that temperature distribution and solidification times correlate with the microsegregation models, as seen in Figures AII.3 and AII.4. Kobayashi-Ohnaka and Scheil models gave rise to distinctive higher thermal gradients than the classic equilibrium rule. Such higher thermal gradients could be responsible for the formation of channel segregates during the cooling process. In addition, the occurrence of less solute diffusion in solid resulted in higher ingot cooling times, passing from about 11 hours 48 minutes for complete solute redistribution determined by the lever rule to 29 hours 18 minutes for no solute diffusion in solid after Scheil mode. These findings indicate that the

latter two models would predict slower solidification process, leaving enough time for the solute-rich interdendritic liquid to redistribute in the ingot, aggravating macroscopic solute segregation.
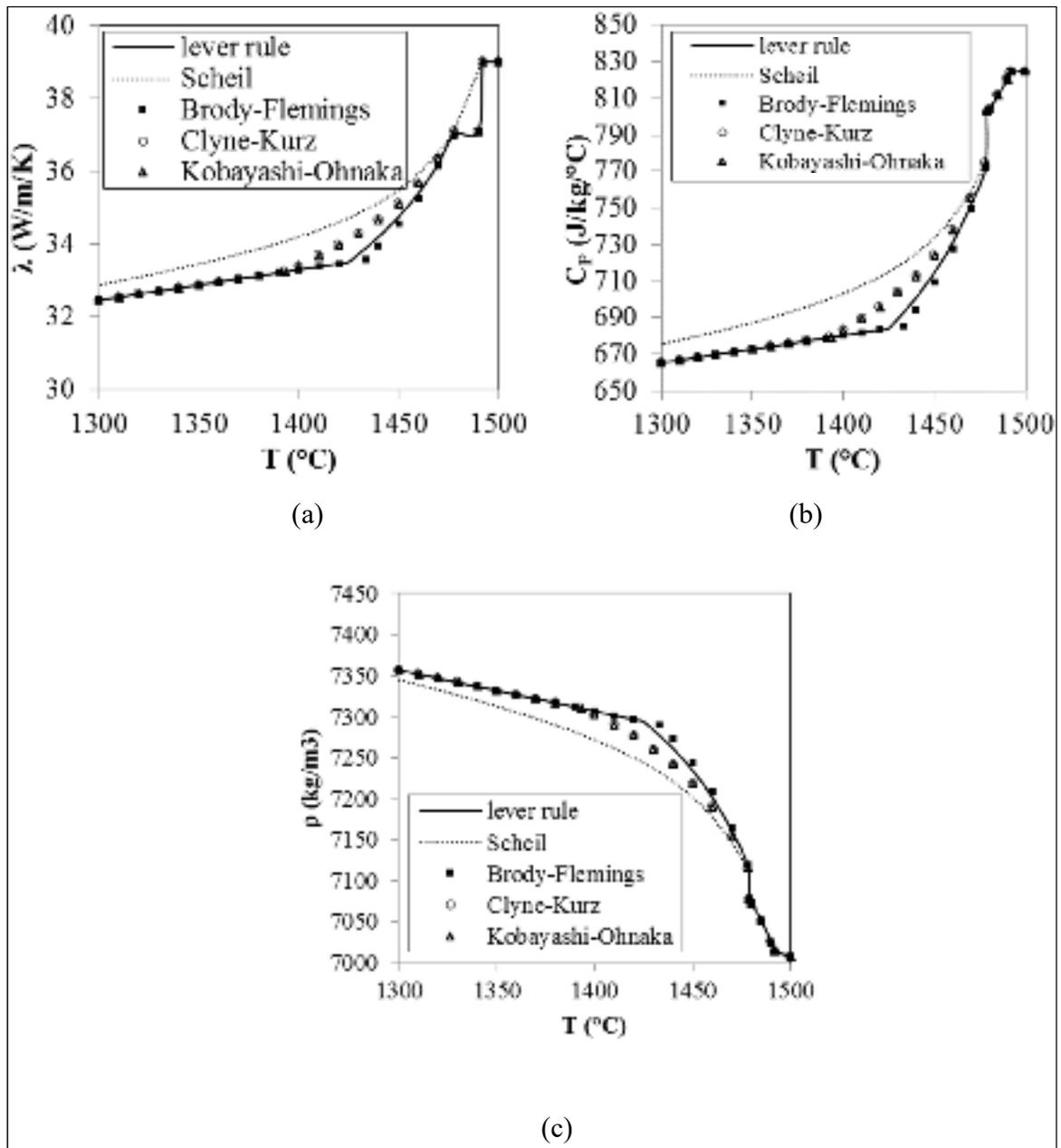
Figure AII.2 Temperature dependence of physical properties for the steel in study according to different microsegregation solidification models for the case $\alpha = 0.616$ (a) thermal conductivity (b) specific heat (c) density.
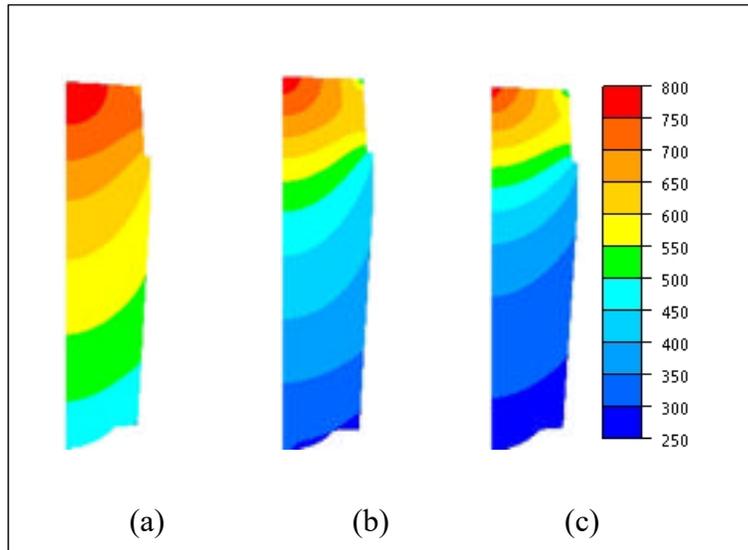
Figure AII.3 Temperature distribution (°C) of the
thermic simulation with the stop condition of 800°C
after different microsegregation models (a) lever rule
(b) Kobayashi-Ohnaka ($\alpha = 0.616$) (c) Scheil.

It should be noted that the empirical relationships used in this work (Equation AII.8) refer to secondary arm spacing measurements. But, the choice of dendritic arm spacing is rather uncertain, although it should probably lie somewhere between the primary and secondary spacings. In general, primary arm spacing is higher than the secondary arm spacing so that the calculated extent of diffusion would constitute a lower limit in this regard. Therefore, further work will focus on experimental microsegregation characterization to test the validity of the proposed microsegregation models and the empirical relationships used to calculate the Fourier number for the purpose to apply the analysis results to macrosegregation modeling.
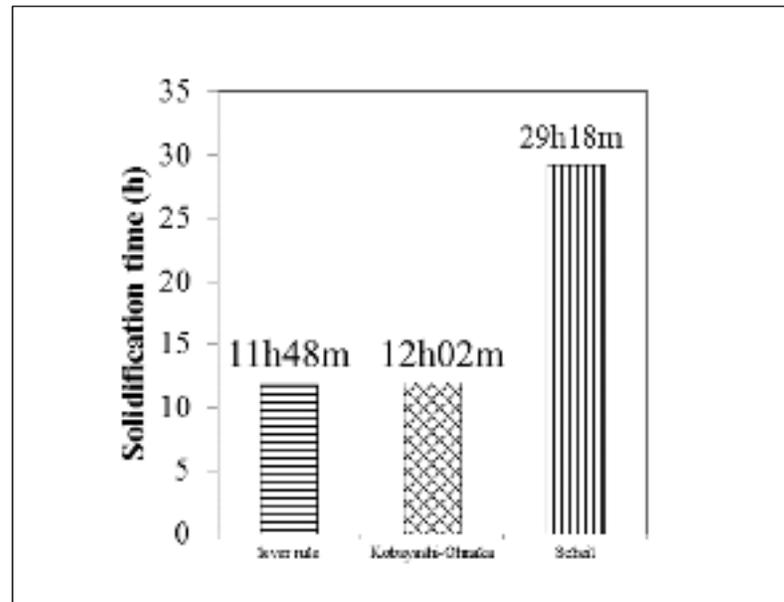
Figure A 0.4 Total solidification time (s) for thermic simulations stopping at 800 °C as the maximum temperature based on microsegregation models of lever rule, Kobayashi-Ohnaka ($\alpha = 0.616$) and Scheil.

AII.6   Conclusions

1) Microsegregation model selection can significantly influence the prediction of the local solid fraction within the mushy zone.

2) For large size steel ingot, solidification behavior next to the chill zone are close to an intermediate state between the extreme lever rule and Scheil equations, while the central part behaves approximatively in the equilibrium state.

3) For the investigated microsegregation models, Brody-Flemings approximation appears not applicable for large ingot cases; Clyne-Kurz and Kobayashi-Ohnaka models can predict similar results, which may be regarded as better approximation for the diffusion behavior in the solid.

AII.7   Acknowledgement

APPENDIX III

ARTICLE 9 INFLUENCE OF NON-UNIFORM TEMPERATURE DISTRIBUTION OF THE MOLD ON SOLIDIFICATION BEHAVIOR IN LARGE SIZE STEEL INGOTS

Chunping Zhang[1, ✉], Abdelhalim Loucif[1], Rami Tremblay[2], Mohammad Jahazi[1]

[1]École de technologie supérieure, Department de Mechanical Engineering, 1100 Notre-Dame Street West, Montreal, Quebec H3C 1K3, Canada
[2] Finkl Steel-Sorel, 100 McCarthy Street, Saint-Joseph-de-Sorel, Quebec J3R 3M8, Canada

AIII.1   Abstract

The influence of initial non-uniform temperature distribution of the mold on solidification behavior in a large size ingot of high strength steel was numerically studied. Finite element modeling on a uniform initial mold temperature case was also performed for comparison. The thermic analyses of the filling and solidification processes were employed in a pseudo-2D model, which were realized using commercial Thercast® software. Pure heat conduction was considered to be the only heat transfer manner. It was predicted that non-uniform initial temperature condition of the mold led to asymmetry in the temperature field, temperature gradient and solidification speed in the casting. This finding is a great contrast to the symmetry patterns in the casting of the case with uniform initial mold temperature. In addition, a higher temperature on one side of the mold tended to retard the proceeding of solidification. This thermal asymmetry and the solidification lag can influence the distribution alloying elements during the cooling process of the large-sized cast ingots, and should be an attention-worth problem in actual industry production. The predicted results were verified with the experimental measurements and discussed in the framework of heat transfer and solidification mechanisms.

Keywords: large size steel ingot, non-uniform mold temperature condition, temperature field, solidification speed, verification of model

AIII.2   Introduction

Large size steel ingots made of high strength steels suffer from the occurrence of chemical heterogeneities, so-call macrosegregation, which result in non-uniform microstructures and mechanical properties. Therefore, their extent and severity need to be controlled. The ingots are often cast inside pits close to a wall or other ingots due to space limitation. These spatial constraints could result in non-uniform-temperature distribution through the diameter and along the height of the mold. Such non-uniformities may induce different solidification patterns, thereby affecting macrosegregation severity and extent in the cast ingots. However, the effect of different casting spatial configurations on the solidification properties is still not clear and needs to be quantified (Pikkarainen et al., 2016; Galkin et al., 2013; Dub et al., 2014; Zhang et al., 2018).

In the present work, the influence of initial temperature distribution pattern on solidification behavior of a 40MT steel ingot was numerically studied. The finite element modeling of the bottom pouring, filling and solidification process of a 40 MT (metric ton) steel ingot was realized using the Finite Element Code Thercast$^{®}$ and a pseudo-2D model (Transvalor, S.A., Cedex, France). Two cases were studied: one was with uniform initial thermal condition on the mold, and the other with different initial temperature levels on the opposite sides of the mold. The temperature field and solidification rate were compared between the two case studies. Material properties were obtained from the literature and authors' experimental work (Zhang et al., 2018). The thermal predictions were compared with the thermal measurements from the casting experiments. The predicted results are discussed in the framework of heat transfer and solidification mechanisms.

AIII.3   Establishment of model

The pseudo-2D model used in the present study was first established using the commercial CAD software CATIA$^{®}$ (CATIA V5 R20, Avions MARCEL DASSAULT, France) and then

transferred into finite element (FE) code Thercast® (Transvalor, S.A., Cedex, France). It was composed of an ingot 250 cm in height and 150 cm in width in a big-end-up cast iron mold, as displayed in Figure AIII.1a. The mold was hot-topped 70cm in height with insulating refractory tiles lined inside. A layer of insulating exothermic refractory board was over laid on the melt top. 3D linear tetrahedral elements were used for the spatial discretization of the part and mold components, as shown in Figure AIII.1b. An average grid size of 35mm was selected based on a mesh size optimization analysis. The thickness of the model was discretized by 2 elements. The numbers of nodes and elements in the steel part were 19662 and 86867, while they were 57243 and 250857 for the pseudo-2D casting system.

Two cases for the initial mold temperature condition were simulated, as seen in Figure AIII.2. The first one, named MS, was with the mold at the *same* initial temperatures (50 °C) for both sides. The other was MD, with the mold at *different* initial temperatures for the left (50 °C) and right sides (150 °C). The material was a medium carbon steel with the nominal chemical composition listed in Table AIII-1. For both cases, the liquid steel was bottom poured into the mold at 1570 °C (with a superheat of 75 °C) with a filling time of 30 min. The calculations were stopped when the entire casting came to complete solidification (i.e. around 1400 °C). For both MS and MD, five sensors (SENs 1-5) were installed in specified positions, at 2.5 cm from the mold outside surface, as presented in Figure AIII.1a, to monitor their temperature changes throughout the casting process.

Volume-averaged solid-liquid two-phase thermic models, as reported detailed in (TherCast 8.2®, 2012), were used for the simulation of mold filling and solidification. An Arbitrary Lagrangian-Eulerian (ALE) formulation was used for managing the time-dependent evolution of metal mass in the mold during the filling phase. Pure heat conduction was assumed as the only heat dissipation manner. Thermal convection, solid and mold deformation, elemental distribution and sedimentation of equiaxed grains were not taken into account, either because they are not considered in the FE code or to reduce the calculation time. The detailed derivation of associated auxiliary equations can be found in reference (TherCast 8.2®, 2012). The determination of relevant material parameters is based on the data provided in (Zhang et al., 2018).
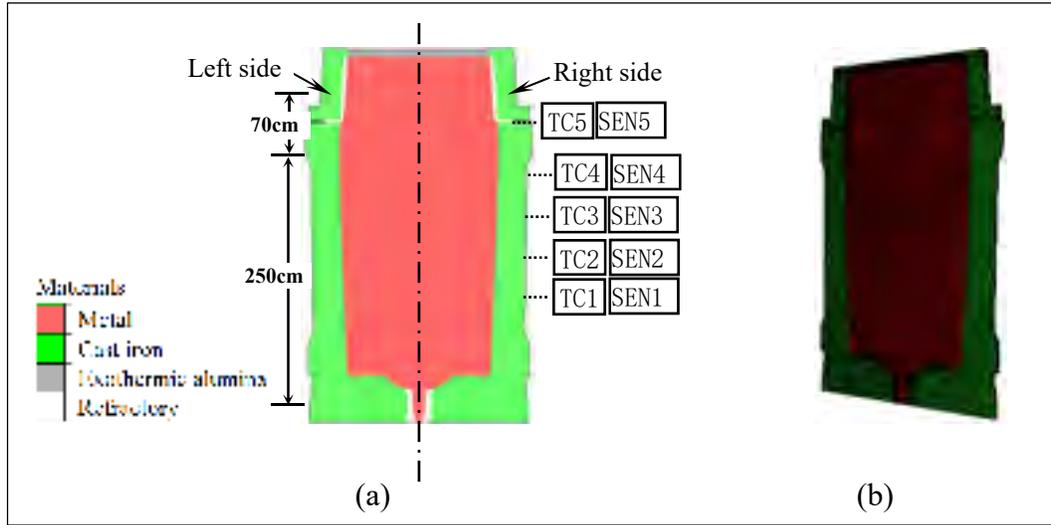
Figure AIII.1 Peudo-2D Finite Element model. (a) Main parts and corresponding materials with sensors (SENs) placed in the same positions as the thermocouples (TCs) (b) Mesh distribution.
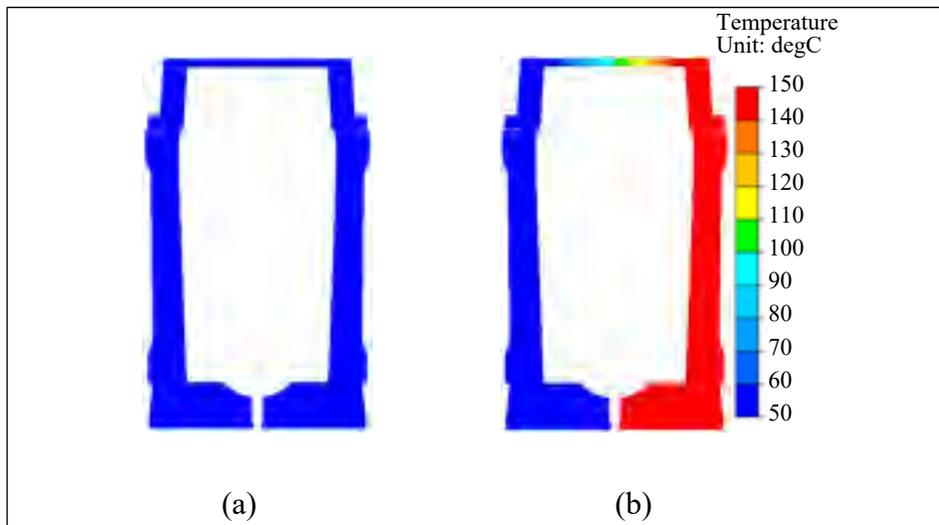
Figure AIII.2 Initial mold temperature conditions of the two case studies. (a) MS with the *same* initial temperature on both sides of the mold (b) MD with *different* temperatures on left and right sides of the mold.

Table AIII-1 Nominal chemical composition of the studied steel (wt.%).

C	Si	Mn	S	Cr	Mo	P	Ni	Fe
0.36	0.4	0.85	0.0023	1.82	0.45	0.01	0.16	balance

AIII.4   Experimental process

To verify the established model and examine the predictions, two cylindrical ingots (IngotS and IngotD), with 250 cm in height and 150 cm in mean diameter, were cast experimentally, in the same material and in the casting system identical to that presented in Figure AIII.1a. IngotS was fabricated under the same casting condition as MS (i.e. at 1570 °C, with a filling time of 30 min, and initial uniform mold temperature of 50 °C), while IngotD was corresponding to that for MD. In order to create the non-uniform initial temperature condition for IngotD, two neighboring ingots, with the layout illustrated in Figure AIII.3, were cast in turn. Ingots Left and Right began their casting processes 6 and 3 hours, respectively, before the beginning of the pouring operation for IngotD. Both IngotD and its neighbors were cast at 1576 °C with a filling time of 34min.
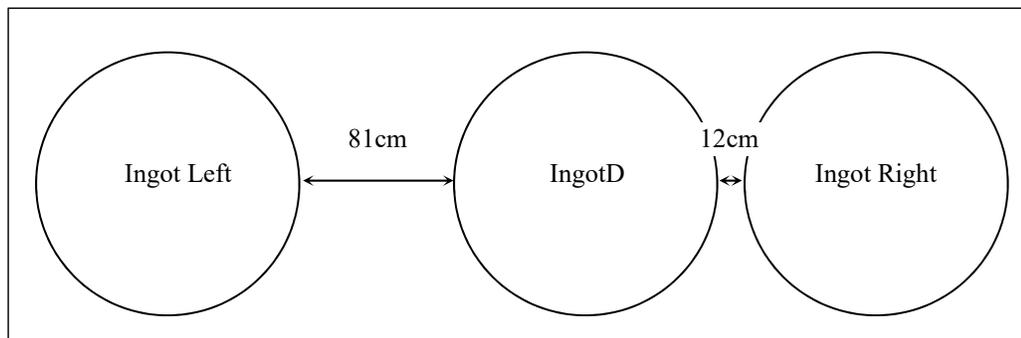
Figure AIII.3 Layout of IngotD and its neighbors.

For IngotS and IngotD, the temperature variations on the outside surface of the mold were monitored throughout the casting process using Chromel-Alumel thermocouples (TCs, type K) located in the same positions as SENs, as presented in Figure AIII.1a. For IngotS, all 5 TCs were installed on the right side of mold surface. For IngotD, only TCs 1-4 were set up

on the mold left and right outside surfaces, respectively. For the two experimental ingots, each thermocouple was cemented into holes drilled 2.5 cm into the mold from the exterior surface. Temperature measurements from each thermocouple were made every 90 seconds from the start of the steel pouring until the ingot was removed from the mold.

AIII.5   Results and discussions

AIII.5.1   Temperature field and solidification speed

Temperature fields for MS (with 50 °C as the initial uniform temperature of the mold) at times of 0.25 h (50 % filling), 0.5 h (end of filling), together with 1.5 h, 2.5 h, 5.5 h, 10.5 h and 15.5 h after pouring are shown in Figure AIII.4. The interface between the ingot and the mold was marked artificially with dashed lines. It can be seen that before the end of the filling stage, in the casting, a slight horizontal temperature gradient is present close to the mold chill wall and a vertical one next to the mold base (Figure AIII.4a). The height of the thermal gradient kept pace with the metal advance front in the vertical direction. This indicates the immediate dissipation of the superheat due to heat conduction from the cold mold wall. The heat from the steel melt was conducted to the mold wall, inducing a weak thermal gradient in the mold interior layer in contact with the ingot skin. When the filling operation was completed, Figure AIII.4b, the horizontal and vertical temperature variation fields became larger, in both the casting and the mold, owing to the increased accumulation of heat from the large liquid bulk. No large temperature variation occurred in the hot-top shell, as compared with the skin region of the ingot body. This delay in heat loss in the hot-top could be due to the effective protection provided by the nonconductive refractory board.

As solidification proceeded, the horizontal isotherms at the bottom became inclined and the spacing between adjacent isotherms widened, as seen in Figures AIII.4c-g. This indicates the progressive development of the solidification, upward from the ingot bottom and inward from the cold mold wall, due to heat conduction. It should be noted that the temperature field on the left half of the casting and the mold was always a symmetric version of the right pattern, through the whole casting process from its start to its completion. The above

evolution of temperature patterns in MS is similar to those reported by Im et al. for pure heat conduction analysis (Im, Kim et lee, 2001).
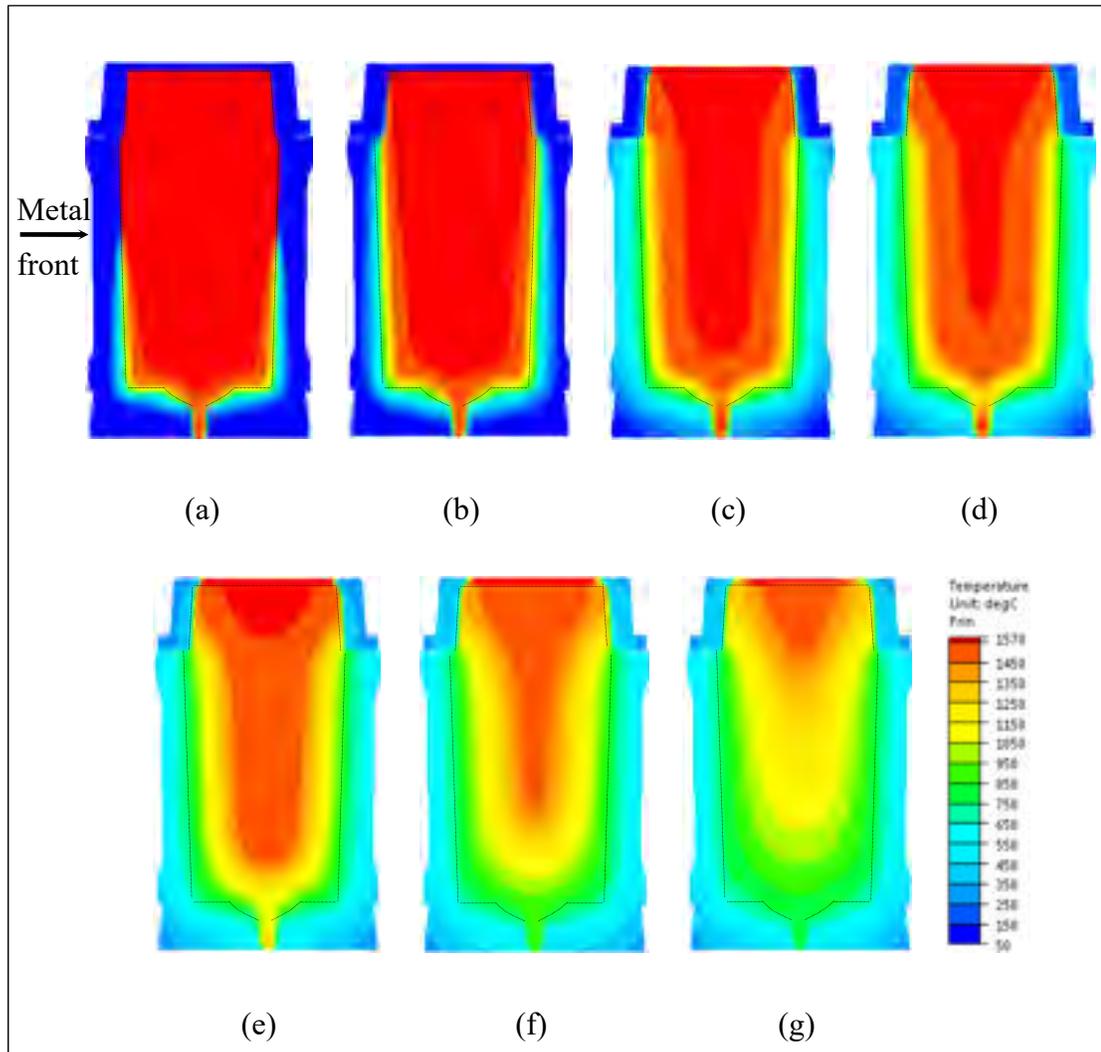
Figure AIII.4 Temperature pattern in the casting process for MS. (a) 0.25 h (50 % filling) (b) 0.5 h (end of filling) (c) 1.5 h (d) 2.5 h (e)5.5 h (f) 10.5 h (g) 15.5 h after pouring.

However, in MD (with 50 °C and 150 °C as the initial temperatures for the left and right sides of the mold), different features in the temperature field during the casting process was observed, as seen in Figure AIII.5. An asymmetry in the temperature field in the mold was developed from the start of the pouring process. When the mold cavity was half filled, as

seen in Figure AIII.5a, a 100 °C higher initial temperature on the mold right gave rise to a heat penetration almost through the entire thickness of the mold. In contrast, on the left side of the mold, the thermal gradient was quite small, and a large area of the mold was thermally unaffected. Particularly, the temperature on the right interior surface of the mold appeared higher. The region with larger thermal gradient and higher temperature value on the right side of MD were maintained up to the completion of the filling operation, as seen in Figure AIII.5b. Then, the tendency decayed with time and came to disappear after 5h, as observed in Figures AIII.5c-g. However, the impact of the initial non-uniform mold temperature on the temperature field in the casting is not that remarkable.

In order to further compare the temperature fields in the casting between MS and MD cases, the temperature profiles of 6 specific points were analyzed. As illustrated in the upper right corner of Figure AIII.6, points 1-4 were located in the skin and center of the mid-height sections of the hot-top and ingot body, respectively, to study the evolution of the radial temperature difference in the two parts. Points 5 and 6 were set at the top and bottom of the casting so that the vertical thermal change along the axis of the whole casting could be examined. For MD, the points on the skin of the casting were selected on both left and right sides, and named 1Left, 1Right and 3Left and 3Right, corresponding to their respective sides. The same labeling rule was applied for all the following analyses unless stated otherwise.

In the hot-top, as given in Figure AIII.6a, the hotter right side of the mold in MD generated higher temperature on the hot-top periphery (point 1Right_MD), while the temperature profiles on the hot-top left skin (point 1Left_MD) and its center (point 2) presented by MD were similar to those of MS in the corresponding locations (points 1_MS and 2_MS). This finding indicates that a smaller temperature gradient was induced in the half of the hot-top with higher initial thermal condition. Quantitative examinations of the radial temperature difference in the mid-height of the hot-top were done for MS, left side of MD and right side of MD. Their temperature gradient reached 0.0228 ºC/cm, 0.0228 ºC/cm, 0.0215 ºC/cm at 5 h, respectively, and then reached 0.0291, 0.0294, 0.028 ºC/cm at 10 h, and further 0.0394, 0.0394, 0.0384 ºC/cm at 15 h. From this, it can be seen that the different temperature

gradients between two halves of the hot-top in MD remain all along the cooling process, and tend to weaken with the solidification proceeding.
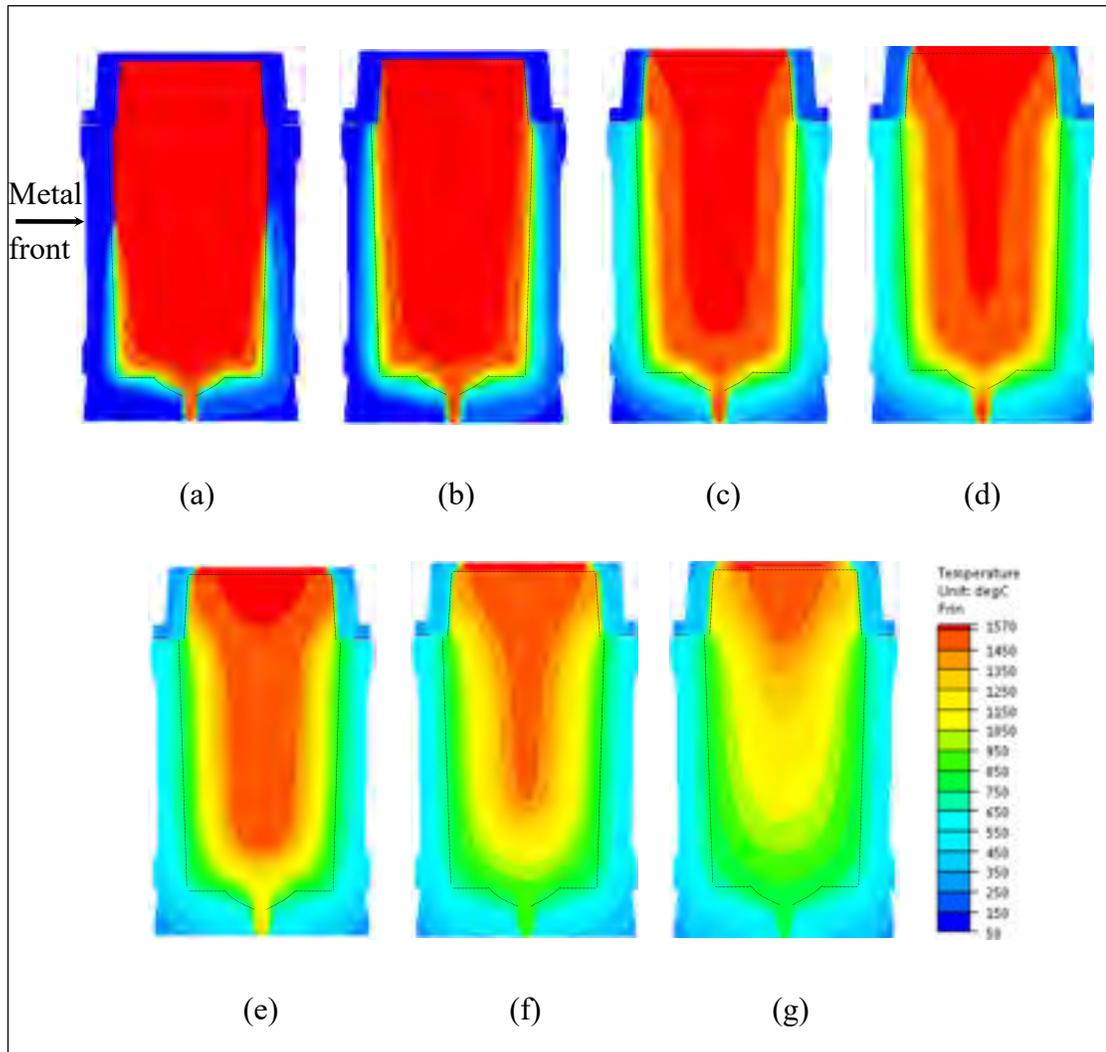
Figure A III.5 Temperature pattern in the casting process for MS. (a) 0.25 h (50 % filling) (b) 0.5 h (end of filling) (c) 1.5 h (d) 2.5h (e)5.5 h (f) 10.5 h (g) 15.5 h after pouring.

In the ingot body, as given in Figure AIII.6b, a smaller temperature gradient in the right half in MD was also obtained (the distance between the points 3Right_MD and 4_MD was smaller at any given moment) until after 8h. This corresponds to the time when solidification occurred almost above the mid-height. For MS, left half of MD and right half of MD, on the

section at the mid-height of the ingot body, the radial temperature gradients were 0.0928, 0.0929, 0.0906 °C/cm at 5h. But at 10h, they reached 0.0935, 0.0937, 0.0937 °C /cm, proving the disappearance of the thermal inconsistency between the two halves in MD.
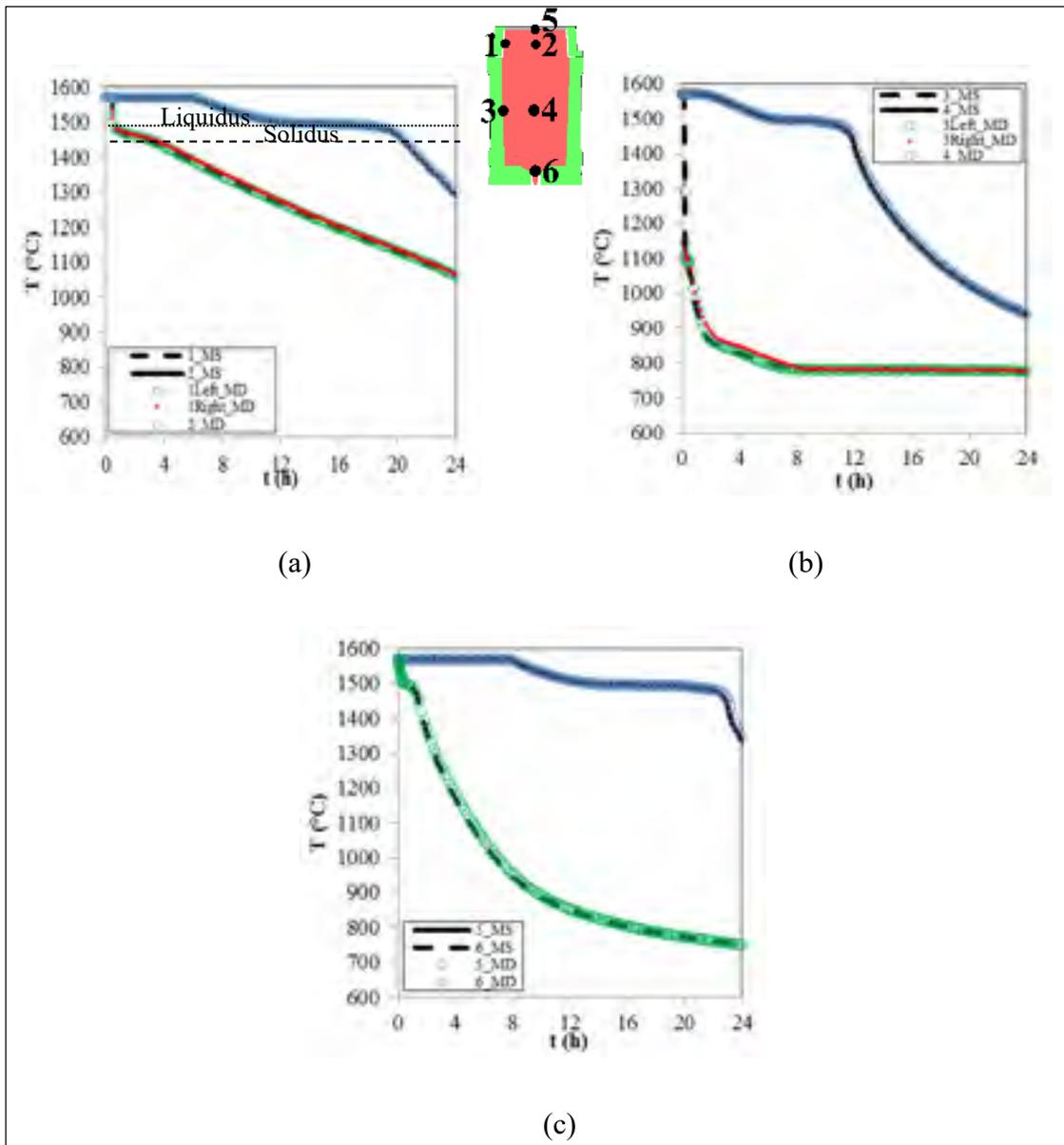
Figure AIII.6 Evolution of the temperature profiles in MS and MD during the casting process. (a) On points 1 and 2 in mid-height of hot-top (b) On points 3 and 4 in mid-height section of ingot body (c) On points 5 and 6 along the casting centerline.
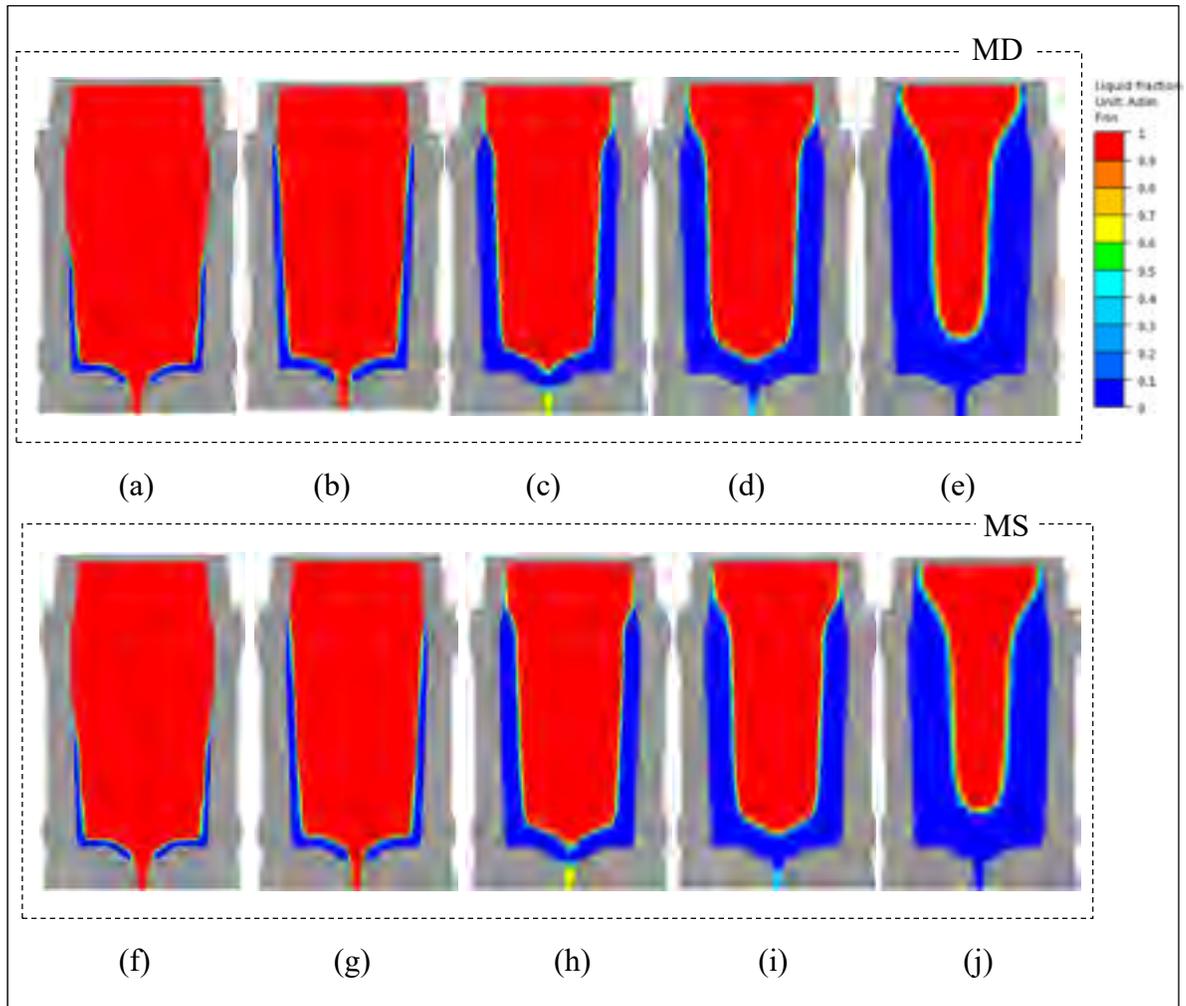
Figure AIII.7 Evolution of the temperature profiles in MS and MD during the casting process. (a) On points 1 and 2 in mid-height of hot-top (b) On points 3 and 4 in mid-height section of ingot body (c) On points 5 and 6 along the casting centerline.

Comparative analysis of the temperatures at the top center of the casting (point 5) in Figure AIII.6c revealed no significant difference between MS and MD. However, at the last solidification stage (after 22 h), MD displayed a slower cooling rate. The temperatures at the bottom base (point 6) in MD showed slightly higher values, indicating decreased thermal gradient along the centerline of the ingot.

The above-mentioned asymmetry in temperature field in MD resulted in different solidification pace between the left and right halves in the whole casting, as given in Figure AIII.7. In MS, the advance speed of the metal solid front kept always the same pace on both halves, as observed in Figures AIII.7a-e. This phenomenon is quite contrary to the lag of the right part behind the left in MD in the first solidification stage, as seen in Figures AIII.7f-j. Such delayed cooling tendency on the right side was more remarkable in the hot-top, the location with longer stay of hot bulk liquid. Examination of the delay along the hot-top/ingot body interface section showed that the solid front on MD right was 0.5 cm, 1.1 cm and 2.2 cm, respectively, behind its left side at 5h, 10h and 15h, as plotted in Figure AIII.8. This slower solidification speed during the casting on the side with initially hotter mold is in accordance with the higher right half temperature profiles reflected in Figure AIII.6. Such delayed solidification on one side results in a longer time necessary for the triggering of the solidification and for the completion of solidification process, as predicted by MS and MD in Figure AIII.9.
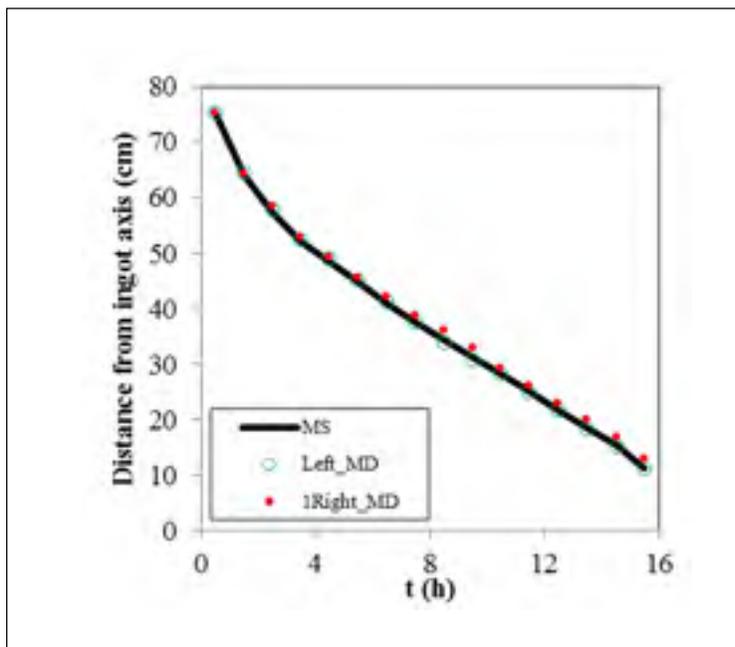
Figure AIII.8 Time-dependent distance of the solid front from the ingot centerline along the hot-top/ingot body for MS, left and right sides of MD.
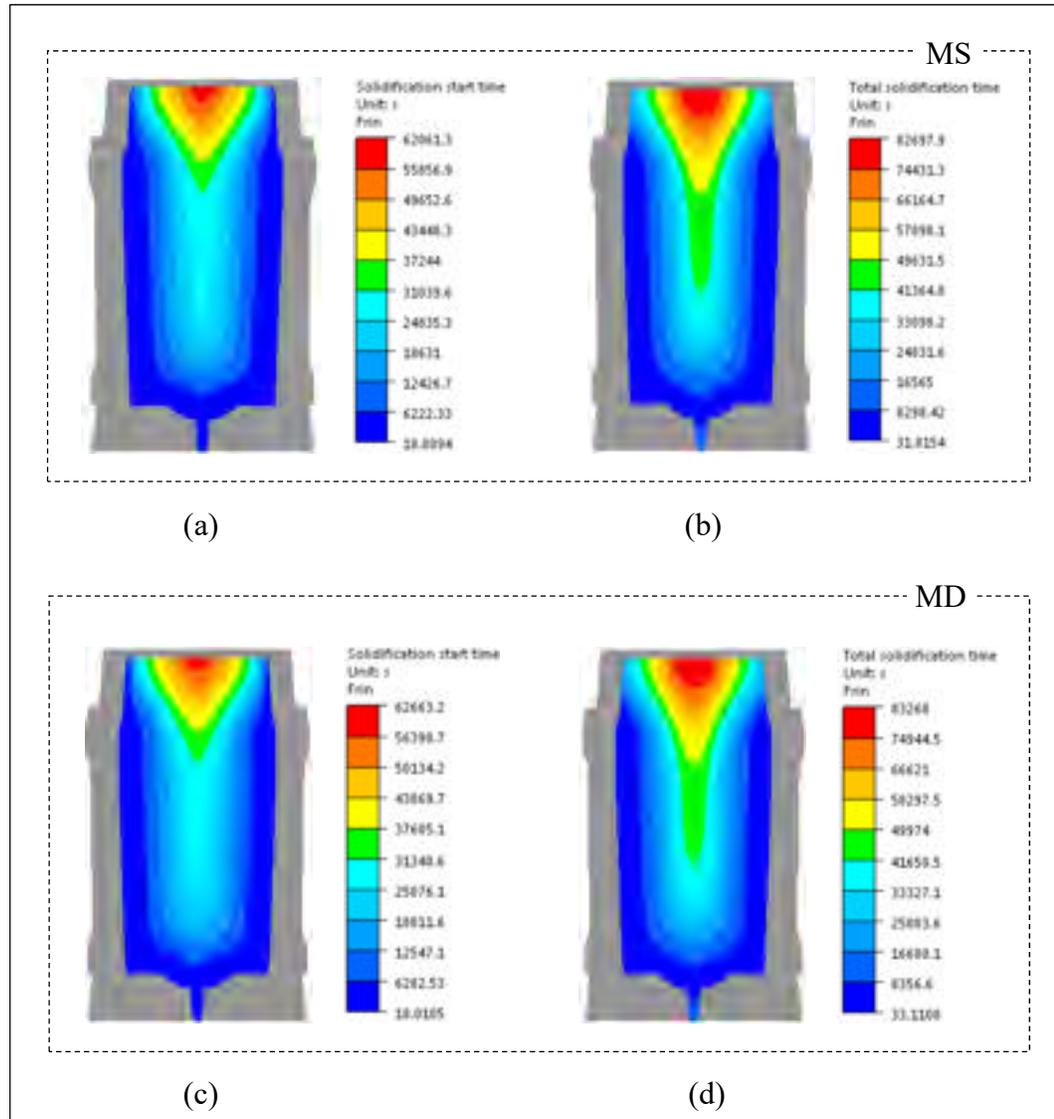
Figure AIII.9 Solidification time predictions from MS and MD. (a, c) Solidification start time (b, d) Total solidification time.

It has been reported that a lower temperature gradient can prolong the thermal convection time in the mold cavity, and delay the development of solutal convection (Liu et al., 2011), and thus can significantly affect the distribution of solutes (Hachani et al., 2012). Lower solidification speed can result in more time available for solutes to transport and increased segregation intensity (Zhang et al., 2018). Thus, the above-mentioned asymmetry in the temperature distribution through the diameter and along the height of the ingot and in the

radial solidification speed in the early stage of solidification can affect the macrosegregation symmetry and severity in the large-sized cast ingots.

AIII.5.2 Verification of the model

For the validation of the thermal predictability of the established model, temperature predictions from the sensors (SENs) for the MS case were compared with thermal readings of thermocouples (TCs) from the experimentally obtained IngotS, in light of their same casting conditions. The thermal sensors were placed at the same characteristic positions as thermocouples, as illustrated in Figure AIII.1a.

According to the experimental measurements from IngotS, as shown in Figure AIII.10a, at first, the temperatures sharply increased one after another, reflecting the successive contact between the melt and mold during pouring. Then, the increasing tendency was slowed down because of the heat loss from the mold wall. Temperatures began to decrease after reaching their individual temperature peaks. Owing to the low conductivity of the insulating tiles inside the hot-top mold, the increasing tendency was slowed, and the lowest peak temperature value was recorded by TC5.

When sensor readings of MS were examined, it was found that all the above features were, at large, reproduced. The 20-50 °C difference in the peak values between the predictions of MS and test results of IngotS could be due to the uncertainty in the exact values of the thermal conductivity of the cast iron mold and the refractory tiles used in the computations. The 3-4h advance in the temperature peak for MS are attributed to the predictive failure of air gap formation, and thus of heat transfer transition from pure conduction to heat radiation. The difference between the spacing of SENs 1-3 and that of TCs 1-3 originates from the shortness of the predictability about the increasing air gap size from the bottom up along the ingot skin. The smaller heat loss after 8h is probably related to the not taking into account the effect of solid contraction and volume shrinkage, which can help to accelerate the solidification in the latter solidification stage.
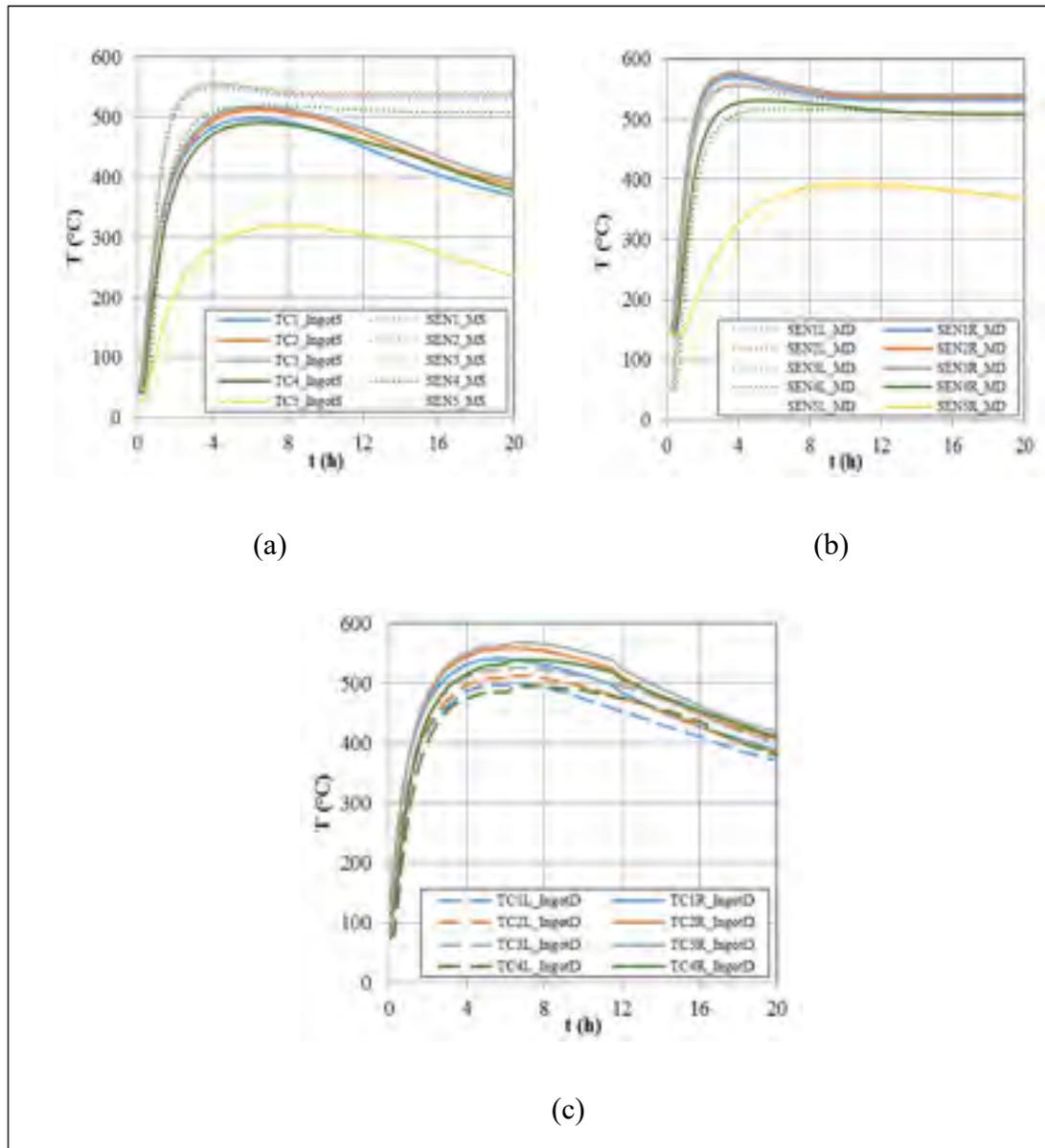
Figure AIII.10 Time-dependent temperature change on the outside of the mold surface in the casting process. (a) Thermal couple readings of the IngotS (TC) and the sensor values of MS (SEN) (b) Sensor values from the left side (SENL) and the right side (SENR) of the mold surface of MD (c) thermal couple readings for the left side (TCL) and the right side (TCR) of the mold surface of IngotD.

The difference in the temperature variation trend between the left and right halves of MD was also reflected on the mold outside surface. As seen in Figure AIII.9b, the temperatures on the side with higher initial mold temperature (right side) increased earlier than the other

colder side. Furthermore, their peak values arrived at 40 °C higher. This difference became smaller with the solidification proceeding, and did not disappear until after as long as 12 h.

As a result of the dissimilarity of the initial temperature conditions between the two opposite mold sides, the temperature difference between two halves predicted by MD was confirmed by experimental results from IngotD, as seen in Figure 9c. Furthermore, the predicted thermal gradients on the two sides appear less severe and last for much shorter time than real industrial production. In the figure, it can be noted that the initial 40 °C difference between left (80 °C) and right (120 °C) mold skins for IngotD kept constant till after 12 h, and then decreased down to 20 °C after 20 h. The long-lasting unchanged thermal difference and its longer effective time in the experimental case are probably due to the continuous thermal gain from the radiation from the neighboring ingots. Therefore, in actual industrial production, the above-discussed asymmetry phenomena in thermal pattern and solidification speed caused by neighboring ingot casting, or non-uniform initial mold temperature, should be taken into consideration.

AIII.6   Conclusions

In the present work, the effect of non-uniform initial mold temperature conditions on the solidification behavior of large-sized steel ingot was numerically studied. A uniform initial mold temperature case was also simulated for comparison. For both cases, pure heat conduction was considered to be the only heat dissipation manner. It was found that non-uniform initial temperature condition of the mold led to asymmetry in the temperature field, temperature gradient and solidification speed in the casting. This finding is in contrast to the symmetry patterns in the casting of the case with uniform initial mold temperature. In addition, a higher temperature on one side of the mold tends to delay solidification process. This asymmetry and the solidification lag should influence the distribution of alloying elements, given that the development of macrosegregation is significantly influenced by the solidification conditions. The predicted results agreed well with experimental measurements. The results of the present study provide original information about the impact of non-uniform initial temperature distribution of a large-size mold in the ingot cooling process.

AIII.7 Acknowledgements

LIST OF REFERENCES

Aboutalebi, M. A. 1994. *Modelling of Turbulent Transport Phenomena and Solidification in Continuous Casting systems*. Ph. D. Thesis. February 1994. Department of Mining and Metallurgical Engineering, McGill University, Montreal, Canada.

Abramoff, M. D., P. J. Magalhaes et S. J. Ram. 2004. « Image Processing with ImageJ ». *Biophotonics International*, vol. 11, n° 7, p. 36-42.

Ahmad, N., H. Combeau, J. L. Desbiolles, T. Jalanti, G. Lesoult, J. Rappaz, M. Rappaz et C. Stomp. 1998. « Numerical Simulation of Macrosegregation: a Comparison between Finite Volume Method and Finite Element Method Predictions and a Confrontation with Experiments ». *Metallurgical and Materials Transactions A*, vol. 29, n° 2, p. 617-630.

Andersson, J. O., T. Helander, L. Höglund, P. F. Shi et B. Sundman. 2002. « Thermo-Calc & DICTRA, Computational Tools for Materials Science ». *Calphad*, vol. 26, n° 2, p. 273-321.

ASM Handbook Volume 11: Failure Analysis and Prevention. 2002. Edited by Becker, W. T., et R. J. Shipley. ASM International, Materials Park, OH, USA, p. 5-81.

Badillo, A., et C. Beckermann. 2006. « Phase-field Simulation of the Columnar-to-equiaxed Transition in Alloy Solidification ». *Acta Materialia*, vol. 54, n° 8, p. 2015-2026.

Bale, C. W. 2017. *Macro Processing Manual*, CRCT.

Banaszek J., C. McFadden, D. J. Browne, L. Sturz L et G. Zimmermann. 2007. « Natural Convection and Columnar-to-equiaxed Transition Prediction in a Front-tracking Model of Alloy Solidification ». *Metallurgical and Materials Transactions A*, vol. 38, n° 7, p. 1476-1484.

Barfield, R. N., et J. A. Kitchener. 1955. « The Viscosity of Liquid Iron and Iron-Carbon Alloys ». *Journal of the Iron and Steel Institute*, vol. 180, p. 324-329.

Beckermann, C. 2002. « Modelling of Macrosegregation: Applications and Future Needs ». *International Materials Reviews*, vol. 47, nº 5, p. 243-261.

Beckermann, C. 2000. « Modeling of Macrosegregation: Past, Present and Future ». Presented at Flemings Symposium, Boston. MA, June 2000.

Beckermann, C., et C. Y. Wang. 1996. « Equiaxed Dendritic Solidification with Convection: Part III. Comparisons with NH4Cl-H2O Experiments ». *Metallurgical and Materials Transactions A*, vol. 27, n° 9, p. 2784-2795.

Beckermann, C., et R. Viskanta. 1988. « Double Diffusive Convection during Dendritic

Solidification of a Binary Mixture ». *PhysioChemical Hydrodynamics*, vol. 10, n° 2, p. 195-213.

Beckermann, C., et R. Viskanta. 1993. « Mathematical Modeling of Transport Phenomena during Alloy Solidification ». *Applied Mechanics Reviews*, vol. 46, n° 1, p. 1-27.

Bellet, M., O. Boughanmi, et G. Fidel. 2012. « A Partitioned Resolution for Concurrent Fluid Flow and Stress Analysis during Solidification: Application to Ingot Casting ». *IOP Conference Series: Materials Science and Engineering*, vol. 33, 012052.

Bennon, W. D., et F. P. Incropera. 1987. « A Continuum Model for Momentum, Heat and Species Transport in Binary Solid-liquid Phase Change Systems - II. Applications to Solidification in a Rectangular Cavity ». *International Journal of Heat and Mass Transfer*, vol. 30, n° 10, p. 2171-2187.

Bennon, W. D., et F. P. Incropera. 1987. « A Continuum Model for Momentum, Heat and Species Transport in Binary Solid-liquid Phase Change System - I. Model Formulation ». *International Journal of Heat and Mass Transfer*, vol. 30, n° 10, p. 2161-2170.

Biscuola, V. B., et M. A. Martorano. 2008. « Mechanical Blocking Mechanism for the Columnar to Equiaxed Transition ». *Metallurgical and Materials Transactions A*, vol. 39, n° 12, p. 2885- 2895.

Boettinger, W. J., U. R. Kattner, S. R. Coriell et Y. A. Chang. 1995. *Modeling of Casting, Welding and Advanced Solidification Processes VII*. The Minerals, Metals and Materials Society, Warrendale, PA. p. 649-656.

Brody, H. D., et M. C. Flemings. 1966. « Solute Redistribution in dendritic solidification ». *Transactions of the Metallurgical Society of AIME*, vol. 236, p. 615-624.

Brookes, B. E., C. Beckermann et V. L. Richards. 2007. « Prediction of Burn-on and Mould Penetration in Steel Casting Using Simulation ». *International Journal of Cast Metals Research*, vol. 20, n° 4, p. 177–190.

Campbell, J. 2011. *Complete Casting Handbook - Metal Casting Processes, Metallurgy, Techniques and Design*. 1st ed. Butterworth-Heinemann, Waltham, MA, USA，p. 105-153.

Campbell, J. 2011. *Complete casting handbook - Metal casting processes, Metallurgy, Techniques and Design*. 2nd ed. Butterworth-Heinemann, USA, p. 119-269.

CATIA V5 R20. Avions Marcel Dassault, France.

Chiang, K. C., et H. L. Tsai. 1992. « Interaction between Shrinkage–Induced Fluid Flow and Natural Convection during Alloy Solidification ». *International Journal of Heat and Mass Transfer*, vol. 35, n° 7, p. 1771-1778.

Chiang, F. C., et H. L. Tsai. 1992. *Transport Phenomena in Material Processing. ASME HTD, Volume 132*. Edited by Charmichi, M., M. K. Chyu, Y. Joshi et S. M. Walsh. ASME, Fairfield, NJ, p. 153-222.

Choudhary, S., et S. Ganguly. 2007. « Morphology and Segregation in Continuously Cast High Carbon ». *The Iron and Steel Institute of Japan International*, vol. 47, n° 12, p. 1759-1766.

Ciobanas, A. I., et Y. Fautrelle. 2007. « Ensemble Averaged Multiphase Eulerian Model for Columnar/equiaxed Solidification of a Binary Alloy: I. the Mathematical Model ». *Journal of Physics D: Applied Physics*, vol. 40, p. 3733-3762.

Ciobanas, A. I., et Y. Fautrelle. 2007. « Ensemble Averaged Multiphase Eulerian Model for Columnar/equiaxed Solidification of a Binary Alloy: II. Simulation of the Columnar-to-equiaxed Transition (CET) ». *Journal of Physics D: Applied Physics*, vol. 40, p. 4310-4336.

Clyne, T. W., et W. Kurz. 1985. « Solute Redistribution during Solidification with Rapid Solid State Diffusion ». *Metallurgical Transactions A*, vol. 12, n° 6, p. 965-971.

Combeau, H., A. Kumar, M. Založnik, I. Poitrault, G. Lacagne, A. Gingell, T. Mazet et G. Lesoult. 2012. « Macrosegregation Prediction in a 65 Ton Steel Ingot ». In: *1st International Conference on Ingot Casting, Rolling and Forging: Ingot casting-simulation, June 5th, 2012*, Aachen, Germany, p. 1-10.

Combeau, H., M. Založnik, S. Hans et P. E. Richy. 2009. « Prediction of Macrosegregation in Steel Ingots: Influence of the Motion and the Morphology of Equiaxed Grains ». *Metallurgical and Materials Transactions B*, vol. 40, nº 3, p. 289-304.

Comon, J., J. Delorme et P. Bastien. 1973. « Heterogeneity of Large Forging Ingots. Study of the Influence of Impurities and Alloying Elements on Segregation. (Hétérogénéité des gros lingots de forge. Étude de l'influence des impuretés et des éléments d'alliage sur la ségrégation) ». *La Revue de Métallurgie (Paris)*, vol. 74, nº 4, p. 251-258.

Dong, H. B., X. L. Yang, P. D. Lee et W. Wang. 2004. « Simulation of Equiaxed Growth Ahead of an Advancing Columnar Front in Directionally Solidified Ni-based Superalloys ». *Journal of Materials Science*, vol. 39, nº 24, p. 7207-7212.

Dong, Q., J. Zhang, Y. Yin et B. Wang. 2017. « Three-dimensional Numerical Modeling of Macrosegregation in Continuously Cast Billets ». *Metals*, vol. 7, nº 6, p. 1-22.

Du, Q., D. G. Eskin et L. Katgerman. 2007. « Modelling Macrosegregation during DC Casting of Multi-component Aluminum Alloys ». *Metallurgical and Materials Transactions A*, vol. 38, nº 1, p. 180-186.

Duan, Z., H. Shen et B. Liu. 2015. « A Numerical Study of the Effect of Multiple Pouring on

Macrosegregation in a 438-Ton Steel Ingot ». *Acta Metallurgica Sinica (English Letters)*, vol. 28, nº 9, p. 1123-1133.

Duan, Z., W. Tu, B. Shen, H. Shen et B. Liu. 2016. « Experimental Measurements for Numerical Simulation of Macrosegregation in a 36-ton Steel Ingot ». *Metallurgical and Materials Transactions A*, vol. 47, nº 7, p. 3597-3605.

Dub, V.S., A.V. Romashkin, A. N. Mal'ginov, I. A. Ivanov et D. S. Tolstykh. 2014. « Effect of the Geometry of an Ingot on its Chemical Heterogeneity. Part I ». *Metallurgist*, vol. 57, nº 11-12, p. 987-995.

Ehlen, G., A. Ludwig, P. R. Sahm et A. Buhrig-Polaczek. 2003. *Split-solid-model to Simulate the Formation of Shrinkage Cavities and Macrosegregations in Steel Casting. Modelling of Casting, Welding and Advanced Solidification Processes X*. Edited by Stefanescu, D. M., J. Warren, M. Jolly et M. Krane. TMS The Minerals, Metals & Materials Society, p. 285-292.

EI-Bealy, M. O. et R. M. Hammouda. 2007. « On the Mechanism of Natural Convection and Equiaxed Structure during Dendritic Solidification Processes ». *Steel Research International*, vol. 78, nº 8, p. 602-611.

El-Bealy, M. 2000. « Modeling of Interdendritic Strain and Macrosegregation for Dendritic Solidification processes: Part I. Theory and Experiments ». *Metallurgical and Materials Transactions B*, vol. 31, nº 2, p. 331-343.

El-Bealy, M. 2000. « Modeling of Interdendritic Strain and Macrosegregation for Dendritic Solidification Processes: Part II. Computation of Interdendritic Strain and Segregation Fields in Steel Ingots ». *Metallurgical and Materials Transactions B*, vol. 31, nº 2, p. 345-355.

Eskin, D. G., V. I. Savran et L. Katgerman. 2005. « Effects of Melt Temperature and Casting Speed on the Structure and Defect Formation during Direct-Chill Casting of an Al-Cu Alloy ». *Metallurgical and Materials Transactions A*, vol. 36, nº 7, p. 1965-1976.

Farup, I. et A. Mo. 2000. « Two-phase Modeling of Mushy Zone Parameters Associated with Hot tearing ». *Metallurgical and Materials Transactions A*, vol. 31A, p. 1461-1472.

Felicelli, S. D., J. C. Heinrich et D. R. Poirier. 1993. « Numerical Model for Dendritic Solidification of Binary Alloys ». *Numerical Heat Transfer Part B*, vol. 23, nº 4, p. 461-481.

Felicelli, S. D., D. R. Poirier et J. C. Heinrich. 1998. « Modelling Freckle Formation in Three Dimensions during Solidification of Multicomponent Alloys ». *Metallurgical and Materials Transactions B*, vol. 29, nº 4, p. 847-855.

Felicelli, S. D., D. R. Poirier, A. F. Giamei et J. C. Heinrich. 1997. « Simulation of

Convection and Macrosegregation in Superalloys ». *Journal of the Minerals, Metals, and Materials Society*, vol. 49, nº 3, p. 21-25.

Ferreira, I. L., V. R. Voller, B. Nestler et A. Garcia. 2009. « Two-dimensional Numerical Model for the Analysis of Macrosegregation during Solidification ». *Computational Materials Science*, vol. 46, p. 358-366.

Fleming, M. C. 2000. « Our Understanding of Macrosegregation: Past and Present ». *ISIJ International - The Iron and Steel Institute of Japan*, vol. 40, p. 833-841.

Fleming, M. C., et G. E. Nereo. 1967. « Macrosegregation: Part I ». *Transactions of the Metallurgical Society of AIME*, vol. 239, p. 1449-1461.

Flemings, M. C. 1975. « Principles of control of soundness and homogeneity of large ingots ». *Scandinavian Journal of Metallurgy*, vol. 5, p. 1-15.

Flemings, M. C. 1974. « Solidification Processing ». *Metallurgical Transactions*, vol. 5, n° 10, p. 2121-2134.

Fridberg, J., L. E. Torndahl et M. Hillert. 1969. « Diffusion in Iron ». *Jernkontorets Annales*, vol. 153, p. 263-276.

Fujii, T., D. R. Poirier et M. C. Flemings. 1979. « Macrosegregation in a Multicomponent Low Alloy Steel ». *Metallurgical Transactions B*, vol. 10, p. 331-339.

Galkin, A. N., N. A. Zyuban, D. V. Rutskii, S. B. Gamanyuk, A. Y. Puzikov et V. V. Firsenko. 2013. « Effect of Chilling of the Top Part of a Steel Ingot on the Conditions of its Crystallization and the Quality of Forgings Obtained from it ». *Metallurgist*, 2013, nº 3-4, p. 199-206.

Gandin, C. A. 2000. « From Constrained to Unconstrained Growth during Directional Solidification ». *Acta Materialia*, vol. 48, n° 10, p. 2483-2501.

Ganesan, S., et D. R. Poirier. 1990. « Conservation of Mass and Momentum for the Flow of Interdendritic Liquid during Solidification ». *Metallurgical Transactions B*, vol. 21, p. 173-181.

Ganesan, S., et D. R. Poirier. 1989. « Solute Redistribution in Dendritic Solidification with Diffusion in the Solid ». *Journal of Crystal Growth*, vol. 97, n° 3-4, p. 851-859.

Gao, Z., W. Jie, Y. Liu et H. Luo. 2017. « Solidification Modelling for Coupling Prediction of Porosity and Segregation ». *Acta Materialia*, vol. 127, p. 277-286.

Gorni, A. A., et S. V. SP. 2015. *Steel Forming and Heat Treating Handbook*, Brazil.

Gouttebroze, S., M. Bellet et H. Combeau. 2007. « 3D Macrosegregation Simulation with

Anisotropic Remeshing ». *Comptes Rendus Mecaniq*ue, vol. 335, n° 5-6, p. 269-279.

Guan, R., C. Ji, M. Zhu et S. Deng. 2018. « Numerical Simulation of V-shaped Segregation in Continuous Casting Blooms Based on a Microsegregation Model ». *Metallurgical and Materials Transactions B*, vol. 49, n° 5, p. 2571-2583.

Hachani, L., B. Saadi, X. D. Wang, A. Nouri et K. Zaidat. 2012. « Experimental Analysis of the Solidification of Sn-3wt.% Pb Alloy under Natural Convection ». *International Journal of Heat and Mass Transfer*, vol. 55, nº 7-8, p. 1986-1996.

Haj, BA. EI., A. Bouayad et M. Alami. 2015. « Effect of Mould Temperature and Melt Treatment on Properties of an AlSi9 Cast Alloy Thermal and Microstructural Investigations ». *International Letters of Chemistry, Physics and Astronomy*, vol. 55, p. 12-18.

He, J. 2015. *21 Chemical Elements and Effects on Steel Mechanical Properties*. Report of OTAI SpecialSteel Co. Ltd.

Heinrich, J. C., et D. R. Poirier. 2004. « The Effect of Volume Change during Directional Solidification of Binary Alloys ». *Modelling and Simulation in Materials Science and Engineering*, vol. 12, nº 5, p. 881-899.

Himemiya, T. et W. Wolczynski. 2002. « Solidification Path and Solute Redistribution of an Iron-based Multi-component Alloy with Solute Diffusion in the Solid ». *Materials Transaction. The Japan Institute of Metals and Materials*, vol. 43, p. 2890-2896.

Hultgren, A. 1929. « Crystallization and Segregation Phenomena in 1.10 Per Cent Carbon Steel Ingots of Smaller Sizes ». *The* Journal *of Iron and Steel Institute*, vol. 120, nº 2, p. 69-125.

Im, I. T., W. S. Kim et K. S. Lee. 2001. « A Unified Analysis of Filling and Solidification in Casting with Natural Convection ». *International Journal of Heat and Mass Transfer*, vol. 44, nº 8, p. 1507-1515.

JMatPro User's Guide. 2005. Sente Software Ltd.

Kai, H., et R. D. Pehlke. 1985. « Metal-mold Interfacial Heat Transfer ». *Metallurgical Transactions B*, vol. 16, n° 3, p. 585-594.

Kermanpur, A., M. Eskandari, H. Purmohamad, M. A. Soltani et R. Shateri. 2010. « Influence of Mould Design on the Solidification of Heavy Forging Ingots of Low Alloy Steels by Numerical Simulation ». *Materials & Design*, vol. 31, nº 3, p. 1096-1104.

Kobayashi, S. 1988. « Solute Redistribution during Solidification with Diffusion in Solid Phase: A Theoretical Analysis ». *Journal of Crystal Growth*, vol. 88, p. 87-96.

Kobayashi, S. 1988. « A Mathermatical Model for Solute Redistribution during Dendritic

Solidification ». *Transactions of the Iron and Steel Institute of Japan*, vol. 28, n° 7, p. 535-542.

Kozeschnik, E., W. Rindler et B. Buchmayr. 2007. « Scheil-Gulliver Simulation with Partial Redistribution of Fast Diffusers and Simultaneous Solid-solid Phase Transformations ». *International Journal of Materials Research*, vol. 98, n° 9, p. 826-831.

Krane, M. J. M., et F. P. Incropera. 1997. « Solidification of Ternary Metal Alloys - I. Model Development ». *International Journal of Heat and Mass Transfer*, vol. 40, n° 16, p. 3827-3835.

Krane M. J. M., et F. P. Incropera. 1997. « Solidification of Ternary Metal Alloys – II. Prediction of Convective Phenomena and Solidification Behavior in Pb-Sb-Sn Alloys ». *International Journal of Heat and Mass Transfer*, vol. 40, n° 16, p. 3837-3847.

Kurz, W., et D. J. Fischer. 1989. *Fundamentals of Solidification*. Trans Tech Publications, Acdermannsdorf, Switzerland.

Lan, P., et J. Q. Zhang. 2014. « Numerical Analysis of Macrosegregation and Shrinkage Porosity in Large Steel Ingot ». *Ironmaking & Steelmaking*, vol. 41, nº 8, p. 598-606.

Lee, J., J. Mok et C. P. Hong. 1999. « Straightforward Numerical Analysis of Casting Process Rectangular Mold: From Filling to Solidification ». *ISIJ International*, vol. 39, nº 12, p. 1252-1261.

Lesoult, G. 2005. « Macrosegregation in Steel Strands and Ingots: Characterization, Formation and Consequences ». *Materials Science and Engineering A*, vol. 413-414, p. 19-29.

Li, J., M. Wu, J. Hao, A. Kharicha et A. Ludwig. 2012. « Simulation of Channel Segregation Using a Two-phase Columnar Solidification Model - Part II: Mechanism and Parameter study ». *Computational Materials Science*, vol. 55, p. 419-429.

Li, J., M. Wu, A. Ludwig et A. Kharicha. 2012. « Modelling Macrosegregation in a 2.45 Ton Steel Ingot ». *IOP Conference Series: Materials Science and Engineering*, vol. 33, 012091.

Li, L., D. Li, J. Gao et Y. Kang Y. 2017. « Influence of Mold Temperature on Microstructure and Shrinkage Porosity of the A357 Alloys in Gravity Die Casting ». *Advances in Materials Processing*, CMC, p. 793-801.

Liu, D. R., X. H. Kang, P. X. Fu et D. Z. Li. 2011. « Modeling of macrosegregation in steel ingot: influence of mold shape and melt superheat ». *Kovove Materialy*, vol. 49, nº 2, p. 143-153.

Liu D. R., B. G. Sang, X. H. Kang et D. Z. Li. 2010. « Numerical Simulation of Macrosegregation in Large Multiconcentration Poured Steel Ingot ». *International*

244

Journal of Cast Metals Research, vol. 23, nº 6, p. 354-363.

Liu, D. R., X. H. Kang, P. X. Fu et D. Z. Li. 2011. « Modeling of Macrosegregation in Steel Ingot: Influence of Mold Shape and Melt Superheat ». *Kovove Materialy*, vol. 19, nº 2, p. 1-11.

Liu, D., X. Kang, B. Sang et D. Li. 2011. « Numerical Study of Macrosegregation Formation of Ingot Cast in Normal Sand Mold and Water-cooled Sand Mold ». *Acta Metallurgica Sinica (English letters)*, vol. 24, nº 1, p. 54-64.

Liu, D. R., X. H. Kang, P. X. Fu et D. Z. Li. 2011. « Modeling of Macrosegregation in Steel Ingot: Influence of Mold Shape and Melt Superheat ». *Kovove Materialy*, vol. 49, nº 2, p. 143-153.

Liu, M., J. Wu, Y. Gan, D. A. H. Hanaor et C. Q. Chen. 2016. « Evaporation Limited Radial Capillary Penetration in Porous Media ». *Langmuir*, vol. 32, nº 38, p. 9899-9904.

Liu, S. F., L. Y. Liu et L. G. Kang. 2008. « Refinement Role of Electromagnetic Stirring and Strontium in AZ91 Magnesium Alloy ». *Journal of Alloys and Compounds*, vol. 450, nº 1-2, p. 546-550.

Liu, W. 2005. *Finite Element Modeling of Macrosegregation and Thermomechanical Phenonmena in Solidification Processes*. Ph. D. Thesis, École des Mines de Paris.

Loucif, A., E. Ben Fredj, N. Harris, D. Shahriari, M. Jahazi et L. P. Lapierre-Boire. 2018. « Evolution of A-type Macrosegregation in Large Size Steel Ingot after Multistep Forging and Heat Treatment ». *Metallurgical and Materials Transactions B*, vol. 49, nº 3, p. 1046-1055.

Ludwig, A., et M. Wu. 2005. « Modeling the Columnar-to-equiaxed Transition with a Three-phase Eulerian Approach ». *Materials Science and Engineering*, vol. 413-414, p. 109-114.

Ma, C. W., H. F. Shen, T. Y. Huang et B. C. Liu. 2004. « Numerical Simulation of Macro-Segregation in Steel Ingot During Solidification ». *Acta Metallurgica Sinica*, vol. 17, nº 9, p. 288-294.

Majka, T. F., D. K. Matlock et G. Krauss. 2002. « Development of Microstructural Banding in Low-alloy Steel with Simulated Mn Segregation ». *Metallurgical and Materials Transactions A*, vol. 33A, nº 6, p. 1627-1637.

Mäkinen, M., et M. Uoti. 2006. « The Effect of Superheat on Micro- and Macrosegregation and Crack Formation in the Continuous Casting of Low-Alloyed Copper ». *Materials Science Forum*, vol. 508, p. 549-554.

Martorano, M. A., C. Beckermann et C. A. Gandin. 2003. « A Solutal Interaction Mechanism for the Columnar-to-equiaxed Transition in Alloy Solidification ». *Metallurgical and*

Materials Transactions A, vol. 34, p. 1657-1674.

Marx, K., S. Rödl, S. Schramhauser et M. Seemann. 2014. « Optimization of the Filling and Solidification of Large Ingots ». In: *Proceedings of the 2nd International Conference Ingot Casting Rolling & Forging ICRF*, May 7-9, 2014, Milan, Italy, vol. 11-12, p. 11-19.

MATLAB and Statistics Toolbox Release 2012b. 2012. The MathWorks Inc., Natick, Massachusetts, USA.

Mehrabian, R., et M. C. Flemings. 1970. « Experiments on Macrosegregation and Freckle Formation ». *Materials Transactions*, vol. 1, nº 11, p. 3238-3241.

Meng, Y., et B. G. Thomas. 2003. « Heat Transfer and Solidification Model of Continuous Slab Casting: CON1D ». *Metallurgical and Materials Transactions B*, vol. 34, n° 5, p. 685-705.

Miettinen, J., et S. Louhenkilpi. 1994. « Calculation of Thermophysical Properties of Carbon and Low Alloyed Steels for Modeling of Solidification Processes ». *Metallurgical and Materials Transactions B*, vol. 25, n° 6, p. 909-916.

Miettinen, J. 1997. « Calculation of Solidification-related Thermophysical Properties for Steels ». *Metallurgical and Materials Transactions B*, vol. 28, nº 2, p. 281-297.

Miller, C. 1924. « The Stokes-Einstein Law for Diffusion in Solution ». *Proceedings of the Royal Society of London, Series A, Containing Papers of a Mathematical and Physical Character*, vol. 106, nº 740, p. 724-749.

Mills, K. C. 2002. *Recommended Values of Thermophysical Properties for Selected Commercial Alloys*. 1st ed. Woodhead Publishing Ltd. p.112.

Nandapurkar, P. J., D. R. Poirier et J. C. Heinrich. 1991. « The Momentum Equation for Dendritic Solidification ». *Numerical Heat Transfer, Part A*, vol. 19, p. 297-311.

Naterer, G. F. 1997. « Simultaneous Pressure - Velocity Coupling in the Two-phase Zone for Solidification Shrinkage in an Open Cavity ». *Modelling and Simulation in Materials Science and Engineering*, vol. 5, p. 595-613.

Ni, J., et C. Beckermann. 1991. « A Volume-averaged Two-phase Model for Transport Phenomena during Solidification ». *Metallurgical Transactions B*, vol. 22, p. 349-363.

Noeppel, A., O. Budenkova, G. Zimmermann, L. Sturz, N. Mangelinck- Noël et H. Jung. 2009. « Numerical Modelling of Columnar to Equiaxed Transition-application to Microgravity Experiments ». *International Journal of Cast Metals Research*, vol. 22, nº 1-4, p. 34-38.

Ohnaka, T. 1984. « Solute Redistribution with Back-diffusion in Solid during Solidification

246

Process ». *Tetsu-to-Hagané*, vol. 70, S913.

Pardeshi, R., V. R. Voller, A. K. Singh et P. Dutta. 2008. « An Explicit–implicit Time Stepping Scheme for Solidification Models ». *International Journal of Heat and Mass Transfer*, vol. 51, nº 13-14, p. 3399-3409.

Physical Constants of Some Commercial Steels at Elevated Temperatures: Based on Measurements Made at the National Physics Laboratory, Teddington. 1953. Edited by the British Iron and Steel Research Association, Metallurgy General Division, Thermal Treatment Sub-Committee, Butterworth.

Pickering, E. J., C. Chesman, S. Al-Bermani, M. Holland, P. Davies et J. Talamantes-Silva. 2015. « A Comprehensive Case Study of Macrosegregation in a Steel Ingot ». *Metallurgical Materials Transactions B*, vol. 46, nº 4, p. 1860-1874.

Pickering, E. J. 2013. « Macrosegregation in Steel Ingots: The Applicability of Modelling and Characterisation Techniques ». *ISIJ International*, vol. 53, n° 6, p. 935-949.

Pikkarainen, T., V. Vuorenmaa, I. Rentola, M. Leinonen et D. Porter. 2016. « Effect of superheat on macrostructure and macrosegregation in continuous cast low-alloy steel slabs ». *4th International Conference on Advances in Solidification Processes (ICASP-4) IOP Publishing IOP Conf. Series: Materials Science and Engineering*, vol. 117, 012064, p. 1-7.

Piwonka, T. S., et M. C. Flemings. 1966. « Pore Formation in Solidification ». *Transactions of the Metallurgical Society of AIME*, vol. 236, p. 1157-1166.

Poirier, D. R., et J. C. Heinrich. 1994. « Continuum Model for Predicting Macrosegregation in Dendritic Alloys ». *Materials Characterization*, vol. 32, p. 287-298.

Poirier, D. R., P. Nandapurkar et S. Ganesan. 1991. « The Energy and Solute Conservation Equations for Dendritic Solidification ». *Metallurgical Transactions B*, vol. 22, p. 889-900.

Poirier, D. R., et P. Nandapurkar. 1988. « Enthalpies of a Binary Alloy during Solidification ». *Metallurgical Transactions A*, vol. 19, p. 3057-3061.

Prakash, C. 1990. « Two-phase Model for Binary Solid-liquid Phase Change, Part I: Governing Equations ». *Numerical Heat Transfer, Part B: Fundamentals*, vol. 18, p. 131-145.

Prakash, C. 1990. « Two-phase Model for Binary Solid-liquid Phase Change, Part II: Some Illustrative Examples ». *Numerical Heat Transfer, Part B: Fundamentals*, vol. 18, p. 147-167.

Prescott, P. J., et F. P. Incropera. 1995. « The Effect of Turbulence on Solidification of a Binary Metal Alloy with Electromagnetic Stirring ». *Transactions of ASME*, vol. 117,

nᵒ 3, p. 716-724.

Qian, S., X. Hu, Y. Cao, X. Kang et D. Li. 2015. « Hot Top Design and Its Influence on Feeder Channel Segregates in 100-ton Steel Ingots ». *Materials & Design*, vol. 87, p. 205-214.

Reikher, A., H. Gerber, K. M. Pillai et T. C. Jen. 2010. « Natural Convection - An Overlooked Phenomenon of the Solidification Process ». *Die Casting Engineer*, vol. 1, p. 28-31.

Rappaz M., et P. Thevoz. 1987. « Solute Diffusion Model for Equiaxed Dendritic Growth ». *Acta Metallurgica*, vol. 35, nᵒ 7, p. 1487-1497.

Rappaz M., et V. R. Voller. 1990. « Modelling of Micro-macrosegregation in Solidification Processes ». *Metallurgical Transactions A*, vol. 21, nᵒ 2, p. 749-753.

Rappaz, M. 1989. « Modeling of microstructure formation in solidification processes ». *International Materials Reviews*, vol. 34, nᵒ 1, p. 93-123.

Ravindran, K., et R. W. Lewis. 1998. « Finite Element Modelling of Solidification Effects in Mould Filling ». *Finite Elements in Analysis and Design*, vol. 31, nᵒ 2, p. 99-116.

Reikher, A., et M. R. Barkhudarov. 2007. *Casting: An Analytical Approach - Engineering Materials and Processes*. Verlag London Ltd., London, UK, p. 23-25.

Ridder, S. D., S. Kou et R. Mehrabian. 1981. « Effect of Fluid Flow on Macrosegregation in Axi-symmetric Ingots ». *Metallurgical Transactions B*, vol. 12, nᵒ 3, p. 435-447.

Rutskii, D. V., S. B. Gamanyuk, N. A. Zyuban, V. F. Petrova et L. V. Palatkina. 2017. « Effect of Liquid-solid Pouring on the As-cast Structure and the Distribution of Non-metallic Inclusions in a 24.2-t Steel 38KhN3MFA Ingot ». *Russian Metallurgy* (*Metally*), vol. 2017, n° 5, p. 376-383.

Sang, B. G., X. H. Kang, D. R. Liu et D. Z. Li. 2010. « Study on Macrosegregation in Heavy Steel Ingots ». *The International Journal of Cast Metals Research*, vol. 23, nᵒ 4, p. 205-210.

Scarabello, D., A. Ghiotti et S. Bruschi. 2010. « FE Modelling of Large Ingot Hot Forging ». *International Journal of Material Forming*, vol. 3, Supp. 1, p. 335-338.

Schaffnit, P., C. Stallybrass, J. Konrad, F. Stein et M. Weinberg. 2015. « A Scheil-Gulliver Model Dedicated to the Solidification of Steel ». *Calphad*, vol. 48, p. 184-188.

Scheil, E., et E. Metallk. 1942. « Bemerkungen zur Schichtkristallbildung ». *Z. Metallkde*, vol. 34, p. 70-72.

Schneider, C. A., W. S. Rasband et K. W. Eliceiri. 2012. « NIH Image to ImageJ: 25 years of

image analysis ». *Nature Methods*, vol. 9, n° 7, p. 671-675.

Schneider, M. C., et C. Beckermann. 1991. « Effects of Simplified Enthalpy Relations on the Prediction of Heat Transfer during Solidification of a Lead-tin Alloy ». *Applied Mathematical Modelling*, vol. 15, n° 11-12, p. 596-605.

Schneider, M. C., et C. Beckermann. 1995. « A Numerical Study of the Combined Effects of Microsegregation, Mushy Zone Permeability and Flow, Caused by Volume Contraction and Thermosolutal Convection, on Macrosegregation and Eutectic Formation in Binary Alloy Solidification ». *International Journal of Heat and Mass Transfer*, vol. 38, p. 3455-3473.

Schneider, M. C., et C. Beckermann. 1995. « Formation of Macrosegregation by Multicomponent Thermosolutal Convection during Solidification of Steel ». *Metallurgical and Materials Transactions A*, vol. 26, n° 9, p. 2373-2388.

Schneider, M. C., J. P. Gu, C. Beckermann, W. J. Boettinger et U. R. Kattner. 1997. « Modeling of Micro and Macrosegregation and Freckle Formation in Single Crystal Nick-based Superalloy Directional Solidification ». *Metallurgical and Materials Transactions A*, vol. 28, p. 1517-1531.

Shahriari, D., A. Loucif, M. Jahazi, R. Tremblay et B. Beauvais. 2015. « 3D Numerical Simulation of Solidification of Large Size Ingots of High Strength Steel ». In: *SteelSim* 2015, *6th International Conference on Modelling and Simulation of Metallurgical Processes in Steelmaking*.

Singh, A. K., B. Basu et A. Ghosh. 2006. « Role of Appropriate Permeability Model on Numerical Prediction of Macrosegregation ». *Metallurgical and Materials Transactions B*, vol. 37, n° 5, p. 799-809.

Singer, A. R. E., et R. W. Evans. 1983. « Incremental solidification and forming. Metals Technology ». *Journals of Materials Science & Technology*, vol. 10, nº 1, p. 61-68.

Smith, W. F., et J. Hashemi. 2006. *Foundations of Materials Science and Engineering*. 4th ed. McGraw-Hill.

Spittle, J. A. 2006. « Columnar to Equiaxed Grain Transition in as Solidified Alloys ». *International Materials Reviews*, vol. 51, p. 247-269.

Su, H., H. Wang, J. Zhang, M. Guo, L. Liu et H. Fu. 2018. « Influence of Melt Superheating Treatment on Solidification Characteristics and Rupture Life of a Third-Generation Ni-Based Single-Crystal Superalloy ». *Metallurgical and Materials Transactions B*, vol. 49, nº 4, p. 1537-1546.

Sun, Q. Y., D. R. Liu, J. J. Zhang, L. P. Wang et E. J. Guo. 2016. « Numerical Simulation of Macrosegregation with Grain Motion during Solidification of Mg-4wt.%Y Alloy ».

Modern Physics Letters B, vol. 30, n° 36, 1450417.

Sung, P. K., D. R. Poirier et S. D. Felicelli. 2002. « Continuum Model for Predicting Microporosity in Steel Castings ». *Modelling and Simulation in Material Science and Engineering*, vol. 10, p. 551-568.

Suzuki, A., T. Suzuki et Y. Nakaoka. 1968. « Nippon Kinzoku Gakkaishi ». *The Japan Institute of Metals*, vol. 32, p. 1301-1305.

Suzuki K., et K. Taniguchi. 1981. « The Mechanism of Reducing "A" Segregates in Steels Ingots ». *Transactions ISIJ*, vol. 21, p. 235-242.

Szekely, J., et A. S. Jassal. 1978. « An Experimental and Analytical Study of the Solidification of a Binary, Dendritic System ». *Metallurgical Transactions B*, vol. 9, n° 3, p. 389-398.

Taguchi, I., K. Miyamura et H. Soga. 1984. « New Evaluation Techniques of Segregation in Continuously Cast Steel ». *Transactions of the Iron and Steel Institute of Japan*, vol. 24, n° 11, p. 883-890.

Tanzer, R., W. Schutzenhofer, G. Reiter, H. P. Fauland, L. Konozsy, A. Ishmurzin, M. Wu et A. Ludwig. 2009. « Validation of a Multiphase Model for the Macrosegregation and Primary Structure of High-grade Steel Ingots ». *Metallurgical and Materials Transactions B*, vol. 40, n° 3, p. 305-311.

TherCast 8.2®. 2012. Transvalor, S. A., Cedex, France

Thermal Properties of Metals, Conductivity, Thermal Expansion, Specific Heat. Metal Products Distributor Supplier. Http://www.engineersedge.com/properties of metals.htm.

*Thermo Scientific ARL*TM *4460 Optical Emission Spectrometer*. Thermo Fisher Scientific Inc., Waltham, MA, USA.

Tu, W. T., H. F. Shen et B. C. Liu. 2015. « Modelling of Macrosegregation in a 231-ton Steel Ingot with Multi-pouring Process ». Materials Research Innovations, vol. 19, p. S59-S63.

Vandersluis, E., et C. Ravindran. 2017. « Comparison of Measurement Methods for Secondary Dendrite Arm spacing ». *Metallography, Microstructure, and Analysis*, vol. 6, n° 1, p. 89-94.

Vannier, I., H. Combeau et G. Lesoul. 1993. « Numerical-model for Prediction of the Final Segregation Pattern of Bearing Steel Ingots ». *Materials Science and Engineering A*, vol. 173, n° 1-2, p. 317-321.

Vives, C., et C. Perry. 1986. « Effects of Electromagnetic Stirring during the Controlled

Solidification of Tin ». *International Journal of Heat and Mass Transfer*, vol. 29, nº 1, p. 21–33.

Voller, V. R., A. Mouchmov et M. Cross. 2004. « An Explicit Method for Coupling Temperature and Concentration Fields in Solidification Models ». *Applied Mathematical Modelling*, vol. 28, n° 1, p. 79-94.

Voller, V. R., et C. Beckermann. 1999. « A Unified Model of Microsegregation and Coarsening ». *Metallurgical Materials Transactions A*, vol. 30, n° 8, p. 2183-2189.

Voller, V. R., et A. D. Brent. 1989. « The Modelling of Heat, Mass and Solute Transport in Solidification Systems ». *International Journal of Heat and Mass Transfer*, vol. 32, n° 9, p. 1719-1731.

Wang, B., Y. Yang et W. Tang. 2008. « Microstructure Refinement of AZ91D Alloy Solidified with Pulsed Magnetic Field ». *Transactions of Nonferrous Metals Society of China*, vol. 18, nº 3, p. 536-540.

Wang, C. Y., et C. Beckermann. 1993. « A Unified Solute Diffusion Model for Columnar and Equiaxed Dendritic Alloy Solidification ». *Materials Science and Engineering A*, vol. 171, n° 1-2, p. 199-221.

Wang, C. Y., et C. Beckermann. 1994. « Prediction of Columnar to Equiaxed Transition during Diffusion-controlled Dendritic Alloy Solidification ». *Metallurgical and Materials Transactions A*, vol. 25, n° 5, p. 1081-1093.

Wang, C. Y., et C. Beckermann. 1996. « Equiaxed Dendritic Solidification with Convection: Part I. Multiscale/multiphase Modeling ». *Metallurgical and Materials Transactions A*, vol. 27, n° 9, p. 2754-2764.

Wang, C. Y., et C. Beckermann. 1996. « Equiaxed Dendritic Solidification with Convection: Part II. Numerical Simulation for an Al-4Wt Pct Cu Alloy ». *Metallurgical and Materials Transactions A*, vol. 27, n° 9, p. 2765-2783.

Wang, X., N. Ma, D. F. Bliss, G. W. Isele et P. Becla. 2007. « Combining Static and Rotating Magnetic Fields during Modified Vertical Bridgman Crystal Growth ». *Journal of Thermophysics and Heat Transfer*, vol. 21, nº 4, p. 736-743.

Willers, B., S. Eckert, U. Michel, I. Haase et G. Zouhar. 2005. « The Column-to-Equiaxed Transition in Pb-Sn Alloys Affected by Electromagnetically Driven Convection ». *Materials Science And Engineering A*, vol. 402, nº 1-2, p. 55-65.

Wolczynski, W.. 2015. « Back-diffusion in Crystal Growth. Eutectics ». *Archives of Metallurgy and Materials*, vol. 60, p. 2403-2407.

Wolczynski, W.. 2015. « Back-diffusion in Crystal Growth. Peritectics ». *Archives of*

Metallurgy and Materials, vol. 60, p. 2409-2414.

Wolczynski, W.. 2018. « Nature of segregation in the steel static and brass continuously cast ingots ». *Archives of Metallurgy and Materials*, vol. 63, p. 1915-1922.

Wolczynski, W., A. A. Ivanwa et P. Kwapisinski. 2018. « Mathematical Prediction of Brass/steel Ingot Structure ». *Scientific Journals of the Maritime University of Szczecin*, vol. 56, p.47-54.

Wolczynski, W., A. A. Ivanwa et P. Kwapisinski. 2019. « On Consonance between a Mathematical Method for the CET Prediction and Constrained/unconstrained Solidification ». Procedia Manufacturing, vol. 30, p. 459-466.

Won, Y. M., et B. G. Thomas. 2011. « Simple Model of Microsegregation during Solidification of Steels ». *Metallurgical and Materials Transactions A*, vol. 32, n° 7, p. 1755-1767.

Wu, M., et A. Ludwig. 2000. « Modeling Equiaxed Solidification with Melt Convection and Grain Sedimentation, Part I: Model Description ». *Acta Materialia*, vol. 57, n° 19, p. 5621-5631.

Wu M., et A. Ludwig. 2000. « Modeling Equiaxed Solidification with Melt Convection and Grain Sedimentation, Part II: Illustrative Modelling Results and Parameter Studies ». *Acta Materialia*, vol. 57, n° 19, p. 5632-5644.

Wu, M., et A. Ludwig. 2006. « A Three-phase Model for Mixed Columna-equiaxed Solidification ». *Metallurgical and Materials Transactions A*, vol. 37, p. 1613-1631.

Wu, M., et A. Ludwig. 2007. « Using a Three-phase Deterministic Model for the Columnar-to-equiaxed Transition ». *Metallurgical and Materials Transactions A*, vol. 38A, p. 1465-1475.

Wu, M., et A. Ludwig. 2009. « Modeling Equiaxed Solidification with Melt Convection and Grain Sedimentation - I: Model Description ». *Acta Materialia*, vol. 57, p. 5621-5631.

Wu, M., A. Fjeld et A. Ludwig. 2010. « Modeling Mixed Columnar-equiaxed Solidification with Melt Convection and Grain Sedimentation - Part I: Model Description ». *Computational Materials Science*, vol. 50, n° 1, p. 32-42.

Wu, M., A. Ludwig et A. Fjeld. 2010. « Modelling Mixed Columnar-equiaxed Solidification with Melt Convection and Grain Sedimentation - Part II: Illustrative Modelling Results and Parameter Studies ». *Computational Materials Science*, vol. 50, n° 1, p. 43-58.

Wu, M., A. Vakhrushev, G. Nummer, C. Pfeiler, A. Kharicha et A. Ludwig. 2010. « Importance of Melt Flow in Solidifying Mushy Zone ». *The Open Transportation Jounral*, vol. 2, p. 16-23.

Xiong, M., et A.V. Kuznetsov. 2001. « Comparison between Lever and Scheil Rules for Modeling of Microporosity Formation during Solidification ». *Flow, Turbulence and Combustion*, vol. 67, n° 4, p. 305-323.

Xu, D., et Q. Li. 1991. « Numerical Simulation of Heat Mass and Momentum Transfers in Metallic Ingots and Prediction of Macrosegregation ». Acta Metallurgica Sinica, vol. 4, n° 7, p. 37-41.

Xu, P. G., F. Yin et K. Nagai. 2006. « Solidification Cooling Rate and As-cast Textures of Low-carbon Steel Strips ». *Materials Science and Engineering A*, vol. 441, nº 1-2, p. 157-166.

Ya, S. Q., D. R. Liu, J. J. Zhang, L. P. Wang et E. J. Guo. 2016. « Numerical Simulation of Macrosegregation with Grain Motion during Solidification of Mg-4wt.%Y Alloy ». Modern Physics Letters B, vol. 30, n° 36, 165047.

Yadav, A., N. Pathak, A. Kumar, P. Dutta, et S. Sarkar. 2009. « Effects of the Filling Process on the Evolution of the Mushy Zone and Macrosegregation in Alloy Casting ». *Modelling and Simulation in Materials Science*, vol. 17, nº 3, p. 1-19.

Zeng, J., et W. Chen. 2015. « Effect of Casting Speed on Solidification Structure and Central Macrosegregation during Continuous Casting of High-carbon Rectangular Billet ». *La Metallurgia Italiana*, vol. 107, nº 7, p. 43-50.

Zhang, B., et J. Cui. 2003. « Structural Materials: Properties, Microstructure and Processing ». *Material Science and Engineering A*, vol. 355, n° 25, p. 325-330.

Zhang, B., J. Cui et G. Lu. 2003. « Effect of Low-frequency Magnetic Field on Macrosegregation of Continuous Casting Aluminum Alloys ». *Materials Letters*, vol. 57, n° 11, p. 1707-1711.

Zhang, C., A. Loucif, M. Jahazi, R. Tremblay et L. P. Lapierre Boire. 2018. « On the Effect of Filling Rate on Positive Macrosegregation Patterns in Large Size Cast Steel Ingots ». *Applied Sciences*, vol. 8, n° 10, 1878, p. 1-11.

Zhang, C., D. Shahriari, A. Loucif, H. Melkonyan et M. Jahazi. 2018. « Influence of Thermomechanical Shrinkage on Macrosegregation during Solidification of a Large-sized High-strength Steel Ingot ». *The International Journal of Advanced Manufacturing Technology*, vol. 99, n° 9-12, p. 3035-3048.

Zhang, C., D. Shahriari, A. Loucif, M. Jahazi, L. P. Lapierre-Boire et R. Tremblay. 2017. « Effect of Segregated Alloying Elements on the High Strength Steel Properties: Application to the Large Size Ingot Casting Simulation ». *TMS 2017 146th Annual Meeting & Exhibition Supplemental Proceedings*, p. 491-500.

Zhang, C., Y. Bao et M. Wang. 2016. « Influence of Casting Parameters on Shrinkage Porosity of a 19 Ton Steel Ingot ». *La Metallurgia Italiana*, vol. 108, nº 1, p. 37-44.

Zhang, S. Y., J. S. Li, H. C. Kou, J. R. Yang, G. Yang et J. Wang. 2016. « Effect of Mold Temperature and Casting Dimension on Microstructure and Tensile Properties of counter-Gravity Casting Ti-6Al-4V Alloys ». *China Foundry*, vol. 13, nº 1, p. 9-14.

Zhang, Y., G .R. Jia, X. J. Xie, S. S. Xie, J. Y. He, D. F. Li, W. S. Sun et M. P. Geng. 2011. « Numerical Simulation and Optimization in Solidification of Zinc Alloy ». *Advanced Materials Research*, vol. 287-290, p. 2902-2905.

Zhao, Z., J. Cui et H. Nagumi. 2005. « Effect of Low-frequency Magnetic Fields on Microstructures of Horizontal Direct Chill Cast 2024 Aluminum Alloys ». *Materials Transactions*, vol. 8, p. 1903-1907.

Zhao, Z., J. Cui, J. Dong et B. Zhang. 2007. « Effect of Low-frequency Magnetic Field on Microstructures and Macrosegregation of Horizontal Direct Chill Casting 7075 Aluminum Alloy ». *Journal of Materials Processing Technology*, vol. 182, nº 1-3, p. 185-190.

Zhong, H., Y. Tan, H. Li, X. Mao et O. Zhai. 2012. « The effect of high superheat on the solidification structure and carbon segregation of ferrite-based alloy ». *Supplemental proceedings: Volume 1: Materials Processing and Interfaces TMS (the Minerals, Metals & Materials Society)*, p. 215-220.

Zhu, Q. F., Z. H. Zhao, J. Z. Cui, Y. B. Zuo et X. J. Wang. 2008. « Effect of Combined Application of Electromagnetic Fields on Horizontal Direct Chill Casting of 7050 Aluminium Alloy ». *Materials Science and Technology*, vol. 24, nº 5, p. 560-566.

Zulaida, Y. M., et Suryana. 2016. « Macrosegregation and Dendritic Structure Formation in Different Solute composition ». *AIP Conference Proceedings*, vol. 1746, 020011.